

## Molecular simulations of vesicles and dendrimers

***Citation for published version (APA):***

Smeijers, A. F. (2021). *Molecular simulations of vesicles and dendrimers*. [Phd Thesis 1 (Research TU/e / Graduation TU/e), Biomedical Engineering]. Technische Universiteit Eindhoven.

***Document status and date:***

Published: 09/03/2021

***Document Version:***

Publisher's PDF, also known as Version of Record (includes final page, issue and volume numbers)

***Please check the document version of this publication:***

- A submitted manuscript is the version of the article upon submission and before peer-review. There can be important differences between the submitted version and the official published version of record. People interested in the research are advised to contact the author for the final version of the publication, or visit the DOI to the publisher's website.
- The final author version and the galley proof are versions of the publication after peer review.
- The final published version features the final layout of the paper including the volume, issue and page numbers.

[Link to publication](#)

***General rights***

Copyright and moral rights for the publications made accessible in the public portal are retained by the authors and/or other copyright owners and it is a condition of accessing publications that users recognise and abide by the legal requirements associated with these rights.

- Users may download and print one copy of any publication from the public portal for the purpose of private study or research.
- You may not further distribute the material or use it for any profit-making activity or commercial gain
- You may freely distribute the URL identifying the publication in the public portal.

If the publication is distributed under the terms of Article 25fa of the Dutch Copyright Act, indicated by the "Taverne" license above, please follow below link for the End User Agreement:

[www.tue.nl/taverne](http://www.tue.nl/taverne)

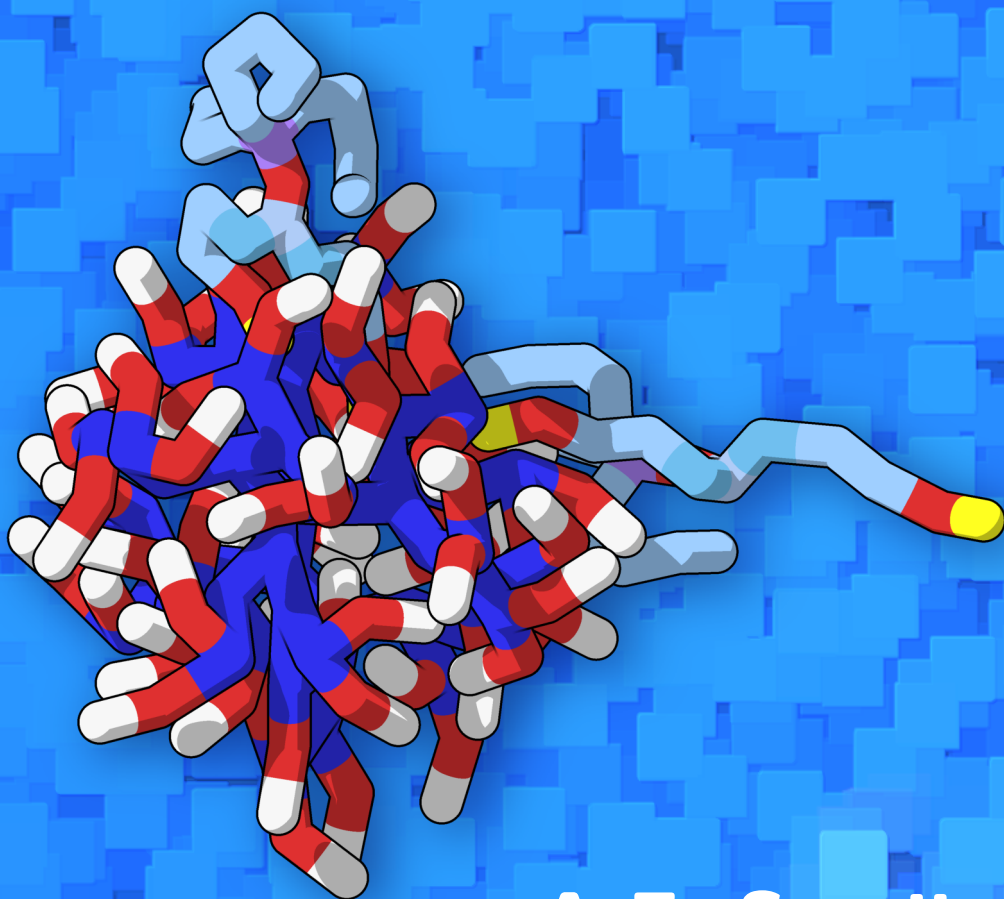
***Take down policy***

If you believe that this document breaches copyright please contact us at:

[openaccess@tue.nl](mailto:openaccess@tue.nl)

providing details and we will investigate your claim.

# Molecular simulations of vesicles and dendrimers



A.F. Smeijers



# **Molecular simulations of vesicles and dendrimers**

A catalogue record is available from the Eindhoven University of Technology Library.

ISBN: 978-90-386-5011-1.

Copyright © 2020 by A.F. Smeijers.

All rights reserved. No part of this publication may be reproduced, stored in a retrieval system, or transmitted in any form or by any means, electronic, mechanical, photocopying, recording, or otherwise, without the prior written permission of the author.

Cover design by A.F. Smeijers.

Printed by Van de Ven Printservice & Drukkerij, Hilvarenbeek.

# Molecular simulations of vesicles and dendrimers

PROEFSCHRIFT

ter verkrijging van de graad van doctor aan de Technische Universiteit Eindhoven, op gezag van de rector magnificus prof.dr.ir. F.P.T. Baaijens, voor een commissie aangewezen door het College voor Promoties, in het openbaar te verdedigen op dinsdag 31 maart 2020 om 16:00 uur

door

Adrianus Franciscus Smeijers

geboren te Tilburg

Dit proefschrift is goedgekeurd door de promotoren en de samenstelling van de promotiecommissie is als volgt:

voorzitter: prof.dr. M. Merkx  
le promotor: prof.dr. P.A.J. Hilbers  
copromotor: dr.ir. A.J. Markvoort  
leden: prof.dr. E.W. Meijer  
prof.dr.ir. J.C.M. van Hest  
prof.dr. S.J. Marrink (Rijksuniversiteit Groningen)  
prof.dr. G.M. Pavan (Politecnico di Torino)

*Het onderzoek dat in dit proefschrift wordt beschreven is uitgevoerd in overeenstemming met de TU/e Gedragscode Wetenschapsbeoefening.*

# Contents

<b>1</b>	<b>Introduction</b>	<b>1</b>
1.1	Nanoparticles	2
1.2	Vesicles	3
1.3	Dendrimers	4
1.4	Molecular dynamics	5
1.5	Coarse-graining	6
1.6	Thesis outline	7
	Bibliography	8
<b>2</b>	<b>A detailed look at vesicle fusion</b>	<b>13</b>
2.1	Introduction	14
2.2	Methods	16
2.2.1	Molecular dynamics	16
2.2.2	Lipid model	18
2.2.3	PumMa	19
2.2.4	Simulations	20
2.3	Results	21
2.3.1	Fusion of large vesicles	21
2.3.2	Fusion of small vesicles	26
2.3.3	Exocytosis: fusion of vesicle and bilayer	26
2.4	Discussion	27
2.4.1	Bridging lipids	27
2.4.2	Stalk	29
2.4.3	Anisotropic stalk expansion and stalk-bending	30
2.4.4	Radial stalk expansion	30
2.4.5	Radial or anisotropical stalk expansion	31
2.4.6	Hemifusion diaphragm	31
2.5	Conclusion	32
	Bibliography	33
<b>3</b>	<b>Transmembrane protein-influenced vesicle fusion</b>	<b>37</b>
3.1	Introduction	38
3.2	Methods	39
3.2.1	Lipid and water	39
3.2.2	Water channel	39
3.2.3	Scramblases	40
3.2.4	Simulations	42
3.3	Results	43
3.3.1	Bilayers	43



3.3.2	Small vesicles . . . . .	47
3.3.3	Small vesicle fusion . . . . .	48
3.3.4	Fusion of large vesicles . . . . .	52
3.3.5	Bilayer fusion . . . . .	53
3.4	Discussion . . . . .	54
3.4.1	Hydrophobic matching and aggregation . . . . .	54
3.4.2	Engulfing lobe . . . . .	55
3.4.3	Scramblase flip-flop . . . . .	56
3.4.4	Fusion facilitated by type B scramblases . . . . .	56
3.5	Conclusion . . . . .	57
	Bibliography . . . . .	58
<b>4</b>	<b>Coarse-grained modeling of poly(propylene imine) dendrimers . . . .</b>	<b>61</b>
4.1	Introduction . . . . .	62
4.2	Model . . . . .	64
4.2.1	Coarse-grained sites . . . . .	64
4.2.2	Interaction potentials . . . . .	65
4.3	Results and discussion . . . . .	73
4.3.1	Simulations . . . . .	73
4.3.2	Radius of gyration . . . . .	74
4.3.3	Aspect ratios . . . . .	76
4.3.4	Asphericity . . . . .	78
4.3.5	Radial monomer density . . . . .	79
4.3.6	Spacer expansion . . . . .	81
4.3.7	Solvent-excluded surface volume . . . . .	82
4.3.8	Form factor . . . . .	83
4.4	Conclusion . . . . .	84
4.5	Appendix . . . . .	86
4.5.1	Modeling: Atomistic input . . . . .	86
4.5.2	Modeling: Iterative coarse-grained simulations . . . . .	86
4.5.3	Measurements: Fully atomistic simulations . . . . .	87
4.5.4	Measurements: Coarse-grained simulations . . . . .	90
4.5.5	A consideration of the asphericity measurement . . . . .	91
	Bibliography . . . . .	91
<b>5</b>	<b>Poly(propylene imine) dendrimers in dilute to melt conditions . . . .</b>	<b>97</b>
5.1	Introduction . . . . .	98
5.2	Model . . . . .	99
5.3	Results and discussion . . . . .	100
5.3.1	Radius of gyration . . . . .	100
5.3.2	Structure factor . . . . .	101
5.3.3	Intermolecular spacing . . . . .	107
5.3.4	Dendrimer interpenetration . . . . .	110
5.3.5	Overlap concentration . . . . .	113

---

5.3.6	Water penetration . . . . .	114
5.4	Conclusion . . . . .	115
5.5	Appendix . . . . .	116
5.5.1	Coarse-grained simulations . . . . .	116
5.5.2	Relaxation times . . . . .	118
	Bibliography . . . . .	120
<b>6</b>	<b>Multivalency in a dendritic host–guest system . . . . .</b>	<b>123</b>
6.1	Introduction . . . . .	124
6.2	Model . . . . .	126
6.2.1	Atomistic assemblies . . . . .	126
6.2.2	Coarse-grained parameter fitting . . . . .	127
6.2.3	Guest parameter fine-tuning . . . . .	130
6.2.4	Coarse-grained simulation setup . . . . .	132
6.3	Results and discussion . . . . .	133
6.3.1	Macromolecular nanostructures . . . . .	133
6.3.2	Guest binding details . . . . .	135
6.3.3	Multivalent guest concentrations . . . . .	136
6.3.4	Effective concentration . . . . .	140
6.3.5	Alternative spacer length . . . . .	142
6.3.6	Competition between guest types . . . . .	144
6.4	Conclusion . . . . .	146
6.5	Appendix . . . . .	148
6.5.1	Modeling: Tetravalent ureido acetic acid guest . . . . .	148
6.5.2	Measurements: Coarse-grained simulation parameters . . . . .	148
6.5.3	Measurements: Atomistic aggregate simulations . . . . .	150
6.5.4	Measurements: Atomistic bivalent ureido acetic acid guest . . . . .	152
	Bibliography . . . . .	152
<b>7</b>	<b>Concluding remarks . . . . .</b>	<b>157</b>
7.1	Summary of contributions . . . . .	158
7.2	Discussion . . . . .	164
	Bibliography . . . . .	167
	<b>Summary . . . . .</b>	<b>173</b>
	<b>Publications . . . . .</b>	<b>175</b>
	<b>Acknowledgments . . . . .</b>	<b>177</b>
	<b>Curriculum vitae . . . . .</b>	<b>179</b>



# Chapter 1

## Introduction

---

**Abstract** The regulated transport of critical molecules is important in drug delivery systems as well as in the living cell. Targeted transport is handled at the molecular level by nanoparticles. In the cell these carriers are vesicles, spherical compartments composed of lipids whose amphiphilic nature provides the vesicles with the remarkable ability to spontaneously mend holes and to fuse with cellular membranes. In drug delivery systems, to exercise control over delivery of pharmaceuticals, apart from artificial vesicles also polymeric nanoparticles are in use. Among these polymers, dendrimers are unique for their distinctive branched structure, a result of their well-controlled synthesis. These dendrimers are ideally suited for host–guest chemistry, as their ends can be functionalized to create a defined number of interaction sites for compatible guests to bind to. Because observing the dynamic behavior of individual molecules in the vesicle and dendrimer systems is experimentally infeasible, we employ molecular dynamics to study the function and behavior of these nanoparticles. As the required time and length scales are too large for conventional all-atom simulations, we use a coarse-graining approach to reduce the complexity of the models while retaining important chemical detail, so that extensive simulations become practical.

---

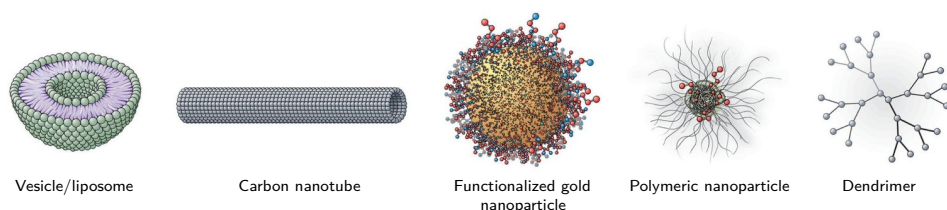


**Figure 1.1:** Various nanoparticles (reproduced from van Rijt et al. [7] with permission of the © ERS 2020).

## 1.1 Nanoparticles

In the living cell as well as in drug delivery systems, accurate control over transport of critical molecules is of vital importance. In both cases, it is desired to precisely regulate which specialized molecules are to be transported to what exact destination and when they are to be released. For that purpose, tiny (<100 nm diameter) vehicles known as *nanoparticles* are used as carriers.<sup>[1-5]</sup>

Conventional parenteral drugs rely on the unimolecular drug to freely reach its destination at the diseased tissue once entered into the blood stream. However, the drug may have non-ideal properties that reduces its therapeutic effect, like poor solubility, rapid breakdown, and lack of selectivity for the target tissue. These pharmacological properties can be improved by designing nanoparticle-based drug delivery systems that enhance the absorption and target the distribution, while reducing premature metabolism and excretion.<sup>[1,2,4]</sup> Release of the drug can be triggered by internal stimuli such as changes in pH, enzyme concentration or redox gradients, or even in response to external stimuli such as variations in temperature, magnetic field, ultrasound intensity, light or electric pulses.<sup>[6]</sup> Thus the drug's efficacy may be enhanced by accumulating drugs in diseased tissues, while the lower overall dosage leads to fewer undesirable side effects.<sup>[1]</sup> Figure 1.1 shows some examples of different kinds of nanoparticles in clinical use, namely artificial vesicles (*liposomes*), carbon nanotubes, metallic nanoparticles, inorganic (ceramic) nanoparticles, polymeric nanoparticles, magnetic nanoparticles, and dendrimers.<sup>[2,5,7]</sup> Each type has unique structural properties, including size, shape, deformability, surface charge, and chemical composition.<sup>[4]</sup> Some particles allow therapeutic agents to reside inside a flexible matrix, while solid ones only allow attachment to the outside.<sup>[2]</sup> All these characteristics affect their *in vivo* pharmacological behavior.<sup>[4]</sup> In this thesis we focus our attention on two types of nanoparticles: vesicles and dendrimers.

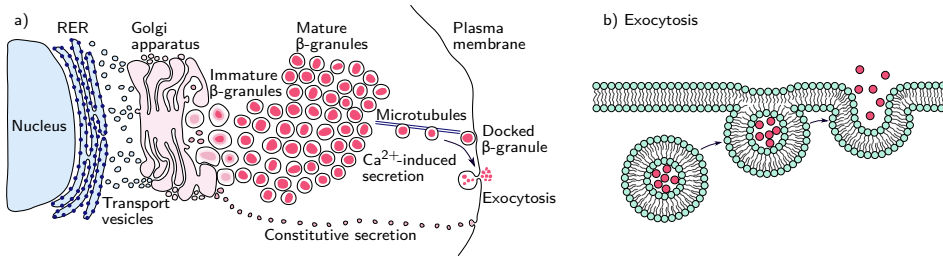


**Figure 1.2:** Vesicle transport. (a) Intracellular vesicle transport in a healthy  $\beta$ -cell (adapted from Boland et al. <sup>[18]</sup>). (b) A detail showing lipid membranes that fuse during exocytosis.

## 1.2 Vesicles

In essence, vesicles are spherical lipid bilayers with an enclosed liquid. In water, the amphiphilic nature of phospholipids makes them spontaneously form micelles, bilayers, and vesicles. Then their hydrophobic tails assemble and are shielded from water by their hydrophilic headgroups. The lipid bilayers thus formed are fluid and can be considered as two-dimensional liquids with distinct monolayers.

As artificial vesicles, liposomes find clinical application in, e.g., gene therapy, <sup>[8,9]</sup> targeted drug delivery, <sup>[3,9,10]</sup> and contrast enhanced MRI. <sup>[11]</sup> With their lipid components, the main advantage of liposomes over other nanoparticles is their excellent biocompatibility. <sup>[3,12]</sup>

The cell membrane is made up of a sea of phospholipids with embedded proteins that are responsible for various biological activities. <sup>[13,14]</sup> The amphiphilic nature of the lipids not only gives rise to the bilayer structure, but also to remarkable characteristics, such as the ability to mend holes spontaneously, to bud off vesicles, and to fuse with other bilayers. <sup>[3,15]</sup> Furthermore, the lipid bilayer being impermeable for most ions, proteins and other hydrophilic molecules, is ideally suited for the principal task of cellular membranes, i.e., compartmentalization. Each cellular process must be carried out in a specific environment in a controlled way. While elementary components like metabolites and nucleotides may diffuse unassisted in the cytosol, <sup>[16,17]</sup> for other molecules intracellular transport is strictly regulated using vesicles. <sup>[13]</sup> Hence, these vesicles can be considered biological nanoparticles.

The uptake of blood glucose in muscle and fat tissue after eating a meal provides an excellent example to highlight various aspects of vesicular action. In the rough endoplasmic reticulum (RER) of the  $\beta$ -cells of the pancreas, proinsulin, a precursor to the signal hormone insulin, is steadily synthesized and immediately cleaved and folded to form proinsulin. <sup>[18]</sup> Vesicles containing proinsulin then bud from the RER and travel along microtubules pulled by motor proteins to the Golgi

apparatus, where they fuse releasing the proinsulin<sup>[19,20]</sup> (Figure 1.2a). At the other end of the Golgi apparatus, again vesicles containing proinsulin bud, however this vesicle serves as bioreactor. Here in an acidic environment (pH 5.5) proinsulin matures into insulin proper.<sup>[18]</sup> Healthy  $\beta$ -cells always maintain a reserve of these matured vesicles ( $\beta$ -granules), while keeping a portion docked at the cell membrane. Docking is mediated by SNARE proteins that are anchored in both apposing membranes, when bound they hold the membranes close together.<sup>[18,21]</sup> These vesicles await a signal cascade, initiated primarily<sup>[18]</sup> by high blood glucose levels, that ultimately instructs them to fuse with the cell membrane, secreting insulin into the circulation, a process called *exocytosis* (Figure 1.2b). Meanwhile, in striated muscles and fat tissue, glucose transporter type 4 (GLUT4) is responsible for the uptake of glucose. It is a transmembrane protein for passive glucose transport, as it transports glucose across the cell membrane down its concentration gradient. In these cells, GLUT4 proteins are also stored in vesicles, embedded in the membrane. The vesicles are similarly waiting for a signal at the end of the insulin transduction pathway that instructs them to fuse with the cell membrane, depositing GLUT4 thereby facilitating glucose transport.<sup>[22,23]</sup> Later, when glucose uptake needs to be reduced, the GLUT4 protein-embedded membrane again forms a storage vesicle that returns to the cytosol, a process called *endocytosis*.<sup>[22]</sup>

Understanding the mechanisms by which vesicles and bilayers undergo fusion is thus essential. In this thesis we elucidate the basic mechanisms of fusion by investigating lipid bilayers in computer simulations of lipids at a molecular scale; first by studying how fusion is initiated between two small lipid vesicles, and also, resembling exocytosis, between a vesicle and a planar bilayer. Later, the effect of proteins is studied with model transmembrane proteins, one resembling a passive water channel and another that facilitates lipid exchange between the monolayers.

## 1.3 Dendrimers

Dendrimers are a class of polymeric macromolecules with a highly branched tree-like architecture.<sup>[24,25]</sup> Compared to other polymeric nanoparticles, they are well-defined due to their controlled iterative synthesis. Herein short branches emanate from a multifunctional core, each an anchoring point for a new set of short branches. Each iteration adds another generational shell of branches, multiplying the number of reactive ends. This process results in well-defined monodisperse structures. Additionally, their ends can be coupled to functional groups to provide specific features to the dendrimer. The large number of possible cores, branches and end-groups<sup>[26-28]</sup> allows for nanoengineering of properties like size, shape, topology, flexibility and surface chemistry. This in turn enables a wide range of applications. For instance, dendrimers have been used as concentrated dis-

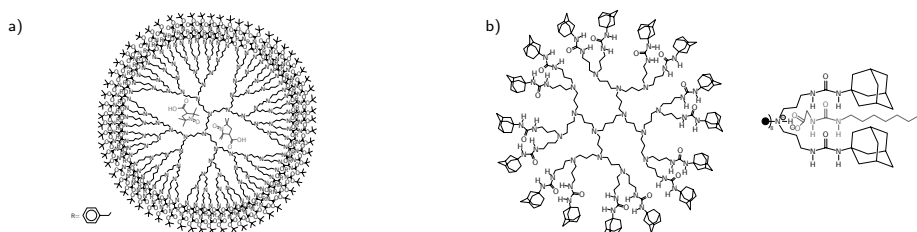


**Figure 1.3:** Two variants of dendrimer-based guest transport. (a) Dendritic box of DAB-*dendr*-(NH-*t*-BOC-L-Phe)<sub>64</sub> dendrimer with two trapped 3-carboxy-proxyl radicals.<sup>[44]</sup> (b) Third-generation adamantylurea-modified poly(propylene imine) dendrimer acting as a host for urea acid guests with its specific peripheral binding sites.<sup>[45]</sup>

plays of contrast agent,<sup>[24,25,29–31]</sup> as (stimuli-responsive) targeted drug delivery vehicles,<sup>[24,25,29,30,32–34]</sup> as DNA-carriers for gene therapy,<sup>[25,29,30,35,36]</sup> as enzyme mimics,<sup>[24,25,30]</sup> as biosensors,<sup>[25,30]</sup> and as building blocks in supramolecular structures.<sup>[24,30,37]</sup> Many of these applications are examples of host-guest chemistry, employing the dendrimer as a temporary host vehicle for non-covalently bound guest compounds.<sup>[24,25,29,30]</sup> The dendrimer is ideally suited for this, as small guests can be loaded in internal cavities and by subsequently modifying the end-groups to form a dense shell the *dendritic box* is closed<sup>[32]</sup> (Figure 1.3a). Alternatively, the ends can be functionalized to create a defined number of interaction sites for compatible guests to bind on the outside (Figure 1.3b).

In this thesis we specifically study poly(propylene imine) (PPI) dendrimers and their urea-adamantyl-functionalized counterparts. Next to poly(amido amine), poly(propylene imine) is one of the most commonly used dendrimer types in supramolecular<sup>[25,27,30,37]</sup> and medicinal chemistry.<sup>[29–31,36]</sup> The PPI dendrimers functionalized with urea-adamantyl ends serve as a host for ureido acetic acid guests.<sup>[38,39]</sup> We take the host-guest paradigm one step further by introducing multivalent guests. The concept of multivalency, i.e., the principle for binding between entities whereby multiple identical ligands bind to multiple identical receptors is often applied in nature.<sup>[40]</sup> Examples include the adhesion of viruses to host cells and the binding of antibodies to pathogens. In evolutionary terms it is easier to multiply a weak interaction to yield a potent collective than to invent a stronger one. The concept of multivalency is also applied successfully in supramolecular chemistry to self-assemble novel complexes.<sup>[41–43]</sup>

## 1.4 Molecular dynamics

It would be immensely helpful for our understanding of the vesicle and dendrimer systems to be able to observe them at the molecular level, but currently that is



rather difficult. For instance, it is possible to view stable intermediates in vesicle fusion of giant unilamellar vesicles using fluorescence microscopy in micrometer and millisecond resolution,<sup>[46–48]</sup> but not to view the phospholipids as they perform the fast transitions between fusion stages. Likewise with cryogenic transmission electron microscopy (cryo-TEM), clusters of dendrimers can be observed,<sup>[39,49]</sup> but not the dynamic interactions that lead to their formation.

To investigate both systems in detail, we use molecular dynamics (MD), a computer simulation technique to study the behavior of classical many-body systems. Given the current positions and velocities of all particles in a system (the state) and knowing their masses and the forces acting upon them (the model), the motion of all individual particles can be inferred for a sufficiently small time step. Thus, by iteratively calculating every particle's position and velocity the system dynamics can be followed through time. The force exerted on a particle is equal to the negative gradient of the potential energy acting on that particle, which is made up of bonded and non-bonded interaction potentials.<sup>[50]</sup>

## 1.5 Coarse-graining

We use MD simulations to recreate and thereby elucidate the behavior of vesicles and dendrimers in water. Although their dynamics are fast on a chemical scale, it is not practical to reproduce this a fair amount of times using conventional fully atomistic MD. The size and time scales required are too large to follow spontaneous vesicle fusion and the interactions between dendrimer and solvent molecules in statistically relevant numbers if every atom of all molecules in these systems needs to be considered. To undertake simulations on sufficiently large length and time scales, the underlying models need to be simplified in order to keep computation times practical. Simulating these phenomena in explicit water is feasible with a coarse-graining (CG) scheme wherein roughly four heavy atoms are lumped together to form a single particle. With this approach, the number of particles is heavily scaled down as are the corresponding interactions (Figure 1.4). As high frequency motions are removed, and the interaction potentials are smoother, larger simulation time steps can be made as well. Moreover, because the coarse-grained system experiences less friction, the apparent dynamics are faster. All in all this gives a total speed-up of up to three orders of magnitude compared to fully atomistic simulations.<sup>[51]</sup>

The origin of coarse-grained (lipid) models can be traced back to the seminal work by Smit et al.<sup>[52,53]</sup> of molecular dynamics of amphiphilic molecules. By having hydrophilic particles, hydrophobic particles, and surfactants made of joined particles, the phase behavior and aggregate structures of lipids in an aqueous environment emerged. Similar coarse-grained models of lipids and amphiphilic

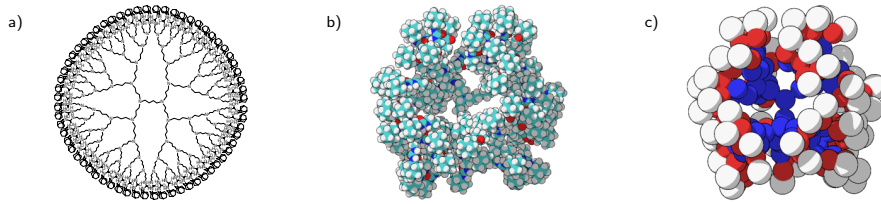


**Figure 1.4:** The coarse-graining approach. (a) The molecular structure of a fifth-generation poly(propylene imine) dendrimer. (b) In atomistic form all 3174 atoms are present. (c) In the coarse-grained form this is reduced to 190 particles.

molecules have since been successfully used to investigate their self-assembly in increasingly extensive simulations.<sup>[54-63]</sup> Apart from amphiphilic molecules, the coarse-grained approach has also been successfully applied to make simulations of other systems computationally viable; these include such diverse systems as liquids,<sup>[64,65]</sup> polymers<sup>[66-73]</sup> and specifically dendrimers,<sup>[74-80]</sup> carbonaceous<sup>[81]</sup> and silica nanoparticles,<sup>[82]</sup> DNA<sup>[83,84]</sup> and peptides.<sup>[85-88]</sup> Our lipid model<sup>[89,90]</sup> distinguishes itself from the extensive models by its relatively simple design, consisting of only three particle types with a select few interaction types. From these particles a proportioned 12-particle lipid molecule is constructed with a hydrophilic head and two hydrophobic tails, while water particles make up the solvent. This generalized lipid model enables us to gain insight into what affects lipid behavior. By changing few parameters it becomes clear what variables are important and what variables are less influential. It is fascinating how complex behavior emerges from such simple interactions. Our dendrimer model on the other hand is built to specifically characterize the adamantylurea-modified poly(propylene imine) dendrimer and urea acid guests in full. It is therefore comprised of nine particle types and a proportionately larger number of interactions. Despite our aspiration to build the optimal dendrimer model, as experimental validation is elusive, the simulation results must still be considered qualitative rather than quantitative.

## 1.6 Thesis outline

In *Chapter 2* we introduce our coarse-grained lipid model and use it to shed light on the spontaneous fusion of vesicles and compare our simulations with a number of theoretical models. We observe how fusion is initiated between small vesicles without forceful collision. For the evolution of that initial contact two conflicting predictions exist in literature, surprisingly the simulations prove they are both equally viable. After fusion, the vesicles do not have their ideal spherical shape due to insufficient water content and a mismatch of the number of lipids in inner and outer monolayers. In *Chapter 3* we investigate which of these discrepancies is decisive by introducing simple transmembrane proteins: a water transport channel

and two proteins that facilitate mixing of the monolayers. These proteins raise issues of their own, e.g., because their hydrophobic height differs slightly from the lipid membrane, they exhibit some level of spontaneous aggregation, but as it turns out there is more than hydrophobic mismatch that determines aggregation strength.

The design and validation of a new coarse-grained poly(propylene imine)-urea-adamantyl dendrimer model is treated in *Chapter 4*. The CG model is compared with atomistic simulations and available experimental data for all generations up to the limiting seventh generation. The results highlight that the dendrimers' structural dynamics originate from flexible chains constrained by configurational and spatial requirements: large dendrimers are quite rigid and spherical, while small ones are much more flexible. After considering individual dendrimers, in *Chapter 5* the model is applied to perform large scale simulations to investigate poly(propylene imine) dendrimers in dilute to concentrated solutions. Among other things, these simulations look at the intermolecular spacing and dendrimer interpenetration to see whether the dendrimers really interweave after the overlap concentration point. Moreover we use the simulations to investigate the validity of assumptions that are typically made to be able to calculate structure factors from experimental scattering studies. The dendrimer model is extended with compatible multivalent guests in *Chapter 6* to create a host-guest complex platform. This enables us to test the multivalency effect, a powerful practice to make strong specific interactions, on a small globular host containing an abundance of receptors. We observe how the complex forms dynamic patchy nanoparticles which in turn self-assemble into various macromolecular nanostructures depending on the host-guest-water mix. Subsequently, we systematically study guest concentration-dependent multivalent binding and find a clear multivalent effect.

## Bibliography

- [1] T.M. Allen and P.R. Cullis, Drug delivery systems: Entering the mainstream. *Science* 2004, *303*, 1818–1822.
- [2] S. Parveen, R. Misra, and S.K. Sahoo, Nanoparticles: A boon to drug delivery, therapeutics, diagnostics and imaging. *Nanomedicine* 2012, *8*, 147–166.
- [3] J. Li, X. Wang, T. Zhang, C. Wang, Z. Huang, X. Luo, and Y. Deng, A review on phospholipids and their main applications in drug delivery systems. *Asian J. Pharm. Sci.* 2015, *10*, 81–98.
- [4] E. Blanco, H. Shen, and M. Ferrari, Principles of nanoparticle design for overcoming biological barriers to drug delivery. *Nat. Biotechnol.* 2015, *33*, 941–951.
- [5] M. Ramezanzpour, S.S.W. Leung, K.H. Delgado-Magnero, B.Y.M. Bashe, J. Thewalt, and D.P. Tieleman, Computational and experimental approaches for investigating nanoparticle-based drug delivery systems. *Biochim. Biophys. Acta, Biomembr.* 2016, *1858*, 1688–1709.
- [6] S. Mura, J. Nicolas, and P. Couvreur, Stimuli-responsive nanocarriers for drug delivery. *Nat. Mater.* 2013, *12*, 991–1003.

- 
- [7] S.H. van Rijt, T. Bein, and S. Meiners, Medical nanoparticles for next generation drug delivery to the lungs. *Eur. Respir. J.* 2014, *44*, 765–774.
- [8] S.A.L. Audouy, L.F.M.H. de Leij, D. Hoekstra, and G. Molema, In vivo characteristics of cationic liposomes as delivery vectors for gene therapy. *Pharm. Res.* 2002, *19*, 1599–1605.
- [9] H. Daraee, A. Etemadi, M. Kouhi, S. Alimirzalu, and A. Akbarzadeh, Application of liposomes in medicine and drug delivery. *Artif. Cell. Nanomed. Biotechnol.* 2016, *44*, 381–391.
- [10] E. Fattal, P. Couvreur, and C. Dubernet, “Smart” delivery of antisense oligonucleotides by anionic pH-sensitive liposomes. *Adv. Drug Delivery Rev.* 2004, *56*, 931–946.
- [11] W.J.M. Mulder, G.J. Strijkers, A.W. Griffioen, L. van Bloois, G. Molema, G. Storm, G.A. Koning, and K. Nicolay, A liposomal system for contrast-enhanced magnetic resonance imaging of molecular targets. *Bioconjug. Chem.* 2004, *15*, 799–806.
- [12] L. Sercombe, T. Veerati, F. Moheimani, S.Y. Wu, A.K. Sood, and S. Hua, Advances and challenges of liposome assisted drug delivery. *Front. Pharmacol.* 2015, *6*, 286.
- [13] B. Alberts, D. Bray, J. Lewis, M. Raff, K. Roberts, and J.D. Watson, *Molecular biology of the cell*. Garland, New York, 1994.
- [14] R.H. Garrett and C.M. Grisham, *Biochemistry*. Saunders College Publishing, Philadelphia, 1995.
- [15] G. van Meer, D.R. Voelker, and G.W. Feigenson, Membrane lipids: Where they are and how they behave. *Nat. Rev. Mol. Cell Biol.* 2008, *9*, 112–124.
- [16] A.S. Verkman, Solute and macromolecule diffusion in cellular aqueous compartments. *Trends Biochem. Sci.* 2002, *27*, 27–33.
- [17] T. Ando and J. Skolnick, Crowding and hydrodynamic interactions likely dominate in vivo macromolecular motion. *Proc. Natl. Acad. Sci.* 2010, *107*, 18457–18462.
- [18] B.B. Boland, C.J. Rhodes, and J.S. Grimsby, The dynamic plasticity of insulin production in  $\beta$ -cells. *Mol. Metab.* 2017, *6*, 958–973.
- [19] R. Khoriaty, M.P. Vasievich, and D. Ginsburg, The COPII pathway and hematologic disease. *Blood* 2012, *120*, 31–38.
- [20] J. Fang, M. Liu, X. Zhang, T. Sakamoto, D.J. Taatjes, B.P. Jena, F. Sun, J. Woods, T. Bryson, A. Kowluru, K. Zhang, and X. Chen, COPII-dependent ER export: A critical component of insulin biogenesis and  $\beta$ -cell ER homeostasis. *Mol. Endocrinol.* 2015, *29*, 1156–1169.
- [21] H.R.B. Pelham, SNAREs and the specificity of membrane fusion. *Trends Cell Biol.* 2001, *11*, 99–101.
- [22] J.E. Pessin, D.C. Thurmond, J.S. Elmendorf, K.J. Coker, and S. Okada, Molecular basis of insulin-stimulated GLUT4 vesicle trafficking: Location! Location! Location! *J. Biol. Chem.* 1999, *274*, 2593–2596.
- [23] D. Leto and A.R. Saltiel, Regulation of glucose transport by insulin: Traffic control of GLUT4. *Nat. Rev. Mol. Cell Biol.* 2012, *13*, 383–396.
- [24] O.A. Matthews, A.N. Shipway, and J.F. Stoddart, Dendrimers—branching out from curiosities into new technologies. *Prog. Polym. Sci.* 1998, *23*, 1–56.
- [25] A.W. Bosman, H.M. Janssen, and E.W. Meijer, About dendrimers: Structure, physical properties, and applications. *Chem. Rev.* 1999, *99*, 1665–1688.
- [26] L. Crespo, G. Sanclimens, M. Pons, E. Giralt, M. Royo, and F. Albericio, Peptide and amide bond-containing dendrimers. *Chem. Rev.* 2005, *105*, 1663–1682.
- [27] G.R. Newkome and C.D. Shreiner, Poly(amidoamine), polypropylenimine, and related dendrimers and dendrons possessing different 1  $\rightarrow$  2 branching motifs: An overview of the divergent procedures. *Polymer* 2008, *49*, 1–173.
- [28] G.R. Newkome and C.D. Shreiner, Dendrimers derived from 1  $\rightarrow$  3 branching motifs. *Chem. Rev.* 2010, *110*, 6338–6442.
- [29] R.K. Tekade, P.V. Kumar, and N.K. Jain, Dendrimers in oncology: An expanding horizon. *Chem. Rev.* 2009, *109*, 49–87.
- [30] D. Astruc, E. Boisselier, and C. Ornelas, Dendrimers designed for functions: From physical, photophysical, and supramolecular properties to applications in sensing, catalysis, molecular electronics, photonics, and nanomedicine. *Chem. Rev.* 2010, *110*, 1857–1959.

- [31] A.J.L. Villaraza, A. Bumb, and M.W. Brechbiel, Macromolecules, dendrimers, and nanomaterials in magnetic resonance imaging: The interplay between size, function, and pharmacokinetics. *Chem. Rev.* 2010, *110*, 2921–2959.
- [32] J.F.G.A. Jansen, E.M.M. de Brabander-van den Berg, and E.W. Meijer, Encapsulation of guest molecules into a dendritic box. *Science* 1994, *266*, 1226–1229.
- [33] M.R. Molla, P. Rangadurai, G.M. Pavan, and S. Thayumanavan, Experimental and theoretical investigations in stimuli responsive dendrimer-based assemblies. *Nanoscale* 2015, *7*, 3817–3837.
- [34] S. Mignani, J. Rodrigues, H. Tomas, R. Roy, X. Shi, and J.P. Majoral, Bench-to bedside translation of dendrimers: Reality or utopia? A concise analysis. *Adv. Drug Delivery Rev.* 2018, *136–137*, 73–81.
- [35] V.A. Kabanov, V.G. Sergeyev, O.A. Pyshkina, A.A. Zinchenko, A.B. Zezin, J.G.H. Joosten, J. Brackman, and K. Yoshikawa, Interpolyelectrolyte complexes formed by DNA and Astramol poly(propylene imine) dendrimers. *Macromolecules* 2000, *33*, 9587–9593.
- [36] M.A. Mintzer and E.E. Simanek, Nonviral vectors for gene delivery. *Chem. Rev.* 2009, *109*, 259–302.
- [37] D.K. Smith, A.R. Hirst, C.S. Love, J.G. Hardy, S.V. Brignell, and B. Huang, Self-assembly using dendritic building blocks—towards controllable nanomaterials. *Prog. Polym. Sci.* 2005, *30*, 220–293.
- [38] T. Chang, K. Pieterse, M.A.C. Broeren, H. Kooijman, A.L. Spek, P.A.J. Hilbers, and E.W. Meijer, Structural elucidation of dendritic host–guest complexes by X-ray crystallography and molecular dynamics simulations. *Chem.–Eur. J.* 2007, *13*, 7883–7889.
- [39] T.M. Hermans, M.A.C. Broeren, N. Gomopoulos, P. van der Schoot, M.H.P. van Genderen, N.A.J.M. Sommerdijk, G. Fytas, and E.W. Meijer, Self-assembly of soft nanoparticles with tunable patchiness. *Nat. Nanotechnol.* 2009, *4*, 721–726.
- [40] M. Mammen, S.K. Choi, and G.M. Whitesides, Polyvalent interactions in biological systems: Implications for design and use of multivalent ligands and inhibitors. *Angew. Chem., Int. Ed.* 1998, *37*, 2754–2794.
- [41] A. Mulder, J. Huskens, and D.N. Reinhoudt, Multivalency in supramolecular chemistry and nanofabrication. *Org. Biomol. Chem.* 2004, *2*, 3409–3424.
- [42] J.D. Badjić, A. Nelson, S.J. Cantrill, W.B. Turnbull, and J.F. Stoddart, Multivalency and cooperativity in supramolecular chemistry. *Acc. Chem. Res.* 2005, *38*, 723–732.
- [43] C. Fasting, C.A. Schalley, M. Weber, O. Seitz, S. Hecht, B. Kocsch, J. Darnedde, C. Graf, E.W. Knapp, and R. Haag, Multivalency as a chemical organization and action principle. *Angew. Chem., Int. Ed.* 2012, *51*, 10472–10498.
- [44] J.F.G.A. Jansen, R.A.J. Janssen, E.M.M. de Brabander-van den Berg, and E.W. Meijer, Triplet radical pairs of 3-carboxypropyl encapsulated in a dendritic box. *Adv. Mater.* 1995, *7*, 561–564.
- [45] M.A.C. Broeren, J.L.J. van Dongen, M. Pittelkow, J.B. Christensen, M.H.P. van Genderen, and E.W. Meijer, Multivalency in the gas phase: The study of dendritic aggregates by mass spectrometry. *Angew. Chem., Int. Ed.* 2004, *43*, 3557–3562.
- [46] G. Lei and R.C. MacDonald, Lipid bilayer vesicle fusion: Intermediates captured by high-speed microfluorescence spectroscopy. *Biophys. J.* 2003, *85*, 1585–1599.
- [47] J. Heuvingh, F. Pincet, and S. Cribier, Hemifusion and fusion of giant vesicles induced by reduction of inter-membrane distance. *Eur. Phys. J. E* 2004, *14*, 269–276.
- [48] J. Nikolaus, M. Stöckl, D. Langosch, R. Volkmer, and A. Herrmann, Direct visualization of large and protein-free hemifusion diaphragms. *Biophys. J.* 2010, *98*, 1192–1199.
- [49] T.M. Hermans, M.A.C. Broeren, N. Gomopoulos, A.F. Smeijers, B. Mezari, E.N.M. van Leeuwen, M.R.J. Vos, P.C.M.M. Magusin, P.A.J. Hilbers, M.H.P. van Genderen, N.A.J.M. Sommerdijk, G. Fytas, and E.W. Meijer, Stepwise noncovalent synthesis leading to dendrimer-based assemblies in water. *J. Am. Chem. Soc.* 2007, *129*, 15631–15638.
- [50] D. Frenkel and B. Smit, *Understanding molecular dynamics*. Academic Press, New York, 2002.
- [51] A.J. Markvoort, Coarse grained molecular dynamics. In *Computational methods in catalysis and materials science: An introduction for scientists and engineers*, eds. R.A. van Santen

- and P. Sautet, chap. 8, 151–166, Wiley, Weinheim, 2009.
- [52] B. Smit, P.A.J. Hilbers, K. Esselink, L.A.M. Rupert, N.M. van Os, and A.G. Schlijper, Computer simulations of a water/oil interface in the presence of micelles. *Nature* 1990, *348*, 624–625.
- [53] B. Smit, P.A.J. Hilbers, K. Esselink, L.A.M. Rupert, N.M. van Os, and A.G. Schlijper, Structure of a water/oil interface in the presence of micelles: A computer simulation study. *J. Phys. Chem.* 1991, *95*, 6361–6368.
- [54] R. Goetz, G. Gompper, and R. Lipowsky, Mobility and elasticity of self-assembled membranes. *Phys. Rev. Lett.* 1999, *82*, 221–224.
- [55] J.C. Shelley, M.Y. Shelley, R.C. Reeder, S. Bandyopadhyay, and M.L. Klein, A coarse grain model for phospholipid simulations. *J. Phys. Chem. B* 2001, *105*, 4464–4470.
- [56] M. Müller, K. Katsov, and M. Schick, A new mechanism of model membrane fusion determined from Monte Carlo simulation. *Biophys. J.* 2003, *85*, 1611–1623.
- [57] S.J. Marrink and A.E. Mark, Molecular dynamics simulation of the formation, structure, and dynamics of small phospholipid vesicles. *J. Am. Chem. Soc.* 2003, *125*, 15233–15242.
- [58] M.J. Stevens, J.H. Hoh, and T.B. Woolf, Insights into the molecular mechanism of membrane fusion from simulation: Evidence for the association of splayed tails. *Phys. Rev. Lett.* 2003, *91*, 188102.
- [59] T. Murtola, M. Karttunen, and I. Vattulainen, Systematic coarse graining from structure using internal states: Application to phospholipid/cholesterol bilayer. *J. Chem. Phys.* 2009, *131*, 055101.
- [60] W. Shinoda, R. DeVane, and M.L. Klein, Zwitterionic lipid assemblies: Molecular dynamics studies of monolayers, bilayers, and vesicles using a new coarse grain force field. *J. Phys. Chem. B* 2010, *114*, 6836–6849.
- [61] R. Xu and X. He, Kinetics of a multilamellar lipid vesicle ripening: Simulation and theory. *J. Phys. Chem. B* 2016, *120*, 2262–2270.
- [62] T.C. Moore, C.R. Iacovella, A.C. Leonhard, A.L. Bunge, and C. McCabe, Molecular dynamics simulations of stratum corneum lipid mixtures: A multiscale perspective. *Biochem. Biophys. Res. Commun.* 2018, *498*, 313–318.
- [63] S.J. Marrink, V. Corradi, P.C.T. Souza, H.I. Ingólfsson, D.P. Tieleman, and M.S.P. Sansom, Computational modeling of realistic cell membranes. *Chem. Rev.* 2019, *119*, 6184–6226.
- [64] A.P. Lyubartsev and A. Laaksonen, Calculation of effective interaction potentials from radial distribution functions: A reverse Monte Carlo approach. *Phys. Rev. E* 1995, *52*, 3730–3737.
- [65] A.K. Soper, Empirical potential Monte Carlo simulation of fluid structure. *Chem. Phys.* 1996, *202*, 295–306.
- [66] D. Reith, H. Meyer, and F. Müller-Plathe, Mapping atomistic to coarse-grained polymer models using automatic simplex optimization to fit structural properties. *Macromolecules* 2001, *34*, 2335–2345.
- [67] R. Faller, Automatic coarse graining of polymers. *Polymer* 2004, *45*, 3869–3876.
- [68] X. Li, X. Ma, L. Huang, and H. Liang, Developing coarse-grained force fields for *cis*-poly(1,4-butadiene) from the atomistic simulation. *Polymer* 2005, *46*, 6507–6512.
- [69] H.J. Limbach and K. Kremer, Multi-scale modelling of polymers: Perspectives for food materials. *Trends Food Sci. Technol.* 2006, *17*, 215–219.
- [70] M. Ghelichi, K. Malek, and M.H. Eikerling, Ionomer self-assembly in dilute solution studied by coarse-grained molecular dynamics. *Macromolecules* 2016, *49*, 1479–1489.
- [71] A. Aramoon, T.D. Breitzman, C. Woodward, and J.A. El-Awady, Coarse-grained molecular dynamics study of the curing and properties of highly cross-linked epoxy polymers. *J. Phys. Chem. B* 2016, *120*, 9495–9505.
- [72] E. Lin, X. You, R.M. Kriegel, R.D. Moffitt, and R.C. Batra, Interdiffusion of small molecules into a glassy polymer film via coarse-grained molecular dynamics simulations. *Polymer* 2017, *115*, 273–284.
- [73] I.V. Volgin, S.V. Larin, A.V. Lyulin, and S.V. Lyulin, Coarse-grained molecular-dynamics simulations of nanoparticle diffusion in polymer nanocomposites. *Polymer* 2018, *145*, 80–87.
- [74] H. Lee and R.G. Larson, Molecular dynamics simulations of PAMAM dendrimer-induced

- pore formation in DPPC bilayers with a coarse-grained model. *J. Phys. Chem. B* 2006, *110*, 18204–18211.
- [75] P. Carbone, F. Negri, and F. Müller-Plathe, A coarse-grained model for polyphenylene dendrimers: Switching and backfolding of planar three-fold core dendrimers. *Macromolecules* 2007, *40*, 7044–7055.
- [76] G. del Río Echenique, R. Rodríguez Schmidt, J.J. Freire, J.G. Hernández Cifre, and J. García de la Torre, A multiscale scheme for the simulation of conformational and solution properties of different dendrimer molecules. *J. Am. Chem. Soc.* 2009, *131*, 8548–8556.
- [77] P.K. Maiti, Y. Li, T. Çağın, and W.A. Goddard III, Structure of polyamidoamide dendrimers up to limiting generations: A mesoscale description. *J. Chem. Phys.* 2009, *130*, 144902.
- [78] W.d. Tian and Y.q. Ma, Coarse-grained molecular simulation of interacting dendrimers. *Soft Matter* 2011, *7*, 500–505.
- [79] J.J. Freire, A.M. Rubio, and C. McBride, Coarse-grained and atomistic simulations for the G=4 PAMAM-EDA dendrimer. *Macromol. Theory Simul.* 2015, *24*, 432–441.
- [80] S. Kavyani, M. Dadvar, H. Modarress, and S. Amjad-Iranagh, Molecular perspective mechanism for drug loading on carbon nanotube–dendrimer: A coarse-grained molecular dynamics study. *J. Phys. Chem. B* 2018, *122*, 7956–7969.
- [81] S. Izvekov, A. Violi, and G.A. Voth, Systematic coarse-graining of nanoparticle interactions in molecular dynamics simulation. *J. Phys. Chem. B* 2005, *109*, 17019–17024.
- [82] A.Z. Summers, C.R. Iacovella, O.M. Cane, P.T. Cummings, and C. McCabe, A transferable, multi-resolution coarse-grained model for amorphous silica nanoparticles. *J. Chem. Theory Comput.* 2019, *15*, 3260–3271.
- [83] J.S. Chen, H. Teng, and A. Nakano, Wavelet-based multi-scale coarse graining approach for DNA molecules. *Finite Elem. Anal. Des.* 2007, *43*, 346–360.
- [84] J.J. Uusitalo, H.I. Ingólfsson, P. Akhshi, D.P. Tieleman, and S.J. Marrink, Martini coarse-grained force field: Extension to DNA. *J. Chem. Theory Comput.* 2015, *11*, 3932–3945.
- [85] A.Y. Shih, A. Arkhipov, P.L. Freddolino, and K. Schulten, Coarse grained protein–lipid model with application to lipoprotein particles. *J. Phys. Chem. B* 2006, *110*, 3674–3684.
- [86] J. Zhou, I.F. Thorpe, S. Izvekov, and G.A. Voth, Coarse-grained peptide modeling using a systematic multiscale approach. *Biophys. J.* 2007, *92*, 4289–4303.
- [87] L. Monticelli, S.K. Kandasamy, X. Periole, R.G. Larson, D.P. Tieleman, and S.J. Marrink, The MARTINI coarse-grained force field: Extension to proteins. *J. Chem. Theory Comput.* 2008, *4*, 819–834.
- [88] S. Kmiecik, D. Gront, M. Kolinski, L. Wieteska, A.E. Dawid, and A. Kolinski, Coarse-grained protein models and their applications. *Chem. Rev.* 2016, *116*, 7898–7936.
- [89] A.J. Markvoort, K. Pieterse, M.N. Steijaert, P. Spijker, and P.A.J. Hilbers, The bilayer–vesicle transition is entropy driven. *J. Phys. Chem. B* 2005, *109*, 22649–22654.
- [90] A.F. Smeijers, A.J. Markvoort, K. Pieterse, and P.A.J. Hilbers, A detailed look at vesicle fusion. *J. Phys. Chem. B* 2006, *110*, 13212–13219.

## Chapter 2

# A detailed look at vesicle fusion

---

**Abstract** Many different hypotheses on the molecular mechanisms of vesicle fusion exist. Because these mechanisms cannot be readily asserted experimentally, we address this issue with coarse-grained molecular dynamics simulations and compare the results with the results of other techniques. The simulations performed include the fusion of small and large vesicles and exocytosis, i.e., the fusion of small vesicles with flat bilayers. We demonstrate that the stalk, the initial contact between two fusing vesicles, is initiated by lipid tails that extend spontaneously. The stalk is revealed to be composed of the contacting monolayers only, yet without hydrophobic voids. Anisotropic and radial expansion of the stalk have been theorized; we show that stalk evolution can proceed via both pathways starting from similar setups and that water triggers the transition from elongated stalk to hemifusion diaphragm.

---

---

This work has been published in:

A.F. Smeijers, A.J. Markvoort, K. Pieterse, and P.A.J. Hilbers, A detailed look at vesicle fusion. *Journal of Physical Chemistry B* 2006, 110, 13 212–13 219.



## 2.1 Introduction

Vesicular trafficking is the means of directed transport between organelles inside the cell and via exocytosis to the outside.<sup>[1]</sup> Vesicles bud from one membrane to fuse with a target membrane, merging both their bilayers and contents. Additionally, liposomes function as carriers in medicine and drug delivery.<sup>[2]</sup> Therefore, the elucidation of vesicle fusion is of great importance. Many *in vitro* fusion experiments have been performed with liposomes, revealing the fusion dynamics at the millisecond and micrometer scale. In the basis, vesicle fusion is straightforward: two vesicles touch and merge to become a single vesicle. The process follows various discrete stages, their presence is relatively easy to observe experimentally in giant unilamellar vesicles with fluorescence microscopy.<sup>[3–5]</sup> Starting with two vesicles that come into close contact, an initial connection is formed involving lipid mixing of the contacting monolayers, while leaving the contents separated—a stage called *hemifusion*. Once the vesicle contents mix, full fusion is reached. The molecular structures and the transitions between these stages, however, cannot be visualized experimentally with the techniques currently available. With modeling techniques, the fusion process can be studied in more detail. Previous studies used elastic continuum models<sup>[6–10]</sup> and simulation techniques such as Brownian dynamics,<sup>[11]</sup> Monte Carlo,<sup>[12]</sup> dissipative particle dynamics,<sup>[13,14]</sup> and coarse-grained molecular dynamics (MD).<sup>[15,16]</sup> Of these techniques, MD is the only one to incorporate solvent explicitly. Here we apply the coarse-grained MD technique to elucidate the fusion of vesicles at the molecular level, and compare the results to theorized structures.

In theory, the vesicle’s inclination to fuse depends on the curvature of the contact zone, and the lipids present. Sonicated vesicles range in size from 21.4 nm<sup>[17]</sup> to >1  $\mu\text{m}$  in diameter; their curvatures change accordingly. The lipids influence the fusion process as they dictate membrane properties, e.g., through their spontaneous curvature.<sup>[18,19]</sup>

In fusion models, the contacting monolayers (the external monolayers of the vesicles) are generally labeled *cis-monolayers*, whereas the inner monolayers are labeled *trans-monolayers*. The initial lipid connection between the vesicles is widely regarded to be a *stalk*, a union of *cis-monolayers* in a toroidal hourglass shape. The original stalk model was envisioned to have the *cis-monolayers* curved circularly.<sup>[6]</sup> This and other stalk models are the product of elastic continuum calculations,<sup>[20]</sup> a method used to calculate the free energy of hypothetical structures. However, the original stalk model has a substantially higher energy than the bilayers from which it is supposed to stem.<sup>[21]</sup> The *stress-free stalk*<sup>[7]</sup> is a revision of the original stalk. It has gained a lower energy by dropping the assumption of a circular geometry, and by allowing the voids to be filled with lipids of different tail lengths<sup>[18]</sup> or small hydrophobic molecules. Another revision, the *transmembrane contact*

*stalk*,<sup>[8]</sup> is so called because its trans-monolayers make contact at the stalk center; in turn, the monolayers are sharply bent to fill any hydrophobic voids. Recently conducted X-ray diffraction experiments support the existence of stalks.<sup>[22]</sup> If in this experiment hydrophobic voids are present in the inverted hexagonal phase (as expected<sup>[23]</sup>), then the images suggest the stalk contains voids as well, although this is not highlighted in that paper.

The stalk model is well received; however, other hemifusion models exist as well. For instance, the *extended lipid hemifusion* model<sup>[24]</sup> implies that the cis-monolayers are stacked and joined together by the tails of stretched lipids, while their head-groups stay in the interface.

To explain complete fusion after contact is made, several pathways were conceived. One is the *stalk-pore* hypothesis.<sup>[9]</sup> It states that the stalk expands *radially*, bringing the trans-monolayers together in a transmembrane contact. The contact expands further so a bilayer, called a *hemifusion diaphragm* (HD), is formed. Because the HD edge is energetically unfavorable, some argue that expansion of the stalk stops before an HD with a radius exceeding the monolayer thickness can be formed,<sup>[9]</sup> whereas others argue that only large diaphragms exist.<sup>[7]</sup> Eventually, a *fusion pore* opens in the HD that is subsequently assimilated. As tensions are concentrated along the rim, that is where the fusion pore is thought to emerge.<sup>[9]</sup> The fusion pore continues to grow due to reduction of the free edge.<sup>[7]</sup> In an alternative hypothesis, the *direct stalk-pore* model,<sup>[9,10]</sup> the fusion pore directly originates from the radially expanding stalk. In the third hypothesis, the *anisotropic stalk-pore* model,<sup>[11,12]</sup> the stalk grows anisotropically, thus forming an elongated connection. Consequently, the stalk destabilizes the bilayers so that holes appear in its vicinity. These holes are then encircled by bending of the stalk, thus a fusion pore is created.

*In vitro* experiments are used to examine vesicle fusion at a microscopic scale, but on a time scale much larger than the actual lipid dynamics, whereas elastic continuum models consider the fusion intermediates at a submicroscopic scale and do not consider dynamics. Molecular dynamics allows for both, the subnanosecond dynamics being on the scale of individual atoms. To perform simulations of complete vesicle fusion in a reasonable amount of time, we use a coarse-graining approach. It is based on the observation that lipids in an aqueous environment and block copolymers in a homopolymer environment exhibit common phase behavior and form similar aggregate structures, despite being chemically very different. Similar coarse-grained models of amphiphilic molecules have been successfully used to investigate their self-assembly.<sup>[25-30]</sup>

## 2.2 Methods

### 2.2.1 Molecular dynamics

In our coarse-grained and atomistic molecular dynamics simulations, The energy of each bond length, angle and torsion is calculated with respect to known equilibrium bond lengths, angles and torsions. Non-bonded interactions include the van der Waals interaction and electrostatic interactions. The van der Waals interaction between two neutral particles is described mathematically by the Lennard-Jones potential. It is mildly attractive as two particles approach each other from a distance, yet strongly repulsive when they come too close. At its minimum (Figure 2.1a) the particles are at equilibrium. The Pauli repulsion part arises from the energetically unfavorable deformation of the electron clouds of colliding atoms. The attraction at larger distances is due to instantaneous dipole–dipole moments between uncharged atoms, known as the London dispersion force.

For two non-bonded particles ( $i$  and  $j$ ) the Lennard-Jones potential is:<sup>[31,32]</sup>

$$V_{\text{LJ}}(r_{ij}) = 4\varepsilon_{ij} \left( \left( \frac{\sigma_{ij}}{r_{ij}} \right)^{12} - \left( \frac{\sigma_{ij}}{r_{ij}} \right)^6 \right) \quad (2.1)$$

where  $r_{ij}$  is the distance between the particles in nm and  $\varepsilon_{ij}$  is the well depth in kJ/mol. The contact distance  $\sigma_{ij}$  is in nm; it relates to the van der Waals radius ( $R_i$ ) as  $\sigma_i = 2^{5/6} R_i$  and unlike particles follow the Lorentz rule:  $\sigma_{ij} = \frac{1}{2}(\sigma_i + \sigma_j)$ . At relatively large distances the Lennard-Jones potential still accounts for some attraction between particles. Although its pull is very low for individual particles, there are much more particles at a large distance than at a small distance, thus incurring substantial computational cost. With only a small loss in accuracy, the Lennard-Jones potential can be truncated at a distance of, e.g.,  $5R$ . To ensure a smooth transition, the potential is shifted toward the baseline:<sup>[32]</sup>

$$V_{\text{tsLJ}}(r_{ij}) = \begin{cases} V_{\text{LJ}}(r_{ij}) - V_{\text{LJ}}(r_c) & \text{if } r_{ij} \leq r_c; \\ 0 & \text{if } r_{ij} > r_c. \end{cases} \quad (2.2)$$

The distance between a pair particles that share a bond is governed by the harmonic bond potential. Attraction and repulsion are symmetrical around a favored, equilibrium bond length. For two bonded particles ( $i$  and  $j$ ), the harmonic bond potential is:

$$V_{\text{bond}}(r_{ij}) = k_{ij} (r_{ij} - r_{0,ij})^2 \quad (2.3)$$

where  $r_{ij}$  is the current bond length and  $r_{0,ij}$  the equilibrium bond length in nm. The spring constant  $k_{ij}$  ( $\text{kJ nm}^{-2} \text{mol}^{-1}$ ) determines the steepness of the potential (Figure 2.1b).

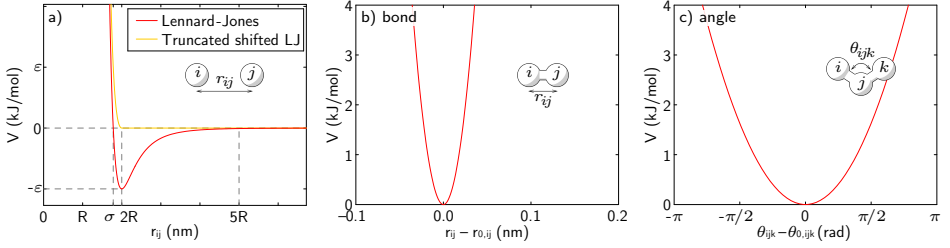


**Figure 2.1:** Bonded and non-bonded potentials: (a) Lennard-Jones potential, (b) harmonic bond potential ( $T$ - $T$ ,  $k_{TT} = 3156 \text{ kJ nm}^{-2} \text{ mol}^{-1}$ ), and (c) harmonic angle potential ( $N$ - $N$ - $N$ ,  $k_{NNN} = 0.66 \text{ kJ rad}^{-2} \text{ mol}^{-1}$ , Chapter 4).

Likewise, the harmonic angle potential between three connected particles  $i$ ,  $j$ , and  $k$  is:

$$V_{\text{angle}}(\theta_{ijk}) = k_{ijk} (\theta_{ijk} - \theta_{0,ijk})^2 \quad (2.4)$$

with  $\theta_{ijk}$  the current angle about  $j$ ,  $\theta_{0,ijk}$  the equilibrium angle in rad, and  $k_{ijk}$  the spring constant in  $\text{kJ rad}^{-2} \text{ mol}^{-1}$  (Figure 2.1c).<sup>[32]</sup>

The simulations are performed in an isothermal–isobaric (NPT) ensemble, meaning with constant number of particles, pressure, and temperature. Typically the pressure is 1 bar and the temperature 298 K. To smoothly adjust the system to the desired temperature and pressure, the Berendsen loose coupling technique<sup>[33]</sup> is used. Conceptually, the system temperature is maintained by exchanging heat with an external heat bath with constant temperature. As heat is exchanged the particles’ velocities change. However, an instantaneous adjustment of the temperature to its target value would impact the system, therefore the velocities are proportionally scaled from  $v$  to  $\lambda v$  with

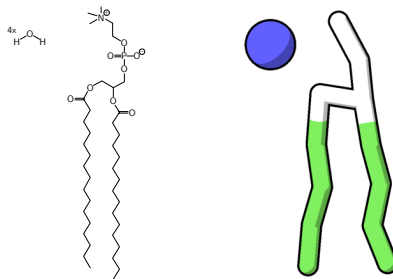
$$\lambda^2 = 1 + \lambda_c \left( \frac{T_0}{T} - 1 \right) \quad (2.5)$$

where  $T_0$  is the desired temperature and  $\lambda_c$  is the coupling constant that determines the rate of adjustment ( $0 \leq \lambda_c \leq 1$ ). Similarly, the volume is adjusted to maintain the pressure  $P$  by rescaling the box length from  $L$  to  $\mu L$  (assuming an isotropic system in a cubic box) and the particles’ positions within, with

$$\mu^3 = 1 + \mu_c \left( \frac{P}{P_0} - 1 \right) \quad (2.6)$$

where  $P_0$  is the desired pressure and  $\mu_c$  is the proportional constant. In our coarse-grained simulations, the pressure and temperature are typically rescaled every 100 time steps with  $\lambda_c = 0.005$  and  $\mu_c = 0.00005$ .

**Figure 2.2:** Structural formulas of water and dipalmitoylphosphatidylcholine on the left as basis for the coarse-grained lipid and water particle on the right.



## 2.2.2 Lipid model

The coarse-grained model for lipid and water used in this thesis is an updated version of the lipid model of Markvoort et al. introduced with a bilayer-vesicle transition study.<sup>[34]</sup> The model performed well in the spontaneous formation of lipid bilayers and vesicles, and it displayed the appropriate area per lipid and bilayer thickness. The coarse-grained lipid is based on the glycerophospholipid class of which dipalmitoylphosphatidylcholine is a representative example, yet it is generic in the sense that the details that draw a distinction between natural phospholipids are omitted. Its two apolar tails are represented by four hydrophobic T particles each and its polar headgroup is represented by four hydrophilic H particles (Figure 2.2); the solvent is represented by hydrophilic W particles. All bonded particles in the system are regulated by harmonic bond potentials; the non-bonded interactions are governed by truncated shifted Lennard-Jones potentials.

In short, derivation of the model parameters went as follows. The fundamental particle, tail particle T represents four methylene groups with a mass of 56.1 u. Scaling the melting temperature of a simulation of T particles to butane defines that  $\varepsilon_{TT} = 1.967 \text{ kJ/mol}$  which is used as the reduced unit of energy ( $1 \varepsilon^*$ ). Particle densities of  $T_3$  and  $T_4$  simulations scaled to match dodecane ( $C_{12}H_{26}$ ) and hexadecane ( $C_{16}H_{34}$ ) gives  $R_T = 2.53 \text{ \AA}$ . A W particle represents four water molecules with a mass of 72.1 u. The melting and boiling temperature scaled to simulations of W particles gives  $\varepsilon_{WW} = 1.88 \varepsilon^*$  and the density requires that  $R_W = 2.59 \text{ \AA}$ . To keep the model as general as possible the hydrophilic particle H gets the same size and mass as the T particle (Table 2.1) and all hydrophilic interactions are identical. Polar-apolar phase separation is incorporated by setting the Lennard-Jones cutoff  $r_{c,ij}$  at  $R_i + R_j$  for these interactions (Equation 2.2), so that only the repulsive part remains<sup>[25]</sup> (Table 2.2). Finally, for the harmonic bond potential (Equation 2.3), the equilibrium bond length is derived from an atomistic simulation of eicosane ( $C_{20}H_{42}$ ):  $r_{0,TT} = 4.73 \text{ \AA}$ . Simulations of  $T_2$  representing octane ( $C_8H_{18}$ ) gives, through harmonic frequency calculations,  $k_{TT} = 3156 \text{ kJ nm}^{-2} \text{ mol}^{-1}$ . These parameters are used by all bonds in the lipid molecule.

**Table 2.1:** Coarse-grained particles

Particle	Approximate chemical name	Formula	Mass (u)	Van der Waals radius (Å)
T	4 methylene groups	$-(\text{CH}_2)_4-$	56.1	2.53
H	—	—	56.1	2.53
W	water	$4\text{H}_2\text{O}$	72.1	2.59

**Table 2.2:** Lennard-Jones well depth ( $\epsilon_{ij}$  ( $\epsilon^*$ );  $1.0\epsilon^* = 1.967$  kJ/mol)

	T	H	W
T	1.0	1.0	1.0
H		1.88	1.88
W			1.88

Thus the model is fitted for water and alkanes, instead of lipids in a bilayer, so there is no *a priori* bias toward membrane formation. To ensure flexibility of our lipids and to enable vesicle fusion with relatively small vesicles, the bending spring constant is set to zero. Lipid shape affects the propensity of the lipid to form differently shaped aggregates. The lipid model has a cylindrical, neutral, shape, not opposed to form different structures.

Due to the smooth potentials and lack of hydrogen bond network, the diffusional time scales of coarse-grained MD simulations are not identical to the time scale implied. One could decide on a calibration factor to make for instance the lateral lipid diffusion a perfect fit. However, in the same system other diffusion coefficients require a different calibration factor, as the factor varies with the mass and size of the particles.<sup>[35]</sup> Because a general calibration factor for a mixed system does not exist, we have chosen to present the time-dependent results without such a factor.

### 2.2.3 PumMa

All coarse-grained simulations described in this and subsequent chapters were performed using our in-house-developed molecular dynamics platform *PumMa*.<sup>[34]</sup> Its name is an acronym of *Parallel Utility for Modeling of Molecular Aggregation*, because it was originally designed for the formation of micelles in oil-water environments. Since then PumMa has been used for coarse-grained simulations on diverse systems as lipid vesicles,<sup>[36–43]</sup> proteins,<sup>[42–45]</sup> flow and heat exchange in microchannels,<sup>[46–49]</sup> and now dendrimer systems.<sup>[50–52]</sup> In the course of these studies, the need to collect bond and angle distributions from atomistic simulations for coarse-graining purposes arose, and PumMa has been extended to also perform atomistic simulations based on the CHARMM27<sup>[53]</sup> force field.

Together with PumMa, a toolkit was developed, *PumMaTK*, which is used to simplify the construction and modification of the various initial molecular system

**Table 2.3:** Overview of vesicle fusion simulations<sup>a</sup>

Label	$N_{\text{out}}$	$N_{\text{in}}$	$N_{\text{W}}$	$D_{\text{B}}$ (nm)	Fusion pathway	$T_{\text{S}}$ (ns)	$L_{\text{S}}$ (ns)	$L_{\text{HD}}$ (ns)
LARGE1	655	369	3483	1.4	Anisotropic, 1 pore	20.6	6.47	34.5
LARGE2	655	369	3497	1.4	Anisotropic, 2 pores	0.12	5.47	
LARGE3	638	380	3555	1.3	Radial	8.42	0.96	>86.8
SMALL1	134	26	17	1.7	Anisotropic, 1 pore	0.26	2.91	0.24
SMALL2	161	39	66	1.3	Anisotropic, 2 pores	8.63	2.02	
SMALL3	181	58	102	1.5	Radial	1.66	1.32	0.26
EXOCY1	181	58	87	1.7	Radial	13.3	2.43	0.87
EXOCY2	181	58	87	1.4	Anisotropic, 1 pore	5.80	2.65	28.0

<sup>a</sup> The simulations are labeled LARGE for large vesicles, SMALL for small vesicles and EXOCY for ‘exocytosis’ simulations involving small vesicle fusion with a bilayer. For these simulations, the number of lipids in the inner and outer monolayer ( $N_{\text{in}}$ ,  $N_{\text{out}}$ ) and the number of encapsulated water particles ( $N_{\text{W}}$ ) for each vesicle, the bridging distance ( $D_{\text{B}}$ ), the fusion pathway, the time to stalk formation ( $T_{\text{S}}$ ), the stalk lifespan ( $L_{\text{S}}$ ) and the HD lifespan ( $L_{\text{HD}}$ ) are given. The bridging distance is the intervesicle distance of the configuration before a connection is made.

states. The simulation analyses in this thesis are predominately done with custom built tools developed in python with computational intensive subroutines written in C.

## 2.2.4 Simulations

The simulations described in this chapter have been performed at constant temperature (307 K) and constant pressure (1 bar) with time steps of 24 fs.

Lipid bilayers were made by randomly distributing a number of lipids in a simulation box filled with water particles. When the simulation is run, a bilayer is formed spontaneously. Pressure scaling was applied independently in all three spatial directions such that no unnatural stress was introduced in the bilayer. Vesicles were made by placing such a bilayer in a larger simulation box. When the simulation is run, in an entropy-driven move,<sup>[34]</sup> the bilayer curls to minimize its edge, ultimately forming a vesicle.

The setup for vesicle fusion is made by duplicating the simulation box with the vesicle inside. Both duplications are translated and placed next to each other in a larger simulation box, such that the vesicles start at a relatively small distance from each other; on average 6.3 layers of water particles remain in between. The parts of the box devoid of particles are filled with water. In contrast to the earlier practices,<sup>[15,16]</sup> no restraints are put on the vesicles during the simulations.

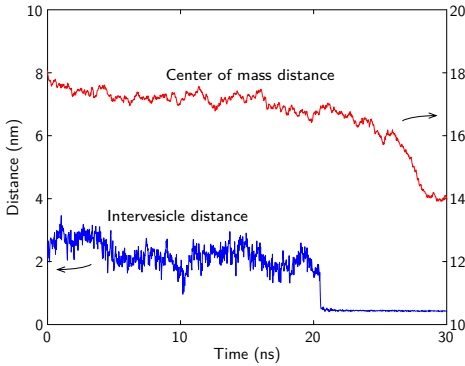


**Figure 2.3:** Graph of the intervesicle distance and the distance between the centers of mass of the vesicles' interiors. Evident are vesicle drift, membrane undulations and lipid movement.

## 2.3 Results

In the following sections, several fusion simulations are discussed. The simulations consist of either large or small vesicles; the large vesicles have a typical diameter of  $\sim 17$  nm, whereas the small vesicles are typically  $\sim 11$  nm in diameter. An overview of the performed simulations and their characteristics is given in Table 2.3.

### 2.3.1 Fusion of large vesicles

The first simulation discussed, `LARGE1`, is one of large vesicles. With large vesicles, the intermediate states of fusion can be visualized properly. This first simulation is treated as a framework for general fusion events that are discussed in detail. Subsequent simulations are treated more concise, focusing on the differences with the events of `LARGE1`.

#### 2.3.1.1 Vesicle movement

In the first simulation (`LARGE1`) a stalk emerged after 20.6 ns. Before a stalk can be formed, the vesicles have to move into contact range. The intervesicle distance is defined as the minimal distance between the lipids of the two vesicles, measured between the tail particles connected to the headgroup particles. This intervesicle distance is affected by movement of the vesicles on different scales, as shown in Figure 2.3. The first is caused by Brownian motion. In this case the vesicles drifted toward each other, the centers of mass got about 1.3 nm closer over 20 ns. As the vesicles undulate, this causes an oscillation of the minimal distance on top of the change caused by Brownian motion. The minimum distance was 2.5 nm at the start, it became as high as 3.5 nm and as low as 1.0 nm. At the actual start of stalk formation the vesicles were 1.4 nm apart. The final effect is caused by lipid



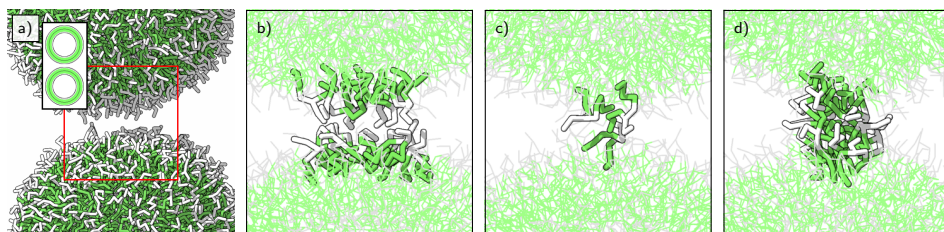


**Figure 2.4:** Stalk formation. Subfigures (b)–(d) show the contact region, highlighted by the red box in subfigure (a). In subfigures (b)–(d) the view is a cross-section along the vesicle–vesicle axis, as depicted in the inset of subfigure a. This orientation is maintained in all figures unless specified otherwise. Lipids are shown in stick representation with white hydrophilic headgroups and green hydrophobic tails; water has been omitted for clarity. (a) Shortly before fusion commences, the vesicles are at a considerable distance (19.48 ns). (b) The vesicles draw closer and hydrophobic patches appear in both (20.49 ns). (c) Lipid tails form a hydrophobic bridge (20.54 ns). (d) Other lipids complete the stalk (20.61 ns).

movement, such as out-of-plane movement, lateral diffusion, and atomic motion. The rapid fluctuation of the intervesicle distance graph is due to this movement.

### 2.3.1.2 Stalk formation

When the vesicles come into close contact, a stalk can be formed. In Figure 2.4 the formation event is illustrated. First hydrophobic patches emerge on opposite sides of the contact zone (Figure 2.4b). In these patches the tail ends are at the surface and as their headgroups are out of the way, the tails are less restricted to move into the interstice. Some lipids extend one of their tails into the interstice, bridging the gap between the vesicles (Figure 2.4c). As these lipids are splayed, this is somewhat reminiscent of extended lipid hemifusion, except for the important fact that the splayed lipids do not interweave the *cis*-monolayers but rather act as a bridge while the vesicles remain at their respective positions. Clearly the bridging lipids have moved out of the bilayer plane to let their tails connect. Several lipids move along the bridge structure, shielding it from water, thus forming a proper stalk (Figure 2.4d). From this point on the outer monolayers are connected and their lipids are allowed to mix. In every fusion simulation we have performed, the stalk never disintegrated once it was formed.

### 2.3.1.3 Anisotropic stalk expansion

Typically, the stalk is formed where the vesicles are closest together, that is, in the center of the contact zone (Figure 2.5). In this first simulation, the stalk expands anisotropically into an elongated stalk (Figure 2.5a, b), which grows and folds

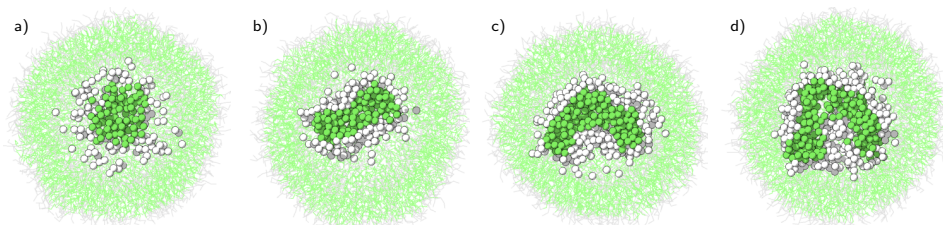


**Figure 2.5:** Anisotropic stalk expansion. The view is a cross-section through the stalk region, perpendicular to the vesicle-vesicle axis. The particles lying in the cross-section are shown individually. (a) The initial stalk (20.6 ns). The stalk proceeds to elongate (b) (22.9 ns), and bend (c) (24.7 ns) until it is about to close (d) (26.5 ns).

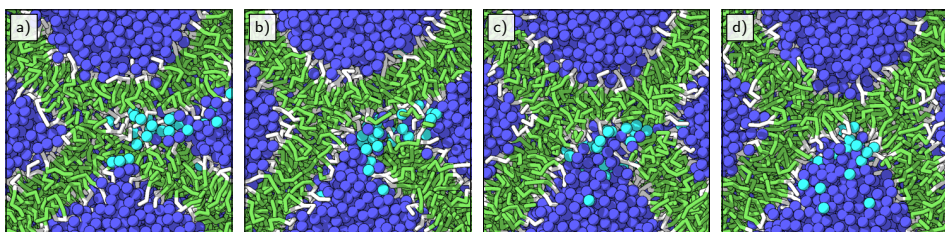


**Figure 2.6:** Hemifusion diaphragm formation via stalk-bending and one small pore. Shown is a cross-section along the vesicle-vesicle axis, through the pocket. Water is shown as dark blue van der Waals spheres, while the water particles that enter the bottom vesicle are light blue. (a) Some water enters the vesicle, and initializes a pore (26.5 ns). (b) The pore is evident (26.8 ns). (c) As the stalk ring closes and the last water particles enter the vesicle, the pocket is internalized (27.0 ns). (d) A hemifusion diaphragm is results (27.2 ns).

to form a ring (Figure 2.5c, d). In its pocket, the movement of water and lipid headgroups is restricted, but as water can move more freely, it is likely to get out of the pocket first. Visible in Figure 2.6a is that some water particles manage to slip past the membrane into one of the vesicles. They function as a trigger for pore formation, as several lipid headgroups and water particles follow, thereby opening up the pocket to that vesicle (Figure 2.6b). Approximately 0.5 ns later, the ring is completed (Figure 2.6c). In this manner the entire pocket has been internalized into the vesicle (measuring 25 lipids and 35 water particles). The resulting hemifusion diaphragm (Figure 2.6d) is not a classical one in the sense that it is formed by a single trans-monolayer complemented by the cis-monolayers instead of the other trans-monolayer.

In the second simulation of large vesicle fusion (LARGE2), the stalk-bending mechanism was different in that 0.2 ns after the pocket opened up to one side, it opened up to the other side as well, thereby causing full fusion instantly. Thus anisotropic stalk expansion can lead to stalk-bending with one or two pores, the latter fusion

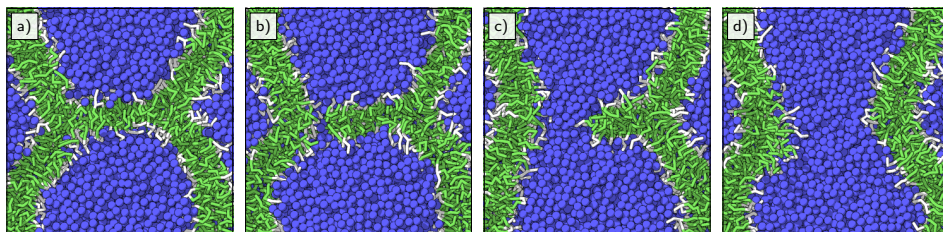


**Figure 2.7:** Hemifusion diaphragm breach and assimilation: (a) the HD (61.1 ns); (b) HD breach (61.6 ns); (c) the HD is assimilated as the pore grows (62.4 ns); (d) full fusion (62.8 ns).

process is markedly faster.

### 2.3.1.4 From hemifusion diaphragm to full fusion

The final interesting stage of the fusion process presented by the *LARGE1* simulation is the transition from an HD to full fusion. In the hemifused state, the vesicles' interiors are largely the same as in the separated state before fusion, whereas the external surface area is reduced. Hence, the surplus exterior lipids must stretch as they have a smaller area to fill. This results in a substantially thicker external membrane compared to the HD (Figure 2.7a), which consequently is the weakest part of the structure. Nonetheless, the HD is quite stable; here it took 34.5 ns before a pore emerged near the HD rim. Pore formation is again triggered by the movement of some water particles across an unstable bilayer (Figure 2.7b). Had the bilayer been stable the pore would have quickly receded, instead, the diaphragm contracted to reduce the area per lipid (Figure 2.7c). Now, in less than 1 ns the HD was assimilated in its entirety (Figure 2.7d).

With the vesicles fully fused, the lipids and water molecules are again confined to their compartments; there is little water transport and no lipid redistribution over the monolayers. The vesicle as a whole therefore does not become spherical in the remaining 57 ns but instead retains its tubular shape.

### 2.3.1.5 Radial stalk expansion

Whereas the prior two fusion simulations follow the anisotropic stalk expansion path, the third simulation (*LARGE3*) follows the radial stalk expansion path. This means the cis-monolayers that make up the stalk expand outward, thereby straightening the outer monolayer. As the cis-monolayers expand outward, the contacting part of the monolayers must separate as well, thus leaving an empty space in their wake (Figure 2.8b). As this void is energetically unfavorable, the mechanism of

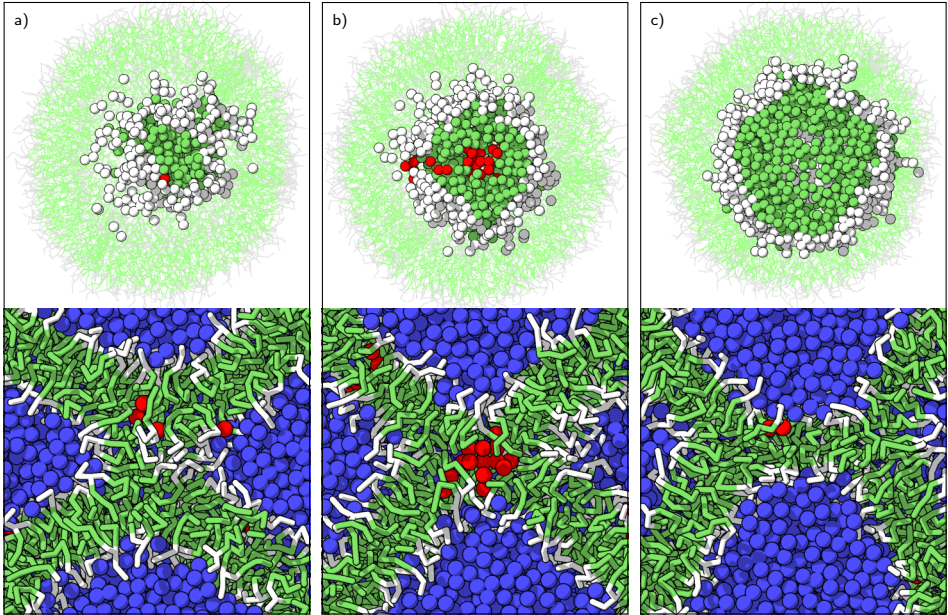


**Figure 2.8:** Radial stalk expansion. The top row is a cross-section through the stalk region, perpendicular to the vesicle–vesicle axis; the bottom row is the normal view along the vesicle–vesicle axis. For clarity, voids are visualized by automatically filling them with additional particles. Note that only clusters of ‘void particles’ indicate substantial voids, whereas solitary ‘void particles’ do not. (a) The stalk is evident (8.7 ns). (b) As the stalk expands radially, a hydrophobic void is present in its center (9.1 ns). (c) When the trans-monolayers connect, a hemifusion diaphragm is formed (9.6 ns).

straightening the outer monolayer now has to compete with the mechanism of reducing void size. Thus, the void size fluctuates, until the inner monolayers plus their contents have changed their shapes to fill the void. Here, the void lasted for 0.5 ns, after which the inner parts of the vesicles have deformed to fill the void and form an HD (Figure 2.8c). In the case of large vesicles, radial stalk expansion is considerably faster than anisotropic stalk expansion. Here within 1 ns after the appearance of the stalk an HD is already formed.

Although the *LARGE3* simulation has been continued for almost 90 ns after HD formation, a fusion pore has not appeared in the HD—it is still expected to however, as it took a long time in *LARGE1* as well. However, a control simulation was performed starting with a configuration of *LARGE3* in which the stalk expanded radially, with a minute difference in particle velocities. In this simulation, the stalk expands normally, but almost immediately after HD formation, it is already punctured. Thus, this small HD lasted for only 0.22 ns.

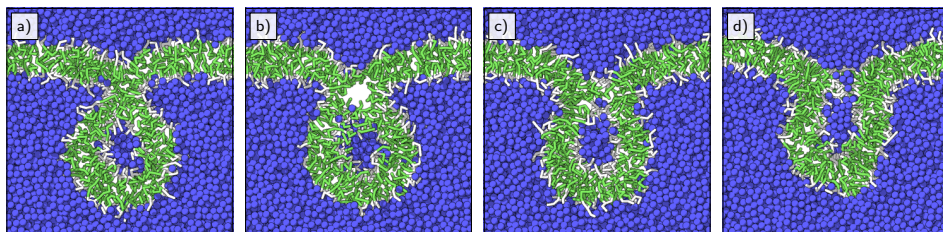


**Figure 2.9:** Thin slices through the center of a small vesicle fusing with a bilayer. (a) The stalk is formed (15.4 ns). (b) It expands radially, so a hydrophobic void is present (15.6 ns). (c) A small HD is formed by adaptation of the trans-monolayers (15.7 ns); (d) Then a pore opens up the HD (16.5 ns), and the water content of the vesicle is released across the bilayer.

### 2.3.2 Fusion of small vesicles

The fusion process has also been studied for smaller vesicles. In the first simulation (SMALL1) the vesicles fuse according to the anisotropic stalk expansion model. A single pore is formed, thus an HD state follows, which is short-lived. In the second simulation (SMALL2) the anisotropic stalk expansion pathway is followed as well, but here two pores are formed, thus the second hemifusion state is bypassed. In the third simulation (SMALL3) the vesicles fuse according to the radial stalk expansion principle. This includes the presence of a transient void. As the inner parts of the vesicles are deformed to fill the void, a short-lived HD is formed. After only 0.12 ns the HD opens when lipid heads and water from both vesicles make contact. During the remainder of all three simulations the vesicles retain an elongated shape. Small vesicle fusion thus follows the general pathways of the large vesicle fusion simulations, providing a fast alternative to study the process.

### 2.3.3 Exocytosis: fusion of vesicle and bilayer

In all previous simulations both vesicles were of equal size. In nature, this is usually not the case. In the process of exocytosis, for example, material is discharged from the cell via fusion of a vesicle with the much larger cell membrane.<sup>[1]</sup> To model exocytosis, we focus on the contact zone between vesicle and cell membrane. Due to differences in size, the cell membrane is modeled as a flat bilayer. In the first simulation a small vesicle and a bilayer of 904 lipids are considered. As the curvature of a bilayer is minute, especially compared to the curvature of small vesicles, it is of interest to investigate whether their combination differs from the fusion process described above.

In the first exocytosis simulation (EXOCY1), a stalk formed after 13.3 ns (Figure 2.9a). Stalk formation is normal as the bridging lipids come from both mono-

layers. The stalk has a tendency to elongate, but little room was available in the contact zone for stalk-bending. Eventually, the concave monolayer was released from the convex monolayer, leaving a hydrophobic void (Figure 2.9b). The void was mainly filled by the distal monolayer of the bilayer and somewhat by deformation of the vesicle interior; the bilayer looks cratered as a result (Figure 2.9c). The curved nature of the hemifusion state imposes a strain on the waist that can be relieved by straightening the membrane. This force pulls at the HD; thus a pore opened up in the center of the HD (Figure 2.9d), and the vesicle contents are released.

In the second exocytosis simulation (`EXOCY2`), with slightly different initial particle velocities, the stalk followed the anisotropic stalk expansion scenario. The HD lasted much longer than in the previous simulation (28.0 ns versus 0.8 ns), and thus had the time to grow larger as well (on average 18 nm<sup>2</sup>). A fusion pore was initiated by water crossing the diaphragm membrane, thus completing the fusion process.

The fusion mechanisms of these simulations are qualitatively similar to the vesicle fusion simulations described above.

## **2.4 Discussion**

In this section the various stages of fusion, as observed in our simulations, are compared to the various hypotheses presented in this chapter's introduction. Additionally, the characteristics of the two modes of stalk expansion are distinguished.

### **2.4.1 Bridging lipids**

We demonstrated the spontaneous formation of a stalk, initiated by splayed lipids forming a bridge structure. Such a transient structure of single lipids was not and cannot be described by elastic continuum models. By using a coarse-grained model, the details of stalk formation can be observed, but what initiates stalk formation? Here explanations are suggested on the basis of these observations.

Apparently, the bridging lipids originate from hydrophobic patches. There is no immediate explanation as to why these patches emerge. The attraction between hydrophilic particles is identical for water and headgroup particles; there is no reason headgroups would preferentially aggregate. However, without a preferred state the system fluctuates between states, thus occasionally sizable hydrophobic patches are present. The appearance of hydrophobic patches does not require imminent fusion.

The position of the lipids that initiate the bridge in these hydrophobic patches is such that one of their tails is folded back toward the headgroup region, but not yet extended into the solvent. Even regular isolated bilayers or vesicles have some amount of back-folded lipids, not limited to hydrophobic patches. In our model bilayers, on average 11 % of the lipid tail ends are folded back, 4.7 % are near water and thus part of a patch with minimal water shielding. These percentages rise with increasing curvature. For the outer monolayer of the large vesicle (*LARGE1*) 15 % of the lipid tails are back-folded 8.8 % are accessible to water. For a small vesicle (*SMALL3*) these values are 19 % and 12 %, respectively. These findings support the notion that stalk formation is easier for smaller vesicles.

Although the flexibility of our model lipids does make back-folding less costly, it is not limited to our model, e.g., it is also found in a united atoms model<sup>[54]</sup> where 2 % of the lipids in a flat bilayer have an alkyl chain outside the average plane and in other coarse-grained vesicles.<sup>[55]</sup> Furthermore, it should be stressed that these back-folded lipids are not in the extended conformation: the lipids are not stretched and their tails are not in the water phase. In fact, in all the bilayer simulations we have performed, a lipid was never found to be in the extended conformation of stable bilayers as suggested,<sup>[24,56]</sup> although the flexibility of our lipids surely would have permitted it.

Among other things, Table 2.3 lists the bridging distance, the distance lipid tails need to span to serve as basis for the stalk. This intervesicle distance ranges from 1.3 to 1.7 nm. This is consistent with GUV fusion experiments, where a reduction of intervesicle distance from 3 to 1 nm was found to trigger (hemi-)fusion.<sup>[4]</sup> However, this distance is beyond the cutoff radius of the Lennard-Jones potential between two T particles. Therefore, the T particles of opposite vesicles are not able to sense each other before fusion. Furthermore, achieving the bridging distance is not sufficient to initiate a lipid bridge. In the simulations, often the bridging distance was reached various times before the stalk actually formed. For instance in *LARGE1* the bridging distance of 1.4 nm was reached at least seven times earlier; once the distance was no more than 1.0 nm (Figure 2.3). Thus the question remains, what triggers lipid bridging?

On closer inspection, another mechanism becomes apparent. Namely, small voids in the water phase accompany the lipids that are forming the bridge between vesicles in the simulations (Figure 2.10). These voids facilitate bridge building, they are empty spaces whose presence allows some lipids to extend their tails without energy gain repercussions. How these voids come to be, may be for entropic reasons. A thin water layer is entropically unfavorable, so the water in the cleft moves aside to the bulk, thus facilitating tail movement. As water and lipid tail particles associate with like particles, the process is self-amplifying; a moving lipid tail instigates a void through which it can move.

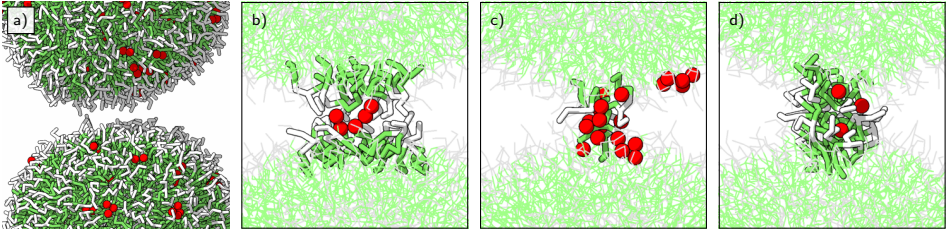


**Figure 2.10:** Stalk formation, the images of Figure 2.4 repeated with added particles filling and thereby highlighting the voids: (a) vesicles (19.48 ns); (b) hydrophobic patches (20.49 ns); (c) hydrophobic bridge (20.54 ns); (d) stalk (20.61 ns).

We have shown that vesicles can fuse spontaneously and the stalk forms in the center of the contact zone, as the lipid bridge forms spontaneously between vesicles at a small but considerable distance. This contradicts with the work of Stevens et al.,<sup>[16]</sup> who, using a similar CG model, conclude that stalks emerge at the edge of the contact zone. However, this is based on the assumption that spontaneous vesicle fusion requires excessive simulation time. Consequently, their simulations are geared toward rapid fusion: the vesicles are constructed by placing lipids on a spherical template, their interior is put under pressure and extra forces are applied to all vesicle particles. With these extra forces the stressed vesicles are pushed together. In the resultant configuration of flattened vesicles, multiple stalks emerge at the strained edge of the contact zone.

## 2.4.2 Stalk

When the bridging lipids are joined by others, a stalk is the result. In all our simulations, the stalk has an identical structure, but how does this structure relate to the various stalk models defined through the elastic continuum theory? The models can be differentiated by the shape of the trans-monolayers (from flat to bent), the accompanying void in the bifurcation, and the associated lipid tilt and splay.

In the simulations, there are no hydrophobic voids present in the membrane core during the transition from separated vesicles to vesicles connected by a stalk. The stalk forming process is sufficiently slow and the lipids are sufficiently flexible to allow the lipid tails to remain connected. The lack of voids is in agreement with the transmembrane contact stalk,<sup>[8]</sup> except that in our case the trans-monolayers do not make contact and are only moderately bent. In this respect, the stress-free stalk model<sup>[7]</sup> better resembles the simulation stalks, despite that they are voidless. Thus we propose a stalk structure closely resembling the stress-free stalk, but without hydrophobic voids; they are ‘filled’ with lipids undergoing tilt and splay.



### 2.4.3 Anisotropic stalk expansion and stalk-bending

When, of the two pathways leading to full fusion, the pathway of stalk elongation and bending is followed, a small transient pore emerges in the pocket formed by the bent stalk. The pore allows the uptake of lipids and water from the cavity. The question whether pore formation is triggered by a trace of water through the membrane, or the pore is only the result of a stressed membrane, is addressed here. To provide insight, an extra simulation has been performed. As a starting-point, the configuration of LARGE1 at 0.04 ns before water pore emergence has been taken, and all water particles have been removed from the cavity. The resulting events are the same, except that indeed the water pore is initiated later (0.41 vs 0.04 ns) as the cavity has to be refilled with water particles before pore formation can be triggered. A transient pore could also be formed by lipids solely, but apparently the energy barrier cannot be overcome without water involvement.

Our simulations support the stalk-bending hypothesis presented in the introduction section fairly well. The fact that the stalk may elongate and bend is in agreement with the model. Furthermore, the case in which two pores are formed and the hemifusion diaphragm is bypassed, is almost entirely analogous. The case where only one pore is formed, suggests a major revision, as the hypothesis does not entail the formation of an HD. Another difference is the manner in which the pores appear. In our simulations the pores always appear in the cavity of the bent stalk, the hypothesis suggests pore formation in the general vicinity of the stalk, followed by enveloping of these pores. Thus, the simulations demonstrate a more ordered mechanism than the hypothesis suggest. This difference is due to the methods used. The Brownian dynamics simulations, with which the anisotropic stalk effect was first demonstrated,<sup>[11]</sup> do not reproduce hydrodynamic behavior<sup>[32]</sup> and utilize small rod-shaped lipids, thus creating unstable vesicles and promoting disordered fusion.

### 2.4.4 Radial stalk expansion

During the transition from radially expanded stalk to hemifusion diaphragm a fairly large void appears. At first glance this might seem incorrect, but it is not as improbable as it may seem. A void is merely an absence of matter, an empty space. A void collapses rapidly because neighboring particles have a greater chance to move into a void than into a mass of other particles, simply because there is nothing to stop them. Granted, a void is not a preferential state. Particles preferably are in the vicinity of particles of the same kind. However, because the mutual attraction of hydrophobic particles is lower than the attraction of hydrophilic particles—they have a lower well depth in the Lennard-Jones potential—it is expected that the tails separate rather than the headgroups separate from water. Indeed, the monolayer attachment is the weakest interaction of the membrane. For instance,

with the freeze–fracture technique, membranes are often split in two monolayers. Furthermore, despite the shortcomings in Brownian dynamics simulations, the appearance of a void during this transition is reported by Noguchi and Takasu<sup>[11]</sup> as well.

### **2.4.5 Radial or anisotropical stalk expansion**

The stalk can expand radially or anisotropically, but what are the characteristic differences that make a stalk expand radially or anisotropically? Both transitions from stalk to (hemi-)fusion have different characteristics. For instance, the amount of lipids occupied in the bent stalk is larger than in the radial expanded stalk. These lipids are extracted from the cis-monolayers, so these must have spare lipids to build an elongated stalk. In this sense, spare lipids are lipids that are not required to shield the trans-monolayers, which depends on the ability of the lipids to flatten and shield a larger area. However, predicting the number of spare lipids is not straightforward. For instance, a simulation of the fusion of two flat bilayers shows that even with the same amount of lipids on cis- and trans-monolayers, lipids can be spared to construct a large elongated stalk. Moreover, bilayer fusion does not go beyond the elongated stalk phase. The stalk elongates and bends but is not steered toward a tight ring that would lead to pore formation. This shows that the shape of the elongated stalk depends on the shape of the contact zone. Whereas a radially expanded stalk would require fewer lipids than a long elongated stalk, there is no immediate gain in expanding radially. On the contrary, radial expansion is accompanied by a transient hydrophobic void. In the small vesicle simulations, this energetically unfavorable phase is readily compensated by reducing bending tension by complete flattening of the outer monolayer—a cylinder shape is preferred over an hourglass-shape. Regardless of the preferences caused by curvature, even if the amount of spare lipids could be calculated and the contact zone mapped, it would still be impossible to predict beforehand which pathway fusion would take. In particular, similar setups (e.g., the exocytosis simulations) evolve via different pathways, showing that subtle differences have major consequences.

### **2.4.6 Hemifusion diaphragm**

After radial stalk expansion and anisotropic stalk expansion with a single pore, a hemifusion diaphragm develops. The size of the HD surface area is controlled by two opposing mechanisms of the external monolayer. One is minimization of bending tension by flattening of the monolayer, the other is minimization of tension caused by overcrowding. Due to the reduced exterior area because of hemifusion, each external lipid must cover a smaller area, which causes tension. In the LARGE1 simulation this causes the HD size to fluctuate around  $38 \text{ nm}^2$  with

amplitude of about  $6 \text{ nm}^2$ . When, in a control simulation, 15% of the exterior lipids were removed, thereby reducing monolayer overcrowding tension, the HD grew to  $65 \text{ nm}^2$ . This means that in the anisotropic stalk expansion scenario, the involvement of the transient pore in HD formation is twofold. On one hand it triggers HD formation, on the other hand it redistributes lipids and water so the HD can grow larger than would be possible otherwise.

Of the fusion hypotheses only the stalk pore hypothesis recognizes a sizable hemifusion diaphragm structure. However, there is no consensus on the size an HD can adopt, although it is agreed that small diaphragms are energetically unfavorable. Some insist that the diameter cannot exceed the thickness of a bilayer,<sup>[9]</sup> whereas others claim that HDs grow to overcome this constraint.<sup>[7]</sup> The simulations are in accordance with both viewpoints, the HD either ruptures almost immediately or grows as much as possible—only limited by the compressibility of the outer monolayer—and is stable for quite a long time.

## 2.5 Conclusion

Vesicle fusion is essentially a mechanism of lipid rearrangement. We have used coarse-grained molecular dynamics to monitor these vast rearrangements over a relatively long time span. We have performed spontaneous unbiased fusion experiments with vesicles ranging between 160 and 1024 lipids, and with combinations of bilayers and small vesicles. In all simulations, the fusion process is analogous, but the stalk evolution may differ. From Table 2.3 it is clear that whether the fusion process follows the radial stalk expansion route or the stalk-bending route is not solely a matter of vesicle size, bridging distance, or acclimatization time. For large vesicles radial stalk expansion is considerably faster than stalk-bending, although the latter is more frequent. Typically, small vesicles fuse faster than large vesicles. They have a high curvature, so their lipids' tails are quite exposed to water and have much freedom of movement. The simulations of exocytosis show that a vesicle can fully fuse with a bilayer, but only if it is small enough to warrant radial stalk expansion or restricted stalk-bending, because two flat fusing bilayers do not overcome the anisotropically expanded stalk state. Generally, the preference for a fusion pathway varies with decreasing curvature at the contact area. Small vesicles develop a radially expanded stalk—reduction of monolayer curvature is a strong driving force here—or a bent stalk if the contact area permits. When the curvature decreases, the contact zone becomes too large to direct an elongated stalk into a tight ring, and the vesicles remain in a hemifused state. The fusion process is thus characterized by rapid transitions between long periods of stability. These transitions are initiated by trigger events that each have a small chance of happening; transitions that can nicely be shown using coarse-grained simulations.

## Bibliography

- [1] B. Alberts, D. Bray, J. Lewis, M. Raff, K. Roberts, and J.D. Watson, *Molecular biology of the cell*. Garland, New York, 1994.
- [2] H. Daraee, A. Etemadi, M. Kouhi, S. Alimirzalu, and A. Akbarzadeh, Application of liposomes in medicine and drug delivery. *Artif. Cell. Nanomed. Biotechnol.* 2016, *44*, 381–391.
- [3] G. Lei and R.C. MacDonald, Lipid bilayer vesicle fusion: Intermediates captured by high-speed microfluorescence spectroscopy. *Biophys. J.* 2003, *85*, 1585–1599.
- [4] J. Heuvingsh, F. Pincet, and S. Cribier, Hemifusion and fusion of giant vesicles induced by reduction of inter-membrane distance. *Eur. Phys. J. E* 2004, *14*, 269–276.
- [5] J. Nikolaus, M. Stöckl, D. Langosch, R. Volkmer, and A. Herrmann, Direct visualization of large and protein-free hemifusion diaphragms. *Biophys. J.* 2010, *98*, 1192–1199.
- [6] M.M. Kozlov and V.S. Markin, Vozmozhnyi mekhanizm sliiania membran. *Biofizika* 1983, *28*, 242–247.
- [7] V.S. Markin and J.P. Albanesi, Membrane fusion: Stalk model revisited. *Biophys. J.* 2002, *82*, 693–712.
- [8] Y. Kozlovsky and M.M. Kozlov, Stalk model of membrane fusion: Solution of energy crisis. *Biophys. J.* 2002, *82*, 882–895.
- [9] Y. Kozlovsky, L.V. Chernomordik, and M.M. Kozlov, Lipid intermediates in membrane fusion: Formation, structure, and decay of hemifusion diaphragm. *Biophys. J.* 2002, *83*, 2634–2651.
- [10] P.I. Kuzmin, J. Zimmerberg, Y.A. Chizmadzhev, and F.S. Cohen, A quantitative model for membrane fusion based on low-energy intermediates. *Proc. Natl. Acad. Sci.* 2001, *98*, 7235–7240.
- [11] H. Noguchi and M. Takasu, Fusion pathways of vesicles: A Brownian dynamics simulation. *J. Chem. Phys.* 2001, *115*, 9547–9551.
- [12] M. Müller, K. Katsov, and M. Schick, New mechanism of membrane fusion. *J. Chem. Phys.* 2002, *116*, 2342–2345.
- [13] D.W. Li and X.Y. Liu, Examination of membrane fusion by dissipative particle dynamics simulation and comparison with continuum elastic models. *J. Chem. Phys.* 2005, *122*, 174909.
- [14] J.C. Shillcock and R. Lipowsky, Tension-induced fusion of bilayer membranes and vesicles. *Nat. Mater.* 2005, *4*, 225–228.
- [15] S.J. Marrink and A.E. Mark, The mechanism of vesicle fusion as revealed by molecular dynamics simulations. *J. Am. Chem. Soc.* 2003, *125*, 11144–11145.
- [16] M.J. Stevens, J.H. Hoh, and T.B. Woolf, Insights into the molecular mechanism of membrane fusion from simulation: Evidence for the association of splayed tails. *Phys. Rev. Lett.* 2003, *91*, 188102.
- [17] B.A. Cornell, G.C. Fletcher, J. Middlehurst, and F. Separovic, The lower limit to the size of small sonicated phospholipid vesicles. *Biochim. Biophys. Acta* 1982, *690*, 15–19.
- [18] M.E. Haque and B.R. Lentz, Roles of curvature and hydrophobic interstice energy in fusion: Studies of lipid perturbant effects. *Biochemistry* 2004, *43*, 3507–3517.
- [19] J. Zimmerberg, Are the curves in all the right places? *Traffic* 2000, *1*, 366–368.
- [20] W. Helfrich, Elastic properties of lipid bilayers: Theory and possible experiments. *Z. Naturforsch., C: Biosci.* 1973, *28*, 693–703.
- [21] B.R. Lentz, D.P. Siegel, and V. Malinin, Filling potholes on the path to fusion pores. *Biophys. J.* 2002, *82*, 555–557.
- [22] L. Yang and H.W. Huang, Observation of a membrane fusion intermediate structure. *Science* 2002, *297*, 1877–1879.
- [23] D.C. Turner and S.M. Gruner, X-ray diffraction reconstruction of the inverted hexagonal (HII) phase in lipid–water systems. *Biochemistry* 1992, *31*, 1340–1355.
- [24] P.K.J. Kinnunen and J.M. Holopainen, Mechanisms of initiation of membrane fusion: Role of lipids. *Biosci. Rep.* 2000, *20*, 465–482.
- [25] B. Smit, P.A.J. Hilbers, K. Esselink, L.A.M. Rupert, N.M. van Os, and A.G. Schlijper,

- Computer simulations of a water/oil interface in the presence of micelles. *Nature* 1990, *348*, 624–625.
- [26] R. Goetz, G. Gompper, and R. Lipowsky, Mobility and elasticity of self-assembled membranes. *Phys. Rev. Lett.* 1999, *82*, 221–224.
- [27] J.C. Shelley, M.Y. Shelley, R.C. Reeder, S. Bandyopadhyay, and M.L. Klein, A coarse grain model for phospholipid simulations. *J. Phys. Chem. B* 2001, *105*, 4464–4470.
- [28] S.J. Marrink and A.E. Mark, Effect of undulations on surface tension in simulated bilayers. *J. Phys. Chem. B* 2001, *105*, 6122–6127.
- [29] M. Müller, K. Katsov, and M. Schick, A new mechanism of model membrane fusion determined from Monte Carlo simulation. *Biophys. J.* 2003, *85*, 1611–1623.
- [30] S.J. Marrink, A.H. de Vries, and A.E. Mark, Coarse grained model for semiquantitative lipid simulations. *J. Phys. Chem. B* 2004, *108*, 750–760.
- [31] J.E. Lennard-Jones, Cohesion. *Proc. Phys. Soc.* 1931, *43*, 461–482.
- [32] D. Frenkel and B. Smit, *Understanding molecular dynamics*. Academic Press, New York, 2002.
- [33] H.J.C. Berendsen, J.P.M. Postma, W.F. van Gunsteren, A. DiNola, and J.R. Haak, Molecular dynamics with coupling to an external bath. *J. Chem. Phys.* 1984, *81*, 3684–3690.
- [34] A.J. Markvoort, K. Pieterse, M.N. Steijaert, P. Spijker, and P.A.J. Hilbers, The bilayer-vesicle transition is entropy driven. *J. Phys. Chem. B* 2005, *109*, 22649–22654.
- [35] S.O. Nielsen, C.F. Lopez, G. Srinivas, and M.L. Klein, Coarse grain models and the computer simulation of soft materials. *J. Phys.: Condens. Matter* 2004, *16*, R481–R512.
- [36] A.F. Smeijers, A.J. Markvoort, K. Pieterse, and P.A.J. Hilbers, A detailed look at vesicle fusion. *J. Phys. Chem. B* 2006, *110*, 13212–13219.
- [37] A.F. Smeijers, K. Pieterse, A.J. Markvoort, and P.A.J. Hilbers, Coarse-grained transmembrane proteins: Hydrophobic matching, aggregation, and their effect on fusion. *J. Phys. Chem. B* 2006, *110*, 13614–13623.
- [38] A.J. Markvoort, R.A. van Santen, and P.A.J. Hilbers, Vesicle shapes from molecular dynamics simulations. *J. Phys. Chem. B* 2006, *110*, 22780–22785.
- [39] A.J. Markvoort, A.F. Smeijers, K. Pieterse, R.A. van Santen, and P.A.J. Hilbers, Lipid-based mechanisms for vesicle fission. *J. Phys. Chem. B* 2007, *111*, 5719–5725.
- [40] A.J. Markvoort, P. Spijker, A.F. Smeijers, K. Pieterse, R.A. van Santen, and P.A.J. Hilbers, Vesicle deformation by draining: Geometrical and topological shape changes. *J. Phys. Chem. B* 2009, *113*, 8731–8737.
- [41] A.J. Markvoort, N. Pfeleger, R. Staffhorst, P.A.J. Hilbers, R.A. van Santen, J.A. Killian, and B. de Kruijff, Self-reproduction of fatty acid vesicles: A combined experimental and simulation study. *Biophys. J.* 2010, *99*, 1520–1528.
- [42] B. van Hoof, A.J. Markvoort, R.A. van Santen, and P.A.J. Hilbers, On protein crowding and bilayer bulging in spontaneous vesicle formation. *J. Phys. Chem. B* 2012, *116*, 12677–12683.
- [43] B. van Hoof, A.J. Markvoort, R.A. van Santen, and P.A.J. Hilbers, Molecular simulation of protein encapsulation in vesicle formation. *J. Phys. Chem. B* 2014, *118*, 3346–3354.
- [44] P. Spijker, B. van Hoof, M. Debertrand, A.J. Markvoort, N. Vaidehi, and P.A.J. Hilbers, Coarse grained molecular dynamics simulations of transmembrane protein-lipid systems. *Int. J. Mol. Sci.* 2010, *11*, 2393–2420.
- [45] B. van Hoof, A.J. Markvoort, R.A. van Santen, and P.A.J. Hilbers, The CUMULUS coarse graining method: Transferable potentials for water and solutes. *J. Phys. Chem. B* 2011, *115*, 10001–10012.
- [46] A.J. Markvoort, P.A.J. Hilbers, and S.V. Nedeia, Molecular dynamics study of the influence of wall-gas interactions on heat flow in nanochannels. *Phys. Rev. E* 2005, *71*, 066702.
- [47] P. Spijker, H.M.M. ten Eikelder, A.J. Markvoort, S.V. Nedeia, and P.A.J. Hilbers, Implicit particle wall boundary condition in molecular dynamics. *Proc. Inst. Mech. Eng. C* 2008, *222*, 855–864.
- [48] P. Spijker, A.J. Markvoort, S.V. Nedeia, and P.A.J. Hilbers, Computation of accommodation coefficients and the use of velocity correlation profiles in molecular dynamics simulations. *Phys. Rev. E* 2010, *81*, 011203.
- [49] J. Kim, A.J.H. Frijns, S.V. Nedeia, and A.A. van Steenhoven, Molecular simulation of water

- vapor outgassing from silica nanopores. *Microfluid. Nanofluid.* 2015, *19*, 565–576.
- [50] A.F. Smeijers, A.J. Markvoort, K. Pieterse, and P.A.J. Hilbers, Coarse-grained modelling of urea–adamantyl functionalised poly(propylene imine) dendrimers. *Mol. Simul.* 2016, *42*, 882–895.
- [51] A.F. Smeijers, A.J. Markvoort, K. Pieterse, and P.A.J. Hilbers, Coarse-grained simulations of poly(propylene imine) dendrimers in solution. *J. Chem. Phys.* 2016, *144*, 074903.
- [52] A.F. Smeijers, K. Pieterse, P.A.J. Hilbers, and A.J. Markvoort, Multivalency in a dendritic host–guest system. *Macromolecules* 2019, *52*, 2778–2788.
- [53] A.D. McKerrel Jr, D. Bashford, M. Bellott, R.L. Dunbrack Jr, J.D. Evanseck, M.J. Field, S. Fischer, J. Gao, H. Guo, S. Ha, D. Joseph-McCarthy, L. Kuchnir, K. Kuczera, F.T.K. Lau, C. Mattos, S. Michnick, T. Ngo, D.T. Nguyen, B. Prodhom, W.E. Reiher III, B. Roux, M. Schlenkrich, J.C. Smith, R. Stote, J. Straub, M. Watanabe, J. Wiorkiewicz-Kuczera, D. Yin, and M. Karplus, All-atom empirical potential for molecular modeling and dynamics studies of proteins. *J. Phys. Chem. B* 1998, *102*, 3586–3616.
- [54] S. Ohta-Iino, M. Pasenkiewicz-Gierula, Y. Takaoka, H. Miyagawa, K. Kitamura, and A. Kusumi, Fast lipid disorientation at the onset of membrane fusion revealed by molecular dynamics simulations. *Biophys. J.* 2001, *81*, 217–224.
- [55] S.J. Marrink and A.E. Mark, Molecular dynamics simulation of the formation, structure, and dynamics of small phospholipid vesicles. *J. Am. Chem. Soc.* 2003, *125*, 15233–15242.
- [56] R.W. Corkery, The anti-parallel, extended or splayed-chain conformation of amphiphilic lipids. *Colloids Surf., B* 2002, *26*, 3–20.



## Chapter 3

# Transmembrane protein-influenced vesicle fusion

---

**Abstract** Experimentally, fused vesicles become spherical promptly. In the available time scale of molecular dynamics simulations they do not, because the lipid and water distribution of the fused state is inappropriate for a spherical vesicle and spontaneous amendment is slow. Here, we study the hypothesis that enhanced transport across the membrane of water, lipids, or both is required to produce spherical vesicles. This is done by introducing several kinds of model proteins to fusing vesicles. The results show that equilibration of both water and lipid content is a requirement for spherical vesicles. In addition, the effect of these transmembrane proteins is studied in bilayers and vesicles, including investigations into hydrophobic matching and aggregation. Our simulations show that the level of aggregation does not only depend on hydrophobic mismatch, but also on protein shape. Additionally, one of the proteins promotes fusion by inducing pore formation. Incorporation of these proteins allows even flat membranes to fuse spontaneously. Finally, we encountered a novel spontaneous vesicle enlargement mechanism we call the engulfing lobe, which may explain how lipids added to a vesicle solution are quickly incorporated into the inner monolayer.

---

---

This work has been published in:

A.F. Smeijers, K. Pieterse, A.J. Markvoort, and P.A.J. Hilbers, Coarse-grained transmembrane proteins: Hydrophobic matching, aggregation, and their effect on fusion. *Journal of Physical Chemistry B* 2006, 110, 13 614–13 623.



## 3.1 Introduction

A vesicle's shape is preferentially spherical so it has minimal membrane tension distributed uniformly over the surface. Whereas the coarse-grained MD vesicle fusion simulations of the previous chapter display the proper fusion processes, the resultant vesicles remain tubular instead of becoming spherical as they do experimentally; the reason being that during fusion the total water content and lipid distribution over the bilayers does not change markedly. Hence, the fused vesicle's volume is too small as compared to its membrane area, and its lipid distribution is not adapted to the new situation. In addition, the membrane's capacity for *water transport* and *lipid flip-flop* is low as compared to the required transport and, more importantly, the accessible simulation time. We hypothesize that, to promote fused vesicles to become spherical, increased water transport, increased lipid flip-flop, or both is needed. To this end, we incorporate functional transmembrane proteins into our lipid membranes. To increase the water permeability, we have reproduced the water channel function of aquaporin. To increase the rate of lipid flip-flop, we built two scramblase proteins; one being a bare transmembrane helix, which is supposed to induce flip-flop;<sup>[1]</sup> the other a prototype of the class of pore-forming antimicrobial peptides, which is reported to form pores and promote flip-flop.<sup>[2]</sup> Aside from fused vesicles becoming spherical or not, the incorporation of coarse-grained proteins presents challenges of its own. The requirements of coarse-grained proteins need to be elucidated. Is it even possible to build authentic transmembrane proteins with a simple coarse-grained model? The proteins need not only perform their desired function, but also exhibit realistic interactions with the membrane and other proteins. Does the membrane adapt to the transmembrane protein, as the hydrophobic matching theory suggests, and do the proteins aggregate when multiple proteins are incorporated in a membrane?

In addition to the effects of the proteins on the vesicles following fusion, they may also have an effect during the initial stages of fusion. In particular, one of the scramblases possesses characteristics displayed by the putative *proteinaceous fusion pore* model;<sup>[3]</sup> does such a protein indeed promote fusion?

In this chapter, we investigate these questions by applying our coarse-grained lipid model described in Chapter 2 to build proteins. However, despite focusing on proteins, we also encountered a novel spontaneous vesicle enlargement mechanism, which functions without protein involvement. This mechanism may explain how lipids added to a solution of vesicles get incorporated into the inner monolayers of these vesicles.

## **3.2 Methods**

### **3.2.1 Lipid and water**

Based on dipalmitoylphosphatidylcholine, the coarse-grained lipid is modeled by four hydrophilic H particles, and two tails of four hydrophobic T particles each (Figure 3.1a). Water particles are denoted by W. All bonds are regulated by harmonic bond potentials; the non-bonded interactions are governed by truncated shifted Lennard-Jones potentials. The model was fitted for water and alkanes, instead of lipids in a bilayer, to avoid unnecessary bias toward membrane formation. To ensure flexibility of our lipids and to be able to investigate vesicle fusion by using relatively small unstressed vesicles, no bending potentials are applied. Time-dependent results are presented without a time scaling factor.

### **3.2.2 Water channel**

In the present chapter, we extend this coarse-grained model with two proteins, the first being a water channel to enhance water transport through bilayers. To keep our model as simple as possible, we only use existing H and T particles and the previously mentioned potentials. The challenges we are presented with are as follows: is it possible to produce a coarse-grained water channel, and what requirements must such a channel adhere to? We base our design on the protein aquaporin.

In nature, when active in a membrane, aquaporin functions as a passive water channel. Its four subunits each make up a narrow pore. Two funnel-shaped apertures lead to the pore, formed by the tilted arrangement of seven helical structures. The channel apertures have series of accessible carbonyl oxygens forming hydrophilic paths leading to the pore. The pore is largely hydrophobic with discrete hydrophilic spots that provide an alternative for the hydration shell of water. The pore lining facilitates fast water transport.<sup>[4–6]</sup>

The coarse-grained water channel is built resembling one aquaporin subunit. An ideal channel is stable in a lipid membrane, stays open most of the time, and provides rapid water transport. However, the simplicity of the underlying model directs the design, as only H and T particles are used and the potentials to favor a specific conformation are limited to Lennard-Jones and bond potentials. Therefore, helical structures are impossible to reproduce. Nonetheless, a simple hollow cylinder suffices to represent a pore.

The cylinder is composed of a stack of 10 rings, whereby all particles are bound in a triangular mesh (Figure 3.1b). The internal ring consists of 8 particles and has

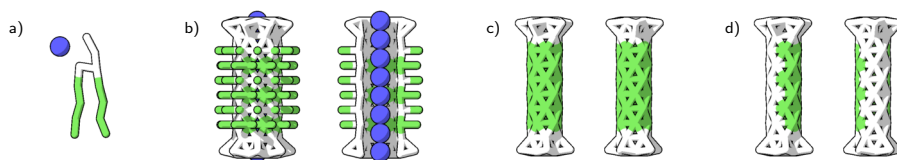


**Figure 3.1:** The coarse-grained water, lipid, and proteins. (a) Stick representation of the coarse-grained lipid molecule with hydrophilic headgroups (white) and hydrophobic tails (green) and a van der Waals representation of the water particle (blue). (b) Stick representation of the coarse-grained water channel showing its structure and a cross-section highlighting the hydrophilic band and rings inside the channel. (c) Front and side view of the type A scramblase; it has a purely hydrophobic transmembrane part. (d) Front and side view of the type B scramblase; it has a hydrophilic band down its side.

an effective diameter of 0.70 nm, whereas the effective diameter of W is 0.52 nm. The pore is wide and flexible enough to occasionally let water particles trade places, just like fully atomistic simulations of aquaporin<sup>[7]</sup> suggest. To ensure the semihydrophilic pore remains stable in the bilayer, it is coated with particles matching the local polarity of the bilayer, just as proteins are *in vivo*. To avoid any loose ends that would obstruct the pore opening, the pore ends are built as tetrahedrons.

Of various pore lining patterns tested, a pattern resembling the hydrophobicity of the aquaporin interior proved to encourage water flow best. Accordingly, the water channel has hydrophilic apertures, the middle consists of alternating hydrophilic and hydrophobic rings, and a hydrophilic band from top to bottom leads water particles through the pore. An additional advantage of this pattern is that the pore will collapse less easily as mutual repulsion between the hydrophilic and hydrophobic parts prevents complete flattening. Furthermore, the channel is filled from the start such that no time is lost on filling the channel.

Our coarse-grained proteins share similarities with a coarse-grained channel developed by Lopez et al.,<sup>[8]</sup> which in turn was made to resemble a fully atomistic carbon nanotube.<sup>[9]</sup> Their protein is a simple hydrophobic cylinder built from a similar mesh either with or without hydrophilic ends. These ends are found to enhance its position in the membrane and reduce occlusion by lipid tails.

### 3.2.3 Scramblases

Next, we add scramblases to our coarse-grained model. These proteins enhance the flip-flop of lipids. Again, we only use H and T particles and base the design on real proteins.

In lipid bilayers, the structural and amphiphilic properties of phospholipids are such that there is hardly any spontaneous flip-flop. The half-times of spontaneous membrane translocation for *in vitro* vesicle membranes are in the order of days,<sup>[10,11]</sup> whereas in eukaryotic plasma membranes flip-flop is in the order of months.<sup>[12]</sup> In cell membranes, the composition of phospholipids in each face of the bilayer is different and stable; this is associated with cellular processes such as membrane recognition and phospholipid–protein interaction.<sup>[12]</sup> On the other hand, sometimes lipid flip-flop is asked for in the cell, for example, with apoptosis or in the biogenic membranes, the membranes where lipid and protein synthesis is localized. To maintain the right lipid distribution, or to disrupt it, several protein groups are present in the cell.

In general, there are two classes of proteins promoting flip-flop, flippases that actively maintain an asymmetric lipid distribution of the membrane by transporting specific lipids in one direction and scramblases that passively equilibrate the membrane.<sup>[13,14]</sup> Examples of the first class are aminophospholipid translocase and ABC transporters, while phospholipid scramblase is a scramblase.<sup>[11,15]</sup>

Another scramblase protein is assumed to exist in *biogenic* membranes. Phospholipids are synthesized exclusively on the cytoplasmic monolayer of the endoplasmic reticulum (ER) in eukaryotes and the plasma membrane in prokaryotes. If not resolved, this would result in unwanted membrane curvature, the lack of which indicates the presence of a scramblase. Its activity has been measured and shown to be passive, bi-directional, headgroup unspecific, partially sensitive to protein denaturing agents, and satiable.<sup>[11,15]</sup> Historically, this putative protein was named flippase, but in fact it functions as a scramblase. With half-times of 8–16 s for phosphatidylcholine and phosphatidylethanolamine,<sup>[16]</sup> it is relatively fast.

Until a scramblase protein is indisputably identified in biogenic membranes, the question remains whether there is a single scramblase, a group of scramblases, or no scramblases at all. In the latter case, as advocated by Kol et al.,<sup>[1,15,17]</sup> flip-flop would be a general property of biogenic membranes resulting from the mere presence of proteins. An intrinsic flip-flop capacity would be advantageous, as newly synthesized lipids would only have to move down their gradient to be evenly distributed over the membrane leaflets. This hypothesis has been tested in various experiments, for example, by using model transmembrane peptides (XALPs) in *E. coli* membrane liposomes. These peptides form helices with a hydrophobic core consisting of alternating alanine and leucine residues. The core is capped with two hydrophilic residues and additional end-groups. With these peptides, half-times were found to increase to the order of minutes at peptide-to-lipid ratios of 1:250.<sup>[1]</sup> Fractionated protein extracts<sup>[18]</sup> and transmembrane proteins with a primary function not linked to flip-flop<sup>[17]</sup> give different flip-flop rates for different proteins, indicating that not all membrane proteins are capable of inducing flip-flop. Two modes of flip-flop were postulated. One is that a transmembrane

protein produces a somewhat more hydrophilic environment.<sup>[1]</sup> The second is that a single transmembrane protein locally disturbs the bilayer with dynamic protein-lipid interactions such as rotational motion, wobbling, tilting, or bending of the helix.<sup>[15]</sup>

Pore-forming antimicrobial peptides are another kind of flip-flop peptide present in nature. They are  $\alpha$ -helical transmembrane peptides with a hydrophilic side covering about 40% of their surface; examples include magainin 2<sup>[2]</sup> and pandinin 2.<sup>[19]</sup> They are believed to form pores in the cell membrane, thereby disrupting the transmembrane electrochemical gradient and inhibiting cell growth or even killing the cell.<sup>[20]</sup> Antimicrobial peptides spark a renewed interest because bacteria become increasingly resistant to conventional antibiotics.

A coarse-grained transmembrane protein has been constructed with the aim of reproducing the fast flippase activity of biogenic membranes and the structure of the XALP model peptides. As its function is fast and indiscriminate flip-flop, our protein is simply called scramblase. The coarse-grained water channel design is used as a basis. Likewise, scramblase is a cylinder measuring 10 rings in height, including tetrahedral hydrophilic caps. The tetrahedral ends remain for their presumed role as shields against water penetrating the membrane. Modifications are the reduced ring size of 5 particles, so the cylinder's core is inaccessible to water particles, and the absence of hydrophobic coating particles (Figure 3.1c). In the configuration where the core is entirely hydrophobic and the scramblase resembles XALPs, we refer to the protein as a type A scramblase. Type B denotes the configuration in which the scramblase is made similar to pore-forming antimicrobial peptides by giving it a two particle wide hydrophilic band down the side (Figure 3.1d).

### 3.2.4 Simulations

All simulations described in this chapter have been performed at constant temperature (307 K) and constant pressure (1 bar) with time steps of 24 fs. Lipid bilayers and vesicles were created as mentioned in the previous chapter, namely by spontaneous formation from randomly distributed molecules. In similar fashion, transmembrane proteins containing bilayers were constructed by adding the proteins to the random initial state.

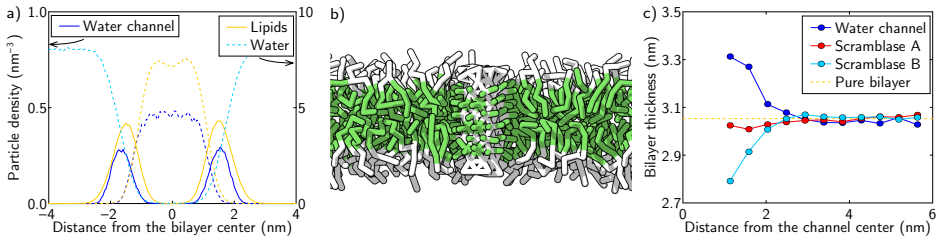


**Figure 3.2:** The water channel embedded in a lipid bilayer. (a) Density profiles of the water channel (left axis) and the bilayer and water (right axis) superimposed. The different scales are due to the different amounts of protein and other particles in the simulation. The lipid data is partitioned into tails (center) and headgroups, the water channel data into the associated pore and ends (dotted and solid lines, respectively). (b) A cross-sectional view showing the water channel. (c) Altered membrane thickness around the water channel and both scramblases. The membrane thickness is measured in concentric rings around the transmembrane protein center and averaged over 72 ns. The bilayer thickness depends on the distance to the transmembrane protein.

## 3.3 Results

### 3.3.1 Bilayers

To start, the effect of transmembrane protein addition is determined in bilayer systems. First, general effects as hydrophobic matching and aggregation are studied, followed by the proteins' specific transport activities.

#### 3.3.1.1 Hydrophobic matching

First, we study the incorporation of a single protein in the bilayer. In a simulation of 144 ns, the water channel remained anchored at both water–lipid interfaces. The channel seems to fit seamlessly in the bilayer (Figure 3.2b). On closer inspection, the peaks in the density profile (Figure 3.2a) show that the channel does not fit perfectly and is somewhat too large. However, shortening the channel by removal of one particle layer would create a larger mismatch. In this simulation, the overall bilayer thickness, as measured by the distance between headgroup density peaks, is on average 3.07 nm. In our simulations, pure lipid bilayers have an average thickness of 3.05 nm, thus the overall membrane thickness is not altered significantly with a transmembrane protein present.

However, a commonly accepted theory suggests that a height mismatch between the hydrophobic part of a transmembrane protein and the hydrophobic part of a lipid bilayer leads to hydrophobic matching; that is, the transmembrane protein locally imposes its hydrophobic height on the membrane. Because contact between

polar and apolar groups is preferably minimized and the lipid phase is much more deformable than a protein, a state of membrane deformation is considered less costly than a state of hydrophobic mismatch. The dimeric  $\beta$ -helical ion channel gramicidin, for instance, has been demonstrated to change membrane thickness.<sup>[21]</sup> Depending on the rigidity of the lipids, at a certain distance from the protein the membrane thickness returns to normal.

The extent of hydrophobic matching in our system is visualized in Figure 3.2c, for the case of both the water channel and the two scramblases. From the figure it is clear that close to the water channel the membrane thickness is about 10 % larger than the normal thickness of 3.05 nm. The transmembrane protein locally changes the structure of the bilayer. For the type A scramblases, despite the identical base height, the hydrophobic mismatch is lower. This is because the water channel's coating particles can spread between the tetrahedral ends, thereby enlarging its hydrophobic length. The difference between the hydrophobic matching patterns of type A and B scramblases is due to the mobility of the lipid headgroups near the hydrophilic band of type B. Close to the protein the thickness has changed significantly, but in all three cases the difference has vanished at about 2.5 nm from the protein center. Because of the inherent flexibility of the lipids in our model, the affected area is quite small.

### 3.3.1.2 Aggregation

Hydrophobic matching putatively drives a membrane-mediated protein-protein attraction. With multiple transmembrane proteins, aggregation is energetically favorable as this reduces the area of the membrane that needs to be deformed. The distance over which this protein attraction functions therefore depends on the rigidity of the bilayer as well. From Figure 3.2c follows that in this model the protein-protein distance at which the mutual attraction is significant is at most 5 nm.

However, in a simulation with 14 type A scramblases and 144 lipids there is little aggregation of scramblases. Instead, a dynamic equilibrium is established in which the scramblases connect and disconnect regularly (Figure 3.3a). Upon closer inspection, it follows that the lack of aggregation is due to the shape of the scramblases. The tetrahedral ends prohibit full contact between the scramblases so there is always room for a lipid tail to interfere, thereby negating stable protein-protein interaction. When the simulation is redone using scramblases without the tetrahedral end-groups (Figure 3.3b), a different picture emerges, despite the hydrophobic matching being markedly similar. As these proteins can connect tightly across their entire length and through optimal packing have maximal van der Waals attraction, one big aggregate is formed after 15 ns of simulation time. In the remainder of the simulation, none of the proteins dissociate from the aggregate.

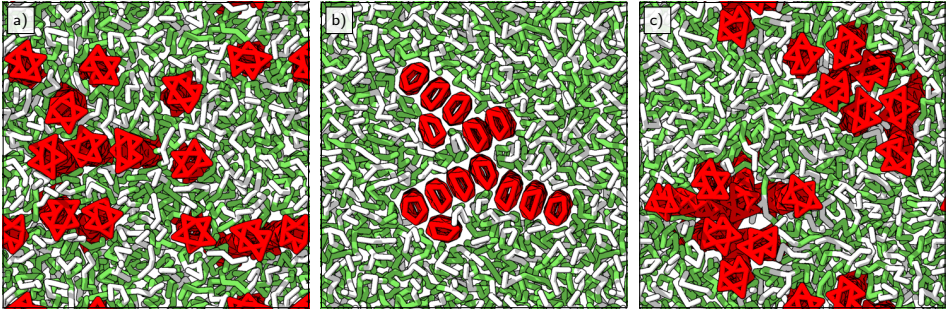


**Figure 3.3:** Several modes of aggregation; shown is a top view of the bilayer with 14 transmembrane proteins. (a) Weak aggregation of regular type A scramblases; they connect and disconnect regularly (72 ns). (b) Strong aggregation of type A scramblases trimmed of the tetrahedral parts; none of the proteins dissociate (72 ns). (c) Intermediate aggregation of type B scramblases; two pore complexes are formed (72 ns).

When type B scramblases are used instead of the hydrophobic ones, the level of aggregation is intermediate (Figure 3.3c). As the tetrahedral ends inhibit full contact, aggregates are still dynamic, but as the hydrophilic bands are preferentially near each other, there is an extra inclination to aggregate. During the course of this simulation, the type B scramblases cluster with their bands together. Eventually these clusters grow into two large clusters of 7 proteins each; each forming a pore complex in the membrane.

### 3.3.1.3 Function

**Water channel** To test the effectiveness of our water channel, W particle permeation rates have been measured and multiplied by 4 to match regular permeation rates. Our coarse-grained water channel thus achieves a rate of  $2.7 \times 10^{-15}$  mol/s. The maximal flow through an aquaporin subunit has been determined to be about  $5 \times 10^{-15}$  mol/s.<sup>[22]</sup> These rates are comparable, despite the fact that our simulations are performed under steady-state conditions, whereas the aquaporin flow has been determined under forced osmotic pressure.

The permeation rate of water through a pure lipid membrane in our model is  $139 \times 10^{-6}$  m/s, which is well within the order of magnitude of the experimental diffusive water permeability of dipalmitoylphosphatidylcholine (DPPC) bilayers ( $50 \times 10^{-6}$  m/s).<sup>[23]</sup> Incorporating 1 water channel in a 225 lipid membrane leads to a permeation rate through the membrane as a whole of  $430 \times 10^{-6}$  m/s.

**Scramblase** First, one type A scramblase is tested in a flat lipid bilayer of 225 lipids to see whether it induces flip-flop and by what mechanism. In all our pure lipid bilayer simulations, no spontaneous flip-flop was ever encountered,



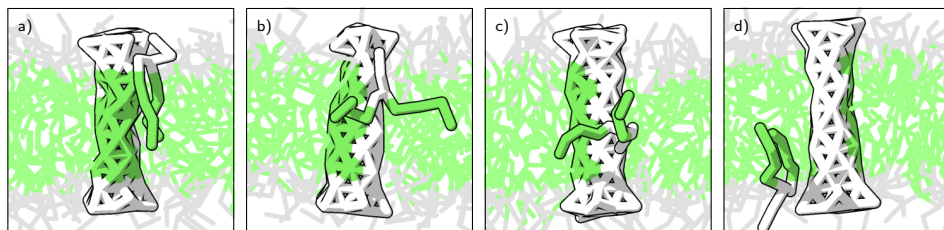


**Figure 3.4:** A lipid flips headfirst along a type B scramblase; each frame is 0.24 ns apart.

so any flip-flop due to the scramblase would be of significance. To stimulate flip-flop, a lipid gradient is created by removing 25% of one monolayer's lipids. However, despite the scramblase, in 72 ns not a single lipid flipped, just as in the control simulation without scramblase. Increasing the protein content (as in the aggregation experiment), while maintaining the lipid gradient, yields a membrane of 14 scramblases and 126 lipids, but still no flip-flop occurs. Instead of locally disturbing the lipid continuum, as predicted by Kol et al.,<sup>[15]</sup> the multitude of type A scramblases stabilizes the bilayer; for instance, the lateral diffusion rate of lipids is reduced by 35%. As the absence of flip-flop might be due to the lack of undulations in the small box, the bilayer length is tripled in one direction. Yet, although this membrane exhibits considerable undulations with large amplitudes, no flip-flop occurs in this simulation as well.

As none of the hydrophobic scramblases prompted lipid flip-flop, configurations with a hydrophilic band have been tested in the small bilayer as well. These type B scramblases do enhance flip-flop, but as a side effect also allow water to traverse the bilayer; during 72 ns, 14 lipids and 221 water particles crossed the bilayer. Each lipid flip is characterized by movement of the headgroup along the hydrophilic band, while the tail ends remain in the bilayer interior (Figure 3.4). The lipid can flip headfirst with tails splayed or sideways with tails together. In a full bilayer, without lipid gradient, the scramblase functions a bit slower; 44 lipids flipped and 1672 water particles traversed the bilayer in 720 ns. The water flux ( $15.4 \times 10^{-15}$  mol/s) is about 10 times faster than through our coarse-grained water channel, so the scramblase also functions as a water channel. Yet, contrary to the aggregation experiment, with a single scramblase a constant water pore is not formed; the type B scramblase merely allows water particles to slip through the bilayer more frequently. Compared to this single scramblase, the flip-flop capacity of the multiple pore-forming scramblases of the aggregation experiments is reduced. As the aggregated scramblases work together during flips, the individual protein flip-flop frequency has diminished from  $6.1 \times 10^{-2} \text{ ns}^{-1}$  to  $1.6 \times 10^{-2} \text{ ns}^{-1}$ .

Whenever flip-flop function is required hereafter, type B scramblase will be used exclusively, whereas type A will be used as a non-functional protein in control experiments.

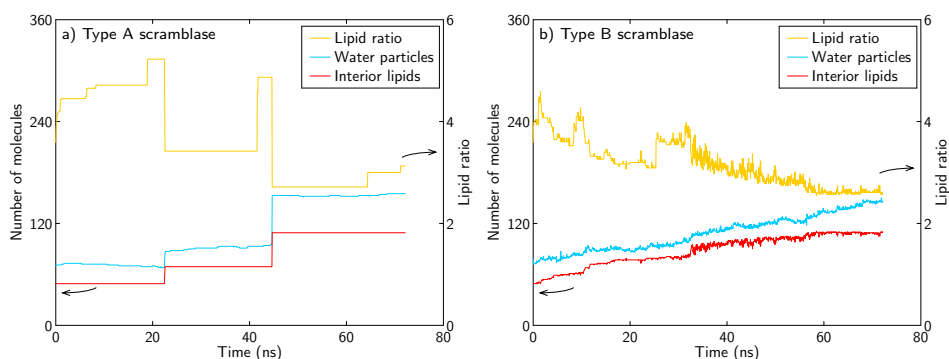


**Figure 3.5:** The vesicular contents (left axis) and outer to inner monolayer lipid ratio (right axis) followed through time as additional lipids are incorporated in a small vesicle with (a) type A scramblase and (b) type B scramblase.

### 3.3.2 Small vesicles

With the effect of the coarse-grained water channel and type B scramblase sufficiently validated in lipid bilayers, the proteins are incorporated in vesicles.

#### 3.3.2.1 Scramblase in an isolated vesicle

To test the effectiveness of one type B scramblase in a vesicle, a lipid gradient has been imposed by placing the vesicle of 255 lipids in a larger water-filled box with another 225 lipids dispersed randomly around it. A portion of these lipids will enter the outer monolayer right from the start, while the rest forms micelles that will, eventually, merge with the outer monolayer. Thus a skewed lipid distribution is generated and as a result the outer monolayer becomes stressed.

In the control simulation, the non-functional type A scramblase is used. Figure 3.5a depicts the time course of the lipid ratio between exterior and interior lipids, and the absolute number of interior lipids and water particles. The number of interior molecules increases stepwise twice. Each step is the result of a novel vesicle enlargement process we will refer to as the *engulfing lobe*.

As the outer monolayer cannot pass on lipids to the inner monolayer, it cannot take in more lipids while maintaining a normal flat structure. Instead, once the uptake limit is reached, additional micelles become part of the outer monolayer and are not fully absorbed but form a bilayer-like attachment (Figure 3.6a). Lipids from the tense outer monolayer allow this lobe to grow larger, as it proceeds to curl into a semivesicle (Figure 3.6b). Before the lobe becomes another vesicle on top of the initial one, a pore opens at its base, allowing enveloped water particles and lipids

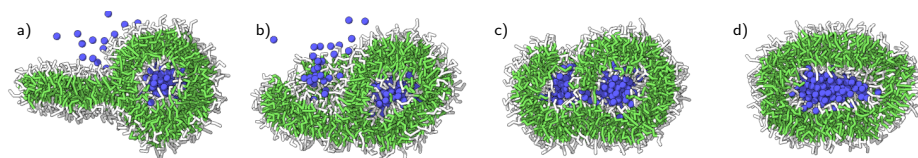


**Figure 3.6:** The engulfing lobe process demonstrated in a small vesicle that takes up additional lipids. (a) A micelle merges with the outer membrane (42.4 ns). (b) The lobe bends (43.6 ns), (c) and a transient pore emerges at its base (44.6 ns). (d) The vesicle after it has taken up lipids and water (46.6 ns).

to enter the initial vesicle (Figures 3.6c,d). Thus, the engulfing lobe mechanism is a spontaneous vesicle enlargement mechanism whereby the vesicle uses surplus exterior lipids to take up a portion of these lipids and additional water.

Over the course of this simulation, all exterior lipids became part of the vesicle; each added lipid raised the lipid ratio and the membrane tension. The first lobe emerged and engulfed water in 3.4 ns at a lipid ratio of 5.1:1; the second lobe cycle took 3.0 ns at a ratio of 4.8:1. At the end of the simulation, the vesicle is elongated and its lipid ratio is 3.1:1.

When the simulation is redone with a type B scramblase, a different growth pattern develops (Figure 3.5b). The banded scramblase quickly redistributes the lipids that merge with the outer monolayer. Hence, the number of interior lipids and water particles increases gradually, while the lipid ratio decreases gradually. This vesicle does eventually adopt a spherical shape.

### 3.3.3 Small vesicle fusion

In the following sections, several vesicle fusion simulations are discussed; their characteristics are summarized in Table 3.1. First, small vesicles are fused, because by utilizing small vesicles we can relatively quickly determine the effect of the various proteins on the vesicles during and after fusion. Subsequently these simulations are verified with larger vesicles.

In the present chapter, the plain vesicle fusion simulations of Chapter 2 serve as control experiments, labeled PURE1–5.

#### 3.3.3.1 Vesicle fusion with water channels

As mentioned in the introduction section, a vesicle's shape is preferentially spherical, yet the resultant vesicles of pure lipid vesicle fusion simulations remain tubular throughout the simulations. Provided that the required membrane tension and

**Table 3.1:** Overview of vesicle fusion simulations<sup>a</sup>

Label	$N_{\text{out}}$	$N_{\text{in}}$	$N_{\text{W}}$	Fusion pathway	$N_{\text{out}}/N_{\text{in}}$
PURE1	134	26	17	Anisotropic, 1 pore	3.78
PURE2	161	39	66	Anisotropic, 2 pores	3.40
PURE3	181	58	102	Radial	3.12
PURE4	655	369	3483	Anisotropic, 1 pore	1.68
PURE5	655	369	3497	Anisotropic, 2 pores	1.70
SCRB1	176	49	70	Anisotropic, scramblase pore	2.98
SCRB2	638	380	3555	Anisotropic, scramblase pore	1.65
WACHA1	180	45	85	Anisotropic, 2 pores	3.59
WACHA2	180	45	92	Radial	4.00

<sup>a</sup> The simulations are labeled PURE for vesicles consisting only of lipids, SCRBB for vesicles with type B scramblases, and WACHA for vesicles with water channels. For these simulations, the number of lipids in the inner ( $N_{\text{in}}$ ) and outer ( $N_{\text{out}}$ ) membrane layer of each vesicle, the number of encapsulated water particles ( $N_{\text{W}}$ ) in each vesicle, the fusion pathways, and the lipid distribution ratio of the vesicle membrane ( $N_{\text{out}}/N_{\text{in}}$ ) are given. The lipid distribution is calculated immediately after the development of a hemifusion diaphragm or a double pore.

water permeability are present, water can simply diffuse through the membrane to increase vesicle volume and thus create a spherical vesicle. Here, we test the hypothesis that increased water permeability, due to the presence of a water channel, enables fused vesicles to become spherical faster.

In this simulation (WACHA1), each vesicle consists of 225 lipids and 1 water channel. Full fusion is reached through the anisotropic stalk expansion pathway, here followed by double pore formation after 4.0 ns. This fast fusion is similar to the fusion of regular small vesicles (PURE1, PURE2). The result is quite similar as well; the vesicle remains tubular and there is no significant increase in volume apart from the uptake during the stalk-bending part of fusion. The effect of the water channels is simply that the water content fluctuates more. Apparently, in their current configuration there is not enough incentive for the vesicles to become spherical.

In this case, aggregation of water channels is significant. Compared to the flat bilayer case, the vesicle's bilayer has a different structure; this causes a larger hydrophobic mismatch, thus increasing the cost of membrane deformation and the strength of aggregation. After 17.8 ns, the inner ends of the water channels make contact, the outer ends 3.0 ns later, and then the last of the intervening lipids departs. For most of the remainder of this simulation, the two water channels remain attached to each other, yet this attachment is by no means fixed. For several short intervals, ranging from 60 ps to a few nanoseconds, the inner or outer ends dissociate.

In a second simulation involving these vesicles, but with a slightly different initial

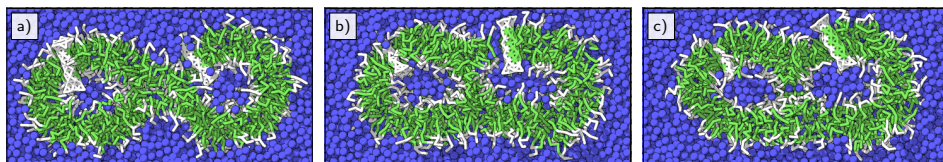


**Figure 3.7:** Cross-sectional view of the stalk–pore transition facilitated by a type B scramblase. (a) While the stalk is expanding anisotropically, a pore is formed next to the hydrophilic band of the scramblase in the vesicle on the right (3.2 ns). (b) A hemifusion diaphragm is already present, while the pore is still open (4.3 ns). (c) When the pore closes, another pore opens in the HD, completing the fusion process (4.4 ns).

configuration (WACHA2), the outcome is quite different. The stalk initially grows anisotropically, but reverts to expand radially. This series of events is analogous to a simulation performed with pure vesicles (PURE3). Because of this fusion pathway, the membrane lipid distribution and water content of the resultant vesicle are identical to (the sum of) those of the vesicles before fusion. Therefore, the vesicle has little water content situated in a thin cylinder of hydrophilic particles, and the outer monolayer experiences more tension than in WACHA1. This structure changes into a spherical vesicle with a large lobe, thereby maximizing hydrophilic interactions and relieving membrane tension. The vesicle proceeds to take up water and lipids through the engulfing lobe process. As the water channels are not involved in the lobe’s appearance, this simulation suggests the engulfing lobe’s applicability in regular vesicle fusion. Despite the improvement in lipid and water distribution made by the engulfing lobe, the vesicle remains tubular in shape. Again, the water channels aggregate.

### 3.3.3.2 Vesicle fusion with type B scramblases

Even though MD simulations of vesicle fusion do not produce spherical vesicles, Brownian dynamics simulations have shown this behavior.<sup>[24]</sup> However, those vesicles have properties inconsistent with naturally occurring vesicles. Spontaneous swelling occurs because their solvent is represented by a potential acting on the lipids rather than by explicit solvent particles. Moreover, the lipids are able to spontaneously exchange between the monolayers. As increased water permeability is insufficient to ensure spherical vesicles in our MD simulations, we hypothesize that frequent flip-flop of lipids is also required.

With the scrambling effect of type B scramblase demonstrated in bilayers (Section 3.3.1.3) and vesicles (Section 3.3.2.1), we next test whether it actually allows small fusing vesicles (SCRIB1) to become spherical. Furthermore, these simulations suggest that scramblase can facilitate fusion via the anisotropic stalk expansion as well. The scramblase, which happens to be near the stalk region, allows the

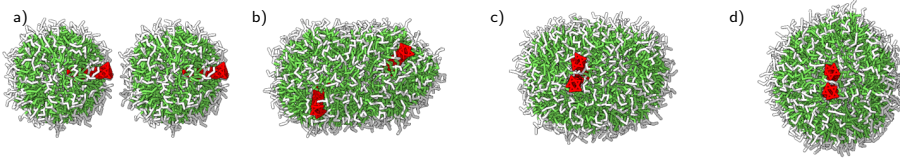


**Figure 3.8:** The fused vesicle becomes spherical when type B scramblases are present. (a) The initial setup (0 ns). (b) After fusion, the resultant vesicle is still elongated (21.6 ns). (c) When the scramblases find each other, they aggregate (91.4 ns). (d) Despite aggregation, the scramblases remain to function and consequently the vesicle becomes spherical (336 ns).

formation of a pore along its hydrophilic band (Figure 3.7a). During the 1.2 ns that the pore lasts, 9 lipids and 30 water particles enter the vesicle. The lipid transfer is in the same order as in comparable simulations that exhibit the anisotropic stalk-pore process (PURE1, PURE2), whereas the water transport is roughly doubled. A hemifusion diaphragm is already present before pore closure (Figure 3.7b); the pore is part of the vesicle wall. The pore closes and another pore opens in the HD immediately thereafter (Figure 3.7c). In this manner, fusion is reached by the same lipid and water dynamics as present in anisotropic stalk-pore process, but the pore is induced by the amphiphilic peptide.

As the vesicles are fully fused within 4.4 ns, the bulk of the simulation time is spent on adaptation of the vesicle (Figure 3.8). Figure 3.9a shows the time course of the contents of the vesicle. In this case the time for equilibration is roughly 100 times as long as the time for fusion. Evidently, the number of internal lipids increases rapidly the first 35 ns and changes only marginally thereafter. The water content increases very fast during the fusion process and steadily thereafter, until about 325 ns, when the vesicle reaches an equilibrium state. The shape of the vesicle can be deduced from the graphs depicting the three principal diameters versus time (Figure 3.9b). A perfect sphere would show three superimposed lines, but this result is not expected. A vesicle with a type B scramblase equilibrates by releasing excess membrane tension. Without tension, the membrane will be able to undulate and thus does not have the shape of a perfect sphere. Nevertheless, the graph shows that the fused vesicle becomes rather spherical.

Apparently, the lipids are faster than water at adapting to the new situation. However, the fact that the vesicle is not spherical in the early stages does not mean that the lipid distribution corresponding to a spherical vesicle is unfavorable; the lipids move from the regions of high membrane tension regardless of the overall shape of the vesicle. Nonetheless, for the vesicle to become spherical, and for the system to gain another level of energy minimization, water has to diffuse into the vesicle. This diffusion is rate limiting as the steady increase in water content shows.

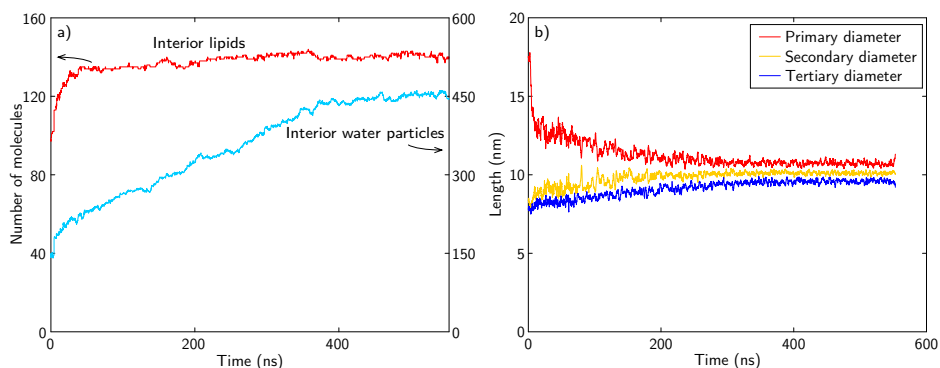


**Figure 3.9:** The growth of the fused vesicle. (a) The number of interior lipid molecules and water particles following vesicle fusion. The lipid content reaches a plateau well before the water content does. (b) The ‘primary’, ‘secondary’, and ‘tertiary diameter’ computed with principal component analysis and smoothed with a moving average window of 1 ns. As the lines converge, the vesicle becomes spherical.

The final vesicle has 140 lipids and 446 water particles inside and 310 exterior lipids. Of those 446 water particles, only 9 were initially present in the vesicles. This shows that there is much water exchange; even though the banded scramblases do not form actual water pores as seen in the aggregation experiment, they vastly increase membrane permeability. The scramblases do aggregate, and after 51 ns they connect and remain so for the rest of the simulation.

### 3.3.4 Fusion of large vesicles

To see whether the effects of type B scramblase in small vesicle fusion can be reproduced in large vesicles, we perform such a simulation as well. The simulation (SCR2) consists of two large vesicles of 1018 lipids and 4 type B scramblases each. Similar to prior large vesicle fusion simulations (PURE4–5), fusion starts by following the anisotropic stalk expansion pathway. Again, the scramblase facilitates fusion; a pore is initiated by a scramblase that happens to be in the center of the stalk ring. Through the pore, 13 lipids and 27 water particles enter the vesicle. With the formation of an HD, the pore closes. As no pore is formed in the HD in the short time after HD formation, the equilibrating properties of the banded scramblases stabilize this hemifusion state. The graphs of Figure 3.10 show that the vesicle labeled II is the one where the pore has formed. However, the scramblases proceed to equilibrate the vesicles so that earlier on the lipid content, and later also the water content, becomes similar for both vesicles. Compared to PURE4, the vesicle loses its hourglass shape and the diaphragm grows into a stable bilayer as thick as the outer membrane (Figure 3.11). Therefore, a destabilizing pore in the HD is not likely to appear.

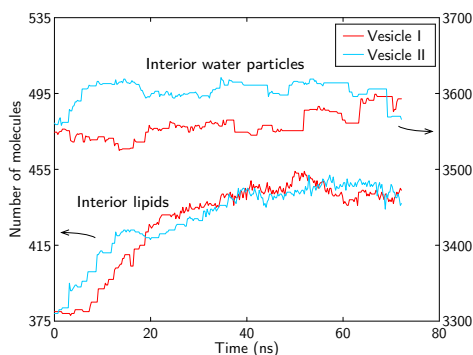


**Figure 3.10:** Development of the number of interior lipid molecules and water particles of the large vesicles of SCR2. Their contents remain separated for the entire simulation.

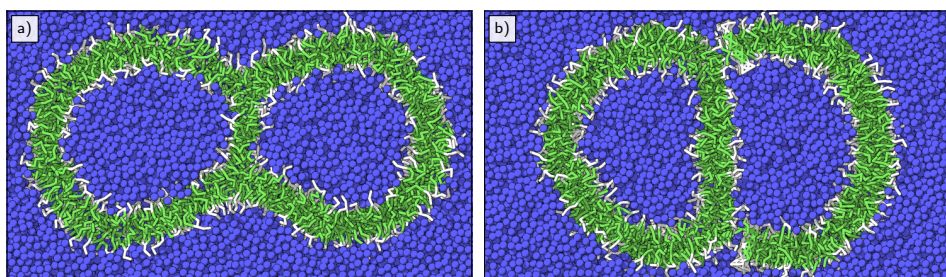


**Figure 3.11:** Cross-sections of the hemifusion diaphragm states of (a) PURE4 and (b) SCR2. Whereas the hemifusion state in PURE4 has a characteristic hourglass shape and a thin HD as compared to the outer membrane, the type B scramblases—here two of them are shown lying to the right of the HD—have equilibrated the HD state in SCR2. Consequently, the whole membrane of SCR2 has obtained a uniform thickness, and the hourglass shape is gone.

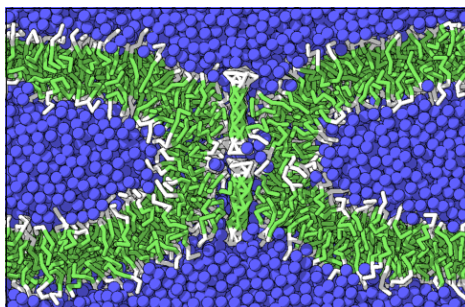
With multiple type B scramblases, a certain level of aggregation, maybe even peptide pore formation, is anticipated. However, only 2 out of 8 scramblases have actually aggregated in the 72 ns the simulation lasted. Nonetheless, the interaction of the peptides with the membrane does stimulate the scramblases to move toward the HD. All but one of the scramblases settle in this region, with their hydrophilic bands turned toward the HD.

### 3.3.5 Bilayer fusion

Giant vesicles are not able to fully fuse without an extra driving force,<sup>[25]</sup> thus various fusion protein models were conceived.<sup>[3]</sup> As an MD simulation of giant vesicle fusion is as yet unfeasible in both the length and the time scale accessible by the currently available fastest computers, we focus on the contact zone. At such a scale the vesicle membrane appears flat, so a representative simulation contains two bilayers with a small water layer in between. Like in *in vitro* experiments,<sup>[26]</sup> two



**Figure 3.12:** Cross-sectional side view of two fused horizontal bilayers. A fusion pore has been established by two paired type B scramblases.



flat bilayers do not fuse spontaneously in our simulations (Section 2.4.5). However, when the bilayers are placed sufficiently close together so they are able to undulate into contact range, a stalk is formed. This stalk then grows anisotropically into one large elongated stalk; it bends depending on the local shape of the contact zone, but not into a small ring. This hemifusion state is stable, and a hemifusion diaphragm state is not reached.

Here we test whether addition of type B scramblases permits two flat membranes to fuse. Our simulation setup consists of two parallel bilayers containing 890 and 899 lipids and 2 type B scramblases each; the adjacent monolayers are separated by an average of 3.4 layers of water particles, the distant monolayers by 12.4 layers. During stalk elongation, all four scramblases end up next to the stalk, but they do not aggregate. As the stalk keeps on growing, it meanders around the scramblases. Moreover, the scramblases in the opposite bilayers form pairs. In effect, the scramblases are linked together at the ends, as they both favor to be next to the bent stalk. The pairs subsequently allow formation of a continuous water pore (Figure 3.12). When the bilayers are regarded as the contact zone of giant vesicles, these pores allow the vesicles' content and inner monolayers to mix. Thus this state corresponds to full fusion facilitated by two pairs of banded scramblases.

## 3.4 Discussion

### 3.4.1 Hydrophobic matching and aggregation

In our simulations, we have verified the existence of changed membrane thickness due to hydrophobic matching of lipid bilayers to transmembrane proteins. On the basis of the structural differences between bilayers and vesicles, the latter having a reduced membrane thickness among other things, it is probable that the mismatch is larger in case of a vesicle. As the fused vesicle in the *WACHA1* simulation did not become spherical, there are areas of minimal curvature. Indeed, the water

channels stay in the areas where hydrophobic mismatch is minimal, in this case areas that resemble a bilayer the most. Therefore, the water channels favor the side of the tubular vesicle as opposed to the rounded ends. In fact, they even pair along the length axis of the vesicle where curvature is minimal. A similar kind of preference is exhibited by the type B scramblases in SCRB2; they group around the hemifusion diaphragm. In the aggregation simulation with multiple scramblases, the level of transmembrane peptide aggregation was shown to be strongly dependent on complementing contact shapes and hydrophobicity.

In the simulations presented here, and in the simulations of others,<sup>[27,28]</sup> the addition of a transmembrane peptide locally altered the membrane thickness. However, the experimental addition of an isolated WALP helix into bilayers did not alter membrane thickness.<sup>[29]</sup> This was attributed to an assumed difference in packing of lipids around a single transmembrane helix as compared to a large protein. The reason for this disagreement in results may be that the membrane thickness is altered only slightly and locally, comparable to our 1.5 % decrease in 2.5 nm around the protein center, which is difficult to detect experimentally.

### **3.4.2 Engulfing lobe**

The engulfing lobe, a novel spontaneous vesicle enlargement process, was observed in the small vesicle simulations. What are the prerequisites for a vesicle to enlarge via an engulfing lobe, and could it be universally present in nature? The most obvious requirement is that the outer monolayer is made up of enough lipids to cover the inner monolayer and simultaneously form a substantial bilayer appendage. In addition, the outer monolayer must be under considerable tension due to crowdedness. Of course, the effective lipid shape is important in lobe formation as well as in lobe curvature. The first two requirements are typically only met in small vesicles after fusion. In MD simulations (e.g, Chapter 2 and Ref<sup>[30]</sup>), vesicles were spontaneously generated with a lipid content of 150 and up. Such tiny vesicles are not easily found in the *in vitro* experiments; we expect they rapidly fuse into larger ones.

The engulfing lobe process might be an additional mechanism for fast flip-flop in biogenic membranes. The reason protein involvement is implied is essentially that *in vitro*, lipids do not spontaneously flip frequently. However, this flip-flop activity is measured under steady state conditions in stable membranes, whereas the biogenic membrane is characterized by growth of a single monolayer and as such inherently unstable. In the simulation of the vesicle with additional lipids, such a condition is quickly resolved by the appearance of multiple engulfing lobes.

### 3.4.3 Scramblase flip-flop

At first glance, the hypothesis that the mere presence of transmembrane proteins causes substantial lipid flip-flop<sup>[1,15]</sup> is not readily supported by our simulations. One of the principles the hypothesis conveys is that transmembrane helices in bilayers produce sufficient disorder for the lipid headgroups to slip into the bilayer, and subsequently pop-up on the other side. Our simulations show little disorder near the type A scramblases. However, the different outcomes of the *in vitro* and *in silico* experiments might simply be due to the different time scales at which they are measured. The flip-flop rate of the *in vitro* experiments is much lower than the perceived rate in the simulations with the type B scramblases. The flip-flop effect of type A scramblases cannot be rejected with certainty, for the bilayer simulations might just have to be extended for the effect to show.

On the other hand, the experimental lipid flips might be linked to a dynamic equilibrium of transmembrane helix insertion and expulsion, instead of helices that are stable in a bilayer. The latter is at least suggested by MD simulations of transmembrane peptide insertion,<sup>[8]</sup> where insertion is accompanied by trans-bilayer movement of lipids chaperoning the hydrophilic ends. The ‘barrel-stave’ mechanism<sup>[20]</sup> is another putative bilayer insertion mechanism for amphiphilic transmembrane helices resembling the type B scramblases. It states that multiple peptides drift over the surface of the membrane, but upon aggregation fold into the membrane together, thus forming an instant hydrophilic pore, which subsequently allows water permeation and lipid flip-flop. We have shown that with multiple amphiphilic helices such pore formation does occur, but aggregation is not quite necessary for an increase in the water permeability and flip-flop rate.

### 3.4.4 Fusion facilitated by type B scramblases

Apart from enhancing spontaneous flip-flop, type B scramblase has been demonstrated to promote fusion as well. It does so by providing a way to relieve membrane tension that results from crowding of the outer monolayer due to growth of the stalk. Normally, the tension rises until it is relieved by a pore appearing in the stalk ring; here the hydrophilic band promotes pore formation. In essence, this is still the result of changing the rates of flip-flop and water permeation. This may explain the results of Müller et al.<sup>[31]</sup> Using Monte Carlo simulations of block copolymers, they found full fusion of two bilayers, something which is not normally found in natural bilayers or MD simulations. However, compared to lipid bilayers, their membranes already have increased flip-flop and water permeation rates. The major difference between their model and our lipid bilayers including scramblase is that, like proteins, the scramblase functions locally; its rate of lipid flip-flop depends on the local gradient. For example, in the SCRB1 simulation, the banded scramblase that formed the pore allowed 9 lipids to enter the vesicle,

and the other let only 2 lipids in. In this simulation, the time from stalk to HD was decreased compared to the equivalent simulations PURE1–2, but not by many orders of magnitude (from 2.91, 2.02, to 1.66 ns). However, the fact that banded scramblases can induce a pore next to a stalk means that much larger vesicles and bilayers are also able to fuse. In this sense, the scramblase functions as a fusion protein. Of the various putative fusion protein models that permit flat membranes to fuse,<sup>[3]</sup> the local perturbation model and the proteinaceous fusion pore model both describe the shape and characteristics of type B scramblase well. The first model is loosely defined; it merely features leaky fusion induced by amphiphilic peptides that are said to disturb the membrane. The second model suggests that multiple amphiphilic transmembrane peptides form pore complexes in both fusing membranes. The complexes of apposing membranes connect, and subsequently the pore subunits dissociate to let the lipids unite the apposing bilayers. Although the type B scramblases can form such an instant pore by aggregation, in the simulation of bilayer fusion, the fusion pore was not of this nature. Association of juxtaposed scramblases did occur, and a fusion pore has been established, but guided by an elongated stalk. Thus, our simulations suggest an alternative proteinaceous fusion pore model with a larger role for lipid dynamics.

### **3.5 Conclusion**

With our coarse-grained molecular dynamics model previously only lipid interactions were simulated; in this chapter, we have demonstrated its use in simulations involving protein–lipid interactions. We introduced model proteins that enhance the bilayer’s ability for water permeability and lipid flip-flop. When incorporated in membranes, these transmembrane proteins induced hydrophobic matching of the membrane and accordingly protein aggregation emerged. The strength of aggregation depends on the fit of the proteins. In some of the simulations, a novel vesicle enlargement process, referred to as the engulfing lobe, was observed. This mechanism might have gone unnoticed experimentally, due to its rapid development on a small membrane area.

Although inclusion of a water channel increased water flow through the membrane, the fused vesicle did not become spherical; the lipid distribution of the membrane needed to adapt as well. To test the hypothesis that protein presence in general promotes fast flip-flop, model transmembrane helices were incorporated in various bilayers and vesicles, but without result. Pore-forming antimicrobial peptides are known to combine pore-formation and flip-flop. The current view is that fully developed proteinaceous pores are needed to promote flip-flop. Using a coarse-grained equivalent, our simulations show that for both increased water transport and lipid flip-flop a single peptide is sufficient, although multiple peptides do aggregate into pore complexes. This peptide was found to equilibrate fused vesicles,

which subsequently became spherical, and also to accelerate and even enable fusion in systems that normally do not fully fuse.

## Bibliography

- [1] M.A. Kol, A.I.P.M. de Kroon, D.T.S. Rijkers, J.A. Killian, and B. de Kruijff, Membrane-spanning peptides induce phospholipid flop: A model for phospholipid translocation across the inner membrane of *E. coli*. *Biochemistry* 2001, *40*, 10500–10506.
- [2] K. Matsuzaki, O. Murase, N. Fujii, and K. Miyajima, An antimicrobial peptide, magainin 2, induced rapid flip-flop of phospholipids coupled with pore formation and peptide translocation. *Biochemistry* 1996, *35*, 11361–11368.
- [3] R. Jahn and H. Grubmüller, Membrane fusion. *Curr. Opin. Cell Biol.* 2002, *14*, 488–495.
- [4] H. Sui, B.G. Han, J.K. Lee, W. Peter, and B.K. Jap, Structural basis of water-specific transport through the AQP1 water channel. *Nature* 2001, *414*, 872–878.
- [5] Y. Fujiyoshi, K. Mitsuka, B.L. de Groot, A. Philippsen, H. Grubmüller, P. Agre, and A. Engel, Structure and function of water channels. *Curr. Opin. Struct. Biol.* 2002, *12*, 509–515.
- [6] D. Alberga, O. Nicolotti, G. Lattanzi, G.P. Nicchia, A. Frigeri, F. Pisani, V. Benfenati, and G.F. Mangiatordi, A new gating site in human aquaporin-4: Insights from molecular dynamics simulations. *Biochim. Biophys. Acta* 2014, *1838*, 3052–3060.
- [7] E. Tajkhorshid, P. Nollert, M.Ø. Jensen, L.J.W. Miercke, J. O’Connell, R.M. Stroud, and K. Schulten, Control of the selectivity of the aquaporin water channel family by global orientational tuning. *Science* 2002, *296*, 525–530.
- [8] C.F. Lopez, S.O. Nielsen, B. Ensing, P.B. Moore, and M.L. Klein, Structure and dynamics of model pore insertion into a membrane. *Biophys. J.* 2005, *88*, 3083–3094.
- [9] G. Hummer, J.C. Rasaiah, and J.P. Noworyta, Water conduction through the hydrophobic channel of a carbon nanotube. *Nature* 2001, *414*, 188–190.
- [10] Y. Sasaki, R. Shukla, and B.D. Smith, Facilitated phosphatidylserine flip-flop across vesicle and cell membranes using urea-derived synthetic translocases. *Org. Biomol. Chem.* 2004, *2*, 214–219.
- [11] A. Tannert, A. Pohl, T. Pomorski, and A. Herrmann, Protein-mediated transbilayer movement of lipids in eukaryotes and prokaryotes: The relevance of ABC transporters. *Int. J. Antimicrob. Agents* 2003, *22*, 177–187.
- [12] B. Alberts, D. Bray, J. Lewis, M. Raff, K. Roberts, and J.D. Watson, *Molecular biology of the cell*. Garland, New York, 1994.
- [13] D.L. Daleke, Regulation of transbilayer plasma membrane phospholipid asymmetry. *J. Lipid Res.* 2003, *44*, 233–242.
- [14] G. van Meer, D.R. Voelker, and G.W. Feigenson, Membrane lipids: Where they are and how they behave. *Nat. Rev. Mol. Cell Biol.* 2008, *9*, 112–124.
- [15] M.A. Kol, A.I.P.M. de Kroon, J.A. Killian, and B. de Kruijff, Transbilayer movement of phospholipids in biogenic membranes. *Biochemistry* 2004, *43*, 2673–2681.
- [16] U. Marx, G. Lassmann, H.G. Holzhütter, D. Wüstner, P. Müller, A. Höhlig, J. Kubelt, and A. Herrmann, Rapid flip-flop of phospholipids in endoplasmic reticulum membranes studied by a stopped-flow approach. *Biophys. J.* 2000, *78*, 2628–2640.
- [17] M.A. Kol, A. van Dalen, A.I.P.M. de Kroon, and B. de Kruijff, Translocation of phospholipids is facilitated by a subset of membrane-spanning proteins of the bacterial cytoplasmic membrane. *J. Biol. Chem.* 2003, *278*, 24586–24593.
- [18] A.K. Menon, W.E. Watkins III, and S. Hrafnadóttir, Specific proteins are required to translocate phosphatidylcholine bidirectionally across the endoplasmic reticulum. *Curr. Biol.* 2000, *10*, 241–252.
- [19] K. Nomura, G. Corzo, T. Nakajima, and T. Iwashita, Orientation and pore-forming mech-

- anism of a scorpion pore-forming peptide bound to magnetically oriented lipid bilayers. *Biophys. J.* 2004, *87*, 2497–2507.
- [20] Y. Shai, Mechanism of the binding, insertion and destabilization of phospholipid bilayer membranes by  $\alpha$ -helical antimicrobial and cell non-selective membrane-lytic peptides. *Biochim. Biophys. Acta* 1999, *1462*, 55–70.
- [21] T.A. Harroun, W.T. Heller, T.M. Weiss, L. Yang, and H.W. Huang, Experimental evidence for hydrophobic matching and membrane-mediated interactions in lipid bilayers containing Gramicidin. *Biophys. J.* 1999, *76*, 937–945.
- [22] M.L. Zeidel, S.V. Ambudkar, B.L. Smith, and P. Agre, Reconstitution of functional water channels in liposomes containing purified red cell CHIP28 protein. *Biochemistry* 1992, *31*, 7436–7440.
- [23] R.H. Garrett and C.M. Grisham, *Biochemistry*. Saunders College Publishing, Philadelphia, 1995.
- [24] H. Noguchi and M. Takasu, Fusion pathways of vesicles: A Brownian dynamics simulation. *J. Chem. Phys.* 2001, *115*, 9547–9551.
- [25] J. Heuvingh, F. Pincet, and S. Cribier, Hemifusion and fusion of giant vesicles induced by reduction of inter-membrane distance. *Eur. Phys. J. E* 2004, *14*, 269–276.
- [26] L. Yang and H.W. Huang, Observation of a membrane fusion intermediate structure. *Science* 2002, *297*, 1877–1879.
- [27] H.I. Petrache, D.M. Zuckerman, J.N. Sachs, J.A. Killian, R.E. Koeppe II, and T.B. Woolf, Hydrophobic matching mechanism investigated by molecular dynamics simulations. *Langmuir* 2002, *18*, 1340–1351.
- [28] S.O. Nielsen, B. Ensing, V. Ortiz, P.B. Moore, and M.L. Klein, Lipid bilayer perturbations around a transmembrane nanotube: A coarse grain molecular dynamics study. *Biophys. J.* 2005, *88*, 3822–3828.
- [29] T.M. Weiss, P.C.A. van der Wel, J.A. Killian, R.E. Koeppe II, and H.W. Huang, Hydrophobic mismatch between helices and lipid bilayers. *Biophys. J.* 2003, *84*, 379–385.
- [30] S.J. Marrink and A.E. Mark, Molecular dynamics simulation of the formation, structure, and dynamics of small phospholipid vesicles. *J. Am. Chem. Soc.* 2003, *125*, 15233–15242.
- [31] M. Müller, K. Katsov, and M. Schick, A new mechanism of model membrane fusion determined from Monte Carlo simulation. *Biophys. J.* 2003, *85*, 1611–1623.



## Chapter 4

# Coarse-grained modeling of poly(propylene imine) dendrimers

---

**Abstract** To investigate the behavior of poly(propylene imine) dendrimers—and urea–adamantyl-functionalized ones—in solution using molecular dynamics simulations, we developed a coarse-grained model to tackle the relatively large system sizes and time scales needed. Harmonic bond and angle potentials were derived from atomistic simulations using an iterative Boltzmann inversion scheme, modified to incorporate Gaussian fits of the bond and angle distributions. With the coarse-grained model and accompanying force field simulations of generations 1 to 7 of both dendrimer types in water were performed. They compare favorably with atomistic simulations and experimental results on the basis of size, shape, monomer density, spacer back-folding and form factor measurements. These results show that the structural dynamics of these dendrimers originate from flexible chains constrained by configurational and spatial requirements. Large dendrimers are more rigid and spherical, while small ones are flexible, alternatively rod-like and globular.

---

---

This work has been published in:

A.F. Smeijers, A.J. Markvoort, K. Pieterse, and P.A.J. Hilbers, Coarse-grained modelling of urea–adamantyl functionalised poly(propylene imine) dendrimers. *Molecular Simulation* 2016, 42, 882–895.



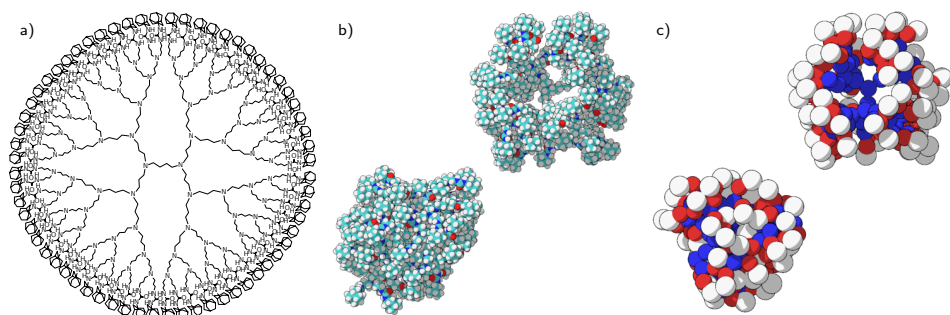


**Figure 4.1:** Three representations of the fifth-generation urea–adamantyl–decorated 1,4-diaminobutane poly(propylene imine) dendrimer. (a) Skeletal formula. (b) Fully atomistic model showing the initial connectivity (top) and the form at the end of the simulation (bottom). (c) Coarse-grained model in initial (top) and ultimate form (bottom).

## 4.1 Introduction

Dendrimers are a class of hyperbranched polymeric macromolecules, <sup>[1,2]</sup> synthesized in a controlled iterative fashion. Each iteration adds another generational shell of branches, multiplying the number of reactive ends. The large number of possible cores, branches and end-groups <sup>[3–5]</sup> allows for nanoengineering of properties like size, shape, topology, flexibility and surface chemistry.

Dendrimers have been investigated using computer models for a long time. The first attempts were made by using the principles of statistical models of macromolecules <sup>[6,7]</sup> to generate dendrimers with a self-avoiding walk algorithm. <sup>[8]</sup> To elucidate the dendrimer structure of an archetypal dendritic molecule, various bead-spring models have been researched using lattice Monte Carlo algorithms <sup>[9–11]</sup> and off-lattice ones, <sup>[12–16]</sup> mostly with implicit solvent. Other models where the solvent was treated implicitly were made with molecular dynamics <sup>[17–19]</sup> (MD) and Brownian dynamics. <sup>[20–23]</sup> One improvement in detail has been the inclusion of explicit solvent particles. <sup>[24–28]</sup> Another was using atomistic MD to model specific dendrimer variants, but still in implicit solvent or actual vacuum. Most notable are poly(propylene imine) (PPI) in vacuum <sup>[29,30]</sup> and melt <sup>[31,32]</sup> and poly(amido amine) (PAMAM) in vacuum <sup>[33–35]</sup> and melt, <sup>[36]</sup> but also various phenyl- <sup>[37–40]</sup> and carbosilane-based <sup>[41,42]</sup> dendrimers have been modeled. As both the solvent and the dendrimer composition influence the behavior, explicit solvent atomistic simulations have also been performed for, e.g., PPI, <sup>[43–46]</sup> PAMAM <sup>[46–50]</sup> and carbosilane <sup>[51]</sup> dendrimers. The early simulations scarcely lasted more than a nanosecond, but the recent examples typically reach time scales of up to tens of nanoseconds. Since experiments are performed with multiple dendrimers in solution and for much longer time scales, these atomistic simulations are only able

to reproduce a limited portion of experimental results. For phenomena where dendrimer–dendrimer interactions play a role, while also maintaining chemical specificity, coarse-grained simulations may provide new insight.

For some dendrimers such coarse-grained models have been published. The difference with earlier bead-spring models is that they are fitted on data obtained from atomistic simulations. The first reported coarse-grained model is a study of PAMAM engaging with a lipid bilayer.<sup>[52]</sup> The dendrimer uses repurposed lipid parameters. The same is true for a recent study of two PAMAM dendrimers interacting.<sup>[53]</sup> Another model is of stiff polyphenylene dendrimers in the melt phase,<sup>[54]</sup> where each bead represents 6 phenyl groups. These dendrimers have been made using a Boltzmann-inversion scheme for non-bonded interactions, and a fit of multiple Gaussians for the bonded interactions. Recently two new coarse-grained models have been published. One is a Monte Carlo model for various dendrimers<sup>[55]</sup> where the atomistic input is based on Langevin dynamics. The second is another PAMAM model in vacuum.<sup>[56]</sup> Despite the suggested use for larger simulations of multiple dendrimers, these recent models are only shown to reproduce structural properties of single dendrimers.

In this chapter, we investigate the behavior in water of poly(propylene imine) dendrimers in regular PPI form ( $G5$ : DAB–dendr– $(\text{NH}_2)_{64}$ ) and functionalized with urea–adamantyl groups (PPIUA,  $G5$ : DAB–dendr–(urea–adamantyl) $_{64}$ ) (Figure 4.1a). The latter are a useful template for acetic acid–urea guests in host–guest chemistry<sup>[57,58]</sup> (Chapter 6). PPIs are often used in experiments, and therefore ideally suited to base the coarse-grained model on.

We use molecular dynamics (MD) simulations to recreate and thereby elucidate the behavior of PPI dendrimers in water. Although the dynamics are fast on a chemical scale, it is impractical to reproduce this a fair amount of times using conventional fully atomistic MD. The size and time scales required are too large to follow dynamic interactions between dendrimer and solvent molecules a reasonable amount of time. With a coarse-graining (CG) scheme, however, it is possible to simulate aggregation in explicit solvent. Herein roughly four heavy atoms are joined into a single particle, significantly reducing the computational cost as fewer particles and interactions need to be calculated. Also, because high frequency motions are removed and the interaction potentials are smoother, larger time steps can be made. Moreover, because the system experiences less friction, the observed dynamics are faster.<sup>[59]</sup>

Simulations were performed using PumMa. The coarse-grained model defined in this chapter is an extension to the lipid model (Chapter 2), meaning the same water parameters are used.

In Section 4.2, we describe the derivation of a coarse-grained model for PPI and

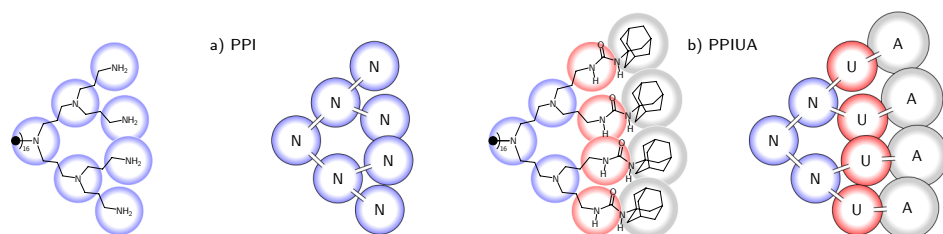


**Figure 4.2:** Molecular structure of a part of the (a) PPI and (b) PPIUA dendrimers with coarse-grained sites indicated (left), and the equivalent coarse-grained structure (right).

PPIUA dendrimers, using a scheme that iteratively adapts to input distributions obtained from a single atomistic PPIUA dendrimer in water simulation. Subsequently, in Section 4.3, the CG model is tested against experimental data and atomistic simulations of these dendrimers over a wide range of generations, both to validate the model and to augment the experimental data with an accurate molecular picture.

## 4.2 Model

Coarse-graining to acquire a correct model consists of two phases: deciding on which atoms to group into coarse-grained sites, and determining effective interaction potentials.

### 4.2.1 Coarse-grained sites

In general, each site should represent a functional group, so chemical specificity can be incorporated as its typical behavior is known. Also the choice to represent it by a single spherical particle should not be detrimental to the structure generated, i.e., a long chain should not be coarse-grained into a single particle.

The fifth-generation dendrimer, subject of the all-atom template simulation, consists of a large branched structure of poly(propylene imine) where each end is functionalized with urea and adamantyl moieties (Figure 4.1a). From a structural point of view, the recurring element of the PPI base is a tertiary amine connected to three other tertiary amines by hydrocarbon branches of 3 carbon atoms. Only the core differs, 1,4-diaminobutane being one carbon atom longer. Considering the branches originate at the nitrogens it is appropriate to take them as centers for a CG site. This leaves two options: either place another site at the center of the intermediate branch or forgo placing additional sites. Not counting hydrogens,

**Table 4.1:** Coarse-grained sites

Particle	Approximate chemical name	Formula	Mass (u)	Van der Waals radius (Å)
N	trimethylamine	$C_3NH_6 + \frac{3}{2}CH_2$	77.2	2.66
U	urea	$CN_2H_2O + \frac{3}{2}CH_2$	79.1	2.71
A	adamantyl	$C_{10}H_{15}$	135.2	3.33
W	water	$4H_2O$	72.1	2.59

the first option results in particles that either represent a branch (2 carbons) or an extended nitrogen (1 nitrogen plus 1.5 carbons). The second option results in particles that represent 1 nitrogen plus 4.5 carbons. While the first option better conveys the idea of focal points and branches, it also limits the degree of coarse-graining, i.e., the reduction of degrees of freedom is not much larger than provided by a united atoms model, and the attainable increase in scope is meager. Furthermore, we wanted to use the same water particles that were previously used in our water-lipid model (Chapter 2), where the water particles represent 4 water molecules. This dictated that each coarse-grained particle should represent roughly 4 heavy atoms. Thus the option with large coarse-grained particles (named N) was chosen, which provides a large reduction while maintaining the branched structure (Figure 4.2). This choice in turn reduced the options for the urea and adamantyl moieties. The urea moiety ( $CN_2H_2O$ ) contains 4 heavy atoms, so it forms a fine coarse-grained site by itself. Yet when the atomistic model is considered, it follows that the urea moiety is linked to the tertiary amine via 3 carbon atoms. So another one and a half carbons had to be placed with the urea particle (U) just to account for all the atoms. The adamantyl group finally consists of 10 heavy atoms, so for that amount at least 2 coarse-grained sites are appropriate. However, since it is a dense bulky group, it is better represented by a single spherical particle (A). The chosen coarse-graining is depicted in Figure 4.2 which results in the dendrimer of Figure 4.1c. The coarse-grained sites' approximate chemical names, molecular formulas, corresponding masses, and van der Waals radii are given in Table 4.1.

## 4.2.2 Interaction potentials

After having defined the coarse-grained particle sites, an appropriate force field governing their interactions was devised. There are several options for developing an effective force field. The input data may be predominantly structural or thermodynamic, the chemical detail may range from highly specific to phenomenological, and the resulting potentials may be of analytical form or tabulated.<sup>[59]</sup> To obtain a fairly general, transferable, force field, i.e., one that does not need to be reparameterized at every new state of interest, while still incorporating as much structural and chemical detail as possible, a combination of techniques was used. The bonded interactions were derived via Boltzmann inversion of a set of fully atomistic simulations. The overall chain structure of a polymer may depend

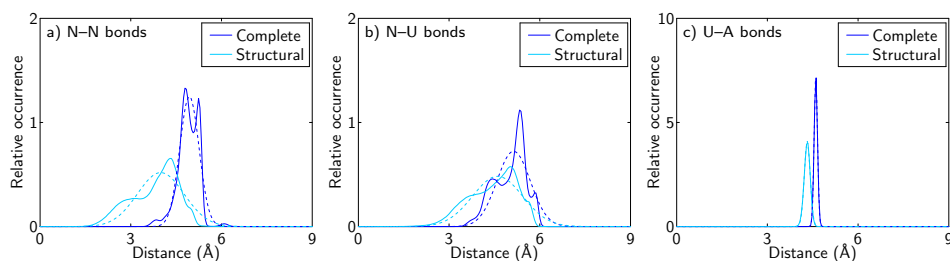


**Figure 4.3:** Distributions of coarse-grained site–site bond lengths from regular atomistic simulations and simulations without non-bonded interactions present. Distributions are normalized so the area under the curves equals 1. Each distribution (solid line) is fitted with a Gaussian distribution (dashed line).

on the solvent in which it is suspended. That is, the same polymer that is expanded in one (good solvent) may be collapsed in another (bad solvent). At the coarse-grained level this is reflected in the angles. For a general model to be applicable to simulations of different dendrimer sizes and concentrations, the influence of the medium must be conducted via non-bonded interactions, instead of being ingrained into the angle potentials. Therefore neutral intrinsic angle distributions were obtained from a separate atomistic simulation performed in vacuum with the Lennard-Jones and electrostatic interactions switched off. The solvent effect will stem from non-bonded interactions. The bond distributions are obtained from regular atomistic simulations, as in the CG model no van der Waals interactions are calculated between atoms directly bound to each other. The distributions were not used for Boltzmann inversion directly, but rather their Gaussian distribution fits, because the coarse-grained model uses harmonic bond and angle potentials, which lead to practically Gaussian distribution functions. For the non-bonded interactions the Lennard-Jones potential is used, initial parameters were defined phenomenologically, while some were refined to reproduce experimental data.

#### 4.2.2.1 Atomistic input

For the bonded interactions fully atomistic simulations of a *G5* PPIUA dendrimer *in vacuo* were used as input (Figure 4.1b, top). Since there is a strict relation between the atoms in the atomistic model and the coarse-grained particles, the center of mass of the constituting heavy atoms was taken as the center of each CG particle. Thus these CG sites were followed during the atomistic simulation run, continuously collecting the distribution of distances  $r_{ij}$  between bonded CG sites  $i$  and  $j$  and angles  $\theta_{ijk}$  between sites  $i$ ,  $j$  and  $k$ . This was achieved with a version of our PumMa code that performed atomistic simulations with CHARMM27<sup>[60]</sup> parameters. Simulations using only the structural parameters (bonds, angles, dihedrals, and improper dihedrals) and none of the non-bonded interactions (van der

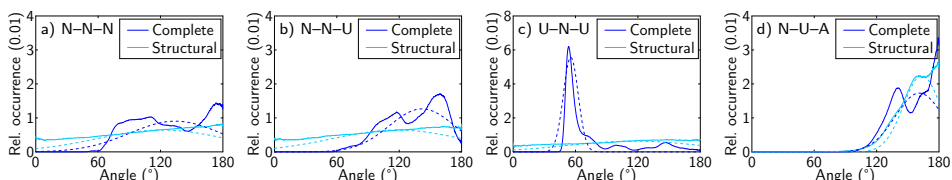


**Figure 4.4:** Distributions of coarse-grained site–site–site angles for regular and structural only atomistic simulations. Distributions are equalized (divided by  $\sin(\text{angle})$ ) and normalized, having the area under the curves equal 1. Each distribution (solid line) is fitted with a Gaussian distribution (dashed line).

Waals and electrostatics) were performed. This highlights the effect of steric hindrance, electrostatic attraction and repulsion and hydrogen bonding on the innate dendrimer structure. The bond and angle distributions for the 2 ns simulations are shown in Figures 4.3 and 4.4. For example, the pincer angle U–N–U normally displays a large sharp peak at  $54^\circ$ . This is entirely the result of steric hindrance. In contrast, the amine–urea–adamantyl (N–U–A) ends are predominately straight independent of the non-bonded interactions. For details of input variables, initial states of the atomistic simulation and partial atomic charges see Appendix 4.5.1.

Separating the derivation of the angles from the bonds in this manner is allowed because they are fairly independent. In principle an angle does not change when its constituent bonds are stretched or compressed. Here for example, while the N–U bonds differ little in both simulations, the U–N–U angle is either  $60^\circ$  or unrestricted. Meanwhile the N–N bonds differ most, while the N–N–N angles remain similar.

#### 4.2.2.2 Structure parameter derivation

Using the Boltzmann inversion scheme, effective model potentials can be derived from structural information in the form of pair correlation functions.<sup>[59,61,62]</sup> The pair distributions can be acquired from experimental data to optimize atomistic potentials, or, as is the case here, from atomistic simulations to optimize coarse-grained potentials. As the model is based on structural information, it will reproduce accurate structural details. The method is based on the notion that a one-to-one correspondence exists between the potentials and the radial distributions that follow. Boltzmann inversion has been used to obtain potentials for liquids,<sup>[63,64]</sup> homopolymers,<sup>[62,65,66]</sup> and copolymers.<sup>[67]</sup> It can be done for any pair correlation function, i.e., for obtaining non-bonded, bond, angle, dihedral, etc. potentials. For the atomistic bond distributions,  $P(r_{ij})$ , the Boltzmann inversion calculation is as follows:

$$V_{\text{bond}}^0(r_{ij}) = -k_B T \ln(P(r_{ij})) \quad (4.1)$$

with  $k_B$  the Boltzmann constant and  $T$  the temperature. Because the bond distribution is influenced by the rest of the system, the result is in fact a free energy function. As the influence is minor, the function serves well as an initial guess for the potential energy function. It can be improved in an iterative process: A simulation using  $V_{\text{bond}}^n(r_{ij})$  is run and afterwards the output distribution  $P^n(r_{ij})$  is compared to the target distribution  $P_T(r_{ij})$ . Distribution differences are reduced iteratively by decreasing (or increasing) the potential at those distances where the output distribution underestimates (or overestimates) the target distribution: [64]

$$V_{\text{bond}}^{n+1}(r_{ij}) = V_{\text{bond}}^n(r_{ij}) - k_B T \ln \left( \frac{P_T(r_{ij})}{P^n(r_{ij})} \right) \quad (4.2)$$

After optimization, this potential is as irregular as the target distribution. Therefore, such potentials are usually applied in tabulated form, i.e., for every interparticle distance sampled, the potential value is stored in a table. During the CG simulation the required potentials are then interpolated from the pre-calculated ones.

When the distribution has a bumpy shape, it implies that the bonds between sites are flexible. For instance, the N–N bond consists of a 3 carbon chain. Depending on its conformation, its end-to-end distance changes, which leads to a narrow bistable distribution (Figure 4.3a). Using tabulated potentials it is straightforward to put this bistability in the N–N bond. However, in the coarse-graining process the origin of the bistability is lost. In the CG model there is no need for the N–N bond to be bistable as it is just a bond, the different conformations of the bond have no meaning. Therefore we opt to use harmonic analytical potentials for the bonded interactions. They are of the form:

$$V_{\text{bond}}(r_{ij}) = k_{ij} (r_{ij} - r_{0,ij})^2 \quad (4.3)$$

To determine the reference bond length  $r_{0,ij}$  and force constant  $k_{ij}$  the Boltzmann inversion scheme needs to be modified. It is known that harmonic bond potentials give rise to Gaussian distributed bonds (Equation 4.4). Therefore a Gaussian distribution fitted to the atomistic distribution shows the best possible outcome a harmonic potential can achieve.

$$P_{\text{Gauss}}(r_{ij}) = \frac{1}{\sigma\sqrt{2\pi}} e^{-\frac{(r_{ij}-\mu)^2}{2\sigma^2}} \quad (4.4)$$

Assuming the bond distribution is indeed Gaussian, the harmonic potential can be attained by Boltzmann inversion:

$$V_{\text{bond}}(r_{ij}) = -k_B T \ln \left( \frac{1}{\sigma\sqrt{2\pi}} \right) + k_B T \frac{(r_{ij} - \mu)^2}{2\sigma^2} \quad (4.5)$$

As the first part on the right hand side is a constant, it can be removed. From the second part the analytical constants for Equation 4.3 can be derived:

$$k_{ij} = \frac{k_B T}{2\sigma^2} \quad \text{and} \quad r_{0,ij} = \mu \quad (4.6)$$

Thus, by fitting a Gaussian distribution to the atomistic data (the dashed lines in Figures 4.3 and 4.4), target parameters for a coarse-grained harmonic potential can be derived that should produce distributions that match this Gaussian fit. Again, the match is not exact so the parameters are adjusted iteratively to minimize the error. At the start ( $n = 0$ ), the bond potential is as follows:

$$V_{\text{bond}}^0(r_{ij}) = k_{ij}^0 (r_{ij} - r_{0,ij}^0)^2 \quad \text{with} \quad (4.7)$$

$$k_{ij}^0 = \frac{k_B T}{2(\sigma_{\text{in}}^0)^2} = \frac{k_B T}{2(\sigma_{\text{T}})^2} \quad \text{and} \quad (4.8)$$

$$r_{0,ij}^0 = \mu_{\text{in}}^0 = \mu_{\text{T}} \quad (4.9)$$

where  $\sigma_{\text{T}}$  and  $\mu_{\text{T}}$  are the target values from the atomistic Gaussian fit. The output distribution is also fitted, giving the first output mean  $\mu_{\text{out}}^0$ , thus the relative error is  $|\mu_{\text{out}}^0 - \mu_{\text{T}}|/\mu_{\text{T}}$ . The input bond length for the next iteration  $r_{0,ij}^{n+1} = \mu_{\text{in}}^{n+1}$  is derived in the following manner, adjusting  $k_{ij}$  with  $\sigma$  works in the same way:

$$\mu_{\text{in}}^{n+1} = \begin{cases} \mu_{\text{in}}^n (1 + \beta) & \text{if } \frac{\mu_{\text{out}}^n}{\mu_{\text{T}}} < 1 - \frac{\beta}{\alpha}; \\ \mu_{\text{in}}^n \left( 1 - \alpha \frac{(\mu_{\text{out}}^n - \mu_{\text{T}})}{\mu_{\text{T}}} \right) & \text{if } 1 - \frac{\beta}{\alpha} \leq \frac{\mu_{\text{out}}^n}{\mu_{\text{T}}} \leq 1 + \frac{\beta}{\alpha}; \\ \mu_{\text{in}}^n (1 - \beta) & \text{if } \frac{\mu_{\text{out}}^n}{\mu_{\text{T}}} > 1 + \frac{\beta}{\alpha}. \end{cases} \quad (4.10)$$

where  $\alpha$  is the adaptation strength and  $\beta$  is the maximum adaptation. The input is thus the previous input with a slight increase or decrease depending on the relative error that input generated. Parameter  $\alpha$  gives the amount of adaptation with respect to the error; at 0 there is no adaptation, at 1 the error is subtracted entirely. Parameter  $\beta$  restricts the amount of adaptation to within limits. During the parameter adjustment phase,  $\alpha$  is set to 0.5 to have a steady approach to the target value where overshoots are purely due to interference from the rest of the system, and  $\beta$  is set to 0.25 to further limit the step size taken each iteration.

For the harmonic angle potentials the procedure is similar. The only difference is the normalization of the distribution by dividing by  $\sin(\theta_{ijk})$ , the random angle distribution, to give each angle the same weight.

$$V_{\text{angle}}(\theta_{ijk}) = -k_B T \ln \left( \frac{P(\theta_{ijk})}{\sin(\theta_{ijk})} \right) \quad (4.11)$$

Because the system is dense, the distributions depend on all potentials so they have to be optimized in batches. First all bond potentials were iterated concurrently,



**Table 4.2:** Harmonic bond and angle parameters

Type	Bond length (Å)	Strength (kJ nm <sup>-2</sup> mol <sup>-1</sup> )	Type	Angle (°)	Strength (kJ rad <sup>-2</sup> mol <sup>-1</sup> )
N-N	4.90	1244	N-N-N	97.0	0.66
N-U	5.01	409	N-N-U	82.7	0.88
U-A	4.60	4856	U-N-U	75.1	1.13
			N-U-A	138.6	19.67

as they do not depend on the others. Then all angle potentials were optimized. To avoid an unnecessary increase of complexity of the model, no dihedrals were incorporated. As they represent interactions over 4 coarse-grained beads (roughly 16 heavy atoms), they should only be added when more limited potentials fail to produce the required structure. Parameter adjustment was stopped after the total error of adjustable parameters reached a steady minimum, small fluctuations may still occur as the simulations inherently will not behave exactly the same. A demonstration of the automatic tuning of the N-N bond is given in Figure 4.5. By matching the parameters derived by Gaussian fitting the atomistic distributions, the parameter error and the distribution error were simultaneously minimized. For details of these coarse-grained tuning simulation see Appendix 4.5.2. The obtained parameters are listed in Table 4.2.

#### 4.2.2.3 Non-bonded interactions

To derive non-bonded interaction potentials, the Boltzmann inversion scheme may be used again, now with the radial distribution function as input. However, usually this is only applied on systems where just one or two particle types are present; e.g., a homopolymer in implicit solvent<sup>[62,65]</sup> or a diblock copolymer in vacuum.<sup>[67]</sup> Moreover, although it has been done recently,<sup>[68,69]</sup> coarse-graining the solvent using Boltzmann inversion is difficult when a single CG bead comprises multiple solvent molecules as the solvent molecules need to be dynamically clustered into beads every time step.

Instead, in our coarse-grained model, the non-bonded interactions between two particle types, being Pauli repulsion, van der Waals attraction, and Coulombic interactions, are all described by a single Lennard-Jones potential. The potentials are parameterized more phenomenologically based on known physical-chemical properties of the chemical compounds best resembling each particle and the overall behavior of the PPIUA dendrimer in water. This is analogous to our water-lipid model (Chapter 2) from which we reuse the W (water) particles. The masses of the particle types can be calculated straightforwardly (Table 4.1) as the sum of the masses of the atoms they represent. Although the physical properties are not known for the exact compounds the particle types represent, they can be found for similar chemical compounds: A being adamantane; N being in between

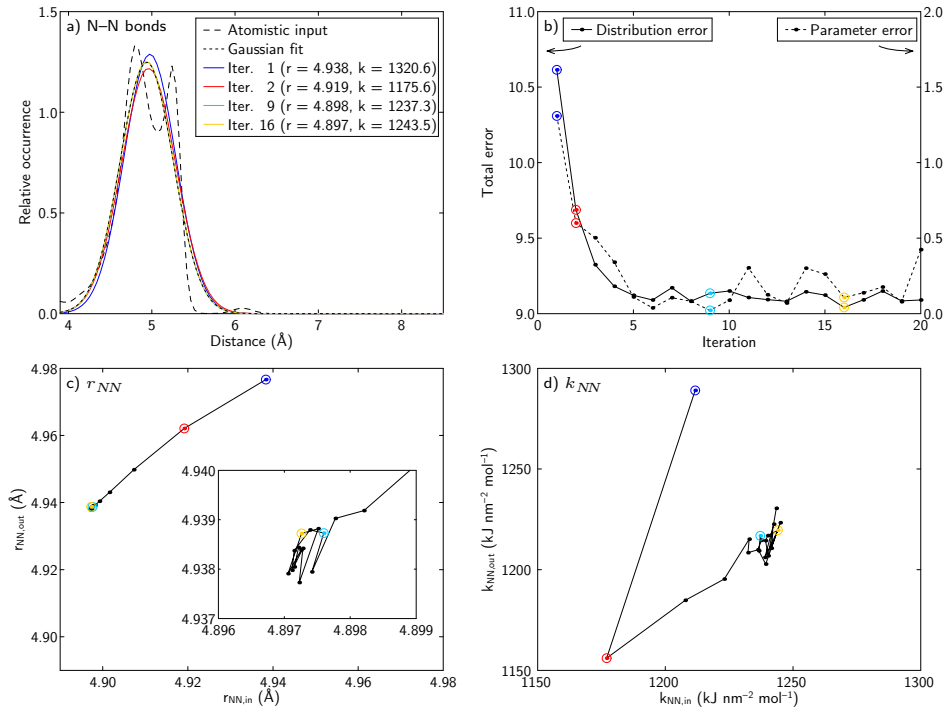


**Figure 4.5:** An example of how the potential parameters are tuned automatically: the N–N bond. Iterations 1 (blue), 2 (red), 9 (best parameter match, cyan), and 16 (best distribution match, orange) are highlighted. (a) The bond distribution from the atomistic simulation is fitted with a Gaussian distribution. This gives the target bond distance ( $r_{NN}$ ) and force ( $k_{NN}$ ) parameters, which are used as the initial input for the coarse-grained simulation. A new distribution is produced which is also fitted. Depending on the magnitude of the difference between target and output parameters, new parameters are calculated. Note that iteration 9 is obscured by iteration 16, which in turn traces the Gaussian fit. The search trajectories for the length (c) and force parameters (d) are shown. The input parameters are on the x-axis, the corresponding output parameters on the y-axis. (b) The differences between the target and output parameters (right axis) and between the atomistic and output distributions (normalized, squared and summed) (left axis), for *all* bond types, are shown. After 6 iterations, the errors have reached a minimum, after which the parameter adjustments are minute, and the distributions fall within line thickness of the target Gaussian fit.

dimethylethylamine and diethylmethylamine; and U being a combination of methylurea, ethylurea and dimethylurea. For each particle type this provides a theoretical density at a certain temperature, a melting point and optionally a boiling point. The van der Waals radii and characteristic Lennard-Jones energies ( $\epsilon$ ) of the particle types are optimized through a series of MD simulations of 2600 particles each. An initial van der Waals radius is calculated from the target density and

**Table 4.3:** Lennard-Jones well depth in water ( $\varepsilon_{ij}$  ( $\varepsilon^*$ );  $1.0 \varepsilon^* = 1.967$  kJ/mol)

	A	N	U	W
A	1.0	1.0	1.0	1.0
N		1.0	1.4	1.4
U			2.2	1.88
W				1.88

known mass assuming sphere packing. An initial  $\varepsilon$  follows from the target melting temperature. Locating the actual melting point starts with 0.5 million time steps of equilibration at a temperature 100 K below the expected melting point, followed by heating the system 350 K over 3 million iterations and subsequently cooling it back down, while checking the density for phase transitions. Due to the fast temperature changes ( $\sim 5$  K/ns) a hysteresis effect occurs such that the observed crystallization and melting points differ. The true melting point is then taken as the average of both phase transition temperatures, and any difference between this and the target melting point leads to an adjustment of the  $\varepsilon$ . If the change is small ( $< 5\%$ ) the simulated annealing process is stopped. The same strategy is applied for the known boiling points. This may lead to a different  $\varepsilon$ . The final  $\varepsilon$  is obtained via a linear interpolation between both points to room temperature and rounded to a single decimal. Finally another simulation of 1 million time steps is performed to measure the density and adjust the van der Waals radius. The so obtained values for the van der Waals radii are reported in Table 4.1 and those for  $\varepsilon$  on the diagonal of Table 4.3. Only for the A particle an exception was made as adamantane has an extraordinarily high melting point (540 K) while it also sublimates at room temperature. Because these unusual properties are incompatible with the above strategy the  $\varepsilon$  of butane from the lipid model was used instead. As in the earlier vesicle simulations of Chapter 2, the water–water interaction is  $1.88 \varepsilon^*$  which also incorporates both melting and boiling points.

Also the interactions between different particle types are based on the physical-chemical properties of the chemical compounds and the overall behavior of the PPIUA dendrimer in water. That is, in water the dendrimers aggregate because of the hydrophobic adamantyl ends, but the urea moieties and in a lesser extent the tertiary amines, are water-soluble. Therefore three additional well depths are used. For the interactions of the hydrophobic adamantyl ends with all other particle types the same value is used as for the hydrophobic interactions like butane–water ( $1.0 \varepsilon^* = 1.967$  kJ/mol) in the lipid model, but with the regular Lennard-Jones cutoff. For the water-soluble urea moieties the well depth for interaction with water is set to the same value as for water–water ( $1.88 \varepsilon^*$ ). For the interaction of the slightly less water-soluble tertiary amines with water, as well as for the N–U interaction, an intermediate value ( $1.4 \varepsilon^*$ ) is taken. The chosen values are also shown as the off diagonal values in Table 4.3. Finally, the collision diameters between unlike particle types are obtained using the Lorentz rule ( $\sigma_{ij} = \frac{1}{2}(\sigma_i + \sigma_j)$ ).

## 4.3 Results and discussion

### 4.3.1 Simulations

To validate the coarse-grained force field derived in the previous section, its results are compared to atomistic simulations of the same dendrimers and results of PPI dendrimer experiments described in literature. Additionally, predictions are made when the model provides more detail than the experiments. Although the CG dendrimer model was derived with the fifth-generation urea–adamantyl-functionalized poly(propylene imine) dendrimer as a reference, the generalized analytical potentials should make the model applicable to similar molecules. This means correct results should be produced for both PPIUA and PPI dendrimers over a range of generations.

The limiting generation is the final generation at which the volume occupied by a dense space-filling dendrimer is smaller than the volume occupied by a dendrimer with all branches stretched outward.<sup>[70]</sup> For our PPI dendrimers this limit is at *G*10, so *G*7 should in principle still be attainable and is an appropriate final generation to study.

For the experimental validation, small-angle neutron scattering (SANS) measurements of PPI dendrimers by Scherrenberg et al.<sup>[29]</sup> in dilute solution are used for structural information. The PPI dendrimers studied range from generation 1 (4 end-groups) to 5 (64 end-groups).

All simulations described here are performed in an NPT ensemble, with constant pressure (1 bar) and constant temperature (298 K). The coarse-grained simulations were performed on single dendrimers of generations 1 through 7 in water. Dendrimers were generated in an extended configuration, minimized, solvated and again minimized (Figure 4.1c). A simulation was performed for each of the generations. Each simulation encompasses 625 ns, of which the first 6 ns are considered equilibration time, and the final 619 ns production run. Every 0.06 ns a configuration was saved for analysis. For details of the input variables and initial states for the coarse-grained simulations see Appendix 4.5.4.

The atomistic simulations were performed on PPI and PPIUA dendrimers of generations 1 through 6 and solvated with TIP3 water (Figure 4.1b). In water, PPI dendrimers are charged through protonation of the nitrogens. The protonation order of PPI dendrimers of generations 1, 2 and 3 at different pH were investigated using natural abundance <sup>15</sup>N-NMR spectroscopy and an Ising model.<sup>[71]</sup> Their findings indicate that, at each protonation level, most of the charge resides at the primary amines of the outer layer. When more charge is present, subsequent layers of tertiary amines become charged, preferably alternating to keep the charges

separate. For the simulations the appropriate extent of protonation was determined performing a series of simulations with varying degrees of protonation, using the G5 PPI dendrimer as calibration point. A protonation level of 37.5 % was found to match the known radius of gyration best. For simulation results of the search for the appropriate protonation level see Appendix 4.5.3.1. All other PPI dendrimers were generated with the same degree of protonation, of these roughly 90 % reside at the outer layer, the others were proportionally distributed on the nitrogens of alternative layers. As the PPIUA dendrimers lack primary amines, they are much less prone to protonation, therefore, as an approximation, only the protonation level of the tertiary amines of the corresponding PPIs was adopted. Generations 1, 2, and 3 were simulated for 30 ns, the others for 20 ns, of which the final 20 ns or 10 ns were used for analysis, respectively. For details of the input variables and initial states for the atomistic simulations see Appendix 4.5.3 and 4.5.3.2.

The structure of a single dendrimer can be characterized by various measures, of which some can be found through experiment, while others can be directly calculated from simulation. In this chapter, we assess the similarities between coarse-grained and all-atom simulations, and, whenever possible, experiments. Specifically measured are the radius of gyration, asphericity, radial monomer density, and the form factor.

### 4.3.2 Radius of gyration

The radius of gyration is a measure of the mass distribution of a molecule around its center of mass. It is used as a measure of size for near-spherical colloids. It is calculated as:

$$\langle R_g^2 \rangle = \frac{1}{\sum_{i=1}^N m_i} \left\langle \sum_{i=1}^N m_i |\mathbf{r}_i - \mathbf{c}|^2 \right\rangle \quad \text{with} \quad \mathbf{c} = \frac{\sum_{i=1}^N m_i \mathbf{r}_i}{\sum_{i=1}^N m_i} \quad (4.12)$$

where  $\langle \rangle$  denotes the ensemble average,  $N$  the number of atoms,  $m_i$  the mass of the  $i$ th atom,  $\mathbf{r}_i$  its position and  $\mathbf{c}$  the center of mass of the molecule. This  $R_g$  is a prime measure to evaluate the merits of the coarse-grained model as it can also be determined with scattering experiments: In dilute solvent, there is no scattering interference between the molecules, so only the averaged internal scattering of each individual molecule is measured. Then  $R_g$  can be derived by using the Guinier approximation:

$$I(q) \simeq I(0) e^{-\frac{q^2 R_g^2}{3}}. \quad (4.13)$$

By plotting the scatter intensity in a Guinier plot,  $\ln(I(q))$  versus  $q^2$ , at low  $q$  (the magnitude of the scattering wave vector) a straight line with a slope proportional to  $R_g^2$  emerges.<sup>[72]</sup>

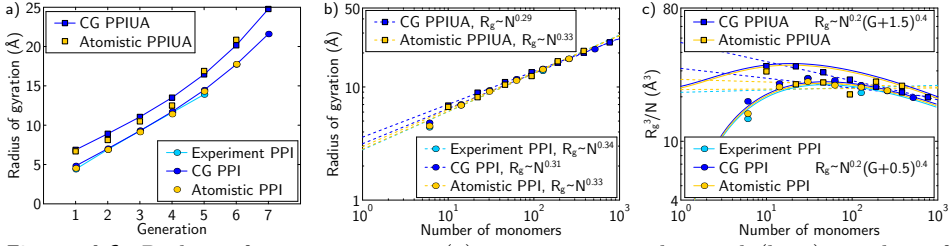


**Figure 4.6:** Radius of gyration versus (a) generation number and (b, c) number of monomers as determined for the coarse-grained, fully atomistic and experimental<sup>[29]</sup> dendrimers. (a) These lines are to guide the eye. (b) The lines are the best linear  $R_g \propto N^\nu$  fits. (c) Best fits for the relation between  $R_g$  and  $N$ :  $R_g \propto N^{1/5}(G+[1+]0.5)^{2/5}$ . The dashed lines are the best linear fits of (b); should the linear relation hold, the data points would follow these.

The lower set of curves shown in Figure 4.6a are for the PPI dendrimers. The experimental values<sup>[29]</sup> match the coarse-grained and atomistic values quite well. Their observation that the relationship  $R_g \propto G$  is linear, seems correct for small generations ( $G1$  to  $G4$ ), but fails once larger generations are also considered. Then the growth appears to be increased. The upper set of curves is for the PPIUA dendrimers. Not only are these dendrimers larger, also the atomistic simulations do not follow the coarse-grained lines as neatly.

To better explain the increase in dendrimer size with larger generations (i.e., number of monomers), usually the relation  $R_g \propto N^\nu$  is determined. The best fits for  $R_g \propto N^\nu$  are shown by the dashed lines in Figures 4.6b,c. The PPI and PPIUA dendrimers follow the same general scaling law. These results, ( $\nu$  ranging from 0.29 to 0.34) compare favorably with other simulations. For instance, a relationship of  $R_g \propto N^{0.29}$  is found with a united atoms simulation of PPI dendrimers ( $G2$  to  $G5$ ) in melt.<sup>[32]</sup> Another molecular dynamics simulation of generic dendrimers ( $G1$  to  $G8$ ) in implicit solvent of various quality follows  $R_g \propto N^{0.30}$  for all cases.<sup>[17]</sup> Reported values for PAMAM dendrimers are  $\nu = 0.34$  in water<sup>[73]</sup> and  $\nu = 0.33$  in water under low, medium, and high pH conditions.<sup>[47]</sup> Results of coarse-grained PAMAM dendrimers in vacuum ( $G1$  to  $G11$ )<sup>[56]</sup> are reported as  $R_g \propto N^{0.32}$ .

However, the scaling law merely gives the impression to follow  $R_g \propto N^{1/3}$  under all solvent conditions. Strictly speaking, it is only valid for bad solvents, where the polymer collapses and becomes a space-filling object with constant density. Under other conditions different relationships can be derived.<sup>[74,75]</sup> The radius of gyration is expected to be proportional to the end-to-end distance ( $R$ ) of a single linear strand emanating from the central core. According to Flory-theory<sup>[76,77]</sup>

the mean-field energy of the strand is

$$\frac{F(R)}{k_B T} \cong \frac{R^2}{R_0^2} + N_S \left( v \frac{N}{R^3} + w \frac{N^2}{R^6} \right) \quad (4.14)$$

with  $R_0$  the ideal chain length,  $N_S$  the number of monomers in the strand,  $N$  the total number of monomers in the dendrimer,  $v$  the excluded volume parameter, and  $w$  the three-body interaction parameter. In the minimum, the derivative should be 0.

$$\frac{F'(R)}{k_B T} \cong 2 R_0^{-2} R - 3 v N_S N R^{-4} - 6 w N_S N^2 R^{-7} = 0 \quad (4.15)$$

Substituting  $R/R_0$  with expansion factor  $\alpha$  gives

$$\alpha^5 \cong \frac{3}{2} v N_S N R_0^{-3} + 3 w N_S N^2 \alpha^{-3} R_0^{-6} \quad (4.16)$$

In a good solvent, the expansion is fairly large, so the  $\alpha^{-3}$  term may be removed (and  $R_0 \propto \sqrt{N_S}$ ). Then the end-to-end distance follows

$$R \cong \left( \frac{3}{2} v \right)^{\frac{1}{5}} N_S^{\frac{2}{5}} N^{\frac{1}{5}} \quad (4.17)$$

with  $v > 0$ . In a bad solvent, the expansion factor is small so  $\alpha^5$  vanishes and indeed

$$R \cong \left( -2 \frac{w}{v} \right)^{\frac{1}{3}} N^{\frac{1}{3}} \quad (4.18)$$

with  $v < 0$ . At the theta point (ideal solvent) the polymer acts like an ideal chain, i.e., without excluded volume effects ( $v = 0$ ) and yields

$$R \cong (3w)^{\frac{1}{3}} N_S^{\frac{1}{4}} N^{\frac{1}{4}} \quad (4.19)$$

For our dendrimers, the number of monomers in a strand  $N_S = (G + 0.5)p$  for PPI and  $(G + 1.5)p$  for PPIUA dendrimers with the number of monomers per spacer  $p = 1$ .

For PPI the good solvent fits  $R_g \propto N^{1/5} (G + 0.5)^{2/5}$  presented in Figure 4.6c are an improvement over the linear fits, the  $G1$  values are no longer outliers. The ideal solvent fits  $R_g \propto N^{1/4} (G + 0.5)^{1/4}$  are almost as good. It is therefore difficult to discern the quality of the solvent from this particular graph, comparing dendrimers of different structures would help.<sup>[78]</sup> For PPIUA the linear fits remain best. Water is not a good solvent for the hydrophobic adamantyl ends.

### 4.3.3 Aspect ratios

The radius of gyration represents the shape of a polymer by a single measure, thus relating it to a sphere. More descriptive measures are available, like the

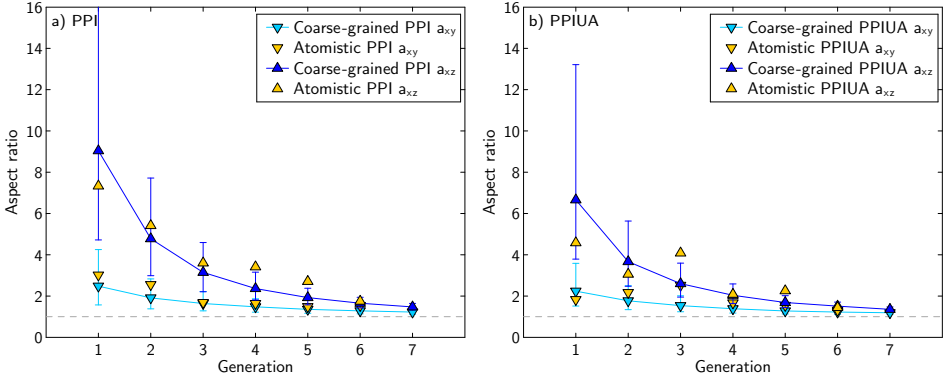


**Figure 4.7:** The first ( $a_{xy}$ ,  $\nabla$ ) and second aspect ratios ( $a_{xz}$ ,  $\triangle$ ) versus generation of the coarse-grained and fully atomistic (a) PPI and (b) PPIUA dendrimers. The coarse-grained values are connected to guide the eye. Shown are the median values and, with error bars, the 15.9th and 84.1th percentiles. The first-generation PPI dendrimer has a 84.1th percentile of 24.0 which has been cut off to permit comparison between dendrimer types; such a large value indicates a flat shape.

aspect ratios of a polymer as defined by the ratios between the principal axes. The principal axes are calculated using the shape or gyration tensor ( $\mathbf{T}$ ):

$$\mathbf{T} = \frac{1}{N} \sum_{i=1}^N \begin{bmatrix} r_{ix}r_{ix} & r_{iy}r_{ix} & r_{iz}r_{ix} \\ r_{ix}r_{iy} & r_{iy}r_{iy} & r_{iz}r_{iy} \\ r_{ix}r_{iz} & r_{iy}r_{iz} & r_{iz}r_{iz} \end{bmatrix} \quad (4.20)$$

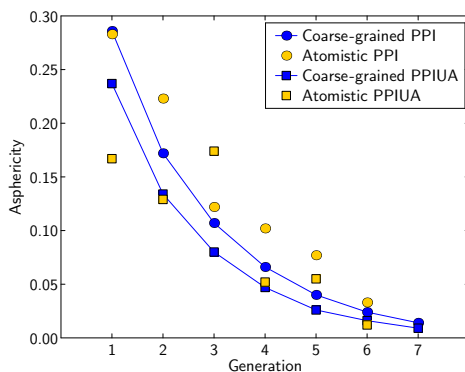
where  $r_{ix}$  represents the  $x$  coordinate of the  $i$ th atom relative to the center. By diagonalizing to matrix  $\mathbf{R}$  the eigenvalues  $g_1 \geq g_2 \geq g_3$  follow, which are the lengths of the three principal axes. Should they all be the same, then the molecule is spherical, should two be the same, then it is cylindrical, etc.

$$\mathbf{R} = \begin{bmatrix} g_1 & 0 & 0 \\ 0 & g_2 & 0 \\ 0 & 0 & g_3 \end{bmatrix} \quad (4.21)$$

The aspect ratios are defined as  $a_{xy} = g_1/g_2$  and  $a_{xz} = g_1/g_3$ . In Figure 4.7 the average aspect ratios are shown for all simulations. It is clear that the lower the dendrimer generation, the farther apart the aspect ratios are. As the coarse-grained simulations are easily equilibrated their results combine into fairly smooth curves. While the atomistic results are more irregular they do follow the general trend, i.e., smaller dendrimers appear rod-like while larger dendrimers are more globular. The  $G_4$  PPI dendrimer values compare well with an atomistic simulation<sup>[44]</sup> with reported aspect ratios between 1 and 2 and between 2 and 3.



**Figure 4.8:** The asphericity versus generation of the coarse-grained and fully atomistic dendrimers.



### 4.3.4 Asphericity

From the principal axes the asphericity<sup>[79,80]</sup><sup>1</sup>

$$A = \frac{T^2 - 3M}{T^2} \quad (4.22)$$

can be calculated with

$$T = g_1 + g_2 + g_3 \quad (4.23)$$

$$M = g_1 g_2 + g_2 g_3 + g_3 g_1 \quad (4.24)$$

This asphericity can take values from 0 for a configuration where the atoms are arranged symmetrically around an origin to 1 for a linear configuration. At 0.25 a planar configuration may exist (e.g.,  $g_1 = g_2 = 1.0$ ,  $g_3 = 0.0$ ), but a cylindrical object is also possible (e.g.,  $g_1 = 1.0$ ,  $g_2 = g_3 = 0.25$ ).

The average asphericity for the generations in solution simulations are shown in Figure 4.8. The larger dendrimers are more spherical whether that size increase is due to more generations or the addition of urea and adamantyl groups. The atomistic values are in the range of the coarse-grained values, but are more erratic than the latter's smooth trend. This is likely due to the calculation wherein small fluctuations of atoms in the molecule lead to significant changes in the principal axes. In turn the asphericity is quite variable. With longer simulation times the atomistic values are expected to converge with the CG data.

In a series of 0.4 ns united atoms simulations of PPI generations 2 to 5 in melt, a decline in asphericity of similar magnitude has been observed.<sup>[32]</sup> Coarse-grained polyphenylene dendrimers have also shown a decline in asphericity, but not nearly as much.<sup>[54]</sup> Those dendrimers are rather rigid, they experience hardly any back-folding, and thus retain their shape with each increased generation.

<sup>1</sup>For a consideration of these two not quite identical asphericity calculations see Appendix 4.5.5.

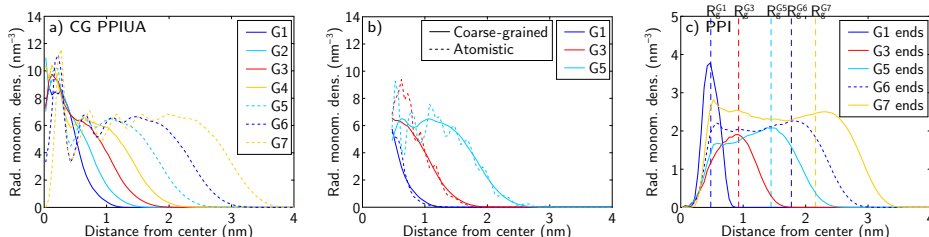


**Figure 4.9:** Radial monomer densities. (a) Overall density of CG PPIUA dendrimers with shell width  $0.5 \text{ \AA}$  and (b) compared to the fully atomistic dendrimers. (c) The radial monomer density of the CG PPI dendrimer ends (solid lines) compared to the dendrimer size represented by the radius of gyration (dashed lines).

### 4.3.5 Radial monomer density

The radial monomer density ( $g_m(r)$ ) is the preferred way to represent the distribution of monomers with respect to the dendrimer's center of mass. The density is defined as the number of monomers ( $N$ ) found within the shell of width  $\Delta r$  starting at  $r - \frac{1}{2}\Delta r$  divided by the volume of this shell:

$$g_m(r) = \frac{N(r)}{\frac{4}{3}\pi \left(r + \frac{\Delta r}{2}\right)^3 - \frac{4}{3}\pi \left(r - \frac{\Delta r}{2}\right)^3}. \quad (4.25)$$

In Figure 4.9a the overall densities are depicted for the coarse-grained PPIUA dendrimers. For low generations ( $G1$ ,  $G2$ ), the density decreases monotonically from the center. At higher generations ( $G3$  to  $G5$ ), a plateau appears after the initial peak. The initial peak is due to the apparent abundance of monomers near the center of mass, which does not necessarily contain the dendritic origin. At even higher generations ( $G6$ ,  $G7$ ) the plateau exhibits oscillations. The radial distribution graph then attains the distinct shape known from simple liquids, i.e., first a high peak a small distance from the origin, followed by several peaks of solvent shells, and finally a plateau when the structure is lost. The radial monomer distribution decays to zero; this shape depends on the roughness of the dendrimer surface. That several peaks are present for  $G6$  and  $G7$ , indicates the dendrimer's CG sites are relatively fixed with respect to each other. This is in agreement with the experienced difficulty to synthesize such large dendrimers correctly in pure form.

In Figure 4.9b the radial monomer densities of a select group of atomistic simulations are depicted with their coarse-grained counterparts. To get comparable results, the positions of the virtual coarse-grained sites were calculated from the atomistic simulations. As there were not enough samples or atoms to get a consistent view of the first few shells, these are omitted. With these caveats, the

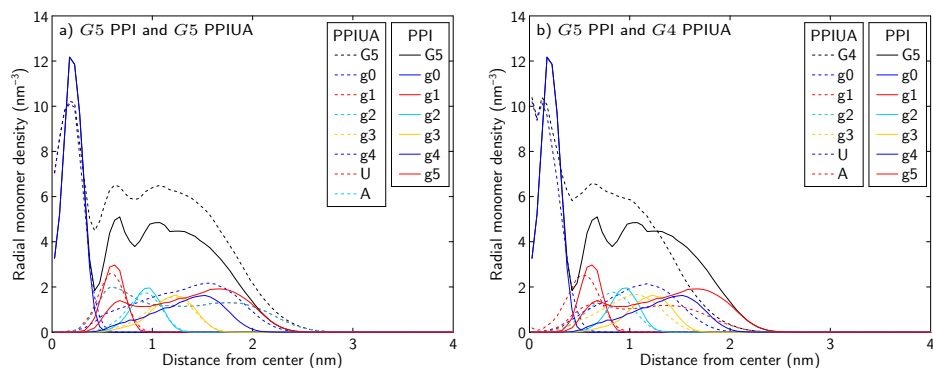


**Figure 4.10:** Comparisons between (a) the radial monomer densities of  $G5$  PPI and its extension  $G5$  PPIUA, and (b)  $G5$  PPI and  $G4$  PPIUA which has a closer number of monomers. Each generational layer of monomers is labeled with a lower case ‘g’ to distinguish it from full generations.

observed behavior, i.e., the monotonic decrease, the plateaus, and the decays, are quite similar.

Looking solely at the distribution of the extremities of the dendrimers, Figure 4.9c shows that for small dendrimers ( $G1$  to  $G3$ ) the end-groups can be found at the periphery, as hinted at by the depicted radius of gyration (N.b., for solid spheres  $R_g = \sqrt{3/5}R$ ). For larger dendrimers ( $G5$  to  $G7$ ) there is not enough room at the periphery for all the end-groups, therefore their branches must bend and distribute them over the available space thus widening the distribution peak. This contrasts with the prediction of Zacharopoulos and Economou,<sup>[32]</sup> that states that for higher dendrimers ( $G > 5$ ) the distribution becomes bimodal with a depletion of end-groups in the region around  $R_g$ . The broad distribution does however coincide with the results of others for large generations.<sup>[17,29]</sup>

The fifth generation of coarse-grained PPI contains 126 monomers, while the PPIUA variant contains 190. The fourth-generation PPIUA with 94 monomers is in fact a closer numerical match. Recalling the similar origins of  $G5$  PPI and PPIUA, DAB–dendr–(NH<sub>2</sub>)<sub>64</sub> and DAB–dendr–(urea–adamantyl)<sub>64</sub>, wherein the secondary amines effectively become ureas, their connectivity is evidently the same up until the final extension with adamantanes. The question which of the  $G4$  or  $G5$  PPIUAs has the better monomer distribution match with  $G5$  PPI, is answered in Figure 4.10. It shows that  $G5$  PPIUA is indeed an extension of  $G5$  PPI. Apart from the 2 monomer  $g0$ -layer, only the  $g5$ -layer distribution is appreciably different having become urea. The added adamantyl ends are spread evenly across the dendrimer, just as the end-groups in Figure 4.9c. Conversely, with  $G4$  PPIUA, where next to the transformations into urea and adamantyl half the monomers of the  $g5$ -layer are removed, the distributions are quite different.

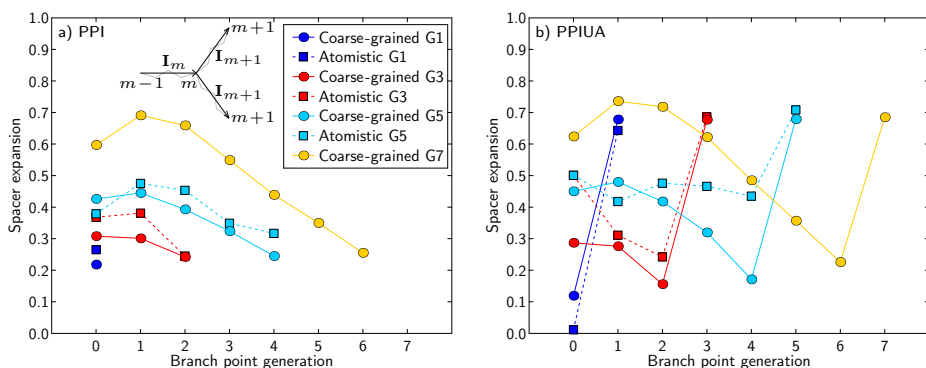


**Figure 4.11:** Relative expansion of the spacers originating at each branch generation of (a) PPI and (b) PPIUA dendrimers. The coarse-grained simulations have solid lines connecting circular points, the atomistic ones have dashed lines and square points. The legends for the PPI graphs also describe the corresponding PPIUA dendrimer graphs. PPI dendrimers of generation 7 have a final marker at branch point generation 6, etc. PPIUA dendrimers have an extra branch.

### 4.3.6 Spacer expansion

The distribution of the monomers depends on the shape of the branches in the dendrimer, whether they are extended or crinkled. This behavior can be assessed with the spacer expansion calculation. The relative expansion ( $S$ ) of a spacer spanning from branch point  $m$  to the next ( $m + 1$ ) is calculated as the projection of its vector ( $\mathbf{I}_{m+1}$ ) on the vector of its parent spacer ( $\mathbf{I}_m$ ) normalized by its theoretical all-trans spacer length ( $l_{m+1}$ ):<sup>[32]</sup>

$$S = \frac{\mathbf{I}_m \cdot \mathbf{I}_{m+1}}{|\mathbf{I}_m| l_{m+1}} \quad (4.26)$$

as shown in the inset of Figure 4.11a.

In the figure the average expansions of the spacers originating at each generation of branch points are shown. The coarse-grained PPI dendrimers show that no matter the size of the dendrimer, the final layer is the least expanded, meaning that its final branches are splayed. For small generations ( $G1$  to  $G4$ ), the spacers are relatively expanded at the origin and this expansion uniformly drops. For higher generations ( $G5$  to  $G7$ ) the expansion around the core is a bit less than in the subsequent shells to accommodate for the greater crowding there. There are two differences in going from PPI to PPIUA via the addition of the urea–adamantyl group. First the change of the final N–N monomers to N–U which show a similar weak expansion. Secondly the extra U–A spacer which shows extensive expansion. The latter is explained by the preferred N–U–A angle, and the fact that each U particle is the origin of only one spacer. Despite the more flexible four-bond

spacers, the atomistic simulations do follow the same trends, albeit more erratic. The least similar is *G5* PPIUA which shows a relatively flat expansion profile across the whole propylene imine part.

Compared with our CG PPI dendrimer, a bead-spring model with a similar topology (except for a trifunctional core), has shown a similar parabolic expansion profile.<sup>[13]</sup> Some united atoms PPI dendrimer melt simulations have shown a different expansion profile, however;<sup>[32]</sup> their small dendrimers (*G2*, *G3*) expand more from the core outward, while the larger dendrimers (*G4*, *G5*) have a uniform expansion profile.

At the onset of theoretical dendrimer research, all branches were envisioned to extend toward the surface,<sup>[81]</sup> leading to a vacant core region and crowding at the surface. This model was thus termed the *dense shell* model. A competing view, the *dense core* model maintains that the branches through bending and back-folding occupy any available space, thereby having a dense core and not-so dense shell. The dense core view was established with computer simulations of dendrimer growth by employing a self-avoiding walk algorithm.<sup>[8]</sup> Although there is some evidence supporting the dense shell theory,<sup>[32]</sup> the dense core model is currently favored. E.g., in *G4* PPI dendrimers decorated with ureaphenyl groups, the ends were found with SANS to be distributed throughout the dendrimer.<sup>[82]</sup> As seen in Section 4.3.2, solvent conditions alter dendrimer conformations. In good solvent the branches are more extended and thus appear to follow the dense shell model on average, while in bad solvent the collapsed dendrimers better resemble the dense core model.<sup>[12]</sup> Even in this updated view of the dense shell concept, the shell is not nearly as dense as the core in the dense core model. The results shown in Figures 4.9a,b, and 4.11 agree well with the prevalent dense core view.

### 4.3.7 Solvent-excluded surface volume

The space a dendrimer occupies in solution is not merely the sum of the atom volumes. It encompasses the space in between these atoms whether empty or occupied by trapped solvent molecules. The surface of a dendrimer can thus be defined as the smallest outer surface that is inaccessible to the bulk of the solvent. This solvent-excluded surface (SES) is computed for every saved state of the simulations with MSMS<sup>[83]</sup> using a probe size of 1.5 Å. From the polygon surface the volume is calculated and averages for all generations are depicted in Figure 4.12.

Both PPIUA simulations match each other exceptionally well, indicating the coarse-grained model is correct in overall size and average dynamic structure. The values for the PPI dendrimers are not alike however. The experimental values are expected to be larger as the solvent-excluded surface constitutes a tight lower bound, while in

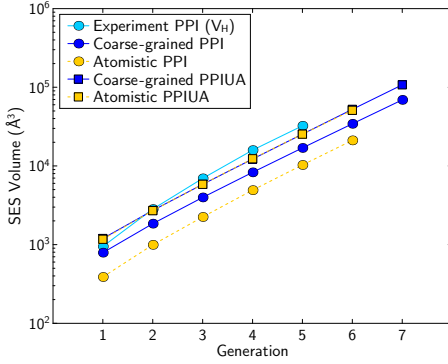


**Figure 4.12:** The volume of the space bounded by the solvent-excluded surface of the dendrimers. To give a size indication, the hydrodynamic volumes ( $V_H$ ) in  $D_2O$  as reported by Scherrenberg et al. [29] are also shown.

the hydrodynamic radius calculations the drag of the dendrimer plus accompanying solvent is accounted for. Still, the SES volume of the coarse-grained PPI simulation is a factor off (about 1.7). This is explained by the fact that while branches of the atomistic model are capped by  $NH_2$ , the coarse-grained model uses a whole N particle (Figure 4.2a). The radius of gyration (Figure 4.6a) is not much affected by this, as the bigger point mass is in the correct position, but the SES is affected for having traced the surface of those particles.

### 4.3.8 Form factor

The final test of the dendrimer shape is done by comparison with SANS experiments. In SANS experiments of dilute dendrimer solutions scattering due to different dendrimers is extremely weak and may be ignored. The resulting form factor thus describes the correlation of scatterers in the dendrimer:

$$F(q) = \frac{1}{N} \left\langle \sum_{j=1}^N \sum_{k=1}^N e^{-i\mathbf{q} \cdot (\mathbf{r}_j - \mathbf{r}_k)} \right\rangle = \frac{1}{N} \left\langle \sum_{j=1}^N \sum_{k=1}^N \frac{\sin(q |\mathbf{r}_j - \mathbf{r}_k|)}{q |\mathbf{r}_j - \mathbf{r}_k|} \right\rangle \quad (4.27)$$

with  $q$  denoting the magnitude of the scattering wave vector  $\mathbf{q}$  in  $\text{\AA}^{-1}$  and  $\mathbf{r}_j$  the position vector of particle  $j$ ; Note that  $F(\mathbf{q}) = F(q)$  because of the angular isotropy. [84] Using the correlation between monomers (or CG particles) from the simulations in Equation 4.27 leads to simulated form factors which can be directly compared with the experimental ones, like in the Kratky plot of Figure 4.13a.

At small angles the scatter intensity comes from large distance scatterers, i.e., the left side of the Kratky plot represents the overall dendrimer shape, while at large angles the small internal distances are represented. The latter is increasingly hard to do well experimentally, and for the coarse-grained simulation the size of the particles puts a limit on the smallest possible distances. This effect is also

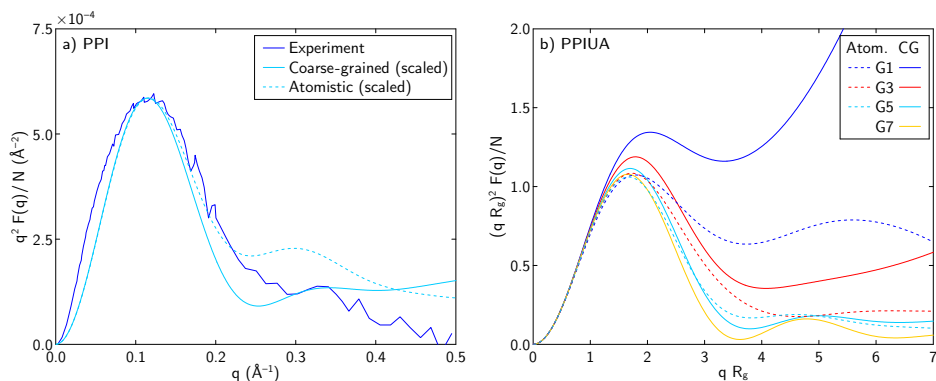


**Figure 4.13:** Kratky plots. (a) The  $G5$  PPI dendrimer from experiment<sup>[29]</sup> and simulations. Simulation values are scaled to match the height of the peak. (b) The coarse-grained (solid lines) and atomistic (dashed lines) PPIUA dendrimers of different generations. For convenience, the dependence of the length scale has been removed by plotting  $(qR_g)^2 F(q)/N$  versus  $qR_g$ .

visible in Figure 4.13b, where the difference between atomistic and coarse-grained simulations becomes more pronounced at larger scattering angles.

The simulated form factors in Figure 4.13a follow the experimental one quite nicely. The atomistic one does a bit better than the coarse-grained one. The clear peak means the dendrimer is a fairly dense globular structure,<sup>[85,86]</sup> which is just as expected. Should the curve form a plateau instead, it would imply a chain-like conformation. Such a plateau is present in Figure 4.13b where the coarse-grained first-generation dendrimer can indeed be viewed as chain-like, as it consists of few particles. On the opposite end, the seventh-generation dendrimer begins to show the characteristic periodicity of a solid sphere.<sup>[72,87]</sup>

## 4.4 Conclusion

We investigated the behavior of poly(propylene imine) (PPI) and urea–adamantyl-modified poly(propylene imine) (PPIUA) dendrimers from generation 1 to 7 in water with coarse-grained simulations.

The coarse-grained model was built to reproduce the bonds and angles of virtual coarse-grained sites accumulated during atomistic simulations of  $G5$  PPIUA. With Boltzmann inversion of Gaussian fits harmonic potentials were obtained. By decoupling the atomistic input into a complete simulation for bond distribution and a structural simulation for angle distribution, correct bond potentials and natural innate angle potentials were derived. Thereby leaving the effect of solvent

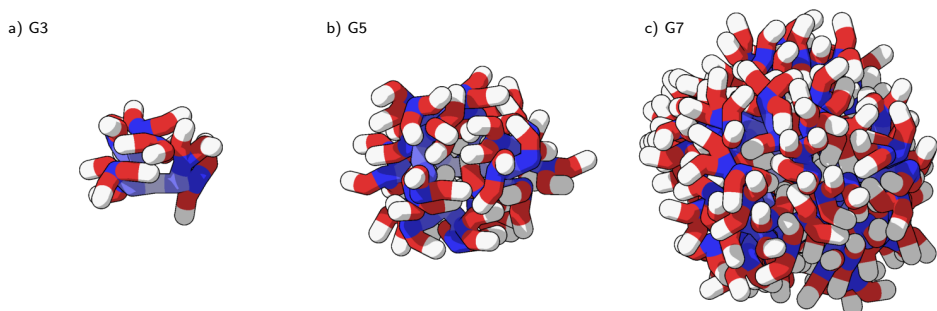


**Figure 4.14:** Representative structures for three PPIUA dendrimer generations at their average radius of gyration and asphericity: (a)  $G3$  ( $R_g = 11.05 \text{ \AA}$ , asphericity = 0.079), (b)  $G5$  ( $R_g = 16.46 \text{ \AA}$ , asphericity = 0.030) and (c)  $G7$  ( $R_g = 24.78 \text{ \AA}$ , asphericity = 0.009). The poly(propylene imine) part is colored light blue at the core to dark blue at the ends, highlighting the propensity for back-folding.

on the dendrimer to separate non-bonded interactions. Thus creating a general model capable to simulate different dendrimer sizes and concentrations.

Although parameterized on  $G5$  atomistic PPIUA, the coarse-grained model compares well with the atomistic variants, and with the available experimental results<sup>[29]</sup> with respect to various structural measurements over a wide range of generations. We have determined the radius of gyration, asphericity, solvent-excluded surface volume, radial monomer densities, spacer expansions and form factors, providing a complete molecular picture. Representative structures for three generations of PPIUA dendrimers are shown in Figure 4.14.

The amine–amine chains of the base PPI dendrimers are flexible. Therefore the dendrimers are flexible provided the chains have sufficient room to move. The small dendrimers ( $\leq G3$ ) are so capricious they sometimes are rod-like and sometimes globular. Their core does not necessarily reside in the center of the molecule, something that is inevitable for the dendrimers that approach the limiting generation ( $\geq G6$ ). The latter even exhibit liquid-like crowding around the center. The middle generations ( $G4, 5$ ) are fairly flexible, fairly spherical and without an exposed core. For all generations, the dendrimer’s extremities are distributed over the complete volume through abundant back-folding—thus pointing to dendrimers of sufficient size having a dense core. Finally, with respect to the distribution of its branches, PPIUA is indeed fully an extended PPI molecule of that generation.

Having demonstrated the effectiveness of this coarse-grained model, the next step is to simulate the behavior of the PPI dendrimers in concentrated solutions.



## 4.5 Appendix

### 4.5.1 Modeling: Atomistic input

Fully atomistic (FA) dendrimer simulations were performed to collect bond and angle distributions to calculate coarse-grained (CG) parameters with. These simulations were based on the atomistic *G5* PPIUA dendrimer-guest simulations<sup>[57]</sup> previously done in NAMD 2.5.<sup>[88]</sup> But as NAMD does not generate the distributions required we have extended PumMa to allow for the use of CHARMM27<sup>[60]</sup> parameters and reporting the desired metrics.

The dendrimer was simulated *in vacuo* using a relative dielectric constant of 1. The neighbor list, used for calculating the non-bonded interactions, was fixed at 22.5 Å and updated every ten steps. Whenever the temperature was controlled, this was done by rescaling the atom velocities. Every 1000 steps, the linear and angular momenta were set to zero.

The first 100 000 time steps, of 1 fs each, were spent on equilibration of the system, followed by a 2 million time steps production run. As the simulation was performed *in vacuo*, the initially open dendrimer rapidly collapsed during the equilibration phase. This part was done in the canonical (NVT) ensemble to ensure the production run starts with the correct temperature (307 K). The second part was done in the microcanonical (NVE) ensemble so no energy was added or subtracted from the system while distributions were gathered. The production run was performed twice, once with non-bonded interactions and once with them nullified.

The initial dendrimer configuration was generated using SYBYL 6.9<sup>[89]</sup> and in-house-developed software, then minimized and converted into appropriate input files for NAMD (PDB and PSF files) with X-PLOR 3.851<sup>[90]</sup> and psfgen.<sup>[88]</sup> Any missing parameters were estimated using chemically similar structures in the CHARMM27 parameters, while partial atomic charges were based on Gasteiger charge calculations as implemented in SYBYL. These files were then converted to PumMa input files. The partial atomic charges are shown in Figure 4.15.

### 4.5.2 Modeling: Iterative coarse-grained simulations

In our Boltzmann inversion scheme, in each iteration the derived bond and angle parameters were tested in a coarse-grained simulation. During these simulations distributions were also generated to check whether they match the distributions of the CG sites in the fully atomistic simulations.

As the PumMa simulation software knows exactly which atoms form a CG site, it

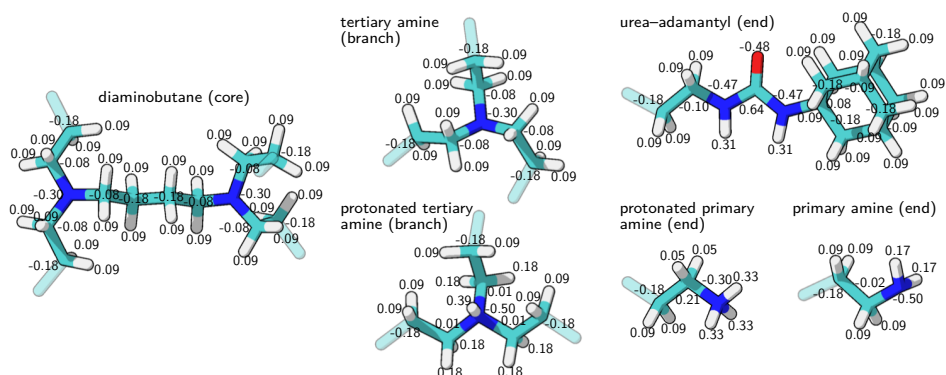


**Figure 4.15:** Residues with partial atomic charges. Oxygen is red, nitrogen is blue, carbon is cyan and hydrogen is white.

is able to generate a coarse-grained structure based on the FA simulation. Thus the original atomistic structure was conveniently converted to a coarse-grained variant. This open, expanded, structure was used as a starting structure for each iteration of the parameter derivation scheme.

The structure was simulated *in vacuo* in the NVT ensemble with a target temperature of 307 K. As the calculated bond and/or angle parameters need not be well suited to the starting structure, first each structure was minimized for 10 000 time steps. Each production run on the other hand consisted of 2 million time steps of 12 fs and a smaller temperature coupling (0.000 01). The linear and angular momenta were removed every 100 time steps. As only the structures were parameterized, Lennard-Jones interactions were not calculated.

### 4.5.3 Measurements: Fully atomistic simulations

Similar to the *G5* PPIUA dendrimer described above, dendrimers of generations 1 through 6 of PPIUA and PPI were generated following the same procedure. They were solvated in a large periodic box of TIP3 water with added chloride ions to get a neutral solution using the modeling extension of VMD 1.8.6.<sup>[91]</sup>

The solvated fully atomistic simulations were performed with NAMD 2.5<sup>[88]</sup> using CHARMM27<sup>[60]</sup> parameters.

The input options of the solvated simulations are such that the non-bonded interactions were smoothly cut off at a distance of 12 Å using a switching function starting at 8 Å. Short-range non-bonded interactions are evaluated every 2 steps. The neighbor list is fixed at 13.5 Å and updated every 10 steps. 1–2 and 1–3 bonded

**Table 4.4:** Atomistic  $G5$  PPI protonation test

Charge %	Atoms	Water particles	Charge & No. of $\text{Cl}^-$	$R_g$ (Å)	Asphericity
0	1382	4742	0	11.57	0.036
10	1395	4493	13	12.38	0.075
25	1414	4454	32	12.68	0.060
37.5	1429	4663	47	15.05	0.081
50	1445	5228	63	15.27	0.034
66	1466	5008	84	15.36	0.018
66 <sup>⊙</sup>	1466	4974	84	15.99	0.047
100	1508	4542	126	16.17	0.013

<sup>⊙</sup> denotes the ‘onion’ configuration

atoms are excluded from non-bonded interactions, for certain 1–4 bonded atoms modified van der Waals parameters are used. Electrostatics were calculated using Particle Mesh Ewald (PME) every 4 steps. The simulations were performed in the NPT ensemble, with constant temperature (300 K, rescaled every 1000 steps) and constant pressure (1 bar). The pressure coupling uses Berendsen’s method every 100th step with a relaxation time of 2000 fs and a compressibility of  $0.000\,05\text{ bar}^{-1}$ . The compressibility relaxation ratio sets the strength of the volume adjustment.

The time steps are again 1 fs, and every 500th is saved for further analysis. The number of time steps spent on each simulation depends on the size of the dendrimer as large ones take a long time to equilibrate but change little when in equilibrium, and small ones require a longer production run as their conformations are more variable. The first 10 million time steps are equilibration time, followed by 20 million steps for  $G1$  to  $G3$ , and 10 million steps for  $G4$  to  $G6$ .

#### 4.5.3.1 Protonation test simulations

The level of protonation of the dendrimers depends on the pH. Each protonated amine has a charge of +1, which in turn may lead to extended spacers and dendrimers. The  $R_g$  of  $G5$  PPI dendrimers as reported in the experimental data is  $13.9\text{ Å}$ .<sup>[29]</sup> To determine the percentage of charge needed to approach this target value we performed a series of 10 ns atomistic simulations of which the second half was production run. As 90% of the charges are present on the primary amines, the rest are randomly distributed over the tertiary amines.<sup>[71]</sup> The details and results are shown in Table 4.4. It is clear that the  $G5$  PPI with 37.5% protonation is closest to the experimental  $R_g$ . While 25% is also a possible choice, from the graph of  $R_g$  versus time (not shown) follows that it remains low, while 37.5% is more variable.

Recently two groups have performed atomistic simulations of  $G5$  PPI with a special interest in the protonation and its effect on the shape in the form of the  $R_g$  and

**Table 4.5:** Atomistic dendrimer simulations

PPI						
Genera- tion	Atoms	Water particles	Charge & No. of Cl <sup>-</sup>	Box size (Å) (edge)	$R_g$ (Å)	Asphericity
1	64	780	2	28.5	4.52	0.283
2	155	1102	5	32.2	6.89	0.223
3	337	1469	11	35.8	9.13	0.122
4	701	3463	23	47.5	11.41	0.102
5	1429	4663	47	52.9	14.31	0.077
6	2885	7797	95	63.2	17.76	0.033
PPIUA						
Genera- tion	Atoms	Water particles	Charge & No. of Cl <sup>-</sup>	Box size (Å) (edge)	$R_g$ (Å)	Asphericity
1	174	1336	0	34.3	6.67	0.167
2	375	2809	1	44.0	8.12	0.129
3	775	3472	1	47.6	10.48	0.174
4	1576	5721	2	56.5	12.50	0.052
5	3179	8310	5	64.6	16.89	0.055
6	6384	10814	10	71.9	20.86	0.012

the asphericity. The first is a series of 5 ns simulations at 0 %, 66 % and 100 % charge by Wu<sup>[45]</sup> utilizing the COMPASS force field. The second is a series by Maingi et al.<sup>[46]</sup> in the Generalized AMBER Force Field that started with a 20 ns equilibration time followed by 1 ns for production of data with charges of 0 % and 66 %. These 66 % dendrimers are in the so-called ‘onion’ configuration, i.e., the odd layers of the dendrimer are fully protonated.<sup>[92]</sup> The Wu  $R_g$  values compare well with ours (12.34 Å, 15.99 Å, 15.83 Å), but their reported asphericity is lower (0.0027, 0.0059, 0.0091). On the other hand, the Maingi asphericity values are of the same order as ours (0.127, 0.020), and while the 66 % charge  $R_g$  value is similar (16.01 Å), the 0 % value is a bit larger (13.11 Å). Indeed it nears the experimental target value of 13.9 Å. To ascertain the influence of the charge distribution, we also simulated the onion configuration. Then for both our 66 % charge simulations the asphericity values are still within the range of the others (0.018, 0.047), and the  $R_g$  differ little (15.36 Å, 15.99 Å). Apparently, as most of the charge is at the periphery, whether the other charges are distributed randomly or according to the ‘onion’ model seems of less importance.

#### 4.5.3.2 Atomistic PPI and PPIUA dendrimers

With the appropriate degree of protonation found, atomistic simulations of generations 1 to 6 of PPI and PPIUA were performed. Generations 1, 2, and 3 were simulated for 30 ns, the others for 20 ns. The first 10 ns are considered equilibration time. The simulation details and select results are listed in Table 4.5.

**Table 4.6:** Coarse-grained dendrimer simulations

PPI						
Gene- ration	Parti- cles	Mass (g/mol)	Water particles	Box size (Å) (edge)	$R_g \pm \text{std}$ (Å)	Convex hull volume $\pm \text{std}$ (Å <sup>3</sup> )
1	6	462.9	482	39.1	$4.82 \pm 0.39$	$61.2 \pm 16.5$
2	14	1080.1	474	39.1	$7.01 \pm 0.46$	$637.4 \pm 117.1$
3	30	2314.5	650	43.7	$9.27 \pm 0.47$	$2718.9 \pm 377.9$
4	62	4783.4	1095	52.1	$11.71 \pm 0.45$	$7949.0 \pm 807.1$
5	126	9721.1	2337	67.0	$14.46 \pm 0.38$	$19\,109.9 \pm 1356.4$
6	254	19\,596.4	2007	65.3	$17.72 \pm 0.29$	$41\,196.6 \pm 1882.1$
7	510	39\,347.1	1751	65.4	$21.59 \pm 0.22$	$82\,750.9 \pm 2491.4$
PPIUA						
Gene- ration	Parti- cles	Mass (g/mol)	Water particles	Box size (Å) (edge)	$R_g \pm \text{std}$ (Å)	Convex hull volume $\pm \text{std}$ (Å <sup>3</sup> )
1	10	1011.5	1114	51.6	$6.86 \pm 0.66$	$287.5 \pm 61.9$
2	22	2177.4	1087	51.4	$8.91 \pm 0.59$	$1589.7 \pm 273.3$
3	46	4509.0	1170	53.2	$11.05 \pm 0.51$	$5163.1 \pm 662.3$
4	94	9172.4	2367	67.2	$13.50 \pm 0.40$	$13\,266.0 \pm 1172.4$
5	190	18\,499.0	2271	67.5	$16.46 \pm 0.29$	$29\,952.1 \pm 1727.7$
6	382	37\,152.3	5778	91.5	$20.16 \pm 0.21$	$62\,784.3 \pm 2321.5$
7	766	74\,458.9	5394	92.1	$24.78 \pm 0.15$	$125\,324.0 \pm 2867.2$

#### 4.5.4 Measurements: Coarse-grained simulations

The coarse-grained simulations were performed on dendrimers of generations 1 through 7. They were built by an in-house-developed software package which generates an extended configuration, and subsequently minimized to reduce steric overlap. They were then put in an equilibrated box of water, and minimized a second time.

With a time step of 24 fs, each simulation lasts 625 ns of which the first 6 are considered equilibration and the final 619 production run. Every 0.06 ns a state is saved for further analysis.

The simulations are performed in an NPT ensemble, with constant pressure (1 bar) and constant temperature (298 K). The pressure and temperature are scaled using Berendsen's loose coupling technique. For the temperature coupling the proportional constant which indicates the rate of the adjustment is 0.005 and for the pressure coupling the proportional constant is 0.000 005. To reduce volume fluctuations the pressure and temperature are rescaled every 100th time step.

Note that the averages in Table 4.6 are calculated over all 10 300 saved states, as are the standard deviations. They show the variation of radius of gyration values, not the standard error of the measurements. The Waters column shows the number of water particles, each represents 4 water molecules.

The manner in which these dendrimers are generated is not supposed to mimic the actual polymerization where steric effects and back-folding increasingly hinder synthesis for every added generation. Indeed the rigid structure of the *G7* dendrimer shows the infeasibility of synthesizing such a molecule.

#### 4.5.5 A consideration of the asphericity measurement

From the shape tensor more intricate measures have been defined to characterize the shape of atomic objects. From the three principal axes, three invariants are formulated:

$$T = \text{trace}(\mathbf{R}) = g_1 + g_2 + g_3 \simeq R_g^2 \quad (4.28)$$

$$M = \sum \text{minors}(\mathbf{R}) = g_1 g_2 + g_2 g_3 + g_3 g_1 \quad (4.29)$$

$$D = \text{determinant}(\mathbf{R}) = g_1 g_2 g_3 \quad (4.30)$$

Note that although often assumed otherwise,  $T$  does not give the same  $R_g$  as defined in Equation 4.12, because the shape tensor is not weighted by mass. From these Theodorou and Suter<sup>[79]</sup> defined an asphericity ( $b$ ), acylindricity ( $c$ ) and relative shape anisotropy ( $\kappa^2$ ) measure:

$$b = g_1^2 - \frac{(g_2^2 + g_3^2)}{2} \quad (4.31)$$

$$c = g_2^2 - g_3^2 \quad (4.32)$$

$$\kappa^2 = b^2 + \frac{3c^2}{4R_g^4} = 1 - 3\langle \frac{M}{T^2} \rangle \quad (4.33)$$

As  $b$  and  $c$  can range from zero to infinity, the often used measure is  $\kappa^2$  which ranges from 0 to 1. Independently, Rudnick and Gaspari<sup>[80]</sup> defined a measure also named asphericity ( $A$ ) which is the same as  $\kappa^2$  when ignoring the placement of  $\langle \rangle$ :

$$\langle A \rangle = \frac{\langle (T^2 - 3M) \rangle}{\langle T^2 \rangle} \quad (4.34)$$

We opt to calculate the asphericity at every saved state independently and average at the end—the same procedure as for all other measurements.

## Bibliography

- [1] O.A. Matthews, A.N. Shipway, and J.F. Stoddart, Dendrimers—branching out from curiosities into new technologies. *Prog. Polym. Sci.* 1998, 23, 1–56.

- [2] A.W. Bosman, H.M. Janssen, and E.W. Meijer, About dendrimers: Structure, physical properties, and applications. *Chem. Rev.* 1999, *99*, 1665–1688.
- [3] L. Crespo, G. Sanclimens, M. Pons, E. Giralt, M. Royo, and F. Albericio, Peptide and amide bond-containing dendrimers. *Chem. Rev.* 2005, *105*, 1663–1682.
- [4] G.R. Newkome and C.D. Shreiner, Poly(amidoamine), polypropylenimine, and related dendrimers and dendrons possessing different  $1 \rightarrow 2$  branching motifs: An overview of the divergent procedures. *Polymer* 2008, *49*, 1–173.
- [5] G.R. Newkome and C.D. Shreiner, Dendrimers derived from  $1 \rightarrow 3$  branching motifs. *Chem. Rev.* 2010, *110*, 6338–6442.
- [6] P.J. Flory, *Statistical mechanics of chain molecules*. Hanser, Munich, 1969.
- [7] A.Y. Grosberg and A.R. Khokhlov, *Statistical physics of macromolecules*. American Institute of Physics Press, New York, 1994.
- [8] R.L. Lescanec and M. Muthukumar, Configurational characteristics and scaling behavior of starburst molecules: A computational study. *Macromolecules* 1990, *23*, 2280–2288.
- [9] M.L. Mansfield and M. Jeong, Simulation of lattice dendrimers by a Monte Carlo technique with detailed balance. *Macromolecules* 2002, *35*, 9794–9798.
- [10] G. Giupponi and D.M.A. Buzza, A Monte Carlo simulation scheme for nonideal dendrimers satisfying detailed balance. *Macromolecules* 2002, *35*, 9799–9812.
- [11] G. Giupponi and D.M.A. Buzza, A Monte Carlo study of amphiphilic dendrimers: Spontaneous asymmetry and dendron separation. *J. Chem. Phys.* 2005, *122*, 194903.
- [12] P. Welch and M. Muthukumar, Tuning the density profile of dendritic polyelectrolytes. *Macromolecules* 1998, *31*, 5892–5897.
- [13] F. Ganazzoli, R. La Ferla, and G. Terragni, Conformational properties and intrinsic viscosity of dendrimers under excluded-volume conditions. *Macromolecules* 2000, *33*, 6611–6620.
- [14] I.O. Götze and C.N. Likos, Conformations of flexible dendrimers: A simulation study. *Macromolecules* 2003, *36*, 8189–8197.
- [15] J.J. Freire, E. Rodríguez, and A.M. Rubio, Monte Carlo calculations for the intrinsic viscosity of several dendrimer molecules. *J. Chem. Phys.* 2005, *123*, 154901.
- [16] E. Rodríguez, J.J. Freire, G. del Río Echenique, J.G. Hernández Cifre, and J. García de la Torre, Improved simulation method for the calculation of the intrinsic viscosity of some dendrimer molecules. *Polymer* 2007, *48*, 1155–1163.
- [17] M. Murat and G.S. Grest, Molecular dynamics study of dendrimer molecules in solvents of varying quality. *Macromolecules* 1996, *29*, 1278–1285.
- [18] T. Terao and T. Nakayama, Molecular dynamics study of dendrimers: Structure and effective interaction. *Macromolecules* 2004, *37*, 4686–4694.
- [19] J.T. Bosko, B.D. Todd, and R.J. Sadus, Internal structure of dendrimers in the melt under shear: A molecular dynamics study. *J. Chem. Phys.* 2004, *121*, 1091–1096.
- [20] S.V. Lyulin, L.J. Evers, P. van der Schoot, A.A. Darinskii, A.V. Lyulin, and M.A.J. Michels, Effect of solvent quality and electrostatic interactions on size and structure of dendrimers. Brownian dynamics simulation and mean-field theory. *Macromolecules* 2004, *37*, 3049–3063.
- [21] T. Zhou and S.B. Chen, A simulation study on dynamics of dendrimer-polymer conjugates. *Macromolecules* 2006, *39*, 6686–6692.
- [22] D.A. Markelov, S.V. Lyulin, Y.Y. Gotlib, A.V. Lyulin, V.V. Matveev, E. Lahderanta, and A.A. Darinskii, Orientational mobility and relaxation spectra of dendrimers: Theory and computer simulation. *J. Chem. Phys.* 2009, *130*, 044907.
- [23] B. Suman and S. Kumar, Brownian dynamics simulations of hydrophobic dendrimer adsorption. *Mol. Simul.* 2009, *35*, 38–49.
- [24] K. Karatasos, D.B. Adolf, and G.R. Davies, Statics and dynamics of model dendrimers as studied by molecular dynamics simulations. *J. Chem. Phys.* 2001, *115*, 5310–5318.
- [25] P.M. Drew and D.B. Adolf, Intrinsic viscosity of dendrimers via equilibrium molecular dynamics. *Soft Matter* 2005, *1*, 146–151.
- [26] A.A. Gurtovenko, S.V. Lyulin, M. Karttunen, and I. Vattulainen, Molecular dynamics study of charged dendrimers in salt-free solution: Effect of counterions. *J. Chem. Phys.* 2006, *124*, 094904.
- [27] N.W. Suek and M.H. Lamm, Effect of terminal group modification on the solution properties

- of dendrimers: A molecular dynamics simulation study. *Macromolecules* 2006, *39*, 4247–4255.
- [28] K. Karatasos, Self-organization in dendrimer polyelectrolytes. *Macromolecules* 2008, *41*, 1025–1033.
- [29] R. Scherrenberg, B. Coussens, P. van Vliet, G. Edouard, J. Brackman, E. de Brabander, and K. Mortensen, The molecular characteristics of poly(propyleneimine) dendrimers as studied with small-angle neutron scattering, viscosimetry, and molecular dynamics. *Macromolecules* 1998, *31*, 456–461.
- [30] L. Cavallo and F. Fraternali, A molecular dynamics study of the first five generations of poly(propylene imine) dendrimers modified with *N*-*t*Boc-L-phenylalanine. *Chem.–Eur. J.* 1998, *4*, 927–934.
- [31] E. Blasizza, M. Fermeglia, and S. Pricl, Dendrimers as functional materials. A molecular simulation study of poly(propylene) imine starburst molecules. *Mol. Simul.* 2000, *24*, 167–189.
- [32] N. Zacharopoulos and I.G. Economou, Morphology and organization of poly(propylene imine) dendrimers in the melt from molecular dynamics simulation. *Macromolecules* 2002, *35*, 1814–1821.
- [33] A. Mecke, I. Lee, J.R. Baker Jr, M.M. Banaszak Holl, and B.G. Orr, Deformability of poly(amidoamine) dendrimers. *Eur. Phys. J. E* 2004, *14*, 7–16.
- [34] P.K. Maiti, T. Çağın, G. Wang, and W.A. Goddard III, Structure of PAMAM dendrimers: Generations 1 through 11. *Macromolecules* 2004, *37*, 6236–6254.
- [35] C.V. Kelly, P.R. Leroueil, E.K. Nett, J.M. Wereszczynski, J.R. Baker Jr, B.G. Orr, M.M. Banaszak Holl, and I. Andricioaei, Poly(amidoamine) dendrimers on lipid bilayers I: Free energy and conformation of binding. *J. Phys. Chem. B* 2008, *112*, 9337–9345.
- [36] P. Carbone and F. Müller-Plathe, Molecular dynamics simulations of polyaminoamide (PAMAM) dendrimer aggregates: Molecular shape, hydrogen bonds and local dynamics. *Soft Matter* 2009, *5*, 2638–2647.
- [37] C.B. Gorman and J.C. Smith, Effect of repeat unit flexibility on dendrimer conformation as studied by atomistic molecular dynamics simulations. *Polymer* 2000, *41*, 675–683.
- [38] S. Pricl, M. Fermeglia, M. Ferrone, and A. Asquini, Scaling properties in the molecular structure of three-dimensional, nanosized phenylene-based dendrimers as studied by atomistic molecular dynamics simulations. *Carbon* 2003, *41*, 2269–2283.
- [39] W. Ortiz, A.E. Roitberg, and J.L. Krause, Molecular dynamics of poly(benzylphenyl ether) dendrimers: Effects of backfolding on Förster energy-transfer rates. *J. Phys. Chem. B* 2004, *108*, 8218–8225.
- [40] P. Carbone, A. Calabretta, M. Di Stefano, F. Negri, and K. Müllen, Shape persistence and bistability of planar three-fold core polyphenylene dendrimers: A molecular dynamics study. *J. Phys. Chem. A* 2006, *110*, 2214–2224.
- [41] K.J. Haxton, D.J. Cole-Hamilton, and R.E. Morris, The structure of phosphine-functionalised silsesquioxane-based dendrimers: A molecular dynamics study. *Dalton Trans.* 2004, 1665–1669.
- [42] K.T. Welch, S. Arévalo, J.F.C. Turner, and G. Rafael, An NMR and molecular modeling study of carbosilane-based dendrimers functionalized with phenolic groups or titanium complexes at the periphery. *Chem.–Eur. J.* 2005, *11*, 1217–1227.
- [43] P. Miklis, T. Çağın, and W.A. Goddard III, Dynamics of Bengal Rose encapsulated in the Meijer dendrimer box. *J. Am. Chem. Soc.* 1997, *119*, 7458–7462.
- [44] G. Teobaldi and F. Zerbetto, Molecular dynamics of a dendrimer–dye guest–host system. *J. Am. Chem. Soc.* 2003, *125*, 7388–7393.
- [45] C. Wu, pH response of conformation of poly(propylene imine) dendrimer in water: A molecular simulation study. *Mol. Simul.* 2010, *36*, 1164–1172.
- [46] V. Maingi, V. Jain, P.V. Bharatam, and P.K. Maiti, Dendrimer building toolkit: Model building and characterization of various dendrimer architectures. *J. Comput. Chem.* 2012, *33*, 1997–2011.
- [47] P.K. Maiti, T. Çağın, S.T. Lin, and W.A. Goddard III, Effect of solvent and pH on the structure of PAMAM dendrimers. *Macromolecules* 2005, *38*, 979–991.



- [48] Y. Liu, V.S. Bryantsev, M.S. Diallo, and W.A. Goddard III, PAMAM dendrimers undergo pH responsive conformational changes without swelling. *J. Am. Chem. Soc.* 2009, *131*, 2798–2799.
- [49] I. Tanis and K. Karatasos, Association of a weakly acidic anti-inflammatory drug (ibuprofen) with a poly(amidoamine) dendrimer as studied by molecular dynamics simulations. *J. Phys. Chem. B* 2009, *113*, 10984–10993.
- [50] G.M. Pavan, L. Albertazzi, and A. Danani, Ability to adapt: Different generations of PAMAM dendrimers show different behaviors in binding siRNA. *J. Phys. Chem. B* 2010, *114*, 2667–2675.
- [51] M.A. Mazo, M.Y. Shamaev, N.K. Balabaev, A.A. Darinskii, and I.M. Neelov, Conformational mobility of carbosilane dendrimer: Molecular dynamics simulation. *Phys. Chem. Chem. Phys.* 2004, *6*, 1285–1289.
- [52] H. Lee and R.G. Larson, Molecular dynamics simulations of PAMAM dendrimer-induced pore formation in DPPC bilayers with a coarse-grained model. *J. Phys. Chem. B* 2006, *110*, 18204–18211.
- [53] W.d. Tian and Y.q. Ma, Coarse-grained molecular simulation of interacting dendrimers. *Soft Matter* 2011, *7*, 500–505.
- [54] P. Carbone, F. Negri, and F. Müller-Plathe, A coarse-grained model for polyphenylene dendrimers: Switching and backfolding of planar three-fold core dendrimers. *Macromolecules* 2007, *40*, 7044–7055.
- [55] G. del Río Echenique, R. Rodríguez Schmidt, J.J. Freire, J.G. Hernández Cifre, and J. García de la Torre, A multiscale scheme for the simulation of conformational and solution properties of different dendrimer molecules. *J. Am. Chem. Soc.* 2009, *131*, 8548–8556.
- [56] P.K. Maiti, Y. Li, T. Çağın, and W.A. Goddard III, Structure of polyamidoamide dendrimers up to limiting generations: A mesoscale description. *J. Chem. Phys.* 2009, *130*, 144902.
- [57] T. Chang, K. Pieterse, M.A.C. Broeren, H. Kooijman, A.L. Spek, P.A.J. Hilbers, and E.W. Meijer, Structural elucidation of dendritic host–guest complexes by X-ray crystallography and molecular dynamics simulations. *Chem.–Eur. J.* 2007, *13*, 7883–7889.
- [58] T.M. Hermans, M.A.C. Broeren, N. Gomopoulos, A.F. Smeijers, B. Mezari, E.N.M. van Leeuwen, M.R.J. Vos, P.C.M.M. Magusin, P.A.J. Hilbers, M.H.P. van Genderen, N.A.J.M. Sommerdijk, G. Fytas, and E.W. Meijer, Stepwise noncovalent synthesis leading to dendrimer-based assemblies in water. *J. Am. Chem. Soc.* 2007, *129*, 15631–15638.
- [59] A.J. Markvoort, Coarse grained molecular dynamics. In *Computational methods in catalysis and materials science: An introduction for scientists and engineers*, eds. R.A. van Santen and P. Sautet, chap. 8, 151–166, Wiley, Weinheim, 2009.
- [60] A.D. McKerrel Jr, D. Bashford, M. Bellott, R.L. Dunbrack Jr, J.D. Evanseck, M.J. Field, S. Fischer, J. Gao, H. Guo, S. Ha, D. Joseph-McCarthy, L. Kuchnir, K. Kuczera, F.T.K. Lau, C. Mattos, S. Michnick, T. Ngo, D.T. Nguyen, B. Prodhom, W.E. Reiher III, B. Roux, M. Schlenkrich, J.C. Smith, R. Stote, J. Straub, M. Watanabe, J. Wiorcikiewicz-Kuczera, D. Yin, and M. Karplus, All-atom empirical potential for molecular modeling and dynamics studies of proteins. *J. Phys. Chem. B* 1998, *102*, 3586–3616.
- [61] F. Müller-Plathe, Coarse-graining in polymer simulation: From the atomistic to the mesoscopic scale and back. *ChemPhysChem* 2002, *3*, 754–769.
- [62] D. Reith, M. Pütz, and F. Müller-Plathe, Deriving effective mesoscale potentials from atomistic simulations. *J. Comput. Chem.* 2003, *24*, 1624–1636.
- [63] A.P. Lyubartsev and A. Laaksonen, Calculation of effective interaction potentials from radial distribution functions: A reverse Monte Carlo approach. *Phys. Rev. E* 1995, *52*, 3730–3737.
- [64] A.K. Soper, Empirical potential Monte Carlo simulation of fluid structure. *Chem. Phys.* 1996, *202*, 295–306.
- [65] D. Reith, H. Meyer, and F. Müller-Plathe, Mapping atomistic to coarse-grained polymer models using automatic simplex optimization to fit structural properties. *Macromolecules* 2001, *34*, 2335–2345.
- [66] X. Li, X. Ma, L. Huang, and H. Liang, Developing coarse-grained force fields for *cis*-poly(1,4-butadiene) from the atomistic simulation. *Polymer* 2005, *46*, 6507–6512.

- [67] X. Li, D. Kou, S. Rao, and H. Liang, Developing a coarse-grained force field for the diblock copolymer poly(styrene-*b*-butadiene) from atomistic simulation. *J. Chem. Phys.* 2006, *124*, 204909.
- [68] K.R. Hadley and C. McCabe, On the investigation of coarse-grained models for water: Balancing computational efficiency and the retention of structural properties. *J. Phys. Chem. B* 2010, *114*, 4590–4599.
- [69] B. van Hoof, A.J. Markvoort, R.A. van Santen, and P.A.J. Hilbers, The CUMULUS coarse graining method: Transferable potentials for water and solutes. *J. Phys. Chem. B* 2011, *115*, 10001–10012.
- [70] D. Boris and M. Rubinstein, A self-consistent mean field model of a starburst dendrimer: Dense core vs dense shell. *Macromolecules* 1996, *29*, 7251–7260.
- [71] G.J.M. Koper, M.H.P. van Genderen, C. Elissen-Román, M.W.P.L. Baars, E.W. Meijer, and M. Borkovec, Protonation mechanism of poly(propylene imine) dendrimers and some associated oligo amines. *J. Am. Chem. Soc.* 1997, *119*, 6512–6521.
- [72] P. Lindner and T. Zemb, *Neutrons, X-rays and light: Scattering methods applied to soft condensed matter*. Elsevier Science, Amsterdam, 2002.
- [73] M. Han, P. Chen, and X. Yang, Molecular dynamics simulation of PAMAM dendrimer in aqueous solution. *Polymer* 2005, *46*, 3481–3488.
- [74] Y.J. Sheng, S. Jiang, and H.K. Tsao, Radial size of a starburst dendrimer in solvents of varying quality. *Macromolecules* 2002, *35*, 7865–7868.
- [75] G. Giupponi and D.M.A. Buzzza, Monte Carlo simulation of dendrimers in variable solvent quality. *J. Chem. Phys.* 2004, *120*, 10290–10298.
- [76] P.J. Flory, *Principles of polymer chemistry*. Cornell University Press, London, 1953.
- [77] P.G. de Gennes, *Scaling concepts in polymer physics*. Cornell University Press, New York, 1979.
- [78] M. Kröger, O. Peleg, and A. Halperin, From dendrimers to dendronized polymers and forests: Scaling theory and its limitations. *Macromolecules* 2010, *43*, 6213–6224.
- [79] D.N. Theodorou and U.W. Suter, Shape of unperturbed linear polymers: Polypropylene. *Macromolecules* 1985, *18*, 1206–1214.
- [80] J. Rudnick and G. Gaspari, The asphericity of random walks. *J. Phys. A: Math. Gen.* 1986, *19*, L191–L193.
- [81] P.G. de Gennes and H. Hervet, Statistics of “starburst” polymers. *J. Physique Lett.* 1983, *44*, 351–360.
- [82] S. Rosenfeldt, N. Dingenouts, M. Ballauff, N. Werner, F. Vögtle, and P. Lindner, Distribution of end groups within a dendritic structure: A SANS study including contrast variation. *Macromolecules* 2002, *35*, 8098–8105.
- [83] M.F. Sanner, A.J. Olson, and J.C. Spohner, Reduced surface: An efficient way to compute molecular surfaces. *Biopolymers* 1996, *38*, 305–320.
- [84] M. Ballauff and C.N. Likos, Dendrimers in solution: Insight from theory and simulation. *Angew. Chem., Int. Ed.* 2004, *43*, 2998–3020.
- [85] M. Kataoka and Y. Goto, X-ray solution scattering studies of protein folding. *Folding Des.* 1996, *1*, R107–R114.
- [86] C.D. Putnam, M. Hammel, G.L. Hura, and J.A. Tainer, X-ray solution scattering (SAXS) combined with crystallography and computation: Defining accurate macromolecular structures, conformations and assemblies in solution. *Q. Rev. Biophys.* 2007, *40*, 191–285.
- [87] M.L. Mansfield and L. Klushin, Monte Carlo studies of dendrimer macromolecules. *Macromolecules* 1993, *26*, 4262–4268.
- [88] L. Kalé, R. Steel, M. Bhandarkar, R. Brunner, A. Gursoy, N. Krawetz, J. Phillips, A. Shinzaki, K. Varadarajan, and K. Schulten, NAMD2: Greater scalability for parallel molecular dynamics. *J. Comput. Phys.* 1999, *151*, 283–312.
- [89] Sybyl. Tripos, Inc., St. Louis, 2003.
- [90] A.T. Brünger, X-PLOR, version 3.1: A system for X-ray crystallography and NMR. Yale University Press, New Haven, 1992.
- [91] W. Humphrey, A. Dalke, and K. Schulten, VMD: Visual molecular dynamics. *J. Mol. Graphics* 1996, *14*, 33–38.

- [92] D. Čakara and M. Borkovec, Microscopic protonation mechanism of branched polyamines: Poly(amidoamine) versus poly(propyleneimine) dendrimers. *Croat. Chem. Acta* 2007, *80*, 421–428.

## Chapter 5

# Poly(propylene imine) dendrimers in dilute to melt conditions

---

**Abstract** The behavior of poly(propylene imine) (PPI) dendrimers in concentrated solutions is investigated using molecular dynamics simulations containing up to a thousand PPI dendrimers of generation 4 or 5 in explicit water. To deal with large system sizes and time scales required to study the solutions over a wide range of dendrimer concentrations, the coarse-grained model was applied. Simulation results on the radius of gyration, structure factor, intermolecular spacing, dendrimer interpenetration, and water penetration are compared with available experimental data, providing a clear concentration-dependent molecular picture of PPI dendrimer solutions. It is shown that with increasing concentration the individual dendrimer volume diminishes accompanied by a reduction of internalized water, ultimately resulting in solvent filled cavities between stacked dendrimers. Concurrently dendrimer interpenetration increases only slightly, leaving each dendrimer a separate entity also at high concentrations. Moreover, we compare apparent structure factors, as calculated in experimental studies relying on the decoupling approximation and the constant form factor assumption, with directly computed structure factors. We demonstrate that these already diverge at rather low concentrations, not because of small changes in form factor, but rather because the decoupling approximation fails as monomer positions of separate dendrimers become correlated at concentrations well below the overlap concentration.

---

---

This work has been published in:

A.F. Smeijers, A.J. Markvoort, K. Pieterse, and P.A.J. Hilbers, Coarse-grained simulations of poly(propylene imine) dendrimers in solution. *Journal of Chemical Physics* 2016, *144*, 074903.

## 5.1 Introduction

Because of their wide range of potential applications,<sup>[1]</sup> dendrimers have been investigated extensively for quite some time, also using computer models. In these computer models the focus commonly is on the average shape or internal structure of a single dendrimer (Chapter 4). These simulations can only reproduce a subset of experimental results, for experiments on dendrimers are typically conducted on solutions of various concentrations. For concentrated solutions the interactions between polymers come into play and dendrimers behave remarkably different than linear polymers. Dendrimers are globular, have fewer entanglements, and offer opportunities to create nanoscale materials with a greater level of control. In simulations of phenomena involving such dendrimer–dendrimer interactions large numbers of dendrimers and solvent molecules need to be regarded and substantial time scales are required. This is prohibitive to fully atomistic molecular dynamics (MD) simulations yet possible with a coarse-graining (CG) scheme wherein groups of atoms are lumped together to form a single interaction site.

Previous endeavors in computational modeling of multiple dendrimers started with the melt phase, i.e., mobile dendrimers without solvent. The earliest examples are short atomistic MD simulations (0.4 ns) of small numbers of PPI dendrimers, i.e., 14 third-generation (14  $G3$ ),<sup>[2]</sup> 8 fourth-generation (8  $G4$ )<sup>[3]</sup> and 4 fifth-generation (4  $G5$ )<sup>[3]</sup> dendrimers. These studies were followed by longer simulations of melt containing larger numbers of dendrimers and using simpler models (125 bead-spring  $G4$ ,<sup>[4]</sup> 100 ns 216  $G4$  (45 beads) CG polyphenylene dendrimers<sup>[5]</sup>) as well as a longer atomistic simulation of poly(amido amine) dendrimers (15 ns 8  $G4$ )<sup>[6]</sup>. In solutions, the behavior of dendrimers is an interplay of dendrimer–solvent and dendrimer–dendrimer interactions. A starting point for simulations is the study of 2 dendrimers in solution. This has been investigated with bead-spring dendrimers of  $G4$  or  $G5$  in implicit solvent<sup>[7,8]</sup> and in explicit water.<sup>[9,10]</sup> Solutions of more dendrimers have been simulated a couple of times with bead-spring models in implicit (Monte Carlo 500  $G4$ ,<sup>[11]</sup> 32  $G3$ )<sup>[12]</sup> and explicit solvent (30  $G4$ )<sup>[13]</sup>.

Compared to those papers, here, we perform larger scale simulations (up to 1430  $G4$  PPI of 62 particles each or 968  $G5$  PPI of 126 particles each) in explicit water, over a full range of concentrations, each simulation covering 24 ns. For this we use our previously developed coarse-grained poly(propylene imine) (PPI,  $G5$ : DAB–dendr–(NH<sub>2</sub>)<sub>64</sub>) dendrimer model (Chapter 4) shown in Figure 5.1.

In the next section we describe the coarse-grained PPI model and the simulation arrangements matching experiments reported in literature. This is followed by the simulation results providing descriptions of the various dendrimer properties measured. First, the radii of gyration, radial distribution functions and structure factors are calculated to demonstrate the similarity between the simulations and

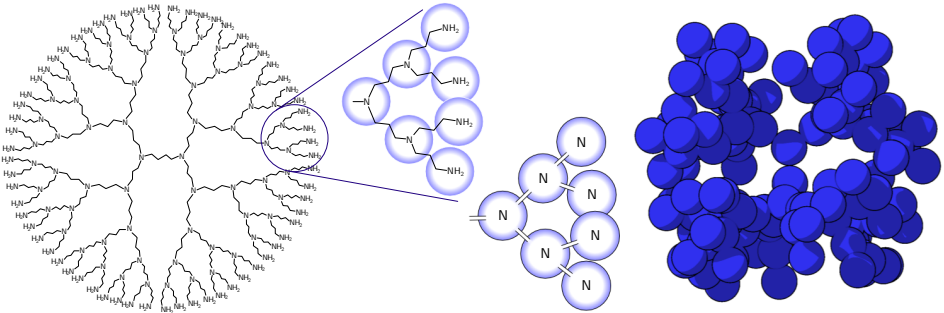


**Figure 5.1:** The fifth-generation 1,4-diaminobutane poly(propylene imine) dendrimer drawn as the molecular structure representation (left) and the coarse-grained form (right) with the coarse-grained sites indicated in the middle.

experiments. Next, the simulations are used to answer further questions raised by experiments, i.e., to quantify the amount of overlap of dendrimer branches under different concentrations, to determine the ‘average distance’ between dendrimers, and to observe possible dendrimer shape changes upon increasing concentration.

## 5.2 Model

In this chapter, we use the coarse-grained poly(propylene imine) (PPI) model which we derived in Chapter 4 as illustrated in Figure 5.1. All simulations were performed using PumMa.

For the validation of the simulations of dendrimer solutions in this chapter two available small-angle neutron scattering (SANS) studies of PPI in good solvent are used. First, the measurements of  $G5$  PPI in  $D_2O$  by Ramzi et al.<sup>[14]</sup> (volume percentages: 5%–60%), and second, the measurements of  $G4$  and  $G5$  PPI in methanol by Topp et al.<sup>[15]</sup> (mass percentages: 1%–80%). To allow for comparison with these experiments, the coarse-grained simulations were also performed on PPI dendrimers of generations 4 and 5, with dendrimer *mass percentages* of approximately 0.1%, 1%, 2%, 6%, 23%, 43%, 64%, 83%, and 100%. Note that the actual volume percentages are rather similar to the mass percentages up to 64% after which they drop (see Appendix 5.5.1).

The simulation boxes (Figure 5.2) initially consist of duplicates of a dendrimer isolated from the earlier simulations (Chapter 4) with the number of water particles reduced to get the desired concentration. To minimize empty space between duplicates, for each generation one dendrimer was selected for its small radius and minimal asphericity. These dendrimers were subsequently desolvated, multiplied, resolvated and minimized. This procedure resulted in 5  $G4$  PPI dendrimers with

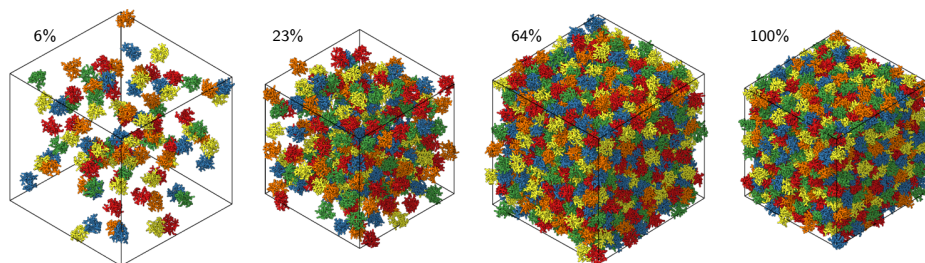


**Figure 5.2:** Snapshots of the simulation states at the end of the  $G5$  PPI simulations for the dendrimer mass percentages indicated.

250 105 water particles for 0.1 % up to 1430 dendrimers for 43 % and beyond and 2  $G5$  PPI dendrimers with 204 078 water particles for 0.1 % up to 968 dendrimers for 43 % and beyond. Simulation box volumes range from 12 203.1 to 37 431.2 nm<sup>3</sup> (for all configurations see Appendix 5.5.1).

For each combination of concentration and generation one simulation was performed with constant pressure (1 bar) and constant temperature (298 K) using Berendsen pressure and temperature coupling. With a time step of 24 fs, each simulation lasts 24 ns, of which the first 6 ns are considered equilibration time, and the final 18 ns production run. Autocorrelation functions for dendrimer  $R_g$ , asphericity and rotation indicate that the 6 ns equilibration time suffices as the relaxation times are well within this time scale (see Appendix Section 5.5.2). During the production run every 0.06 ns a configuration was saved for further analysis.

## 5.3 Results and discussion

The final configurations of simulations at four different concentrations are shown in Figure 5.2. Overall the dendrimers do not form large aggregates, instead they constantly collide and separate over the course of the simulations. Yet in concentrations as low as 23 % mutual distances are often so small that any clustering algorithm would still lump most dendrimers together.

### 5.3.1 Radius of gyration

We first investigate the dendrimer size as a function of concentration. This dendrimer size is again calculated by the radius of gyration, a measure of the mass distribution of a molecule around its center of mass ( $R_g$ , Equation 4.12). In Figure 5.3, these values are compared to the radii of the solitary  $G4$  and  $G5$  dendrimers as calculated in Section 4.3.2. Evidently in low concentrations the radii are the

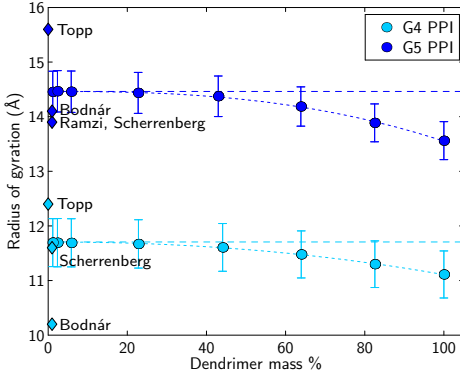


**Figure 5.3:** Radius of gyration at varying concentrations. The dashed lines represent the  $R_g$  calculated for solitary dendrimers (Section 4.3.2). The dotted lines are the best fits for  $R_g$  as a function of mass fraction  $\varphi$ , for  $G4$ :  $R_g(\varphi) = R_{g,0} (1 - (\varphi/4.08)^{2.12})$  and  $G5$ :  $R_g(\varphi) = R_{g,0} (1 - (\varphi/2.92)^{2.58})$ . Averages and standard deviations have been calculated over all dendrimers. Diamonds represent experimental values from Ramzi et al.,<sup>[14]</sup> Topp et al.,<sup>[15]</sup> Scherrenberg et al.,<sup>[16]</sup> and Bodnár et al.<sup>[17]</sup>

same, but with increased concentration the dendrimers become more and more compacted.

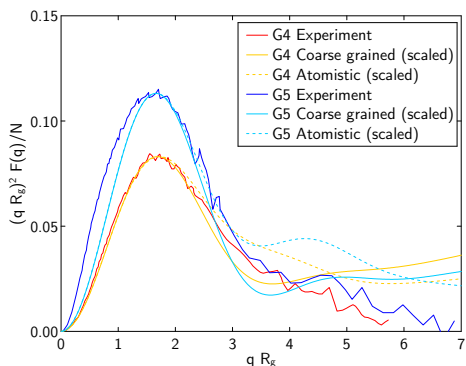
The  $R_g$  values of PPI dendrimers at dilute concentrations (1%) were measured experimentally in water as  $10.2 \text{ \AA}$ <sup>[17]</sup> and  $11.6 \text{ \AA}$ <sup>[16]</sup> for  $G4$  and  $13.9 \text{ \AA}$ <sup>[14,16]</sup> and  $14.1 \text{ \AA}$ <sup>[17]</sup> for  $G5$ . In methanol the measured values were  $12.4 \text{ \AA}$  for  $G4$  PPI<sup>[15]</sup> and  $15.6 \text{ \AA}$  for  $G5$  PPI.<sup>[15]</sup> Our simulation values lie between these reported values. The shape-persistence at low to medium concentrations is in agreement with SANS measurements of  $G4$  PPI functionalized with urea phenyl in dimethylacetamide,<sup>[18]</sup> where no difference in shapes was observed between volume percentages 15% and 23%. Under those conditions similarly flexible linear polymers show much more pronounced shape changes. Over a larger concentration range (0.5%–50% in water) solution densitometry and viscometry measurements of  $G4$  and  $G5$  PPI functionalized with acetyl chloride did show their hydrodynamic volumes decreasing.<sup>[17]</sup> The authors postulated that these dendrimers either interpenetrate at high concentrations, or expel solvent. We will examine the extent of both phenomena in Sections 5.3.4 and 5.3.6, but first continue with a direct comparison of the simulations with experimental SANS measurements.

### 5.3.2 Structure factor

Small-angle neutron scattering is a technique for examining the structure of, e.g., a solution of dendrimers by casting a beam of neutrons at it and measuring the deflections caused by the nuclei of the atoms within. The structure may then be reconstructed from the measured total coherent scattering intensity which is a function of the scattering angle ( $I(\mathbf{q})$ ). The randomness of the orientation of the dendrimers in solution results in angular isotropy of the signal such that  $I(\mathbf{q}) = I(q)$ , where  $q$  denotes the magnitude of the scattering wave vector  $\mathbf{q}$  in  $\text{\AA}^{-1}$ .



**Figure 5.4:** Kratky plot of G4 and G5 PPI from experiments,<sup>[16]</sup> current 0.1 % coarse-grained simulations and atomistic simulations of a single dendrimer (Section 4.3.8). Simulation values are scaled to match the height of the peaks.



In dilute solutions the scattering due to distant dendrimers is extremely weak and may be ignored. The measured scattering is dominated by scatterers within the individual dendrimers, which can be used to assess their shape. This form factor ( $F(q)$ , Equation 4.27) thus describes the correlation of scatterers in the dendrimer.

The form factors from simulations are compared with experimental ones in a Kratky plot (Figure 5.4). At small angles the scatter intensity is associated with distant scatterers. The left hand side of the Kratky plot thus represents the overall dendrimer shape, while at the right hand side (large angles) the local internal structure is expressed. In experiments the latter is increasingly difficult to do well, while for the coarse-grained simulation the particles' size limits the smallest possible distances. As a result the difference between the form factor graphs becomes more pronounced at larger angles. Still, the simulated form factors follow the experimental one quite well. The clear peak means the dendrimer is a fairly dense globular structure.<sup>[19,20]</sup> The difference between the isolated atomistic dendrimers of Chapter 4 and the current dilute coarse-grained simulations is imperceptible on the upwards slope of the peak.

From simulations  $F(q)$  can also be calculated for higher concentrations. The actual form factors for these higher concentrations differ only slightly, as evidenced in Figure 5.5. An inset is required to illustrate that the form factor broadens with rising concentration, which is expected as the dendrimers become more compressed as observed in Figure 5.3.

In experiments this  $F(q)$  cannot be measured directly for higher concentrations. Measured is the full scattering intensity  $I(q)$  which can be calculated similarly

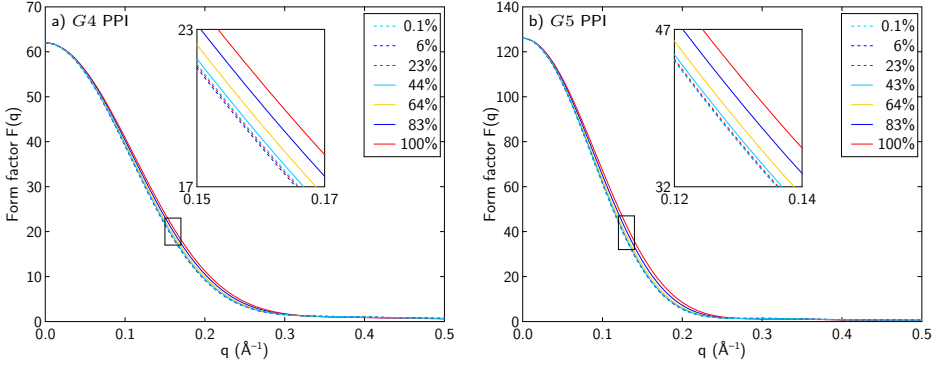


**Figure 5.5:** The form factors of generations (a) 4 and (b) 5 in various concentrations. The inset is to highlight the increasing differences between the least concentrated and beyond.

as:

$$\begin{aligned}
 I(q) &= \frac{1}{\nu N} \left\langle \sum_{m=1}^{\nu} \sum_{n=1}^{\nu} \sum_{j=1}^N \sum_{k=1}^N e^{-i\mathbf{q} \cdot (\mathbf{r}_{m,j} - \mathbf{r}_{n,k})} \right\rangle \\
 &= \frac{1}{\nu N} \left\langle \sum_{m=1}^{\nu} \sum_{n=1}^{\nu} \sum_{j=1}^N \sum_{k=1}^N \frac{\sin(q |\mathbf{r}_{m,j} - \mathbf{r}_{n,k}|)}{q |\mathbf{r}_{m,j} - \mathbf{r}_{n,k}|} \right\rangle \quad (5.1)
 \end{aligned}$$

where  $\nu$  is the number of dendrimers in solution and periodic boundary conditions are applied.

The coherent scattering plots shown in Figure 5.6 are comparable to experimental ones<sup>[14]</sup> with the caveat that the latter were only investigated for concentrations up to 60%. The change in internal dendrimer structure with increasing concentration shows in the divergence from a single curve at high  $q$ -values.

As shown in Figure 5.6 the overall scattering intensity changes dramatically with concentration. This is mostly due to scattering between dendrimers. Two measures for the short range order of the dendrimers in the solution are the structure factor ( $S(q)$ ) and the radial distribution function ( $g(r)$ ) of the dendrimer centers. The calculation for the structure factor is effectively the same as for the form factor, but with the dendrimers' centers of mass instead of their atoms:<sup>[11]</sup>

$$S(q) = \frac{1}{\nu} \left\langle \sum_{m=1}^{\nu} \sum_{n=1}^{\nu} e^{-i\mathbf{q} \cdot (\mathbf{c}_m - \mathbf{c}_n)} \right\rangle \quad (5.2)$$

Analogous to the radial monomer distribution, the radial distribution function  $g(r)$  describes the probability of finding a dendrimer at a certain distance of another

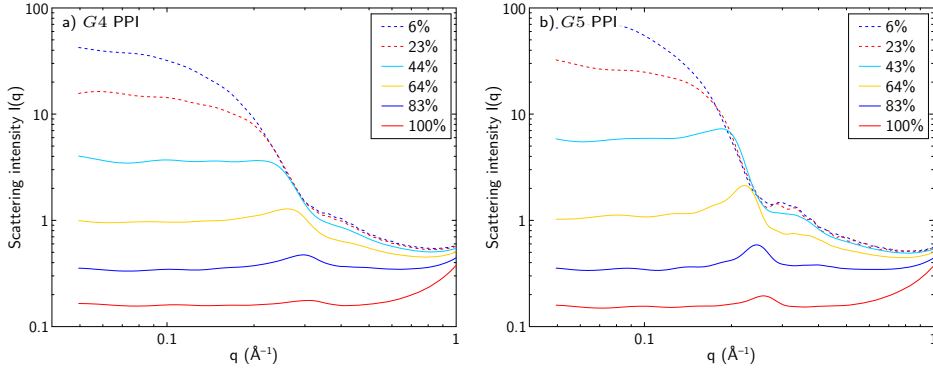


**Figure 5.6:** Log-log plot of the scattering intensities  $I(q)$  of PPI dendrimers of generations (a) 4 and (b) 5 at various concentrations as indicated by the legends.

dendrimer relative to this same probability in a random distribution with equal density:

$$g(r) = \frac{2 n_{\text{hist}}(r)}{\nu \rho_0 \frac{4}{3} \pi \left( \left( r + \frac{dr}{2} \right)^3 - \left( r - \frac{dr}{2} \right)^3 \right)} \quad (5.3)$$

where  $n_{\text{hist}}(r)$  is a histogram of interdendrimer distances ( $r = |\mathbf{c}_m - \mathbf{c}_n|$ ,  $n > m$ ) with bin size  $dr$ , and  $\rho_0$  is the overall density, i.e., the number of dendrimers divided by the volume of the simulation box ( $\rho_0 = \nu/V$ ). Note that  $g(r)$  can only be calculated for  $r \leq R$ , half the minimum box length;  $g(r)$  is set to 1 for  $r > R$  as per the definition of non-correlation at large distances.

The structure factor and the radial distribution function are related via:

$$S(q) = 1 + 4\pi\rho_0 \int_0^R dr r^2 \frac{\sin(qr)}{qr} (g(r) - 1) \quad (5.4)$$

Both have their own interesting features and both are shown for a subset of the simulations in Figure 5.7.

The spatial correlation between dendrimers is shown in the radial distribution graphs wherein the level of order in a system is represented by the number and steepness of peaks. For example, in 6%  $G5$  the first peak is hardly discernible, indicating the dendrimer distribution is unordered. For 23%  $G5$  and 6 to 23%  $G4$  one clear peak is present, representing weak correlation between first neighbors only. The higher concentrations show secondary and tertiary peaks corresponding with a liquid-like order. Real crystalline distributions with dendrimers at discrete distances would show as sharp discrete peaks, but no such distribution is observed here.

While less intuitive, the structure factor graphs are better suited for comparison

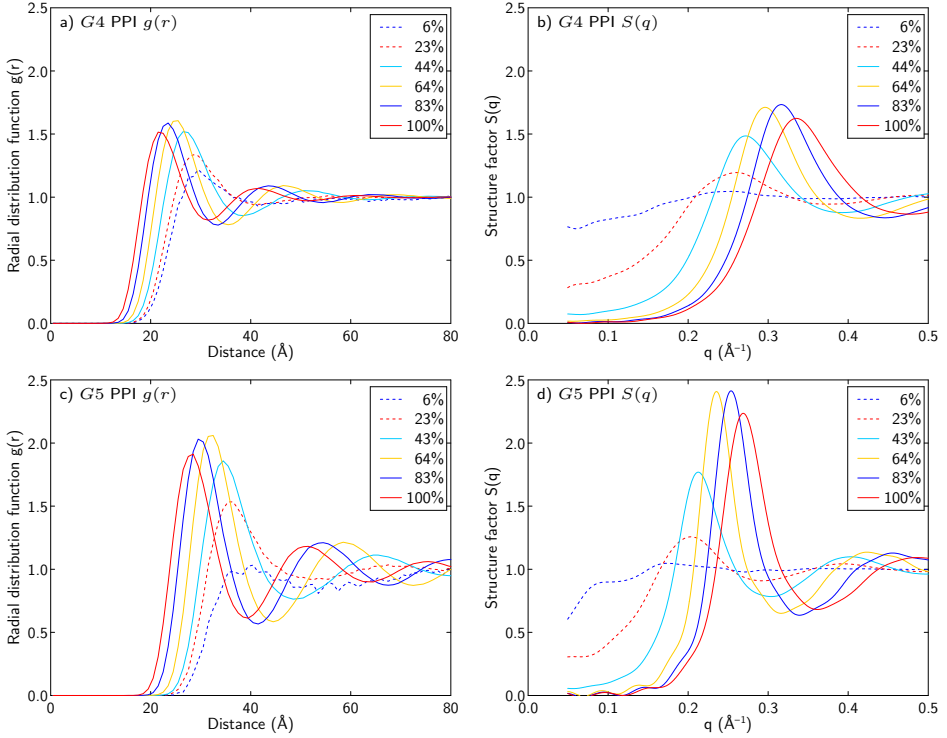


**Figure 5.7:** Interdendrimer distances of generations 4 and 5 in various concentrations. (a, c) Radial distribution functions (bin size 1 Å). (b, d) Corresponding structure factors.

with experiments. The trend exhibited by the curves at low  $q$ -values is quite similar to the experimental ones. In these graphs the height of the primary  $S(q)$  peak is said to represent the level of crystallinity of the solution. Crystallization occurs at  $S(q)$  values near 2.85,<sup>[21]</sup> while 1.5 suggests liquid-like order.<sup>[14]</sup> Following this rule of thumb, it seems unusual that the 64% and 83% simulations have a higher peak than the 100% simulations. For both  $G4$  and  $G5$  dendrimer simulations, even at 100% the dendrimers exhibit no long range order, as evidenced by  $g(r)$  and  $S(q)$ . In the  $g(r)$  graphs the 100% simulations exhibit closer packing, but not increased order. Visual inspection of the simulations shows the dendrimers remain mobile with respect to each other, even if their size and crowdedness lead to a high viscosity. Similar  $S(q)$  peak height progression is apparent in the experimental results of Topp et al.<sup>[15]</sup> where the highest peaks are around 20%  $G5$ , while for  $G4$  the structure factors plateau early. The 5%–60% structure factor results of Ramzi et al.<sup>[14]</sup> do not show any peak (in Figures 5.8c,f these experimental results are reproduced).

Knowing all atom positions in the simulations, the differentiation between internal

scatterers for the form factor and scattering between dendrimers for the structure factor is straightforward. For the SANS experiments it is more difficult to make this distinction in order to determine the structure factor. Recall that the total coherent scattering intensity is a combination of internal scattering and scattering due to other dendrimers. Assuming the correlation of interdendrimer distances and the correlation of intradendrimer monomer distances is completely separate, i.e., the positions of individual monomers of one dendrimer do not correlate with the positions of monomers of any other dendrimer, the total coherent scattering intensity can be factorized as the product of the form factor and the structure factor ( $I(q) \cong F(q)S(q)$ ). Thus with this decoupling or factorization approximation the structure factor can be calculated if the form factor is known. At least in infinitely diluted solution  $S_0(q) = 1$  and  $F_0(q) = I_0(q)$ . One must then assume this form factor is constant over all concentrations for the apparent structure factor to be calculated:  $S_{\text{app}}(q) = I(q)/F_0(q)$ .

It is clear that with increasing concentration, dendrimers come in close contact and the validity of both the decoupling approximation and the constant form factor assumption weakens. By comparing the actual structure factor with the apparent structure factor(s), the vulnerability of the experimental procedure for increased concentrations is examined. The results are shown in Figure 5.8. For comparison the actual structure factors from Figure 5.7 are repeated. That comparison does not appear favorable for the indirect calculations. Only the lowest concentrations of 6 % are reproduced with minimal disparity. At 23 % the  $S_{\text{app}}(q)$ 's are still quite similar, but the divergence becomes progressively larger. At 43 % the peaks become subdued. The same is true for 64 %, but now the required asymptotic value of 1 is not reached anymore. At 83 % the expected peak is only visible for  $G_5$ , and at 100 % the peaks are practically nonexistent. Utilizing the actual form factors changes the apparent structure factors only slightly—which is expected as they do not differ by much (Figure 5.5)—but not for the better either considering the peak values. The very assumption that  $I(q)$  can be decoupled into factors  $S(q)$  and  $F(q)$  is what fails; the monomers of separate dendrimers are correlated even at fairly low concentrations. The error in the assumption that  $F(q)$  remains  $F_0(q)$  is of lesser importance.

These results compare well to Monte Carlo simulations of archetypical  $G_4$  dendrimers where a dilute state and the overlap concentration state were simulated.<sup>[11]</sup> Especially the 43 % state is surprisingly similar to their overlap concentration simulation. That in our simulations the decoupling approximation deteriorates well before the overlap concentration is reached may be because the explicit solvent molecules actively conduct monomer movement thereby increasing their correlation.

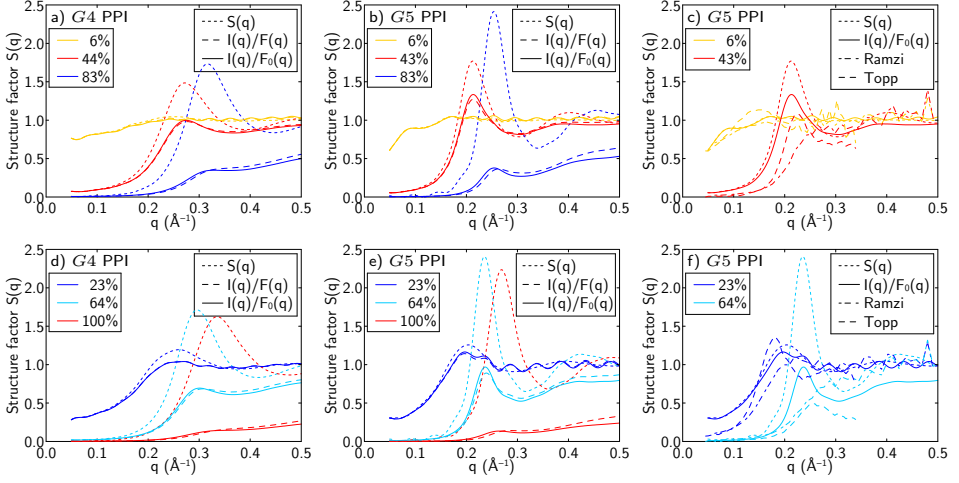


**Figure 5.8:** The differently calculated structure factors of generations 4 (a, d) and 5 (b, e) in multiple concentrations. The dotted lines are the actual  $S(q)$  values directly calculated from the simulations as in Figure 5.7. The dashed lines are the apparent structure factors calculated by dividing the coherent scattering by the current form factor, while the solid lines are the apparent structure factors ( $S_{\text{app}}(q)$ ) calculated with the form factor of the diluted dendrimers as is customary in experiments (here 0.1 %). (c, f) The results of such experiments by Ramzi et al. <sup>[14]</sup> and Topp et al. <sup>[15]</sup> for similar concentrations of G5 PPI.

### 5.3.3 Intermolecular spacing

Ever since the application of small angle scattering techniques to particles dispersed in solvent, researchers have noticed a small peak appearing in the scattering curve at higher concentrations (e.g., Figure 5.6). A common interpretation ties the position of this peak ( $q_{\text{max}}$ ) to the so-called average distance between neighboring particles ( $\bar{d}$ ) using a theoretical validation provided by Guinier and Fournet <sup>[22]</sup>—who simultaneously warned of the fallacy in defining neighbors in a substance without long-range order. By assuming the system consists of spherically symmetric particles that lie on a distorted face-centered cubic lattice (an fcc-paracrystal) they derived an average nearest neighbor distance function:

$$\bar{d} = \sqrt{\frac{3}{2}} \frac{2\pi}{q_{\text{max}}} \approx 1.225 \frac{2\pi}{q_{\text{max}}} \quad (5.5)$$

This relation has been used to infer the average dendrimer–dendrimer distance in many experimental sources including PPI–PPI. <sup>[14,15]</sup> We applied this technique to our simulations to see whether it yields distances comparable to those that were measured directly, namely the most common nearest neighbor distance given by the first peak in the radial distribution function  $g(r)$  (Figures 5.7a,c).

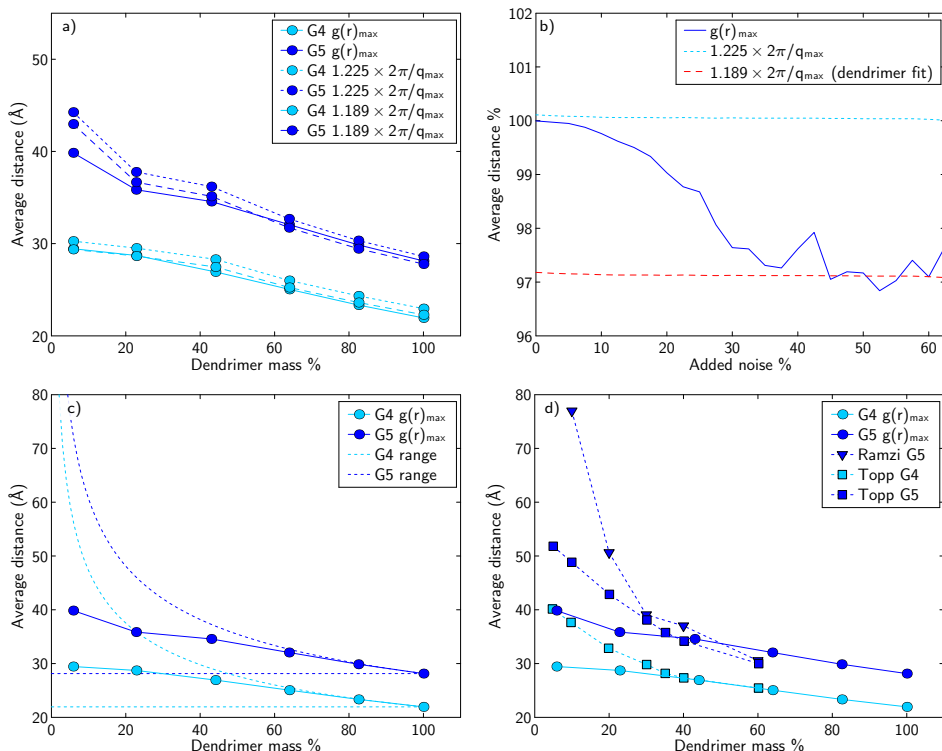


**Figure 5.9:** Average nearest neighbor distances between dendrimers as derived from the radial distribution function. (a) The distance compared to calculations from the structure factor. The common factor 1.225 overstates the distance, 1.189 provides a better fit. (b) The performance of both factors in average distance calculations of distorted fcc lattices. (c) Dendrimer–dendrimer distance with dashed ranges denoting complete aggregate (horizontal line) and maximal dispersion (exponential line,  $d(\varphi)$ ). (d) The distance compared with experimental results.<sup>[14,15]</sup>

First, using the peak positions of the scattering curve  $I(q)$  for  $q_{\max}$  in Equation 5.5, just like in the experiments,<sup>[14,15]</sup> decidedly overestimates the distance values. Fitting the clear peak positions (60%–100%) to the known distances results in a smaller factor, namely 1.122.

The difference between the fitted value and  $\sqrt[3]{2}$  may stem from the fact that the Guinier model<sup>[22]</sup> originally assumed hard spheres for which the interparticle distances correspond with the structure factor. By taking for  $q_{\max}$  the peak position of  $S(q)$  as calculated from the dendrimer centers in our simulations (Figure 5.7), the factor  $\sqrt[3]{2}$  indeed performs better (Figure 5.9a), although it still slightly overstates the average distance. Fitting these peak positions, which are visible for all concentrations (5%–100%), yields a factor of 1.189.

To test whether the slight overestimation of the average particle distance is specific to the dendrimer simulations or not, we performed the same radial distribution function and structure factor methods on a trial system of 108 000 particles. These were placed on an fcc lattice with increasing levels of noise added to simulate distortion of the lattice. The noise is a random displacement of each particle within a sphere whose diameter is a percentage of the fcc unit length. At 65 % noise and up, the radial distribution is too random to calculate a meaningful  $g(r)_{\max}$ . Figure 5.9b shows that with increasing noise  $g(r)_{\max}$  decreases (up to 3 %), while  $q_{\max}$  increases almost imperceptibly (up to 0.1 %). The theoretical factor of  $\sqrt{3/2}$  is very good for unperturbed fcc lattices, but should become smaller with increased randomness. Indeed the factor determined by fitting the *G4* and *G5* PPI simulations, 1.189, matches the graph at large noise.

Given that the apparent structure factor as derived in experiments is only an approximation of  $S(q)$ , we also considered  $q_{\max}$  from  $S_{\text{app}}(q)$  (Figure 5.8, *G4*: 20 %–80 %; *G5*: 40 %–100 %). This leads to a factor of 1.203 upon fitting. In conclusion, while the common factor of 1.22 seems an overestimate, especially in case  $q_{\max}$  is determined from  $I(q)$ , it provides a reasonable estimate for the average distance given experimental error in determining the peaks.

How dispersed are the dendrimers in the simulations? At the 100 % end of the concentration range the dendrimers are packed in a smeared fcc lattice, the densest possible packing for spherical particles. Should the dendrimers not dissolve in water, they would form an equally dense aggregate where the nearest neighboring distance does not change upon dilution. Should the dendrimers however be completely dispersed through solvation, conceptually an expanded fcc lattice remains a convenient representation for their positions, as an fcc lattice is merely the most efficient way of packing spheres with the largest possible nearest neighbor distances. The volume of an fcc box ( $V_{\text{fcc}}$ ) is defined as  $2\sqrt{2}d^3$  with  $d$  the nearest neighbor distance. It contains 4 spherical dendrimer volumes ( $V_{\text{D}}$ , fit at 100 %) with a volume fraction ( $\eta$  defined as  $\pi/\sqrt{18} \approx 0.74$ ). Then the maximal minimum distance between dendrimers as a function of the mass fraction  $\varphi$  is:

$$d(\varphi) = \sqrt[3]{\sqrt{2} \frac{1}{\varphi} \frac{1}{\eta} V_{\text{D}}} = \sqrt[3]{\frac{6 V_{\text{D}}}{\pi \varphi}} \quad (5.6)$$

In dilute solvent the dendrimers behave somewhere between complete aggregation and maximal dispersion (Figure 5.9c). From visual inspection, it is clear they do not aggregate, yet fleeting pair forming is observed. As for concentrations of 64 % and above the upper bound  $d(\varphi)$  converges to the dendrimer diameter, the dendrimers are forced into an aggregate, albeit a porous one at first.

Figure 5.9d shows the simulation results combined with results from the SANS



experiments on PPI. While the simulations go up to 100%, at the 64% end of the experiments the results are similar (especially for  $G4$ ), which is an indication that the subsequent trend is plausible. Lower than 30% however, the experimental distances rise faster than the simulation equivalents. The simulation dendrimers are often closer together than in the experiments, which would indicate that the dendrimers should be a little more repulsive. This is probably due to the fact that the charges in the dendrimer are made implicit in the CG particles. Thus, while the splaying of dendrimer branches due to interparticle repulsion is correct, the long range repulsion between dendrimers is not made explicit. On the other hand, the most striking outlier (experimental measurement of  $76.7 \text{ \AA}$  at 10%<sup>[14]</sup>) would, according to Equation 5.6, only be possible in solutions with concentrations up to 5%.

Recently 30 bead-spring trifunctional core dendrimers at 60 mass percent were studied.<sup>[13]</sup> The novelty being that the end-groups are charged, there are explicit counterions, and the electrostatic interactions are varied with the dielectric permittivity constant. Noteworthy is that apparently the third-generation dendrimers (91 beads) form structures in accordance with the body-centered cubic (bcc) lattice, while the fourth-generation dendrimers build fcc structures. For both our dendrimer sizes, from 20 mass percent and up, the emerging structures adhere to the smeared fcc pattern.

### 5.3.4 Dendrimer interpenetration

When the intermolecular spacing is low, the dendrimers come into close contact with each other. What happens at the interface? Do the dendrimers interpenetrate and become part of a larger entity or do they repel each other so each dendrimer retains its independence while being a bit compressed? And what method is most suitable to calculate such interpenetration?

Attempts have been made to examine dendrimer aggregates *in vitro*. Cryo-TEM of dilute  $G10$  poly(amido amine) (PAMAM) in water shows clustering but no apparent interpenetration in the clusters.<sup>[23]</sup> That is, instead of a single large blob, discrete dendrimers can be recognized. However, the fact that these large aggregates emerge in such dilute conditions leads the authors to speculate that this could be a side effect of the preparation of the specimen.

To calculate the level of interpenetration in the simulations of increased densities, we used a *convex hull method*. This method entails the creation of a convex hull for each dendrimer, i.e., the minimal polygon which encompasses all the positions of the dendrimer's particles. Then the number of particles of other dendrimers that fall within the hull are counted as penetrating the dendrimer. The penetration percentage is that amount divided by the number of original dendrimer particles,

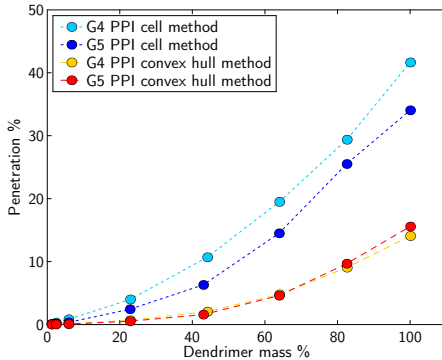


**Figure 5.10:** Dendrimer interpenetration in various concentrations, calculated using the *cell method* and the *convex hull method*. See the text for the different meaning of penetration percentage for these methods. The percentages calculated per saved time step are so alike that all standard deviation bars fall within the symbols drawn for the averages.

times 100. Note that the convex hull does not span the van der Waals radii of the particles, but rather the particles' centers.

The results are shown as the lower two lines of Figure 5.10. It is clear the interpenetration is practically the same for both generations. At low concentrations there is almost no interpenetration, the dendrimers are separate although they may collide. Even at 64% dendrimers, the penetration percentage is lower than 5%. In melt the penetration percentage reaches approximately 15%, that is on average 8.7 invading particles for G4 (62 particles) and 19.6 invading particles for G5 (126 particles).

Previously Zacharopoulos and Economou came to a different view for their PPI melt simulations,<sup>[3]</sup> namely that with larger dendrimers the amount of interpenetration decreases considerably. They calculated an interpenetration percentage with a *cell method* by dividing the simulation box into cubic cells. From the perspective of an individual dendrimer, it is said to be penetrated if a cell containing its particles also contains other dendrimers' particles. The penetration percentage of the dendrimer is then defined as the number of cells with a mixed presence divided by the number of occupied cells, times 100. Applying this methodology on our simulation data yields the upper lines shown in Figure 5.10, whereby the cell size is chosen such that at 100% the interpenetration values match with their results<sup>[3]</sup> (i.e., 6.2 Å gives 41.6% vs. the original 40.9% for G4 and 34.0% vs. 33.2% for G5, for a maximum of 6 particles per cell). These results would indeed imply G4 has a higher interpenetration than G5, even across all concentrations. However, note that the cell size greatly influences the result in such a setup. Even in a hypothetical case with no actual interpenetration, at high concentrations all cells at dendrimer interfaces contribute to the penetration score. Furthermore, the smaller the dendrimers considered, the larger the part of the simulation box that contains interfaces. This effect is the root cause of the difference with our results.

Yet another method was applied on a melt of general bead-spring trifunctional

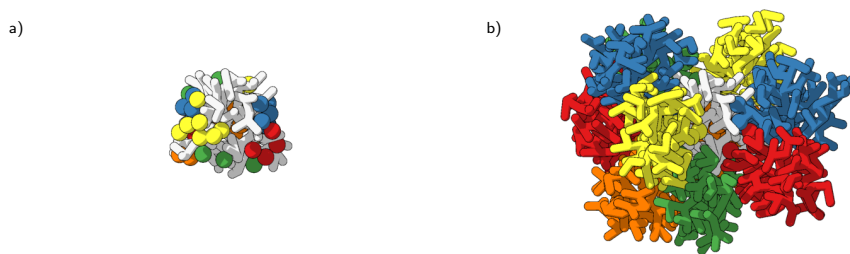


**Figure 5.11:** A view of the dendrimer with most overlap according to the convex hull method, at the end of the simulation (in white), including (a) just the hull penetrating particles and (b) the associated dendrimers.

core dendrimers under increasing temperatures.<sup>[24]</sup> There the interpenetration was calculated by looking at the average radial monomer density from the core bead, and where this graph overlaps with the average monomer density of other dendrimers this is counted as interpenetration (A comparable graph is Figure 5.12c). First, this assumes that dendrimers are perfectly spherical, and second, as the monomer density slowly approaches zero, more and more monomers are included that merely have the good fortune to be at the same distance from the core bead as one monomer once was. Still the interesting observation that interpenetration increases with decreasing temperature, and this dependence is greater for smaller dendrimers,<sup>[24]</sup> deserves further investigation.

Given that even in melt the number of hull penetrating particles is fairly low, what does this mean for the opposing views on dendrimer structure simplified as dense shell or dense core? Recall that in the *dense shell* model all branches are envisioned to extend toward the surface, leading to a vacant core region and crowding at the surface.<sup>[25]</sup> In the *dense core* model the branches occupy any possible region through bending and back-folding, thereby having a dense core and not-so dense shell.<sup>[26]</sup> Even the dendrimer with the most particles penetrating the hull at the end of the simulation (48 particles, 38.1 %) is still easily recognized as a separate dendrimer (Figure 5.11). In fact, although the dendrimer hull is highly permeated, one side is not penetrated at all. A high level of penetration does not mean a bunch of intertwined branches, nor overlapping splayed dendrimers with each other's branches in cavities near their cores. In this sense, the view that dendrimers in melt are dense impenetrable spherical cores with permeable shells may be a tad simplistic, it at least gives the right impression. It is also in agreement with our previous simulations where the radial monomer densities and spacer expansion profiles support the dense core view (Section 4.3.6).

### 5.3.5 Overlap concentration

A commonly used term in classifying the behavior of polymers in solution is the overlap concentration ( $C^*$ ). It is loosely defined as the concentration where the distance between macromolecules equals their size.<sup>[27]</sup> At concentrations below  $C^*$  the solution is dilute, whilst above  $C^*$  it becomes concentrated. In concentrated solutions the macromolecules either interpenetrate or deform to accommodate the high concentration. Because dendrimers are pretty dense compared to linear molecules, their overlap concentration is fairly high.

While excellent for formulating ideas, difficulties arise when actually calculating the overlap concentration, as the size of macromolecules is not clearly defined. We use the average convex hull volumes of the single dendrimer simulations to calculate appropriate diameters of unconstrained dendrimers:

$$D = 2 \sqrt[3]{\frac{V_{\text{hull}}}{\frac{4}{3}\pi}} \quad (5.7)$$

resulting in  $D_{G4} = 24.8 \text{ \AA}$  and  $D_{G5} = 33.2 \text{ \AA}$ .

By taking the average distance between dendrimers as  $g(r)_{\text{max}}$  as shown in Figure 5.9c and looking at where the diameter intersects, we obtain the overlap concentration. For  $G5$  it is at 55 %, for  $G4$  even at 68 %. From the fairly flat character of the distance graph, it is clear that slightly larger calculated sizes would lead to lower overlap concentrations. Nevertheless, such high overlap concentrations are not unheard of with dendrimers (e.g., 56.6 %<sup>[11]</sup>).

As all experimental graphs shown in Figure 5.9d are steeper, and their molecular sizes are calculated differently, the reported overlap concentrations are lower. Topp et al.<sup>[15]</sup> use the relationship  $R = \sqrt[5]{3}R_g$  for the dendrimer size ( $D_{G4} = 32.0 \text{ \AA}$  and  $D_{G5} = 40.3 \text{ \AA}$ ) so the intersection with the average distance graph puts  $C^*$  for both  $G4$  and  $G5$  at 25 %. Ramzi et al.<sup>[14]</sup> calculated  $C^*$  by dividing the theoretical bulk volume by the measured hydrodynamic volume, arriving at 36.5 % for  $G5$  PPI.

While the calculated overlap concentration of around 60 % is high compared to the SANS experiments, in the simulations (Figure 5.10) the penetration percentage does indeed shift between practically non-existent before  $C^*$  and increasing thereafter. Moreover, Figure 5.9c shows overlapping after  $C^*$  is unavoidable, even if the dendrimers were maximally dispersed.

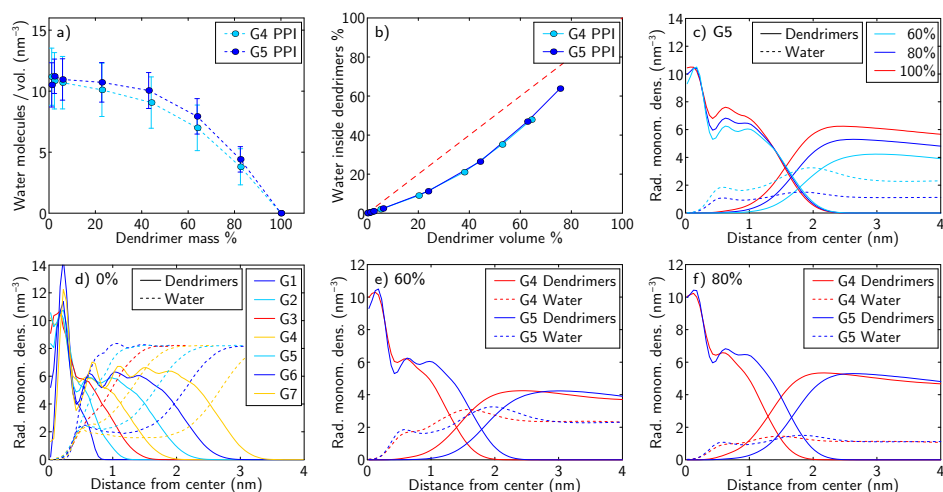


**Figure 5.12:** The level of water penetration into the dendrimers at the final state at varying concentrations. (a) The number of water molecules per dendrimer convex hull volume. (b) The percentage of water particles that fall inside the convex hulls plotted against the percentage of box volume occupied by dendrimers. The dotted diagonal indicates the theoretical percentage should the water particles be distributed uniformly over the simulation box. Even at 100% dendrimers, the total volume occupied by convex hulls amounts to 73.2% for *G4* and 84.8% for *G5* (see Appendix 5.5.1). (c) Radial monomer densities of *G5* PPI dendrimers and water (0.5 Å shell width). (d) The solitary dendrimers of *G1* to *G7* (Chapter 4); and *G4* and *G5* PPI dendrimers at a concentration of (e) 60% and (f) 80%.

### 5.3.6 Water penetration

Aside from what the fate of the dendrimer branches is with increasing dendrimer concentration, the destination of the diminishing solvent has its own hypotheses. In one view the solvent enters pockets within the dendrimers while the dendrimers expand to fill the space, which can be imagined like stacked sponges. In another view the solvent fills cavities between stacked dendrimers, comparable with submerged marbles.

The level of water penetration in the dendrimers can be calculated by counting the water particles inside the convex hull of each dendrimer. The water density, the number of water particles divided by the volume of each convex hull, is shown in Figure 5.12a as a function of the dendrimer concentration. For convenience, the water density is calculated to molecular values (i.e., 1 particle represents 4 water molecules). The dilute dendrimers at 2% contain on average 217.3 internal water molecules in *G5* and 88.1 molecules in *G4*. The most concentrated dendrimers, at 83%, contain 75.9 water molecules in *G5* and 27.7 molecules in *G4*. Even then

**Table 5.1:** *G4* and *G5* PPI: Radius of gyration and convex hull volume

<i>G4</i> PPI			<i>G5</i> PPI		
Mass %	$R_g \pm \text{std}$ (Å)	Volume $\pm$ std (nm <sup>3</sup> )	Mass %	$R_g \pm \text{std}$ (Å)	Volume $\pm$ std (nm <sup>3</sup> )
0.133	11.65 $\pm$ 0.44	7.87 $\pm$ 0.78	0.132	14.46 $\pm$ 0.38	19.12 $\pm$ 1.30
1.18	11.69 $\pm$ 0.44	7.93 $\pm$ 0.79	1.18	14.46 $\pm$ 0.38	19.08 $\pm$ 1.33
2.36	11.69 $\pm$ 0.44	7.93 $\pm$ 0.78	2.35	14.47 $\pm$ 0.38	19.11 $\pm$ 1.33
5.86	11.69 $\pm$ 0.44	7.93 $\pm$ 0.79	5.84	14.46 $\pm$ 0.38	19.08 $\pm$ 1.33
22.82	11.67 $\pm$ 0.44	7.88 $\pm$ 0.78	22.75	14.44 $\pm$ 0.38	18.99 $\pm$ 1.31
44.09	11.61 $\pm$ 0.44	7.76 $\pm$ 0.77	42.98	14.37 $\pm$ 0.37	18.76 $\pm$ 1.29
63.95	11.48 $\pm$ 0.43	7.52 $\pm$ 0.74	63.86	14.19 $\pm$ 0.36	18.10 $\pm$ 1.24
82.55	11.30 $\pm$ 0.43	7.19 $\pm$ 0.71	82.50	13.89 $\pm$ 0.35	17.08 $\pm$ 1.18
100.0	11.11 $\pm$ 0.43	6.85 $\pm$ 0.70	100.0	13.56 $\pm$ 0.35	16.04 $\pm$ 1.14

the number of water particles that appear in two convex hulls is quite low, for in *G5* it happens to only 2.4 % of the 27 714 water particles. With increasing concentration the convex hull volume average decreases from 7.9 to 6.8 nm<sup>3</sup> for *G4* dendrimers (Table 5.1). For *G5* dendrimers this decrease is from 19.1 to 16.0 nm<sup>3</sup>. By comparing the convex hull volumes for the 0.1 % dendrimer simulations with those in bulk follows that for dilute *G4* PPI 12.9 % of the dendrimer volume is from solvent and for *G5* that percentage is 16.1 %. Figure 5.12a suggests that the larger *G5* dendrimers absorb relatively more water than the *G4* dendrimers. However, when the total absorbed water percentage is plotted against the percentage of box volume occupied by dendrimers (as calculated with the convex hull method), both generations behave alike (Figure 5.12b). That is, more water particles remain outside the dendrimers than if they were uniformly distributed. The same can be seen in the radial monomer densities ( $g_m(r)$ , Equation 4.25) Figures 5.12c–f which show the distribution of monomers with respect to each dendrimer’s center of mass. In the dilute dendrimers of Chapter 4 in Figure 5.12d the internal as well as external water level is equal for all generations. Also at high concentrations, *G4* and *G5* are similar, see Figures 5.12e,f. Those figures and Figure 5.12c reveal an increased overlap between dendrimers at higher concentrations, while the density peak of the water on the interface gradually recedes to more uniform levels. These observations lead to the conclusion that, although water is present in both domains, of the views presented in the introductory paragraph the one with water filling cavities between dendrimers is more accurate than the one with water filling cavities inside the dendrimers.

## 5.4 Conclusion

We examined the behavior of generation 4 and 5 poly(propylene imine) dendrimers in water at concentrations ranging from dilute to dendrimer melt, by performing coarse-grained simulations to compare with SANS experiments.<sup>[14,15]</sup> The overlap concentration is said to be the point marking the transition between a dilute and

semidilute solution. Calculations located them at 55 % for  $G5$  and 68 % for  $G4$ . Indeed at 64 % and up the average nearest neighbor dendrimer–dendrimer distance follows the limit for purely repulsive particles; the dendrimers cannot move farther apart. However as the overlap concentration is not a tipping point, the various properties—average nearest neighbor distance, radius of gyration, water content, and interpenetration—steadily change with increasing concentrations.

From using experimental procedures with simulation calculations it follows that the interdendrimer distance calculated from  $q_{\max}$  with the traditional factor 1.22 is somewhat overestimated. On the same grounds the utilization of the decoupling approximation and constant form factor assumption to calculate apparent structure factors gives correct results only up to concentrations of  $\sim 20\%$ . This is well below the overlap concentration, not because of form factor changes, they are small, but because the monomer positions of separate dendrimers are already correlated.

With increasing dendrimer concentrations and increased competition, the dendrimers' volume diminishes. In the dilute situation there is quite some water inside the dendrimers. With increasing concentration the dendrimer volume decreases as water content decreases. Instead of being uniformly distributed, the solvent fills cavities between stacked dendrimers. Concurrently interpenetration of dendrimer branches does increase, but remains quite subdued. Only 15 % external particles enter each dendrimers' space. Each dendrimer remains a separate entity. Contrary to other publications, we found that when accounting for their size there is no difference between dendrimer generations  $G4$  and  $G5$  for both water penetration and dendrimer interpenetration. Together, this gives a clear molecular picture of PPI dendrimers from dilute solutions to melts in comparison with the available experimental data.

## 5.5 Appendix

### 5.5.1 Coarse-grained simulations

With a time step of 24 fs, each simulation lasts 24 ns of which the final 18 are considered production run and the first 6 equilibration time. We have confirmed that the simulations reach equilibrium in that time by checking the radius of gyration and dendrimer interpenetration versus time and using autocorrelation functions (see next Section). Every 0.06 ns a state is saved for further analysis.

The simulations are performed in an NPT ensemble, with constant pressure (1 bar) and constant temperature (298 K). The pressure and temperature are scaled using Berendsen's method, with temperature coupling constant 0.005 and pressure

**Table 5.2:** Volume and mass percentages for  $G4$  and  $G5$  PPI dendrimer simulations

$G4$					
Theoretical volume %	Dendrimers	Water particles	Mass %	Convex hull volume %	Box volume (nm <sup>3</sup> )
0.11	5	250 105	0.133	0.12	30 498.5
0.83	45	303 795	0.97	0.87	37 368.9
1.0	45	250 105	1.18	1.05	30 830.5
2.0	72	198 063	2.36	2.10	24 716.9
5.0	240	256 000	5.86	5.23	33 166.5
20.0	720	161 684	22.82	20.14	25 676.9
40.0	1430	120 421	44.09	38.01	26 612.5
60.0	1430	53 520	63.95	52.87	18 543.0
80.0	1430	20 070	82.55	64.33	14 558.2
100.0	1430	0	100.0	73.16	12 203.1
$G5$					
Theoretical volume %	Dendrimers	Water particles	Mass %	Convex hull volume %	Box volume (nm <sup>3</sup> )
0.11	2	204 078	0.132	0.14	24 885.8
1.0	18	204 078	1.18	1.24	25 154.3
2.0	48	269 356	2.35	2.49	33 607.2
5.0	100	217 592	5.84	6.17	28 176.0
20.0	245	112 232	22.75	23.84	17 786.2
40.0	968	173 272	42.98	44.21	37 431.2
60.0	968	73 905	63.86	62.74	25 435.4
80.0	968	27 714	82.50	75.55	19 936.6
100.0	968	0	100.0	84.83	16 687.5

coupling constant 0.000 05. The pressure and temperature are rescaled every 2.4 ps.

The number of dendrimers and water particles in the simulations and the resulting volume and mass percentages are shown in Table 5.2. Note that initially an estimated theoretical volume was used to generate the starting configurations by dendrimer to water ratios. To minimize confusion, because for some measurements the actual dendrimer volumes were determined, all graphs show the dendrimer mass fractions expressed as percentages. This is why there are differences between the concentrations used for  $G4$  and  $G5$ . Additionally, for comparison with the SANS experiments mass fractions are convenient. The data of Topp et al. [15] with methanol as solvent are provided in this manner. The data of Ramzi et al. [14] with water as solvent are given in volume fraction, but as they mention the dendrimer density is approximated to 1 g/cm<sup>3</sup>, here volume fraction equals mass fraction.

To calculate dendrimer volumes from the atom positions, the convex hull method is used, which utilizes the quickhull algorithm [28] via MATLAB. [29] In the penultimate column the percentage of box volume occupied by these convex hulls is shown. At concentrations approaching the bulk concentration this value deviates more from the theoretical values, which is counterintuitive as a box with only dendrimers, has 100 % of its volume filled with dendrimers. However, the convex



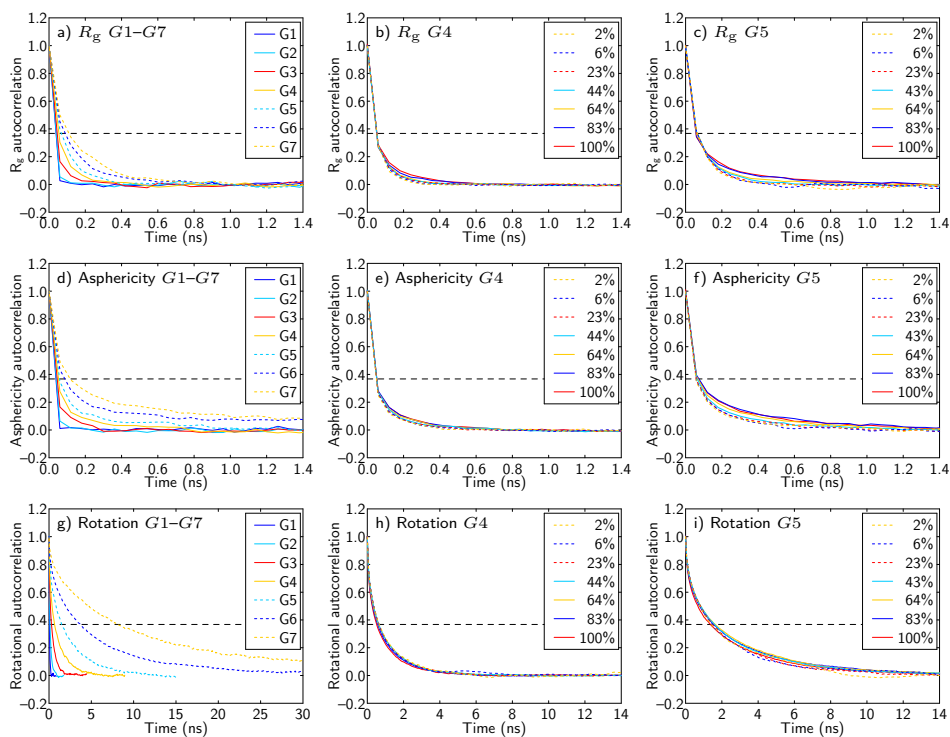


**Figure 5.13:** Autocorrelation functions for the PPI dendrimers. The first column contains the graphs for the solitary dendrimers (Chapter 4) of generations 1 through 7, the second column is for the  $G4$  PPI concentrations and the third for the  $G5$  concentrations. Row 1 (a, b, c) depicts the  $R_g$  autocorrelation, row 2 (d, e, f) the asphericity autocorrelation and row 3 (g, h, i) the rotational autocorrelation. The dashed line shows the equilibration value of  $1/e$ .

hull method uses the atom positions as vertices for its polygons, without taking the van der Waals radius into account. This is also why the discrepancy is larger in the case of  $G4$  than in the case of  $G5$ , as the latter has a lower surface to volume ratio.

## 5.5.2 Relaxation times

Relaxation times of  $R_g$ , asphericity and rotation are calculated from autocorrelation functions:

$$C(t) = \frac{\langle \delta X(t) \cdot \delta X(0) \rangle}{\langle \delta X^2 \rangle} \quad \text{with} \quad \delta X(t) = X(t) - \langle X \rangle \quad (5.8)$$

**Table 5.3:** Comparison between first and final periods of 100 %  $G5$  PPI

Time (ns)	$R_g \pm \text{std}$ (Å)	Asphericity $\pm \text{std}$	Interpenetration $\pm \text{std}$ (%)
6–24	$13.561 \pm 0.348$	$0.046 \pm 0.026$	$19.61 \pm 0.25$
222–240	$13.563 \pm 0.348$	$0.046 \pm 0.026$	$19.67 \pm 0.24$

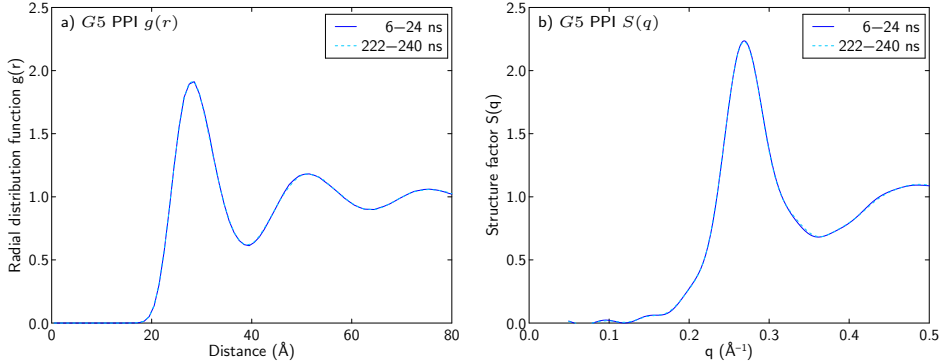


**Figure 5.14:** Interdendrimer distances of generations 5 in the melt. (a) Radial distribution function (bin size 1 Å) and (b) structure factor of 100 %  $G5$  PPI. For comparison the graphs of the first production run period are overlaid with the dotted graphs of the final period.

where  $X$  is any measurement.<sup>[30]</sup> The relaxation time  $\tau$  is defined as the time at which  $C(t)$  reaches  $\frac{1}{e}$ . Calculated are the radius of gyration autocorrelation with  $R_g$  (Equation 4.12), the asphericity autocorrelation with  $A$  (Equation 4.22) and the rotational autocorrelation with vectors from the center of mass to a number of end-groups (4: $G1$ , 8: $G2$ – $G5$ , 16: $G6$ , 32: $G7$ ).

In Figure 5.13 the autocorrelation functions calculated over the 6–24 ns production run are shown for the solitary dendrimers (Chapter 4) of generations 1 through 7 (a, d, g) and for the simulations of  $G4$  (b, e, h) and  $G5$  (c, f, i) PPI in various concentrations. Both  $R_g$  and  $A$  demonstrate that shape change is rapid with relaxation times smaller than 0.1 ns, even for large dendrimers. Rotational relaxation times are larger and also increase with dendrimer size, but are rather independent on the concentration ( $G4$ :  $\tau_{\text{rot}} \approx 0.6$  ns,  $G5$ :  $\tau_{\text{rot}} \approx 1.5$  ns). These relaxation times as well as those for  $R_g$  and asphericity fall well within the 6 ns equilibration time used.

To further confirm that the applied equilibration time suffices, we extended the most concentrated simulation (100 %  $G5$  PPI) to 240 ns. We compare properties calculated from the 6–24 ns period with properties calculated from the final 18 ns, corresponding to an equilibration time of 222 ns. In Table 5.3 the results are shown: the differences in average shape and convex hull interpenetration are minute. The graphs for the corresponding radial distribution functions and structure factors as

shown in Figure 5.14 are also quite identical.

## Bibliography

- [1] D. Astruc, E. Boisselier, and C. Ornelas, Dendrimers designed for functions: From physical, photophysical, and supramolecular properties to applications in sensing, catalysis, molecular electronics, photonics, and nanomedicine. *Chem. Rev.* 2010, *110*, 1857–1959.
- [2] E. Blasizza, M. Ferneglia, and S. Pricl, Dendrimers as functional materials. A molecular simulation study of poly(propylene) imine starburst molecules. *Mol. Simul.* 2000, *24*, 167–189.
- [3] N. Zacharopoulos and I.G. Economou, Morphology and organization of poly(propylene imine) dendrimers in the melt from molecular dynamics simulation. *Macromolecules* 2002, *35*, 1814–1821.
- [4] J.T. Bosko, B.D. Todd, and R.J. Sadus, Viscoelastic properties of dendrimers in the melt from nonequilibrium molecular dynamics. *J. Chem. Phys.* 2004, *121*, 12050–12059.
- [5] P. Carbone, F. Negri, and F. Müller-Plathe, A coarse-grained model for polyphenylene dendrimers: Switching and backfolding of planar three-fold core dendrimers. *Macromolecules* 2007, *40*, 7044–7055.
- [6] P. Carbone and F. Müller-Plathe, Molecular dynamics simulations of polyaminoamide (PAMAM) dendrimer aggregates: Molecular shape, hydrogen bonds and local dynamics. *Soft Matter* 2009, *5*, 2638–2647.
- [7] T. Terao and T. Nakayama, Molecular dynamics study of dendrimers: Structure and effective interaction. *Macromolecules* 2004, *37*, 4686–4694.
- [8] I.O. Götze, H.M. Harreis, and C.N. Likos, Tunable effective interactions between dendritic macromolecules. *J. Chem. Phys.* 2004, *120*, 7761–7771.
- [9] H. Lee and R.G. Larson, Molecular dynamics study of the structure and interparticle interactions of polyethylene glycol-conjugated PAMAM dendrimers. *J. Phys. Chem. B* 2009, *113*, 13202–13207.
- [10] W.d. Tian and Y.q. Ma, Coarse-grained molecular simulation of interacting dendrimers. *Soft Matter* 2011, *7*, 500–505.
- [11] I.O. Götze and C.N. Likos, Microscopic and coarse-grained correlation functions of concentrated dendrimer solutions. *J. Phys.: Condens. Matter* 2005, *17*, S1777–S1797.
- [12] T. Terao, Crystallization in concentrated dendrimer solutions. *Chem. Phys. Lett.* 2007, *446*, 350–353.
- [13] K. Karatasos, Self-organization in dendrimer polyelectrolytes. *Macromolecules* 2008, *41*, 1025–1033.
- [14] A. Ramzi, R. Scherrenberg, J. Brackman, J. Jacques, and K. Mortensen, Intermolecular interactions between dendrimer molecules in solution studied by small-angle neutron scattering. *Macromolecules* 1998, *31*, 1621–1626.
- [15] A. Topp, B.J. Bauer, T.J. Prosa, R. Scherrenberg, and E.J. Amis, Size change of dendrimers in concentrated solution. *Macromolecules* 1999, *32*, 8923–8931.
- [16] R. Scherrenberg, B. Coussens, P. van Vliet, G. Edouard, J. Brackman, E. de Brabander, and K. Mortensen, The molecular characteristics of poly(propyleneimine) dendrimers as studied with small-angle neutron scattering, viscosimetry, and molecular dynamics. *Macromolecules* 1998, *31*, 456–461.
- [17] I. Bodnár, A.S. Silva, R.W. Deitcher, N.E. Weisman, Y.H. Kim, and N.J. Wagner, Structure and rheology of hyperbranched and dendritic polymers. I. Modification and characterization of poly(propyleneimine) dendrimers with acetyl groups. *J. Polym. Sci., Part B: Polym. Phys.* 2000, *38*, 857–873.
- [18] S. Rosenfeldt, M. Ballauff, P. Lindner, and L. Harnau, Structure and interaction of flexible dendrimers in concentrated solution. *J. Chem. Phys.* 2009, *130*, 244901.

- [19] M. Kataoka and Y. Goto, X-ray solution scattering studies of protein folding. *Folding Des.* 1996, *1*, R107–R114.
- [20] C.D. Putnam, M. Hammel, G.L. Hura, and J.A. Tainer, X-ray solution scattering (SAXS) combined with crystallography and computation: Defining accurate macromolecular structures, conformations and assemblies in solution. *Q. Rev. Biophys.* 2007, *40*, 191–285.
- [21] J.P. Hansen and L. Verlet, Phase transitions of the Lennard-Jones system. *Phys. Rev.* 1969, *184*, 151–161.
- [22] A. Guinier and G. Fournet, *Small-angle scattering of X-rays*. John Wiley & Sons, New York, 1955.
- [23] C.L. Jackson, H.D. Chanzy, F.P. Booy, B.J. Drake, D.A. Tomalia, B.J. Bauer, and E.J. Amis, Visualization of dendrimer molecules by transmission electron microscopy (TEM): Staining methods and cryo-TEM of vitrified solutions. *Macromolecules* 1998, *31*, 6259–6265.
- [24] K. Karatasos, Static and dynamic behavior in model dendrimer melts: Toward the glass transition. *Macromolecules* 2005, *38*, 4472–4483.
- [25] P.G. de Gennes and H. Hervet, Statistics of “starburst” polymers. *J. Physique Lett.* 1983, *44*, 351–360.
- [26] R.L. Lescanec and M. Muthukumar, Configurational characteristics and scaling behavior of starburst molecules: A computational study. *Macromolecules* 1990, *23*, 2280–2288.
- [27] M. Daoud, H.E. Stanley, and D. Stauffer, Scaling, exponents, and fractal dimensions. In *Physical properties of polymers handbook*, ed. J.E. Mark, chap. 6, 83–89, Springer, New York, 2007.
- [28] C.B. Barber, D.P. Dobkin, and H. Huhdanpaa, The quickhull algorithm for convex hulls. *ACM Trans. Math. Softw.* 1996, *22*, 469–483.
- [29] MATLAB release 2014a. The MathWorks, Inc., Natick, 2014.
- [30] F. Fürstenberg, A.A. Gurtovenko, M. Dolgushev, and A. Blumen, Molecular dynamics simulations of hyperbranched PAMAM Vicsek fractals. *Macromol. Theory Simul.* 2015, *24*, 100–109.



## Chapter 6

# Multivalency in a dendritic host–guest system

---

**Abstract** Multivalency is an important instrument in the supramolecular chemistry toolkit for the creation of strong specific interactions. In this chapter we investigate the multivalency effect in a dendritic host–guest system using molecular dynamics simulations. Specifically, we consider urea–adamantyl-decorated poly(propylene imine) dendrimers that together with compatible mono-, bi-, and tetravalent ureido acetic acid guests can form dynamic patchy nanoparticles. First, we simulate the self-assembly of these particles into macromolecular nanostructures, showing guest-controlled reduction of dendrimer aggregation. Subsequently, we systematically study guest concentration-dependent multivalent binding. At low guest concentrations multivalency of the guests clearly increases relative binding as tethered headgroups bind more often than free guests’ headgroups. We find that despite an abundance of binding sites, most of the tethered headgroups bind in close proximity, irrespective of the spacer length; nevertheless, longer spacers do increase binding. At high guest concentrations the dendrimer becomes saturated with bound headgroups, independent of guest valency. However, in direct competition the tetravalent guests prevail over the monovalent ones. This demonstrates the benefit of multivalency at high as well as low concentrations.

---

---

This work has been published in:

A.F. Smeijers, Koen Pieterse, Peter A.J. Hilbers, and Albert J. Markvoort, Multivalency in a dendritic host–guest system. *Macromolecules* 2019, 52, 2778–2788.

It also contains the molecular dynamics simulation part of:

Thomas M. Hermans, Maarten A.C. Broeren, Nikos Gomopoulos, A.F. Smeijers, Brahim Mezari, Ellen N.M. van Leeuwen, Matthijn R.J. Vos, Pieter C.M.M. Magusin, Peter A.J. Hilbers, Marcel H.P. van Genderen, Nico A.J.M. Sommerdijk, George Fytas, and E.W. Meijer, Stepwise noncovalent synthesis leading to dendrimer-based assemblies in water. *Journal of the American Chemical Society* 2007, 129, 15 631–15 638.

## 6.1 Introduction

For many processes, nature relies on reversible non-covalent interactions. To ensure these interactions are sufficiently strong, it often employs the concept of multivalency, i.e., the principle for binding between entities whereby multiple identical ligands bind to multiple identical receptors.<sup>[1]</sup> Examples of the use of multivalency include the adhesion of viruses to host cells and the binding of antibodies to pathogens. Not only is it in evolutionary terms often easier to multiply a weak interaction to yield a strong collective one than to newly construct a stronger one, it also allows for enhanced specificity in the binding. The concept of multivalency is nowadays also applied successfully in supramolecular chemistry to self-assemble novel complexes.<sup>[2–4]</sup>

Of course, dendrimers enhanced with functional end-groups, thus having a definite number of interaction sites with specific properties (Figure 6.1a), are frequently studied in supramolecular chemistry. The versatility of the dendrimer components and attachments allows for a multitude of applications; e.g., dendrimers have been used in targeted drug delivery, contrast agents, gene therapy, enzyme mimics, biosensors, and supramolecular structures.<sup>[5–8]</sup> Many of these applications are examples of host–guest chemistry, whereby the dendrimer acts as a temporary host vehicle for non-covalently bound guest compounds.

An interesting example of supramolecular chemistry with dendrimers is provided by urea–adamantyl-decorated dendrimers, which aggregate in water due to the hydrophobic nature of their bulky adamantyl end-groups but can be solubilized by coating them with guests featuring ethylene oxide tails.<sup>[9,10]</sup> When the dendrimer is only partially covered with guests, it forms a complex with both hydrophilic and hydrophobic domains, which in turn facilitates aggregation into larger nanostructures<sup>[11]</sup> in a process of hierarchical self-assembly.<sup>[12]</sup> In contrast to regular anisotropic nanoparticles with static interaction domains—where the formed supramolecular nanostructure is predetermined by the number and shape of these domains<sup>[13]</sup>—with these dynamic patchy nanoparticles the non-covalent coating offers opportunities to tune the aggregation. That different guest concentrations change the coverage and thereby the size and branching of the nanostructures has been observed in cryogenic transmission electron microscopy (cryo-TEM) images.<sup>[10,11]</sup> Exerting control over the nanostructures formed, however, requires thorough understanding of how the nanoparticles are coated with the non-covalently bound guests. The coverage will not only depend on the guest concentration, but also on the host–guest interaction. As dendrimers provide a relatively controlled presentation of binding sites on a spherical macromolecule, a way to enhance the dendrimer–guest interaction may be by employing multivalent guests.

Here, we study the aggregation of dendritic host–guest complexes as well as the

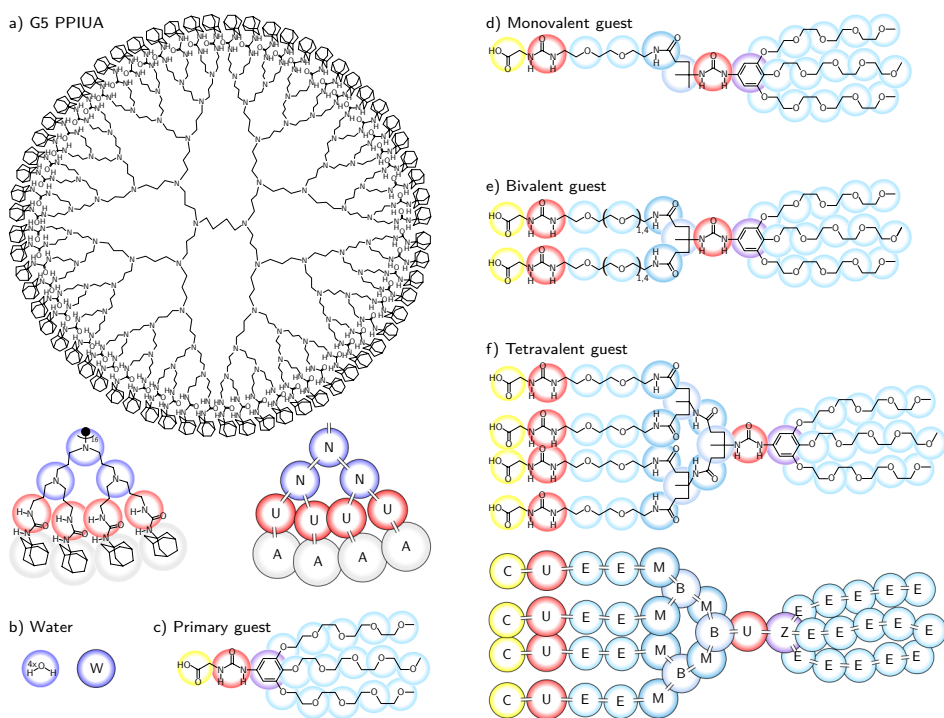


**Figure 6.1:** Two-dimensional representations of the molecules, showing the coarse-grained sites and the equivalent coarse-grained structures. (a) *G5* PPIUA, the fifth-generation urea–adamantyl-decorated (U–A) poly(propylene imine) dendrimer made from trimethylamines (N). (b) Water particle (W) representing four water molecules. (c) Primary ureido acetic acid guest. (d) Monovalent guest. (e) Bivalent guest. (f) Tetravalent guest. The multivalent guests may bind to the dendrimer with their head-groups containing an acetic acid (carboxylic acid, C) and urea moiety (U), each followed by a spacer of ethylene oxide (E). These are connected to a bifurcating part consisting of *N*-methylacetamide (M) and isobutane (B) which is linked to a hub made up of an urea and a benzene group (Z). The hub further holds three ethylene oxide tails. The ethylene oxide spacers are two moieties long, except for the elongated bivalent guests which contain three additional moieties per spacer.

host–guest interactions using molecular dynamics (MD) simulations for monovalent as well as multivalent guest compounds. Specifically, we consider the fifth-generation urea–adamantyl-terminated poly(propylene imine) dendrimer (PPIUA, *G5*: DAB–dendr–(urea–adamantyl)<sub>64</sub>, Figure 6.1a) in combination with mono-, bi-, and tetravalent ureido acetic acid guests (Figure 6.1d–f). For this purpose we expand our coarse-grained (CG) PPIUA dendrimer model (Chapter 4) with multivalent acetic acid guests.

Simulations of dendrimers with non-covalently bound molecules have been reported



before.<sup>[14–16]</sup> They typically come in two varieties. Either they concern a dendrimer encapsulating small guest molecules in the interior<sup>[17–23]</sup> where the dendrimer functions as a dendritic box,<sup>[24]</sup> or they simulate gene delivery with the dendrimer as a nanoparticle. The latter case involves the coiling of single-stranded DNA around a dendrimer<sup>[25,26]</sup> or the adhesion of dendrimers to double-stranded RNA (short interfering RNA, siRNA)<sup>[27–30]</sup> and DNA.<sup>[30–33]</sup> As the many negatively charged phosphate groups of RNA and DNA interact with the many positively charged amines of e.g., PAMAM and PPI dendrimers, this can be regarded as a multivalent complex where the dendrimers act as multivalent guests to the RNA or DNA host. In fact, simulations show that the generation of the dendrimers involved determines to a great extent the nature of the adhesion. Low generation dendrimers are flexible and dynamic, as seen in Chapter 4, so they can cover the helical siRNA reaching many phosphate groups at an entropic cost, while rigid large generation dendrimers lack the ability to adapt to the siRNA.<sup>[29]</sup> In contrast, we focus on how small multivalent guests bind to a stable multivalent dendrimer scaffold. Such simulations of dendrimers with many small multivalent guests are novel. Moreover, this dendrimer–guest system provides a nice platform to investigate the multivalency effect on a small spherical object containing an abundance of receptors.

In the next section we describe the CG models of PPIUA and primary and multivalent guests, as well as the simulation arrangements. This is followed by simulation results of macromolecular structure formation through self-assembly of patchy nanoparticles. Subsequently, we use the high temporal and spatial resolution of MD simulations to zoom in on the binding sites to uncover the ligand–receptor binding details. Next, we investigate the effect of multivalency by checking the concentration-dependent binding strength, the effective concentration of binding sites, and how the length of the spacer connecting the headgroups impacts binding. Finally, we show the benefit of multivalency through a competition between mono- and tetravalent guests.

## 6.2 Model

### 6.2.1 Atomistic assemblies

First, we demonstrate an application of fully atomistic MD simulations, namely as a way to determine how many dendrimers are present in spherical host–guest assemblies formed in water.<sup>[10]</sup> These aggregates were observed, using cryo-TEM imaging (Figure 6.2a) and dynamic light scattering analyses, to mostly have a hydrodynamic radius ( $R_H$ ) of  $4.1 \pm 0.45$  nm.<sup>[10]</sup> To this end we have constructed assemblies ranging from 1 to 6 dendrimers, coated them with 32 primary guests per dendrimer, and simulated them for 1 ns *in vacuo* (Figure 6.2b) (for simulation

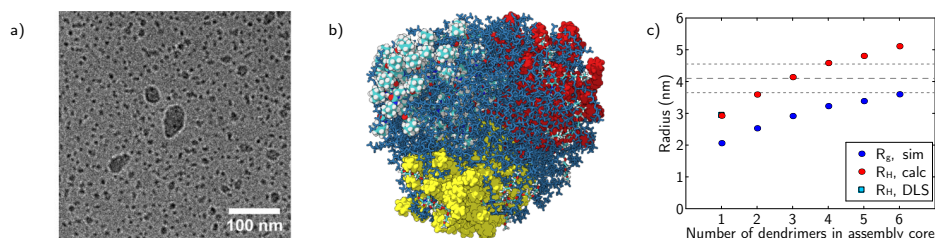


**Figure 6.2:** Determining the average radius of host–guest assemblies. (a) A cryo-TEM image with mostly complexes of  $\sim 4$  nm in radius from a guest concentration of  $1.23 \times 10^{-2}$  mol/L and guest-to-host ratio of 32, reproduced with permission from Hermans et al.,<sup>[10]</sup> © 2020 ACS. (b) Snapshot of an atomistic simulation of a complex of 3 dendrimers with 96 guests. (c) Relating radius of gyration to hydrodynamic radius.

details see Appendix 6.5.3). To obtain their hydrodynamic radii we applied an established conversion factor for PPI to the radius of gyration ( $R_g$ , Equation 4.12), namely  $R_H \approx 1.42R_g$ .<sup>[34]</sup> The factor correctly relates the single coated dendrimer simulation to dynamic light scattering measurements of dendrimer–guest complexes in chloroform. Combining these measurements, even though the solutions display a distribution of particle sizes, the supramolecular assemblies containing three dendrimers at the core were found to be the most abundant (Figure 6.2c).

These six pre-built assemblies in a vacuum, can be comfortably simulated with atomistic molecular dynamics. Yet, although chemically speaking association and dissociation of a guest to the dendrimer is fast—in chloroform equilibrium is reached within 2.4 ms,<sup>[10]</sup> the temporal resolution of  $^{13}\text{C}$  NMR—it is impractical to reproduce these events a statistically relevant number of times using fully atomistic MD. The size and time scales required are too large to follow dynamic interactions between host, guest, and solvent molecules in a reasonable amount of time. To simulate the dynamic host–guest complexation and complex aggregation in explicit solvent, we again use a coarse-graining scheme, wherein roughly four heavy atoms are united to form a single particle, reducing the computational cost considerably. Therefore we expanded the dendrimer model of Chapter 4 with primary, mono-, bi-, and tetravalent ureido acetic acid guest molecules, as illustrated in Figure 6.1.

## 6.2.2 Coarse-grained parameter fitting

The coarse-grained (CG) model for the urea–adamantyl-functionalized poly(propylene imine) (PPIUA) dendrimer was previously derived as detailed in Chapter 4. We followed the same procedures to derive a model for the multivalent ureido acetic acid guests. In summary, first CG sites were defined, such that small groups of atoms comprising a chemical moiety are represented by one CG particle (see Table 6.1 and Figure 6.1). During 20 fully atomistic simulations of a tetravalent

**Table 6.1:** Coarse-grained sites

Particle	Approximate chemical name	Formula	Mass (u)	Van der Waals radius (Å)
A	adamantyl	$C_{10}H_{15}$	135.2	3.33
B	isobutane	$C_4H_7$	55.1	2.64
C	acetic acid	$C_2H_3O_2$	59.0	2.41
E	dimethyl ether	$C_2H_4O$	44.1	2.29
M	N-methylacetamide	$C_2NH_3O + \frac{2}{3}CH_2$	65.2	2.67
N	trimethylamine	$C_3NH_6 + \frac{3}{2}CH_2$	77.2	2.66
U	urea	$CN_2H_2O + \frac{3}{2}CH_2$	79.1	2.71
W	water	$4H_2O$	72.1	2.59
Z	benzene	$C_6H_2$	74.1	2.75

guest in vacuum, the positions of these sites were tracked (for simulation details see Appendix 6.5.1). Resulting distributions of bond lengths and angles between connected sites were used as input in a Boltzmann inversion scheme to generate bond and angle potentials. As our CG model uses harmonic bond and angle potentials which lead to essentially Gaussian distributions, the atomistic distributions were first Gaussian fitted. The fits thus form the target distributions and Boltzmann inversions of these fits generate initial harmonic potentials. A CG simulation with these potentials provides new distributions and the error between these and target distributions determines a change in the potentials. This process is iterated until the error reaches a minimum.

The expansion or collapse of a polymer depends on the quality of the solvent. In the CG model these shapes are governed by the angles between particles. For a generally applicable model the influence of the medium should not be ingrained into the angle potentials but conducted via non-bonded interactions. Therefore intrinsic angle distributions were obtained from a separate atomistic simulation with the Lennard-Jones and electrostatic interactions switched off. As in reality, the solvent effect will stem from non-bonded interactions with the medium. The bond distributions were obtained from regular simulations, as in the CG model no van der Waals interactions are calculated between directly bound atoms. The obtained harmonic bond and angle parameters are listed in Table 6.2.

In the CG model non-bonded interactions between particles are described by Lennard-Jones potentials parameterized phenomenologically based on their physical-chemical properties: mass, density at a certain temperature, melting point, boiling point, and behavior in water. The mass of each particle type is the sum of the masses of the atoms they represent (Table 6.1). Van der Waals radii and characteristic Lennard-Jones energies ( $\epsilon$ ) were optimized through a series of molecular dynamics simulations. The van der Waals radius is initially calculated from the target density and known mass and  $\epsilon$  follows from the target melting temperature. Then the actual melting point is detected via heating while checking for phase transitions, and again via cooling. The observed crystallization and melting points

**Table 6.2:** Harmonic bond and angle parameters

Type	Bond length (Å)	Strength (kJ nm <sup>-2</sup> mol <sup>-1</sup> )	Type	Angle (°)	Strength (kJ rad <sup>-2</sup> mol <sup>-1</sup> )
A–U	4.60	4856	A–U–N	138.6	19.67
B–M	3.30	397	B–M–B	120.7	10.24
B–U	2.90	4856	B–M–E	95.1	6.05
C–U	3.70	2443	B–U–Z	166.0	19.67
E–E	3.61	4856	C–U–E	163.7	8.16
E–M	4.77	2061	C–U–Z	180.0	1.46
E–U	4.67	1164	E–Z–E	180.0	0.00
E–Z	3.19	4856	E–Z–U	180.0	3.70
N–N	4.90	1244	E–E–E	176.4	0.89
N–U	5.01	409	E–E–M	170.9	0.73
U–Z	3.85	4856	E–E–U	171.3	0.74
			E–E–Z	180.0	1.74
			M–B–M	124.7	0.81
			M–B–U	101.0	1.72
			N–N–N	97.0	0.66
			N–N–U	82.7	0.88
			U–N–U	75.1	1.13

**Table 6.3:** Lennard-Jones well depth in water ( $\epsilon_{ij}$  ( $\epsilon^*$ );  $1.0\epsilon^* = 1.967$  kJ/mol)

	A	B	C	E	M	N	U	W	Z
A	1.0	1.0	1.0	1.0	1.0	1.0	1.0	1.0	1.0
B		1.0	1.0	1.0	1.0	1.0	1.0	1.0	1.0
C			1.2	1.2	1.2	3.0	1.4	1.88	1.0
E				1.0	1.2	1.0	1.2	1.2	1.0
M					1.4	1.2	1.4	1.4	1.0
N						1.0	1.4	1.4	1.0
U							2.2	1.88	1.0
W								1.88	1.0
Z									1.0

differ due to the fast temperature changes, thus their average is then taken as the true melting point. If it differs from the target melting point the  $\epsilon$  is augmented for another simulated annealing round. The same strategy is applied for the boiling point, leading to a different  $\epsilon$ . The final  $\epsilon$  is obtained by interpolating both points to room temperature and rounding to a single decimal. An ultimate simulation is performed to measure the density and optimize the van der Waals radius. The obtained van der Waals radii are listed in Table 6.1 and the  $\epsilon$  on the diagonal of Table 6.3.

Interactions between different particle types are based on the physical–chemical properties of the chemical compounds and the behavior of the compounds in water. In water the dendrimers aggregate because of the hydrophobic adamantyl ends. Guests are water-soluble, when bound they confer that property to the dendrimer via their tails. To bind, their carboxylic acid ends must bind to the amines optionally supported by mutual urea bonds. As the number of particle types in the model increased from 4 to 9 by adding the multivalent guests, the

number of non-bonded interaction pairs increased from 10 to 45. To keep the model relatively simple, in addition to the previous unlike well depths ( $1.0\epsilon^*$ ,  $1.4\epsilon^*$ ,  $1.88\epsilon^*$ ) only a weak one ( $1.2\epsilon^*$ ) for lower strength interactions was added to fill out the interaction table. That is except for the C··N and E··W interactions as they control the host–guest and guest–water partitioning, see next section. The more generic interactions are first specified. The hydrophobic particles isobutane (B) and benzene (Z) are given the same treatment as adamantyl (A), namely their interactions with all other particle types use the same value as the butane–water hydrophobic interaction ( $1.0\epsilon^* = 1.967\text{ kJ/mol}$ ) in the preceding lipid model (Chapter 2). For the water-soluble urea (U) and carboxylic acid (C) moieties the well depth for interaction with water (W) is set to the same value as for water–water ( $1.88\epsilon^*$ ). For the interaction of the slightly less water-soluble trimethylamine (N) and N-methylacetamide (M) with water, as well as their interaction with urea, an intermediate value ( $1.4\epsilon^*$ ) is taken. That is also the value of C··U. The interaction of dimethyl ether (E) with carboxylic acid, N-methylacetamide and urea has been set at a modest  $1.2\epsilon^*$ . Idem for N-methylacetamide with carboxylic acid and trimethylamine. To discourage the ethylene oxide tails from bonding with the amine base of the dendrimer, the E··N interaction has also been set to  $1.0\epsilon^*$ . The chosen values are shown as the off diagonal values in Table 6.3. Finally, the collision diameters between unlike particle types are obtained using the Lorentz rule ( $\sigma_{ij} = \frac{1}{2}(\sigma_i + \sigma_j)$ ).

### 6.2.3 Guest parameter fine-tuning

The percentage of primary guests bound to dendrimers at a  $4.92 \times 10^{-2}$  mol/L guest concentration and a guest-to-host ratio of 64 has been estimated to be 53%.<sup>[11]</sup> This was derived from the results of  $^1\text{H-DOSY}$  NMR measurements which yielded the diffusion coefficients of all primary guests ( $D_{\text{g,obs}} = 1.63 \times 10^{-10} \text{ m}^2/\text{s}$ ), only bound guests (approximated by the dendrimers themselves,  $D_{\text{g,dendrimer}} = 0.79 \times 10^{-10} \text{ m}^2/\text{s}$ ) and only unbound guests (approximated by diluted guests without dendrimers,  $D_{\text{g,mono}} = 2.64 \times 10^{-10} \text{ m}^2/\text{s}$ ). Thus the observed guest diffusion coefficient was 53% down from the upper value of free guests to the lower value of dendrimers, which leads to the estimation by assuming a linear relation between diffusion coefficient and fraction bound ( $f_b$ )<sup>1</sup>:

$$f_b = \frac{D_{\text{g,unbound}} - D_{\text{g,obs}}}{D_{\text{g,unbound}} - D_{\text{g,bound}}} \approx \frac{D_{\text{g,mono}} - D_{\text{g,obs}}}{D_{\text{g,mono}} - D_{\text{g,dendrimer}}} = \frac{(2.64 - 1.63) \times 10^{-10} \text{ m}^2/\text{s}}{(2.64 - 0.79) \times 10^{-10} \text{ m}^2/\text{s}} = 0.55 \quad (6.1)$$

The guests in the simulation should exhibit the same equilibrium as in the experiments: roughly half of guests move with the dendrimer, the other half is free. On the one hand the guest is bound to the dendrimer via an interaction between

<sup>1</sup>Using these diffusion values gathered from the provided graph,<sup>[11]</sup>  $f_b$  amounts to 0.55.

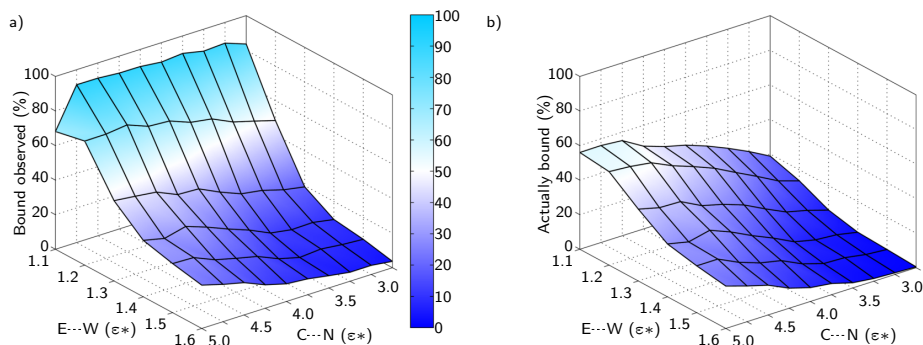


**Figure 6.3:** Guest parameter fine-tuning to match 53% observed binding. (a) Percentage of primary guests that are observed to be bound, i.e., they move with the dendrimer. (b) Percentage of actually bound guests.

the carboxylic acid (C) and tertiary amines (N). On the other hand the guest is pulled into the solvent via an interaction between its ethylene oxide (E) tails and water (W). Thus the tail–water interaction needs to be balanced with the headgroup–dendrimer interaction to attain the preferred equilibrium, given the guest and dendrimer concentrations from the experiment.

The parameter calibration series of simulations contain one dendrimer, 64 primary guests, and 16 564 water particles. The guests start off evenly distributed around the dendrimer. Each simulation begins with 45 ns of equilibration time followed by a 27 ns production run. The carboxylic acid–tertiary amine interaction (C..N) is varied between  $2.75 \epsilon^*$  and  $5 \epsilon^*$  with steps of  $0.25 \epsilon^*$  and the hydrophilic interaction with the tails (E..W) is varied between  $1.1 \epsilon^*$  and  $1.5 \epsilon^*$  with steps of  $0.1 \epsilon^*$ . The effect of these 60 parameter combinations on the fraction of guests bound to the host is shown in Figure 6.3. Here guests are categorized as bound to the dendrimer (C within 0.70 nm of N), held at the interface (any guest particle within 0.73 nm of any dendrimer particle), or free.

For the guests to be seen moving along with the dendrimer (Figure 6.3a), the tail–water interaction is the dominant parameter: a small change has a large effect. This is mainly because for every guest there are 15 tail particles interacting with water and only a single C particle interacting with the dendrimer. To have a large amount of actually bound guests (Figure 6.3b), it is clear that a high C..N value in conjunction with a low E..W value is needed. Otherwise many of the guests that move with the dendrimer are located at the interface. However, with a strong binding guest it is hard to obtain a good dynamic equilibrium: there is little exchange between the solvent and the dendrimer. This problem is exacerbated for the simulations with multivalent guests, as those guests are expected to bind stronger than these primary guests. Given the constraints of 50% observed binding

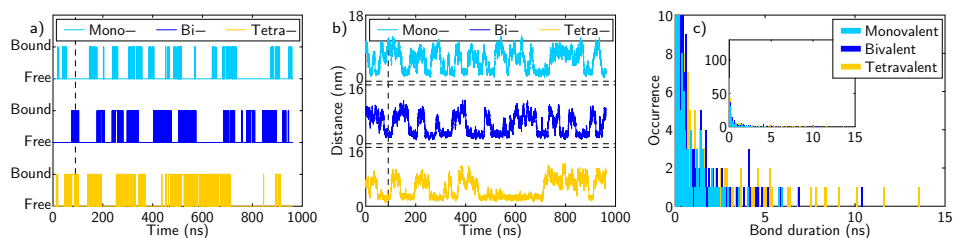


**Figure 6.4:** Binding events of representative mono-, bi- and tetravalent guests. Selected are guests with a binding percentage nearest to the average binding percentage of the simulations with 1, 2 and 4 guests. (a) Timelines of association and dissociation. The dotted line marks the equilibration time. (b) The distance between center of mass of the dendrimer and the guest. (c) Histogram of bond durations.

in conjunction with fast dynamics, the optimal guest parameters were found to be  $C\cdots N = 3.0\epsilon^*$  and  $E\cdots W = 1.2\epsilon^*$ .

These parameters lead to the dynamic binding of multivalent guests in a low guest concentration environment shown in Figure 6.4a. The dissociation and association events are grouped into blocks; before a dissociated guest diffuses away, it can rebind. Likewise, the binding state correlates strongly with the guest's average distance from the dendrimer (Figure 6.4b). The average bond lifetimes of these mono-, bi-, and tetravalent guests are 0.54 ns, 0.63 ns, and 0.99 ns, respectively. It is clear that these averages are skewed by the many rapid dissociation and association events that take place (Figure 6.4c). These guests do exhibit longer binding lifetimes. Here the longest are 5.9 ns, 10.4 ns, and 13.6 ns, respectively. Multivalency evidently helps increase binding lifetimes. The longest lifetimes are found in high concentration simulations with 21.0 ns, 36.5 ns, and 62.0 ns, respectively.

## 6.2.4 Coarse-grained simulation setup

Unless explicitly noted otherwise, all simulations are performed using this coarse-grained model. The initial configuration of the simulations consist of either a single centered dendrimer or 16 dendrimers spread over the simulation box, with guests evenly distributed in explicit solvent. For lower concentrations guests were randomly pruned. These simulations were performed using PumMa under constant pressure (1 bar) and temperature (298 K) using Berendsen pressure and temperature coupling. With time steps of 24 fs, every 0.06 ns a configuration was saved for further analysis. Further simulation details are given in Appendix 6.5.2.

In the simulations we consider a headgroup bound to the dendrimer if the carboxylic acid particle is within 0.70 nm of a tertiary amine, a distance at which no water

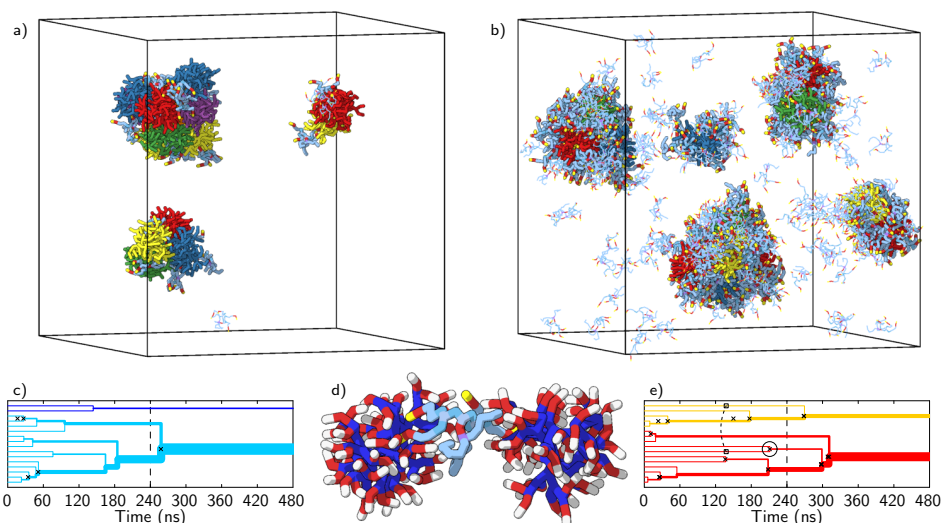


**Figure 6.5:** Aggregation of dendrimers and tetraivalent guests. (a, b) Snapshots of the complexes formed halfway into the simulation (after 240 ns) for the low and high guest concentrations, respectively. Each dendrimer is colored distinctly, guests not bound to a dendrimer are drawn thinner, and water is omitted for clarity. (c, e) Timelines of the dendrimer aggregation for the low and high guest concentration simulations, respectively. Each line represents an aggregate, its width proportional to the number of incorporated dendrimers. Upon fusion of two aggregates, their lines are likewise merged. Guests bridging aggregates leading to fusion are marked with a cross. (d) Details showing a bridge, colored as in Figure 6.1. It is the instance marked with a dashed circle in (e) where a link is formed 0.3 ns before the two dendrimers aggregate, resulting in the rightmost cluster in (b). Not all bridges precede fusion; the dashed curve linking two lines in (e) represents such a fleeting connection.

particle fits in between. Guests are deemed bound if any headgroup is bound. Being unbound thus does not necessarily mean the guest is freely floating in the solvent. It may still be located at the dendrimer–water interface.

## 6.3 Results and discussion

### 6.3.1 Macromolecular nanostructures

To investigate how the formation of macromolecular nanostructures through self-assembly of dynamic patchy nanoparticles is affected by the guest concentration, we simulate 16 dendrimers in a  $2.56 \times 10^4 \text{ nm}^3$  water box with a low guest concentration (24 tetraivalent guests,  $1.54 \times 10^{-3} \text{ mol/L}$ ) and with a high guest concentration (300 tetraivalent guests,  $1.96 \times 10^{-2} \text{ mol/L}$ ) for 480 ns. At the start the guests are



distributed in the solvent (details available in Appendix 6.5.2.1).

Figures 6.5a,b depict the aggregation states after 240 ns, i.e., halfway into the simulations, for the low and high guest concentrations, respectively. In the low concentration simulation the dendrimers form one large cluster (10 dendrimers) and two smaller ones. In the high concentration simulation five small clusters are present, although they look quite bulky because of the associated guests. To investigate the aggregation as a function of time, we created clustering timelines (Figures 6.5c,e). These show that in the initial 60 ns there is little difference between both regimes; dendrimers coming into contact aggregate swiftly and the guests have not yet coated them. The subsequent 140 ns, aggregation is rare for the high concentration simulation, while it continues apace in the low concentration simulation. Eventually aggregation slows down because it takes time for the larger clusters to come into contact. At low guest concentration aggregation proceeds at approximately the same rate as in a control simulation without guests, showing that the guests are unable to impede aggregation. While aggregation is slower for the high guest concentration simulation, the outcome after 480 ns is similar for both simulations: two spherical assemblies, one containing the majority of the dendrimers and the other containing the rest.

The hypothesis put forward with the cryo-TEM experiments<sup>[11]</sup> that different guest concentrations lead to different aggregate structures via altered hydrophobic patches—e.g., two hydrophobic patches per dendrimer make for a dendrimer string while more patches build a network—could not be verified with these simulations as the high guest concentration simulation ultimately resulted in similar globular clusters as in the low guest concentration simulation. Rather, these clusters evoke an alternative experimentally observed result, namely, the globular *trapped core* structures<sup>[10,11]</sup> that were formed at a primary guest-to-host ratio of 32 irrespective of the guest concentration. Because of their dynamic nature, the guests are so mobile that while they do hinder aggregation some of the time, at other moments they leave parts of the dendrimer exposed. Once dendrimers come into contact at these hydrophobic patches, the guests simply continue to move out of their way, further increasing the binding surface. As the guests do not separate previously aggregated dendrimers, eventually the clusters become spherical as the guests do not impose otherwise.

An interesting side effect of the tetravalent guests is their ability to bind to multiple dendrimers, effectively keeping otherwise separate dendrimer–guest complexes near (Figure 6.5d). Multiple times, such a bridge formation precedes actual aggregation, reminiscent of the way a splayed lipid bridges the watery divide between vesicles at the onset of their fusion (Section 2.3.1.2). Other times, the dendrimers separate despite the bridge, bringing to mind the kiss-and-say-goodbye mechanism of micelles in solution.<sup>[35]</sup> A similar bridging effect was exploited to create transient networks between dendrimers in chloroform by means of long linear chains with

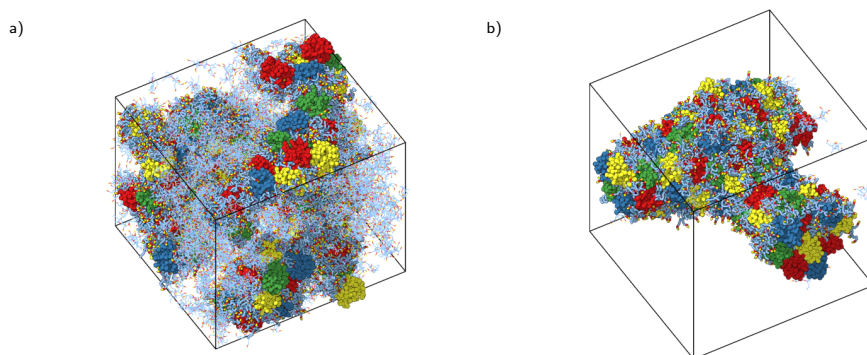


**Figure 6.6:** Self-assembly with a high dendrimer concentration (125 dendrimers). Both snapshots are taken after a 240 ns simulation. (a) A stable macromolecular network with fibers of single dendrimers (2500 tetraivalent guests). (b) A coalesced box-spanning network with massive strands. (625 tetraivalent guests).

headgroups at both ends.<sup>[36]</sup>

Note that even though the guest concentration  $1.96 \times 10^{-2}$  mol/L lies in the range tried in the cryo-TEM experiments<sup>[11]</sup> (i.e.,  $0.31 \times 10^{-2}$  to  $4.92 \times 10^{-2}$  mol/L), there the (primary) guest-to-host ratio remained at 64, whereas here it differs per simulation. This is due to a restriction of methodology: they keep doubling the water content, here the simulation box size is kept constant. Furthermore, in the experiment the complexes become more connected upon dilution, from linear structures to densely branched networks. This is impossible to reproduce in a simulation as a box with the correct number of host and guest particles corresponding to the overall concentration does not contain the mass to form such a structure. E.g.,  $2.49 \times 10^{-2}$  mol/L should produce a branched network but contains, given our box size, 384 guests and only 6 dendrimers. Therefore, two extra simulations with 125 dendrimers and 5 and 20 guests per dendrimer ( $3.68 \times 10^{-2}$  mol/L and  $16.60 \times 10^{-2}$  mol/L) were also performed. These do indeed produce box-spanning nanostructures. Namely with 2500 tetraivalent guests a stable macromolecular network is formed where the dendrimers form single strands (Figure 6.6a), while with 625 guests they aggregate into a solid network (Figure 6.6b), which may well turn into a single layer eventually. Again the guest concentration determines the shape of the dendrimer complex by controlling aggregation.

### 6.3.2 Guest binding details

Having demonstrated the solubility effect the bound guests have on the dendrimers, we now take a closer look at how they are bound using simulations with a single dendrimer in a  $3007 \text{ nm}^3$  water box and 8 guests lasting 960 ns or 96 guests lasting

480 ns (simulation details are available in Appendix 6.5.2.2).

Figure 6.7b shows a cross-section of a dendrimer with a bound monovalent guest. Originally, the dendrimers were conceived to have discrete receptors acting as *pincers*.<sup>[37–39]</sup> The ends bifurcate at a tertiary amine, which is flanked by two ureas each capped by an adamantyl moiety. The guest headgroup was envisioned to bind to the amine with its carboxylic acid end in an acid–base electrostatic interaction, its urea would form hydrogen bonds with both ureas of the pincer, and the benzene ring would be matched by the adamantyl groups for a hydrophobic interaction. In practice any of these interactions may be present, but not all in the same pincer, as the headgroup is too large to fit.<sup>[40]</sup> Examples of typical interactions are depicted in the schematic of Figure 6.7a. In accordance with the schematic, in the CG simulations binding is more intricate than the pincer ideal suggests. The important host–guest interactions are present, just not limited to groups of one bifurcated branch. Additionally, the ethylene oxide tails are shown to project into the surrounding water.

To compare the binding under different guest conditions, radial monomer density profiles ( $g_m(r)$ , Equation 4.25) were created that depict the monomer density as a function of the distance from the dendrimer’s center of mass. The difference between bound mono-, bi-, and tetravalent guests was studied in a simulation with 8 guests present (Figure 6.7c). The dendrimer is unaffected by the change in guest valency. As only bound guests are taken into account in the profiles, the differences for the headgroups (C, U) beyond the dendrimer’s periphery stem from additional unbound headgroups. All guests’ carboxylic acid ends manage to penetrate toward the center of the dendrimer, followed by the urea particle. The hub (U, Z) represents the part where the tails originate. It is located near the periphery, although for the tetravalent guests it is shifted away from the center because of its larger connecting part (B, M).

Subsequently, the effect of saturation of a dendrimer with monovalent guests was investigated by adding an excess of 96 guests (Figure 6.7d). This leads the dendrimer to become swollen, while the adamantyl (A) distribution shifts from the center toward the perimeter with less back-folding ends on account of the first three generational branches being straighter. Whenever possible, the headgroups are forced a little toward the center of the dendrimer while the tails (Z, E) stick out into the solution. Thus, to accommodate more bound guests, each guest loses some freedom of movement and becomes more stretched.

### 6.3.3 Multivalent guest concentrations

To investigate the degree of guest binding as a function of the concentration, we performed additional simulations of the single dendrimer with numbers of guests

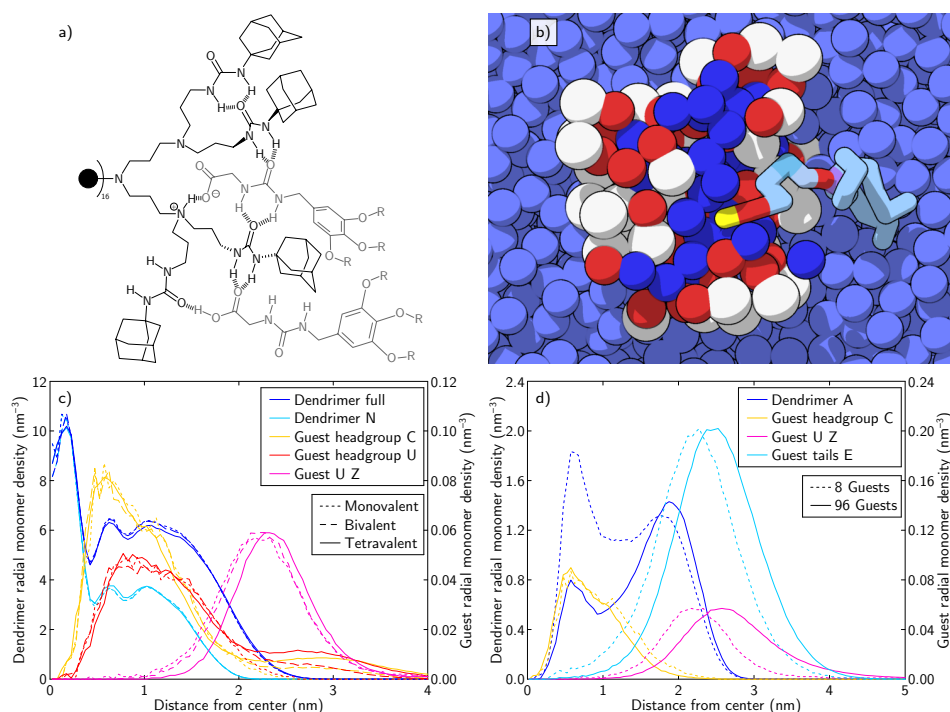


**Figure 6.7:** Binding of the guests to a dendrimer host. (a) Schematic of the predominant interaction modes of a PPIUA dendrimer with primary ureido acetic acid guests adapted from Chang et al.<sup>[40]</sup> (b) A cross-sectional view of a simulated dendrimer with bound monovalent guest, colored as in Figure 6.1. (c) Radial monomer density profiles of a dendrimer with 8 mono-, bi-, or tetraivalent guests. (d) Radial monomer density profiles of a dendrimer with 8 or 96 monovalent guests. In the density profiles only bound guests are considered. Guest curves are scaled to match the height of the curves from the 8 monovalent guests simulation to emphasize shape differences.

varying between 1 and 96, where the simulations up to 8 guests lasted for 960 ns and those with more than 8 guests 480 ns. The average percentage of guests bound in these simulations, which characterizes the guest's binding strength, is shown in Figure 6.8a.

With few guests present, there clearly is increased binding achieved by multivalency. As the inset in Figure 6.8a shows, at low guest concentrations the bivalent guest binds 1.7 times as much as a monovalent one, and the tetraivalent guest binds 3.3 times as much. Viewed another way, the two headgroups of the bivalent guest contribute 85 % of the binding strength of the monovalent headgroup each and each of the tetraivalent headgroups provides 82 %. However, the benefit of multivalency is highly concentration-dependent. The graph shows that with increasing guest

concentrations the difference in binding percentage diminishes. At 80 guests present ( $4.6 \times 10^{-2}$  mol/L), only 15 % is bound independent of their valency.

An alternative perspective is that by tying headgroups together their binding incidence is increased. A *tethering effect* increases headgroup binding as when one is bound the others are also near a binding site. Figure 6.8b shows that the number of headgroups bound as a function of the total number of headgroups present is rather independent of guest valency. Only at low guest numbers ( $< 32$  guests) more than 4 times as many tetravalent headgroups are bound than monovalent headgroups. The bivalent guests are worse off with a cutoff at fewer than 8 guests. Thus, from the perspective of a headgroup, when other headgroups are attached its relative binding performance improves only at low guest concentrations. At higher guest concentrations the competition for the binding sites by headgroups from free guests suffices to overcome the adjacency advantage of the tethered headgroups. In fact, surrounding the dendrimer, the concentration of tethered headgroups is indeed larger than the concentration of headgroups of free tetravalent guests in the simulations of up to 32 guests.

When a receptor changes binding affinity upon binding of a ligand, it is called *cooperative binding*. A well-known example is the positive cooperative binding of oxygen to hemoglobin. Upon binding of one oxygen molecule the three other binding sites become more accessible.<sup>[41]</sup> Though the dendrimer is not specifically designed to exhibit cooperative binding in this manner, we investigated its presence using the Hill equation<sup>[42]</sup>

$$\theta = \frac{1}{\left(\frac{G_{50}}{[G]}\right)^n + 1} \quad (6.2)$$

which describes the fraction of occupied binding sites ( $\theta$ ) as a function of the guest concentration ( $[G]$ ) where  $G_{50}$  is the guest concentration producing half occupation. The Hill coefficient ( $n$ ) varies with the kind of cooperativity, i.e., positively ( $n > 1$ ) or negatively cooperative ( $n < 1$ ). The tetravalent headgroup data are nicely fit with  $n = 1$  (Figure 6.8b), i.e., assuming completely independent binding, confirming the noncooperativity. The dendrimer's affinity for headgroups thus does not measurably change upon binding of headgroups.

Finally, the stacked area graphs in Figures 6.8c,d show the binding stoichiometry, i.e., the number of headgroups responsible for the binding of the guests. Most of the bound guests are only held by a single headgroup. In the case of the bivalent guests, roughly 72 % of the bound guests are bound by a single headgroup only. The tetravalent guests are more frequently bound by multiple headgroups. Yet the fraction bound with all four headgroups is almost negligible, and still approximately half are bound by a single one.

The figures all indicate that with increased guest concentration the returns for guest

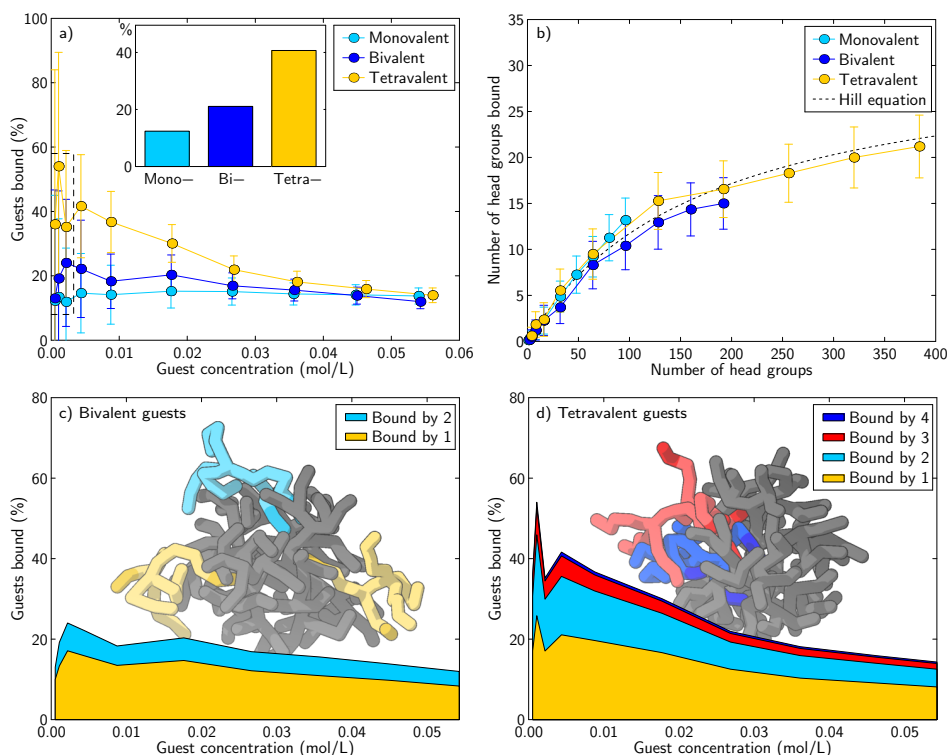


**Figure 6.8:** Guest concentration-dependent host-guest binding. (a) Percentage of guests bound as a function of the guest concentration. Error bars indicate the variability throughout the simulation by showing the standard deviation around the mean. The bar plot inset shows the weighted average of the three lowest guest concentrations. (b) Number of headgroups bound as a function of the number of headgroups present, including a Hill equation fit to the tetravalent data for noncooperative binding with 32 binding sites. (c, d) Reiteration of (a) with the curves split into stacked areas indicating the number of headgroups bound for the bivalent and tetravalent guests, respectively. Background illustrations are snapshots of a dendrimer with guests colored according to the number of headgroups bound; headgroups darkened for clarity.

binding diminish. This raises the question how many headgroups the dendrimer can accommodate before it is saturated. The fifth-generation PPIUA dendrimer has 32 pincers, but the actual binding sites are ill-defined. In a series of reference simulations with very strong binding guests ( $C \cdots N = 5 \epsilon^*$ ,  $E \cdots W = 1.3 \epsilon^*$ ) in systems with up to 32 headgroups all headgroups were bound all the time regardless of guest valency. Moreover, with 64 tetravalent guests on average 58 headgroups were bound, demonstrating that there are no steric reasons for having fewer than 32 headgroups bound.

Collectively, these results show that although the dendrimer–guest binding is non-cooperative, at low guest concentrations the guest binding does increase with guest valency and that although the dendrimer provides plenty of space for headgroups, most multivalent guests leave part of their headgroups unbound.

### 6.3.4 Effective concentration

In the previous section we observed that when bivalent guests are bound to the dendrimer, frequently one headgroup has not found a binding site. We now further examine how such a pair of headgroups connected by a flexible linker fares. In particular, we analyze the distances between the headgroups, differentiating cases where both headgroups are free, one is bound, or both are bound (Figure 6.9b). The end-to-end headgroup distributions from all bivalent guest simulations combined (2 401 851 samples) are shown in Figure 6.9a.

The unbound guests display a wide ranging end-to-end distribution, from headgroups touching to totally spread apart, with an average end-to-end distance of 1.7 nm. To further validate the free guest behavior, we compare the CG simulations with a separate 20 ns fully atomistic simulation of a solvated bivalent guest (simulation details in Appendix 6.5.4) and with the freely jointed ideal chain<sup>[43,44]</sup> model. According to this model, which considers a polymer chain sufficiently long to be characterized as a random walk of  $N$  segments of length  $l$ , the distribution of the end-to-end distances ( $r$ ) is given by

$$P(r) = 4 \pi r^2 \left( \frac{3}{2 \pi N l^2} \right)^{\frac{3}{2}} e^{-\frac{3 r^2}{2 N l^2}}, \quad (6.3)$$

with an average end-to-end distance of  $\sqrt{N l^2}$ . The atomistic simulation’s distribution consisting of 20 000 samples of the distance between carboxylic acid ends is obviously not as smooth. The observed mismatch with the ideal chain distribution stems from the guest’s chain being too short (34 bonds between ends) to warrant the model’s usage. Such mismatch was earlier shown for alkane chains of 43 bonds, while it vanished with 99 bonds.<sup>[45]</sup> Also, due to excluded volume effects, the CG ends cannot come nearer than 0.4 nm. Nevertheless, comparing the CG free guests with their atomistic counterpart shows their end-to-end distributions breadth to be quite similar. The agreement with the ideal chain model underlines that, despite the presence of other guests and the dendrimer, the headgroups of the free bivalent guest actually experience free movement in the solvent. The chains consisting of headgroups, spacers, and connectors are flexible and sufficiently water-soluble. Remarkably, when the guests are fully bound, their headgroups are usually quite close together. Even though the guests are flexible and can span sites 3 nm apart, the majority of the headgroups end up bound near each other. The first peak, for end-groups in direct contact, contains 21 % of the fully bound guests. Only 4 %

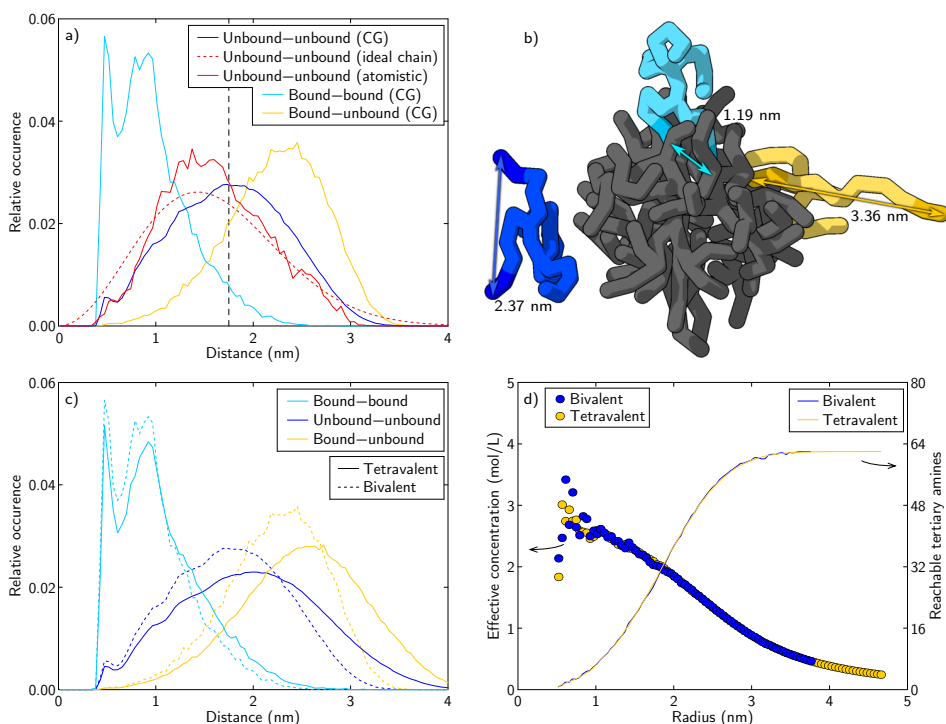


**Figure 6.9:** Connected headgroup pairs. (a) Normalized distributions of the CG headgroup–headgroup distances of the bivalent guests categorized by the number of headgroups bound. Also present are atomistic simulation and ideal chain model distributions of the free guest. The model is fitted to the average end-to-end distance (1.7 nm, dashed line) of the CG simulations. (b) A snapshot of a dendrimer with 3 bivalent guests illustrating the different binding states colored as in (a). Arrows highlight the headgroup–headgroup distances. (c) Normalized distributions of the end-to-end distances comparing the tetravalent to the bivalent guests. (d) The number of tertiary amines (right y-axis) found within a sphere centered at the anchoring headgroup of a semibound guest with the end-to-end distance as its radius, and the concentration ( $C_{\text{eff,max}}$ , left y-axis) of tertiary amines within said sphere.

are found further than 1.7 nm apart. Conversely, for the semibound guests the distribution is shifted to the right as free ends coming near a bound end have a tendency to become bound themselves. Finally, despite that the tetravalent guest effectively has six headgroup pairs, and that these are correlated, their end-to-end distributions shown in Figure 6.9c are remarkably similar to the bivalent ones. In fact, the bound–bound results are almost the same, only the tail is 10% wider and the peaks are diminished accordingly. The bound–unbound and unbound–unbound distributions are flattened in the same way, as their reach is 20% larger due to the extra bifurcating part of the molecule which elongates the connecting chains



in four of the six pairs.

When one headgroup of a multivalent guest is bound to a host with multiple binding sites, the binding chance of the unbound headgroups depends on the number of unoccupied binding sites within reach. This quantity, used in certain binding models, is known as the effective concentration:<sup>[46]</sup>

$$C_{\text{eff,max}} = \frac{n_{\text{H}}(L)}{N_{\text{A}}V(L)} \quad (6.4)$$

with the number of accessible host sites ( $n_{\text{H}}$ ) found in the volume ( $V$ ) that can be probed by a headgroup tethered with a linker of length  $L$ , and  $N_{\text{A}}$  is Avogadro's number. The 'max' subscript denotes occupied host sites are also deemed available.

In the simulations, we can directly derive the instantaneous effective concentration by observing the distance between bound and unbound ends and counting the number of host sites that lie within the sphere originating at the bound end with that distance as its radius. Then  $C_{\text{eff,max}}$  is the concentration of tertiary amines within the volume enclosed by that sphere. From Figure 6.9d it is clear that as the bivalent guest's total chain length is larger than 3 nm, when one end is bound, in principle the whole dendrimer is within reach of the free end. Thus, while the tetravalent guest has a 20 % larger reach it attains the same number of reachable sites and the  $C_{\text{eff,max}}$  is similar, except at small distances where irregularities are magnified. Precisely because there the concentration of possible binding sites is large, few data points are available for semibound distances that small. Our calculated  $C_{\text{eff,max}}$  is high in comparison with literature values of other systems (e.g., 0.8 mol/L<sup>[46]</sup>). This is mainly due to the flexible and open nature of the receptor (Figure 6.7): it is not just a surface layer of binding sites, instead there is a large assembly of binding sites in the dendrimer interior that are all accessible. Additionally, the accessibility of the binding sites is overestimated as it is unlikely that sites on the far side of the dendrimer are actually preferred over nearby sites.

### 6.3.5 Alternative spacer length

To investigate the effect of the headgroup–headgroup chain length on the binding of the multivalent guests, elongated bivalent guests were created with five instead of two ethylene oxide spacer moieties (Figure 6.1e). The molecule's total chain length was thus increased from 4.0 to 6.2 nm. This elongated guest was simulated at various concentrations together with a single dendrimer, following the same procedure as the regular bivalent guest simulations of Section 6.3.3 (simulation details in Appendix 6.5.2.2).

As shown in Figure 6.10a, the elongated spacers increase the binding by fifty

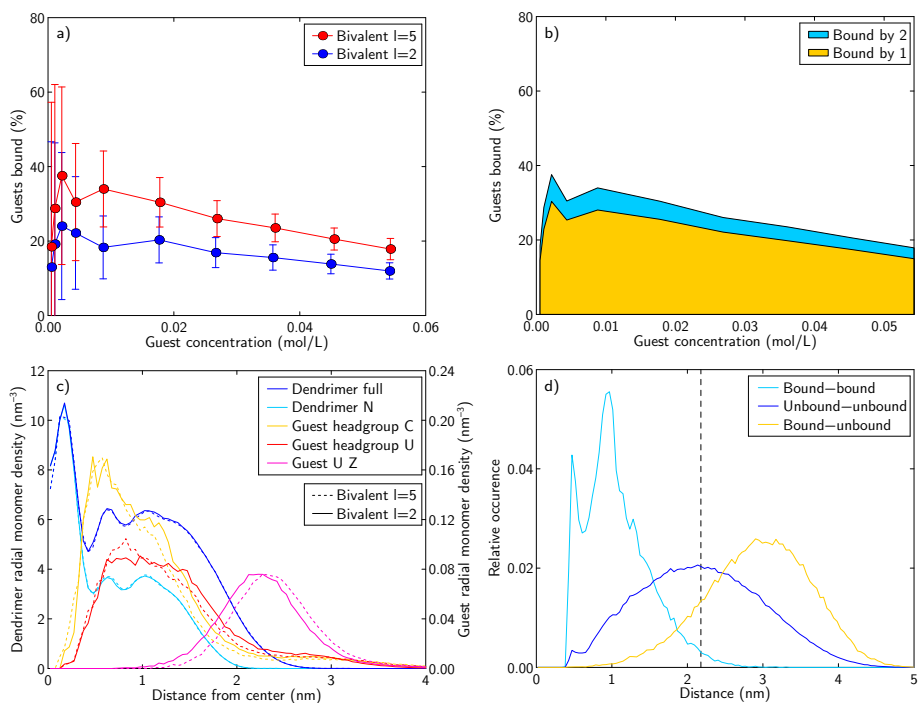


**Figure 6.10:** Elongated bivalent guests. (a) Percentage of elongated ( $l = 5$ ) and regular ( $l = 2$ ) bivalent guests bound as a function of the guest concentration. (b) Percentage bound shown in a stacked area graph. (c) Radial monomer density profiles of a dendrimer with 8 elongated and regular bivalent guests. In the density profiles only bound guests are considered. Guest curves are scaled to match the height of the curves from the regular bivalent guest simulation to emphasize shape differences. (d) Normalized end-to-end distance distributions of the elongated bivalent guests categorized by the number of headgroups bound. The average free end-to-end distance (dashed line) is 2.1 nm.

percent. A first hypothesis for this enhanced binding is that because the chain is longer, each headgroup may find an optimal binding site without having to reckon with the headgroup at the other end. If the elongated guest is better in this regard, then one would expect that it has the higher percentage of doubly bound guests, because each headgroup is held longer. Comparing Figures 6.8c and 6.10b this proves not the case. Quite the contrary: whereas 28% of the regular bound guests was fully bound, this is true for only 17% of the bound elongated ones. In simulations with up to 16 guests, the absolute number of fully bound guests are approximately the same. At higher concentrations the regular guest is more fully bound. Examining the radial monomer densities ( $g_m(r)$ , Equation 4.25) of the 8 regular and elongated guests with a single dendrimer (Figure 6.10c) shows the elongated guest's headgroup particles (C, U) to be similarly distributed as in

Figure 6.7c, indicating no physical change in binding. As expected the rest of the molecule is situated further from the dendrimer center of mass.

An alternative hypothesis for increased binding is that because the end-to-end distance is longer, more of the dendrimer is within reach once the first headgroup is bound. While the premise is true, it does not lead to increased binding. As we have seen in the previous section, the longer tether also probes more of the environment, thus it rather lowers the effective concentration. Moreover the regular bivalent guest is already sufficiently long to theoretically span the whole dendrimer. All amines lie within 3 nm from a binding site (Figure 6.9d) while the bivalent guest can extend a bit further (Figure 6.9a). Besides, Figure 6.10d shows that despite the longer spacer, the bound headgroups still prefer to bind close together. Although in theory the most effective bivalent guest exactly fits two binding sites without a longer than necessary spacer and is rigid rather than flexible, as the excess chain only adds more unfavorable conformations and thus increases the entropic cost of association,<sup>[1]</sup> several experimental studies on multivalent binding involving functional guests connected by long flexible spacers<sup>[2,47,48]</sup> have also shown that in practice these entropic concerns are not insurmountable.

Ultimately, larger guests are simply more likely to encounter the dendrimer. Even though the headgroup concentration for both guest variants is the same, the guests consist of more than the parts that prefer to bind to the binding sites. The other parts do come into contact with the dendrimer and cause the guest to linger there through aspecific interactions because their solubility is not absolute. The extended spacers increase the average end-to-end distance between headgroups of the free guests from 1.7 to 2.1 nm (Figures 6.9a and 6.10d), increasing their chance to encounter the dendrimer and remain there. These results also confirm the picture Weber et al.<sup>[49]</sup> painted using a Markov chain Monte Carlo model of weak binding ligands attached with flexible spacers to a slow moving particle: The complex is strong because dissociated ligands can rebind before the particle diffuses away. The lingering effect is also visible in Figure 6.5b, where many unbound, line-drawn, tetravalent guests are free in solution but roughly equal as many are in the vicinity of the dendrimers. In conclusion, the spacer contributes more to the guest than just additional length.

### 6.3.6 Competition between guest types

The observed host–guest systems exhibit striking differences in binding strength at low guest concentrations ( $<0.01$  mol/L), but at high concentrations ( $>0.04$  mol/L) the percentage bound drops to 14% for all multivalent types (see Figure 6.8a). This should not suggest that there is no difference in binding strength between the guest types at these concentrations, but rather that the binding sites begin to fail to optimally accommodate the larger number of guests. To investigate

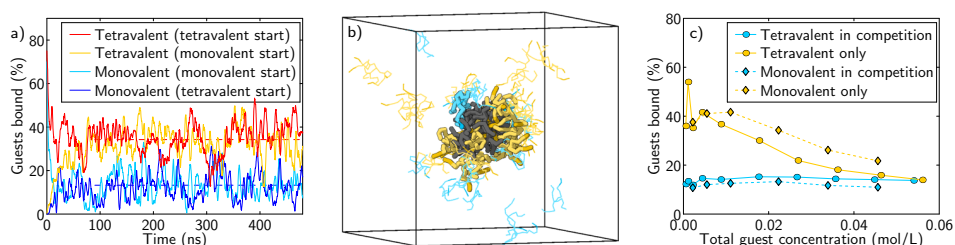


**Figure 6.11:** Competition between mono- and tetravalent guests binding to a dendrimer. (a) Percentage of monovalent and tetravalent guests bound to the dendrimer as a function of time for two simulations; one starting with 20 monovalent guests bound to the dendrimer and 20 tetravalent guests dispersed in the surrounding solvent, the other vice versa. Average bound percentages are shown as dashed lines (13.3% and 34.2%). For clarity the curves are smoothed with a 3 ns moving average window. (b) Snapshot from the simulation that started with 20 bound monovalent guests featuring a dendrimer with the average number of monovalent (3) and tetravalent (7) guests bound (479.2 ns). (c) Competition shown as percentage of guests bound as a function of the guest concentration, averaged from two starting simulations for each data point. The unmixed values are from Figure 6.8a.

whether tetravalent guests continue to bind better than monovalent guests at high concentrations, we let them compete for binding space on the dendrimer.

For this experiment, simulations were performed of a single dendrimer with equal numbers of mono- and tetravalent guests in explicit water. For each guest concentration two simulations were performed: one starting with the dendrimer covered in monovalent guests and the tetravalent guests randomly distributed through the solvent and another with the guest types swapped (for simulation details see Appendix 6.5.2.3). These disparate starting positions were chosen to test the adequacy of our equilibration time, for if these disparate simulations produce similar binding percentages, then any random starting distribution will as well.

In the simulations the guests switch between the bound and unbound states, establishing a new equilibrium with a new ratio of tetravalent and monovalent guests bound to the dendrimer. Figure 6.11a shows the percentages of bound monovalent and tetravalent guests for both simulations with 20 guests of each type as a function of time. For each guest type the average bound percentage converges to a single value within the standard equilibration time of 90 ns, demonstrating the latter is sufficiently long. On average 2.65 monovalent and 6.85 tetravalent guests are bound to the dendrimer. Tetravalent guests thus indeed also bind better at high concentration. Figure 6.11b provides an impression of such an average.

Comparing the previous unmixed simulations with simulations containing a range of competing guests (2, 5, 10, 20, 30, and 40 each; Figure 6.11c) shows there is

little difference at low guest numbers. As an abundance of binding sites is available, both guest types can work independently of each other, thus yielding fractions of guests bound similar to the unmixed simulations. However, when the availability of binding sites becomes an issue, the stronger binding tetravalent guest has a clear advantage over the monovalent guest and does bind relatively more.

The strong binding of multivalent guests is confirmed by competition experiments of trivalent vancomycin hosts and D-alanine-D-alanine guests in trivalent and monovalent variants.<sup>[50]</sup> The trivalent-trivalent host-guest complex is very stable with an estimated half-life of 200 days.<sup>[2]</sup> Only by adding over 3900 monovalent DADA guests for every trivalent one the equilibrium could be shifted so that just 60 % of the complex remained within 45 min.

## 6.4 Conclusion

To investigate multivalent dendritic host-guest interactions as well as the aggregation of their complexes into macromolecular nanostructures, we expanded our coarse-grained urea-adamantyl-terminated poly(propylene imine) dendrimer model to include multivalent ureido acetic acid guests. The host-guest interactions were calibrated to experimental values.

The first investigation involved the formation of macromolecular nanostructures through aggregation of the host-guest complexes. As the non-covalently bound guests lend their solubility to the otherwise hydrophobic dendrimers, these complexes serve as dynamic patchy nanoparticles. Hereby the guest concentration determines the coverage into hydrophilic and hydrophobic domains and in turn the self-assembly. The first simulation set, comprised of 16 fifth-generation dendrimers with tetravalent guests at a 1.5- or 19-fold guest-to-host ratio, corroborated that the presence of more guests slows down dendrimer self-assembly. However, the continual dissociation and association of guests ultimately resulted in spherical aggregates independent of the host-guest ratio. Moreover, these simulations showed that the multivalent guests not only solubilize dendrimer aggregates but may also keep separate aggregates close together by establishing a bridge between them. These simulation boxes did not contain the mass needed to form network structures. A second set of simulations having considerably more dendrimers, namely 125 dendrimers and a 5- or 20-fold guest-to-host ratio, did result in box-spanning branched networks. Here the guest concentration did determine the specifics of the nanostructure shape, low coverage resulted in a few massive branches and high coverage in many thin strands.

The other simulations concern a single dendrimer with a range of guest concentrations. The way guests' headgroups are physically bound to the dendrimer is the

same for the mono-, bi-, and tetravalent guests: the receptor does not conform to the pincer ideal; rather, the carboxylic acid–tertiary amine and urea–urea interactions readily occur with different branches of the dendrimer. When an excess of monovalent guests is present, the guests become stretched to accommodate additional guests.

At low guest concentrations, the multivalency effect is clear: tetravalent guests bind relatively more than bivalent ones, which in turn bind more than monovalent ones. Headgroups united into multivalent guests are bound more often, as when the first is bound, the others are also near binding sites. This adjacency advantage diminishes with higher guest concentrations: with over 32 guests in the simulation box, the concentration of unbound guests' headgroups surrounding the dendrimer exceeds the concentration of tethered headgroups. Indeed, only 28 % of the bivalent guests are fully bound and tetravalent guests rarely have all four headgroups bound, yet approximately half are bound by multiple headgroups. Despite the abundance of binding sites, these headgroups tend to bind in close proximity: only 4 % are bound further apart than the free guest's average end-to-end distance.

Using the semibound guests, we measured the effective concentration; i.e., the concentration of accessible host sites in the volume that can be probed by the tethered headgroups. The simulations reinforce that while these multivalent guests' chains are long enough to reach all the dendrimer's tertiary amines, for the highest  $C_{\text{eff,max}}$  the end-to-end distance should be small. Nevertheless, elongation of the chain by 55 % enhances guest binding, as it raises the chance for free guests to encounter the dendrimer and increases lingering of dissociated headgroups in the periphery, thus promoting rebinding.

At high guest concentrations the dendrimer becomes saturated with bound headgroups regardless of the guest valency, thus diminishing the effect of multivalency. Yet, when the monovalent and tetravalent guests are put in direct competition for binding sites, the multivalent guests displace the monovalent guests from the dendrimer, thus reaffirming the increased binding power provided by multivalency also at high concentration.

In the current model, for computational efficiency, electrostatic and van der Waals interactions were integrated into the Lennard-Jones potentials. Other coarse-graining strategies apply electrostatic interactions with a similar short-range cut-off<sup>[51]</sup> or even apply long-range electrostatics with particle mesh Ewald summation.<sup>[52]</sup> Given the importance of the acid–base interactions for host–guest binding it could be advantageous to treat the Coulombic interactions in more detail in future work.

This study illustrates how computer simulations aid in the design of functional multivalent host–guest systems. All together, the results show the enhancing effect

of multivalency on guest binding over a full concentration range. Although these coarse-grained molecular dynamics simulations focused on a specific dendrimer with compatible multivalent guests, we expect these findings to be generally applicable to other multivalent host-guest systems, dendritic or otherwise.

## 6.5 Appendix

### 6.5.1 Modeling: Tetravalent ureido acetic acid guest

An atomistic model of a tetravalent ureido acetic acid guest was created to provide a template for the coarse-grained model. Just like the in the dendrimer case (Chapter 4), the initial configuration was constructed, minimized and finally converted to PumMa input files using MOE,<sup>[53]</sup> X-PLOR 3.851,<sup>[54]</sup> psfgen<sup>[55]</sup> and in-house-developed software. Any missing parameters were estimated using chemically similar structures from CHARMM27 parameters. These files were then converted to PumMa input files. The partial atomic charges are shown in Figure 6.12.

To provide sufficient bond and angle distribution samples 20 simulations with different initial velocities were performed. Each production simulation lasted for 1 million time steps of 1 fs. The guest was simulated *in vacuo* at a temperature of (307 K). Every 1000 steps, the linear and angular momenta were set to zero. The production run was performed once with and once without non-bonded interactions.

### 6.5.2 Measurements: Coarse-grained simulation parameters

The coarse-grained simulations all follow the same procedure. First the simulation box is filled with the required number of dendrimers (1 or 16) in an extended configuration and a multitude of guests. At this point all molecules are evenly distributed over the box. Then randomly selected excess guests are converted to water so the correct number remains. After filling the empty space with water, the box is energy minimized for a number of steps to reduce steric overlap.

The simulations differ in total length, but otherwise the input parameters are the same. The time steps are 24 fs and every 0.06 ns a state is saved for further analysis. The simulations cover at least 480 ns of which the first 90 ns is equilibration and the rest is production run. The simulations are performed in an NPT ensemble, with constant pressure (1 bar) and constant temperature (298 K). The pressure and temperature are scaled using Berendsen's method, with temperature coupling constant 0.005 and pressure coupling constant 0.000 05. The pressure and temperature are rescaled every 2.4 ps.

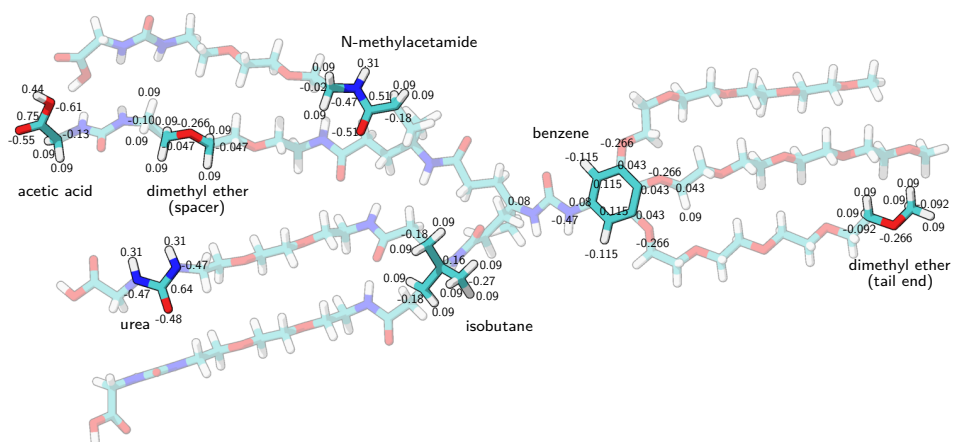


**Figure 6.12:** Tetraivalent guest with highlighted residues with partial atomic charges. Oxygen is red, nitrogen is blue, carbon is cyan and hydrogen is white. Overall the guest is neutral.

### 6.5.2.1 Macromolecular nanostructures

Initially the 16 dendrimers were placed at equal distance in a body-centered cubic formation. Energy minimization was done for 1000 steps. The total simulation time is 480 ns for the 16 dendrimer simulations and 240 ns for the 125 dendrimer simulations. Further details are listed in Table 6.4.

**Table 6.4:** Macromolecular nanostructures

Dendrimers	Guests	Water particles	Average volume (nm <sup>3</sup> )	Guest concentration (mol/L)
16	24	207 470	25 843.1	$0.15 \times 10^{-2}$
16	300	195 878	25 373.8	$1.96 \times 10^{-2}$
125	625	183 182	28 231.0	$3.68 \times 10^{-2}$
125	2500	104 432	25 018.9	$16.60 \times 10^{-2}$

### 6.5.2.2 Multivalent guest concentrations and alternative spacer length

These simulations start with a single dendrimer surrounded by 1, 2, 4, 8, 16, 32, 48, 64, 80, or 96 guests of one type ( $0.05 \times 10^{-2}$  to  $5.61 \times 10^{-2}$  mol/L). Energy minimization was done for 500 steps. As simulations of fewer guests require more time for sufficient data, they are twice as long. Namely, 1–8 guests: 960 ns and 16–96 guests: 480 ns. The number of water particles ranges from 20 372 in the 96 tetraivalent guest simulation to 24 751 in the 1 monovalent guest simulation. On average the system volume is 3007 nm<sup>3</sup>. The radial monomer density graphs for guest binding details (Section 6.3.2) are taken from the simulations with 8 or 96 guests.



### 6.5.2.3 Competition

In this series of simulations we observe how competition for binding space on a single dendrimer is resolved between monovalent and tetravalent guests. Guests are present in equal amounts, namely, 2, 5, 10, 20, 30, and 40 each. For every combination two simulations were performed. One starting with the dendrimer covered in monovalent guests and the tetravalent guests randomly placed in the solvent. Another with the guest types reversed. The bound starting complexes were lifted from the states with the most bound guests of the previous ‘Guest Concentrations’ simulations with 96 monovalent guests or 64 tetravalent guests, supplemented with unbound guests in contact with the dendrimer for the simulations with 30 and 40 guests. In particular, step 4 142 500 with 21 bound monovalent guests and step 10 340 000 with 20 bound tetravalent guests.

The complexes combined with the distributed free guests were first minimized for 500 steps. The simulation parameters are the same as for the guest concentration simulations, with the following simulation lengths: 960 ns for 4–20 guests and 480 ns for 40–80 guests.

To test the impact of the starting conditions, we performed additional simulations starting with randomized positions of 10, 40, and 80 guests. These give congruent results.

### 6.5.3 Measurements: Atomistic aggregate simulations

Using NAMD 2.6<sup>[56]</sup> (CHARMM27<sup>[57]</sup> parameters), molecular dynamics simulations were performed on aggregates of 1 to 6 dendrimers. The aggregates were complexed with 32 primary ureido acetic acid guests per dendrimer. The complexes were simulated for 1 ns using 1 fs time steps, and atom coordinates and velocities were sampled every 5 ps, of which the second half was used for radius calculations.

For these simulations we use the same dendrimer and one of the guest molecules (i.e., the primary guest) and setup as Chang et al.<sup>[40]</sup> used to investigate various single dendrimer host–guest complexes. Molecules were generated using SYBYL 6.9<sup>[58]</sup> and in-house-developed software, and then minimized and converted into appropriate input files for NAMD with the aid of psfgen.<sup>[56]</sup> Any missing parameters were estimated using chemically similar structures in the CHARMM27 parameters.

Initial structures of dendrimer clusters without guests were generated in short 75 ps pre-simulations from extended dendrimer structures uniformly distributed on the surface of a small sphere. Then, guest molecules were similarly distributed over



**Figure 6.13:** Partial atomic charges without (normal) and with polarization.

multiple layers, enclosing the dendrimer complex. Each layer was placed 2.25 nm further outward, and the number of guests per layer was scaled with the surface area of each layer. To aid the complexation process, the temperature was kept constant at 500 K to yield an internally mobile dendrimer structure and allow penetration of the dendrimer periphery by the guest molecules. To encourage a uniformly distributed occupation of the dendrimer cluster, the linear momentum of guest molecules was initially directed toward the cluster center. These dispersed structures quickly collapse to form a single more compact structure as favorable van der Waals interactions and hydrogen bonds are formed between different parts of the complex.

The dendrimers and their complexes were simulated *in vacuo* using a relative dielectric constant of 1. The van der Waals interactions were smoothly cut off at a distance of 12 Å using a switching function starting at a distance of 10 Å. The electrostatic interactions were also cut off at a distance of 12 Å, however, a shifting function was used in this case. A neighbor list, used for calculating the non-bonded interactions, was kept at 14 Å and updated every five steps. 1–2 and 1–3 bonded atoms were excluded from the non-bonded interaction calculations, while for 1–4 bonded atoms special van der Waals parameters were used (as stated in the CHARMM27 parameter file) in combination with full electrostatic interactions.

One key feature of the dendrimer-guest complexes is the ability of the ureido acetic acid guests to protonate the tertiary amines of the dendrimers in an aqueous environment. *In vacuo*, however, proton transfer only occurs between strong acids and strong bases. Since in our case proton transfer is not very likely,<sup>[59]</sup> we have chosen to model the acid-base reaction by means of a strong hydrogen bond (acid-base interaction) between the acidic proton of the guests and the nitrogen atom of the tertiary amines of the dendrimer.<sup>[40]</sup> To achieve such a strong hydrogen bond, the partial charges of atoms involved are increased, thus increasing their Coulombic attraction. As these molecules no longer have an overall net charge of zero, this speeds up the complexation process considerably. Nevertheless, changing the partial charges of the atoms (polarization) may lead to the undesirable side-effect that these atoms also have stronger Coulombic interactions with all other atoms. Therefore, the polarization is only switched on when the acidic proton of the carboxylic acid group is within 5 Å of the nitrogen atom of a tertiary amine. This is checked every 1 ps. Figure 6.13 shows the partial charges of the atoms involved in the acid-base interaction with and without polarization.

## 6.5.4 Measurements: Atomistic bivalent ureido acetic acid guest

For comparison with the CG bivalent guest, an atomistic bivalent guest was created and simulated in a water box. It was generated using a similar protocol as the tetravalent guest shown in Figure 6.12. The guest started in a loosely extended state, the central carbons of the carboxylic acid moieties 1.26 nm apart. It was solvated using VMD's modeling extension<sup>[60]</sup> with a solvation box of 5.8 nm × 5.8 nm × 5.8 nm, thus comprising 6711 TIP3 water molecules. The periodic simulation box was first equilibrated and then run using NAMD 2.6<sup>[56]</sup> with CHARMM27<sup>[57]</sup> parameters. The production run lasted 20 million time steps of 1 fs each for a total of 20 ns. The van der Waals interactions were smoothly cut off at a distance of 1.2 nm using a switching function starting at a distance of 0.8 nm. The electrostatic interactions were also cut off at a distance of 1.2 nm using a shifting function. A neighbor list, used for calculating the non-bonded interactions, was kept at 1.35 nm and updated every ten steps. 1–2 and 1–3 bonded atoms were excluded from the non-bonded interaction calculations, while for 1–4 bonded atoms special van der Waals parameters were used (as stated in the CHARMM27 parameter file). The Particle Mesh Ewald method was used to calculate the full electrostatic interactions. The simulation was performed in the NPT ensemble at a pressure of 1.0 bar and a temperature of 300 K. The pressure was controlled via the Berendsen pressure coupling method every 4 steps with a relaxation time of 500 ps. The temperature was rescaled to 300 K every 1000 steps.

Every 1000<sup>th</sup> of the 20 million steps was saved for further analysis. For the end-to-end distance calculations, the central carbon atom of the carboxylic acid moieties were selected (instead of the oxygens or the hydrogen at the tip) to coincide with the center of the coarse-grained carboxylic ends.

## Bibliography

- [1] M. Mammen, S.K. Choi, and G.M. Whitesides, Polyvalent interactions in biological systems: Implications for design and use of multivalent ligands and inhibitors. *Angew. Chem., Int. Ed.* 1998, *37*, 2754–2794.
- [2] A. Mulder, J. Huskens, and D.N. Reinhoudt, Multivalency in supramolecular chemistry and nanofabrication. *Org. Biomol. Chem.* 2004, *2*, 3409–3424.
- [3] J.D. Badjić, A. Nelson, S.J. Cantrill, W.B. Turnbull, and J.F. Stoddart, Multivalency and cooperativity in supramolecular chemistry. *Acc. Chem. Res.* 2005, *38*, 723–732.
- [4] C. Fasting, C.A. Schalley, M. Weber, O. Seitz, S. Hecht, B. Kocsch, J. Darnedde, C. Graf, E.W. Knapp, and R. Haag, Multivalency as a chemical organization and action principle. *Angew. Chem., Int. Ed.* 2012, *51*, 10472–10498.
- [5] O.A. Matthews, A.N. Shipway, and J.F. Stoddart, Dendrimers—branching out from curiosities into new technologies. *Prog. Polym. Sci.* 1998, *23*, 1–56.
- [6] A.W. Bosman, H.M. Janssen, and E.W. Meijer, About dendrimers: Structure, physical properties, and applications. *Chem. Rev.* 1999, *99*, 1665–1688.

- [7] R.K. Tekade, P.V. Kumar, and N.K. Jain, Dendrimers in oncology: An expanding horizon. *Chem. Rev.* 2009, *109*, 49–87.
- [8] D. Astruc, E. Boisselier, and C. Ornelas, Dendrimers designed for functions: From physical, photophysical, and supramolecular properties to applications in sensing, catalysis, molecular electronics, photonics, and nanomedicine. *Chem. Rev.* 2010, *110*, 1857–1959.
- [9] M.A.C. Broeren, J.G. Linhardt, H. Malda, B.F.M. de Waal, R.M. Versteegen, J.T. Meijer, D.W.P.M. Löwik, J.C.M. van Hest, M.H.P. van Genderen, and E.W. Meijer, Noncovalent synthesis of supramolecular dendritic architectures in water. *J. Polym. Sci., Part A: Polym. Chem.* 2005, *43*, 6431–6437.
- [10] T.M. Hermans, M.A.C. Broeren, N. Gomopoulos, A.F. Smeijers, B. Mezari, E.N.M. van Leeuwen, M.R.J. Vos, P.C.M.M. Magusin, P.A.J. Hilbers, M.H.P. van Genderen, N.A.J.M. Sommerdijk, G. Fytas, and E.W. Meijer, Stepwise noncovalent synthesis leading to dendrimer-based assemblies in water. *J. Am. Chem. Soc.* 2007, *129*, 15631–15638.
- [11] T.M. Hermans, M.A.C. Broeren, N. Gomopoulos, P. van der Schoot, M.H.P. van Genderen, N.A.J.M. Sommerdijk, G. Fytas, and E.W. Meijer, Self-assembly of soft nanoparticles with tunable patchiness. *Nat. Nanotechnol.* 2009, *4*, 721–726.
- [12] A. Wang, J. Huang, and Y. Yan, Hierarchical molecular self-assemblies: Construction and advantages. *Soft Matter* 2014, *10*, 3362–3373.
- [13] S.C. Glotzer and M.J. Solomon, Anisotropy of building blocks and their assembly into complex structures. *Nat. Mater.* 2007, *6*, 557–562.
- [14] W.d. Tian and Y.q. Ma, Theoretical and computational studies of dendrimers as delivery vectors. *Chem. Soc. Rev.* 2013, *42*, 705–727.
- [15] N. Martinho, H. Florindo, L. Silva, S. Brocchini, M. Zloh, and T. Barata, Molecular modeling to study dendrimers for biomedical applications. *Molecules* 2014, *19*, 20424–20467.
- [16] M. Ramezani, S.S.W. Leung, K.H. Delgado-Magnero, B.Y.M. Bashe, J. Thewalt, and D.P. Tieleman, Computational and experimental approaches for investigating nanoparticle-based drug delivery systems. *Biochim. Biophys. Acta, Biomembr.* 2016, *1858*, 1688–1709.
- [17] P. Miklis, T. Çağın, and W.A. Goddard III, Dynamics of Bengal Rose encapsulated in the Meijer dendrimer box. *J. Am. Chem. Soc.* 1997, *119*, 7458–7462.
- [18] G. Teobaldi and F. Zerbetto, Molecular dynamics of a dendrimer–dye guest–host system. *J. Am. Chem. Soc.* 2003, *125*, 7388–7393.
- [19] I. Tanis and K. Karatasos, Association of a weakly acidic anti-inflammatory drug (ibuprofen) with a poly(amidoamine) dendrimer as studied by molecular dynamics simulations. *J. Phys. Chem. B* 2009, *113*, 10984–10993.
- [20] J. Lim, G.M. Pavan, O. Annunziata, and E.E. Simanek, Experimental and computational evidence for an inversion in guest capacity in high-generation triazine dendrimer hosts. *J. Am. Chem. Soc.* 2012, *134*, 1942–1945.
- [21] R.S. DeFever and S. Sarupria, Association of small aromatic molecules with PAMAM dendrimers. *Phys. Chem. Chem. Phys.* 2015, *17*, 29548–29557.
- [22] V. Jain, P.K. Maiti, and P.V. Bharatam, Atomic level insights into realistic molecular models of dendrimer–drug complexes through MD simulations. *J. Chem. Phys.* 2016, *145*, 124902.
- [23] F. Badalkhani-Khamseh, A. Ebrahim-Habibi, and N.L. Hadipour, Atomistic computer simulations on multi-loaded PAMAM dendrimers: A comparison of amine- and hydroxyl-terminated dendrimers. *J. Comput.-Aided Mol. Des.* 2017, *31*, 1097–1111.
- [24] J.F.G.A. Jansen, E.M.M. de Brabander-van den Berg, and E.W. Meijer, Encapsulation of guest molecules into a dendritic box. *Science* 1994, *266*, 1226–1229.
- [25] P.K. Maiti and B. Bagchi, Structure and dynamics of DNA–dendrimer complexation: Role of counterions, water, and base pair sequence. *Nano Lett.* 2006, *6*, 2478–2485.
- [26] S.V. Lyulin, I. Vattulainen, and A.A. Gurtovenko, Complexes comprised of charged dendrimers, linear polyelectrolytes, and counterions: Insight through coarse-grained molecular dynamics simulations. *Macromolecules* 2008, *41*, 4961–4968.
- [27] G.M. Pavan, L. Albertazzi, and A. Danani, Ability to adapt: Different generations of PAMAM dendrimers show different behaviors in binding siRNA. *J. Phys. Chem. B* 2010, *114*, 2667–2675.
- [28] V. Vasumathi and P.K. Maiti, Complexation of siRNA with dendrimer: A molecular mod-

- eling approach. *Macromolecules* 2010, *43*, 8264–8274.
- [29] G.M. Pavan and A. Danani, Dendrimers and dendrons for siRNA binding: Computational insights. *J. Drug Del. Sci. Tech.* 2012, *22*, 83–89.
- [30] G.M. Pavan, Modeling the interaction between dendrimers and nucleic acids: A molecular perspective through hierarchical scales. *ChemMedChem* 2014, *9*, 2623–2631.
- [31] G.M. Pavan, A. Danani, S. Pricl, and D.K. Smith, Modeling the multivalent recognition between dendritic molecules and DNA: Understanding how ligand “sacrifice” and screening can enhance binding. *J. Am. Chem. Soc.* 2009, *131*, 9686–9694.
- [32] B. Nandy and P.K. Maiti, DNA compaction by a dendrimer. *J. Phys. Chem. B* 2011, *115*, 217–230.
- [33] S. Yu and R.G. Larson, Monte-Carlo simulations of PAMAM dendrimer–DNA interactions. *Soft Matter* 2014, *10*, 5325–5336.
- [34] R. Scherrenberg, B. Coussens, P. van Vliet, G. Edouard, J. Brackman, E. de Brabander, and K. Mortensen, The molecular characteristics of poly(propyleneimine) dendrimers as studied with small-angle neutron scattering, viscosimetry, and molecular dynamics. *Macromolecules* 1998, *31*, 456–461.
- [35] B. Smit, K. Esselink, P.A.J. Hilbers, N.M. van Os, L.A.M. Rupert, and I. Szleifer, Computer simulations of surfactant self-assembly. *Langmuir* 1993, *9*, 9–11.
- [36] R.M. Versteegen, D.J.M. van Beek, R.P. Sijbesma, D. Vlassopoulos, G. Fytas, and E.W. Meijer, Dendrimer-based transient supramolecular networks. *J. Am. Chem. Soc.* 2005, *127*, 13862–13868.
- [37] M.W.P.L. Baars, A.J. Karlsson, V. Sorokin, B.F.W. de Waal, and E.W. Meijer, Supramolecular modification of the periphery of dendrimers resulting in rigidity and functionality. *Angew. Chem., Int. Ed.* 2000, *39*, 4262–4265.
- [38] M.A.C. Broeren, J.L.J. van Dongen, M. Pittelkow, J.B. Christensen, M.H.P. van Genderen, and E.W. Meijer, Multivalency in the gas phase: The study of dendritic aggregates by mass spectrometry. *Angew. Chem., Int. Ed.* 2004, *43*, 3557–3562.
- [39] D. Banerjee, M.A.C. Broeren, M.H.P. van Genderen, E.W. Meijer, and P.L. Rinaldi, An NMR study of the supramolecular chemistry of modified poly(propyleneimine) dendrimers. *Macromolecules* 2004, *37*, 8313–8318.
- [40] T. Chang, K. Pieterse, M.A.C. Broeren, H. Kooijman, A.L. Spek, P.A.J. Hilbers, and E.W. Meijer, Structural elucidation of dendritic host–guest complexes by X-ray crystallography and molecular dynamics simulations. *Chem.–Eur. J.* 2007, *13*, 7883–7889.
- [41] R.H. Garrett and C.M. Grisham, *Biochemistry*. Saunders College Publishing, Philadelphia, 1995.
- [42] M.I. Stefan and N. Le Novère, Cooperative binding. *PLoS Comput. Biol.* 2013, *9*, 1–6.
- [43] P.J. Flory, *Statistical mechanics of chain molecules*. Hanser, Munich, 1969.
- [44] A.Y. Grosberg and A.R. Khokhlov, *Statistical physics of macromolecules*. American Institute of Physics Press, New York, 1994.
- [45] J. Han, R.J. Jaffe, and D.Y. Yoon, Conformational characteristics of polymethylene chains in melts and in various phantom chains from explicit atom molecular dynamics simulations. *Macromolecules* 1997, *30*, 7245–7252.
- [46] J. Huskens, A. Mulder, T. Auletta, C.A. Nijhuis, M.J.W. Ludden, and D.N. Reinhoudt, A model for describing the thermodynamics of multivalent host–guest interactions at interfaces. *J. Am. Chem. Soc.* 2004, *126*, 6784–6797.
- [47] R.H. Kramer and J.W. Karpen, Spanning binding sites on allosteric proteins with polymer-linked ligand dimers. *Nature* 1998, *395*, 710–713.
- [48] F.J. Martínez-Veracochea and M.E. Leunissen, The entropic impact of tethering, multivalency and dynamic recruitment in systems with specific binding groups. *Soft Matter* 2013, *9*, 3213–3219.
- [49] M. Weber, A. Bujotzek, and R. Haag, Quantifying the rebinding effect in multivalent chemical ligand–receptor systems. *J. Chem. Phys.* 2012, *137*, 054111.
- [50] J. Rao, J. Lahiri, R.M. Weis, and G.M. Whitesides, Design, synthesis, and characterization of a high-affinity trivalent system derived from vancomycin and L-Lys-D-Ala-D-Ala. *J. Am. Chem. Soc.* 2000, *122*, 2698–2710.

- [51] S.J. Marrink and D.P. Tieleman, Perspective on the Martini model. *Chem. Soc. Rev.* 2013, *42*, 6801–6822.
- [52] H. Lee and R.G. Larson, Coarse-grained molecular dynamics studies of the concentration and size dependence of fifth- and seventh-generation PAMAM dendrimers on pore formation in DMPC bilayer. *J. Phys. Chem. B* 2008, *112*, 7778–7784.
- [53] Molecular Operating Environment (MOE), version 2005.06. Chemical Computing Group, Inc., Montreal, 2005.
- [54] A.T. Brünger, X-PLOR, version 3.1: A system for X-ray crystallography and NMR. Yale University Press, New Haven, 1992.
- [55] L. Kalé, R. Steel, M. Bhandarkar, R. Brunner, A. Gursoy, N. Krawetz, J. Phillips, A. Shinzaki, K. Varadarajan, and K. Schulten, NAMD2: Greater scalability for parallel molecular dynamics. *J. Comput. Phys.* 1999, *151*, 283–312.
- [56] J.C. Phillips, R. Braun, W. Wang, J. Gumbart, E. Tajkhorshid, E. Villa, C. Chipot, R.D. Skeel, L. Kalé, and K. Schulten, Scalable molecular dynamics with NAMD. *J. Comput. Chem.* 2005, *26*, 1781–1802.
- [57] A.D. McKerrel Jr, D. Bashford, M. Bellott, R.L. Dunbrack Jr, J.D. Evanseck, M.J. Field, S. Fischer, J. Gao, H. Guo, S. Ha, D. Joseph-McCarthy, L. Kuchnir, K. Kuczera, F.T.K. Lau, C. Mattos, S. Michnick, T. Ngo, D.T. Nguyen, B. Prodhom, W.E. Reiher III, B. Roux, M. Schlenkrich, J.C. Smith, R. Stote, J. Straub, M. Watanabe, J. Wiorcikiewicz-Kuczera, D. Yin, and M. Karplus, All-atom empirical potential for molecular modeling and dynamics studies of proteins. *J. Phys. Chem. B* 1998, *102*, 3586–3616.
- [58] Sybyl. Tripos, Inc., St. Louis, 2003.
- [59] S. Alavi and D.L. Thompson, Effects of alkyl-group substitution on the proton-transfer barriers in ammonium and hydroxylammonium nitrate salts. *J. Phys. Chem. A* 2004, *108*, 8801–8809.
- [60] W. Humphrey, A. Dalke, and K. Schulten, VMD: Visual molecular dynamics. *J. Mol. Graphics* 1996, *14*, 33–38.



# Chapter 7

## Concluding remarks

---

**Abstract** In this thesis, the development and application of coarse-grained models of phospholipid vesicles and poly(propylene imine) dendrimers for molecular dynamics simulations have been described. Here we summarize the most interesting results of both nanoparticle systems with an eye toward shared characteristics and further take a look at possible new developments.

---



## 7.1 Summary of contributions

**Stalk initiation** With the coarse-grained lipid model introduced in *Chapter 2*, we discovered how fusion is initiated between small unperturbed spherical vesicles at the point where the apposing monolayers are closest together. There lipids may bridge the gap between monolayers by extending one of their tails. That hydrophobic connection is immediately strengthened by other lipids that coat the initial bridge, thus forming the stalk. Depending on membrane curvature, consistently a portion of the lipids has back-folded tails that may feature in such a connection. This precondition for fusion is a common characteristic of lipid membranes, and has been extensively studied in atomistic simulations of membranes containing a variety of lipids.<sup>[1]</sup> Our observed stalk initiation mechanism contrasts with earlier simulations that either prompted the observation that “the fusion process is triggered by a fluctuation in one monolayer resulting in some headgroups merging with the opposing monolayer”,<sup>[2]</sup> or where prefabricated vesicles were pushed together until an initial stalk was formed at the edge of the flattened contact zone.<sup>[3]</sup> The splayed lipid forming a pre-stalk intermediate has since been observed in coarse-grained<sup>[4]</sup> as well as in atomistic simulations;<sup>[5–8]</sup> it is now considered part of the canonical membrane fusion pathway,<sup>[9]</sup> and efforts have been made to view the splayed lipid initiating stalk formation with X-ray diffraction.<sup>[10]</sup>

**Stalk structure** The stalk with its slim structure of curved monolayers presents a challenge for elastic continuum calculations. Theoretical models posit that the stalk consists of either loosely bent cis-monolayers and thus hydrophobic voids are present in the stress-free stalk<sup>[11]</sup> or that all monolayers are sharply bent to prevent any voids while the trans-monolayers touch in the transmembrane contact stalk.<sup>[12]</sup> We found the stalk could be formed without voids as the lipids freely tilt and splay and the stalk does not involve the trans-monolayers at all. Currently, molecular dynamics simulations are recognized as a valuable method to investigate membrane fusion intermediates in addition to these elastic continuum models.<sup>[9,13–15]</sup>

**Stalk evolution** Two competing predictions of stalk evolution exist, i.e., radial<sup>[16]</sup> and anisotropic expansion.<sup>[17,18]</sup> Remarkably, in uniform conditions both stalk expansion pathways appear in our simulations. In the first case, the stalk expands radially and the inner monolayers touch to form a hemifusion diaphragm. In the second case, the stalk expands anisotropically into a crescent shape along the contact zone. Then either one pore emerges in the center of the crescent and a hemifusion diaphragm forms, or two pores emerge and fusion is complete. The presence of both pathways is in agreement with coarse-grained simulations<sup>[2]</sup> and is reaffirmed in atomistic<sup>[5]</sup> and large coarse-grained simulations.<sup>[19]</sup>

**Fusion pore** In the simulations the hemifusion diaphragm is either short-lived (<1 ns) or it gets to grow quite stable (>28 ns). Even then it is inherently thinner

than the outer bilayer and it eventually collapses triggered by water particles crossing at the hemifusion diaphragm edge. Atomistic simulations show the same hemifusion diaphragm to full fusion process.<sup>[5,6,20]</sup>

**Transmembrane proteins** The fused vesicles are not yet spherical, due to insufficient water content and a mismatched amount of lipids in the monolayers. As water transport and lipid flip-flop is slow compared to the simulation time, in *Chapter 3* we introduced simple transmembrane proteins to facilitate both. To embed the transmembrane proteins in bilayers, we took advantage of the inherent propensity of lipids to self-assemble into bilayers by adding a protein to the randomized lipid–water mix; this procedure also works in atomistic simulations of  $\alpha$ -helical transmembrane proteins.<sup>[21]</sup> The spontaneous insertion into already formed bilayers is also of interest for such amphiphilic transmembrane proteins. It has been investigated in e.g., coarse-grained simulations of simple hydrophobic nanotubes,<sup>[22]</sup> solid cylinders patterned like scramblase type B,<sup>[23]</sup> and generic amphiphilic  $\alpha$ -helical transmembrane peptides,<sup>[24]</sup> and in atomistic and CG simulations of the antimicrobial peptide alamethicin.<sup>[25]</sup>

**Hydrophobic matching** Even though our proteins fit the bilayer, the hydrophobic match is not perfect and the more malleable lipid membrane adapts to the height of the proteins.<sup>[26,27]</sup> Consequently, when multiple proteins are present, they aggregate in order to minimize the total area of membrane deformation. We observed that aggregation is strong when the proteins can fit together perfectly, but if there is room for the lipids to interject, proteins with the same mismatched height experience weak aggregation. A related effect, that we did not encounter in our simulations, emerges if the hydrophobic mismatch is too severe for the lipids to overcome by stretching; then the proteins tilt to fit the bilayer. Hydrophobic matching and protein tilt is important for protein function<sup>[28]</sup> and thus frequently investigated, e.g., in coarse-grained simulations of model proteins similar to ours,<sup>[23,29,30]</sup> nanotubes,<sup>[31]</sup> generalized  $\alpha$ -helical peptides,<sup>[24,32]</sup> peptide nanopores,<sup>[33]</sup> and specific proteins including aquaporin,<sup>[34]</sup> glucose transporter,<sup>[34]</sup>  $\delta$ -opioid receptor,<sup>[34]</sup> and sodium-potassium pump.<sup>[34]</sup> Atomistic simulations that regard hydrophobic matching include  $\beta$ -helical transmembrane protein gramicidin A,<sup>[35–37]</sup> the  $\alpha$ -helical transmembrane domains of dimeric platelet-derived growth factor receptor  $\beta$ ,<sup>[38]</sup> and  $\beta$ -barrel protein OmpA.<sup>[39]</sup> The effect of lipid-mediated protein aggregation<sup>[40]</sup> is by comparison less frequently studied, but because of the time scales required it presents a good case for coarse-graining simulations:<sup>[41]</sup> e.g., the effect of aggregation on the function of the antimicrobial peptide alamethicin has been studied comparing atomistic and CG simulations,<sup>[25]</sup> coarse-grained simulations of  $\alpha$ -helical and  $\beta$ -barrel transmembrane proteins showed aggregation also in vesicles,<sup>[42]</sup> and the dimerization of glycophorin A has been studied in CG simulations of red blood cell membranes.<sup>[43]</sup> A coarse-grained simulation of cylindrical transmembrane model proteins, also studied the effect of protein surface composition (smooth vs. side-chained) on aggregation.<sup>[44]</sup> Finally, large coarse-grained simulations of

bacterial outer membrane proteins demonstrated similar clustering structures as our trimmed type A scramblases.<sup>[45]</sup> Our coarse-grained lipid model has been used in protein-mediated vesicle formation studies.<sup>[46,47]</sup> Embedded scramblase type A transmembrane proteins to circular lipid bilayers were found to reduce the vesicle formation speed, depending on the concentration of proteins stiffening the membrane.<sup>[47]</sup>

**Water channel** For the design of our tubular water channel protein, we looked at the passive water transport protein aquaporin.<sup>[34,48–50]</sup> Even in this simple model, we found the naturalistic pore lining consisting of alternating hydrophilic rings in an otherwise hydrophobic channel essential for fast water transport. Although inclusion of a water channel did increase water flow through the membrane, the fused vesicle did not become spherical, the lipid distribution of the two leaflets of the membrane needs to adapt as well. Atomistic simulations have been used to gain further insight into the pore lining of aquaporin<sup>[50]</sup> and the dependence of the radius of transmembrane cyclic peptide nanotubes on water transport.<sup>[33,51]</sup>

**Scramblase** Increased water penetration is not enough to induce sphericalness, lipid redistribution is required. To test the hypothesis that the mere presence of proteins promotes fast flip-flop,<sup>[52,53]</sup> model transmembrane proteins with fully hydrophobic transmembrane domain (scramblase type A) were incorporated in various bilayers and vesicles, but this proved without effect. Pore-forming antimicrobial peptides like magainin<sup>[54]</sup> are known to combine pore-formation and flip-flop. Type B scramblase was created by mimicking this amphiphilic protein's hydrophilic band down the side. Our simulations show that for increased water transport and lipid flip-flop a single peptide is sufficient, no fully developed proteinaceous pore<sup>[55]</sup> is required. Yet, multiple peptides do indeed aggregate into pore complexes. Scramblase type B was found to equilibrate fused vesicles enabling them to become spherical, and even to enable fusion in apposed bilayers. In coarse-grained simulations of pore formation with scramblase type B-like cylinders, similar proteinaceous pore aggregates were observed.<sup>[23]</sup> Pore-forming amphiphilic antimicrobial peptides have been investigated with simulations: e.g., coarse-grained simulations of synthetic amphiphilic peptide LS3,<sup>[24]</sup> atomistic simulations of spontaneous pore formation with magainin,<sup>[56]</sup> alamethicin,<sup>[25]</sup> and gramicidin A.<sup>[36]</sup> Note that with gramicidin A one peptide appears sufficient for spontaneous pore formation.<sup>[36]</sup> Another antimicrobial peptide, BPC194, adopts a  $\beta$ -sheet structure upon interaction with a lipid membrane and was shown to facilitate stalk formation between membranes, leading to leaky fusion.<sup>[57]</sup> Finally, for the influenza virus the peptide hemagglutinin is responsible for enabling fusion of the virus with the host membrane. Atomistic simulations show that hemagglutinin disorders the lipid bilayer, by increasing back-folding of lipid tails the peptide facilitates the lipid bridge and stalk formation.<sup>[6,58]</sup> Interestingly, the putative scramblase protein that indiscriminately mixes lipids to prevent deformation of the endoplasmic reticulum membrane as phospholipids are synthesized exclusively

on the cytoplasmic monolayer, is still not identified.<sup>[59]</sup>

**Engulfing lobe** The engulfing lobe, a mechanism for vesicle growth we observed, has not reappeared in literature as such. The growth mechanism is a result of the fact that the inner and outer monolayers are two separate fluid layers and lipid exchange between them is slow. When the uptake of excess lipids from the solvent is faster than lipid flip-flop, the density of the outer layer grows considerably until it produces a bilayer fold that subsequently encapsulates solvent and merges with the original vesicle. It does resemble the bilayer fold that appears when a lipid monolayer at the air–water interface is laterally compressed, thus reducing the interfacial area.<sup>[60]</sup> First the monolayer starts to undulate, but then it buckles and folds into a bilayer projected into the water phase. As the fold grows, it ultimately collapses into a vesicle. Another instance which resembles the engulfing lobe is found in a coarse-grained simulation of amphiphilic copolymers.<sup>[61]</sup> Here a vesicle merges with a lagging bilayer disc, which proceeds to curve into an attached vesicle, subsequently both fuse into a tubular vesicle.

**Coarse-graining dendrimers** To investigate the behavior of poly(propylene imine) (PPI) and urea–adamantyl-functionalized PPI dendrimers (PPIUA) in solvent, a coarse-grained dendrimer model was developed in *Chapter 4*. Harmonic bond and angle potentials were derived from all-atom simulations of *G5* PPIUA, utilizing an iterative Boltzmann inversion scheme, modified to incorporate Gaussian fits of the bond and angle distributions. By decoupling the atomistic input into a complete simulation for bond distribution and a structural simulation for angle distribution, accurate bond and angle potentials were derived, leaving the effect of solvent to non-bonded interactions. Thereby creating a general model capable to simulate different dendrimer sizes and concentrations.

**Dendrimer structure** Although parameterized on *G5* atomistic PPIUA, the coarse-grained model compares well with the atomistic variants, and with the available experimental results<sup>[62]</sup> with respect to various structural measurements over a wide range of generations. The experimental SANS measurements give the radius of gyration and the form factor; these results compare well with their computed variants, demonstrating the validity of the coarse-grained model. At first glance the radius of gyration versus the number of monomers seems to follow the linear relation for bad solvent ( $R_g \propto N^{1/3}$ ). This is true for the hydrophobic-ended PPIUA dendrimers, but upon closer inspection the PPI dendrimers follow a good solvent relation of  $R_g \propto N^{1/5}(G + 0.5)^{2/5}$ . A clear trend emerges from aspect ratio and asphericity calculation of coarse-grained and atomistic simulations. Small dendrimers ( $\leq G3$ ) appear rod-like but can assume globular structure while large dendrimers ( $\geq G5$ ) are always globular. Indeed, the radial monomer distribution shows that for small dendrimers the end-groups are found mostly at the periphery, but for large dendrimers the end-groups are distributed throughout the volume. Because at the periphery there is not enough room for all the end-groups, their

branches must bend and back-fold filling out the available space. These dendrimers thus adhere to the prevalent dense core<sup>[63]</sup> concept. Finally, the radial monomer distributions and spacer expansion calculations clearly show that PPIUA is indeed a clear extension of PPI.

**Dendrimer solutions** In *Chapter 5* the interactions between dendrimers come into play as the coarse-grained model is applied to perform large scale simulations of concentrated dendrimer solutions. We provide a complete description of specifically *G4* and *G5* poly(propylene imine) dendrimers in dilute to melt conditions as these simulations are directly comparable to two SANS studies of PPI dendrimers in good solvent.<sup>[64,65]</sup> The overlap concentration ( $C^*$ ) marks the transition between a dilute and semidilute solution. The simulations locate it at  $\sim 60\%$ . Indeed at  $64\%$  and up the average nearest neighbor dendrimer–dendrimer distance follows the limit for purely repulsive particles. The overlap concentration is not a strict tipping point, however, characteristics such as the average nearest neighbor distance, radius of gyration, water content, and interpenetration gradually change with increasing concentration. With increasing dendrimer concentrations and increased competition, the dendrimers' volume diminishes. This is evident as the radii of gyration in low concentrations ( $\leq 23\%$ ) are the same as in the simulations of *Chapter 4*. With increasing concentration the dendrimer volume decreases as the water content decreases. The solvent is not uniformly distributed, a greater amount is found in the space between dendrimers. Simultaneously interpenetration of dendrimer branches increases, although at most  $15\%$  external particles enter each dendrimers' convex hull. Contrary to other measurements reported,<sup>[66]</sup> we found dendrimer interpenetration is equal for *G4* and *G5*, as is water penetration.

**SANS measurements and calculations** In dilute concentrations, the radius of gyration and form factor ( $F(q)$ ) of separate dendrimers can be calculated from SANS measurements. In these experiments, to calculate the solution's structure factor ( $S(q)$ ), one must assume that the form factor is independent of concentration and uncorrelated with the structure factor. Calculating the structure factor of the simulated concentrated solutions using the experimental assumptions and comparing these with direct calculations, shows that they start to diverge at rather low concentrations ( $\geq 23\%$ ). Not because the form factor changes, indeed in the simulations the form factor changes only slightly with concentration, but because the monomer positions of separate dendrimers are already correlated. This also establishes the necessity of explicitly simulating the solvent. The factor often used in SANS measurements to relate the peak position in the structure factor to the peak in the radial distribution function ( $g(r)$ ),  $\sqrt{3/2}$ , is correct for a strict fcc lattice, but for the noisier dendrimer packing a  $3\%$  smaller factor is optimal.

**Macromolecular nanostructures** The coarse-grained PPIUA dendrimer model was expanded with multivalent ureido acetic acid guests in *Chapter 6* to study multivalent host–guest interactions as well as the hierarchical self-assembly of

their complexes into macromolecular nanostructures. The guest parameters were fine-tuned to match the experimental binding values of primary guests.<sup>[67]</sup> As the guests solubilize the dendrimers, these complexes act as dynamic patchy nanoparticles wherein the guest concentration determines the coverage into hydrophilic and hydrophobic domains and in turn the self-assembly into nanostructures. That the presence of guests slows down dendrimer self-assembly was demonstrated in simulations with 16 dendrimers. Box-spanning network structures were achieved in simulations with 125 dendrimers, here the guest concentration indeed determined the mass of the network branches. A comparable example of the patchy nanoparticle concept is the construction of PPI dendrimer-based nanofibers.<sup>[68]</sup> G4 PPI dendrimers in the presence of cadmium acetate ( $\text{Cd}^{2+}$  and  $\text{CH}_3\text{COO}^-$ ) form unidirectional aggregates as seen with atomic force and transmission electron microscopy. The precise binding mechanism was elucidated by 100 ns atomistic simulations of a stable complex of two PPI dendrimers. First the transition metal cadmium forms transition complexes with the lone pair possessing  $\text{NH}_2$  ends. Successively, the acetate ions coordinate to the  $\text{NH}_2\text{-Cd}^{2+}$  groups generating a complex with hydrophobic ends. These ends tend to aggregate due to ionic attraction and hydrophobic association, dividing the surface into hydrophobic and hydrophilic ( $\text{NH}_3^+$ ) domains. The now asymmetric dendrimers subsequently self-assemble into supramolecular fibers. Furthermore, when symmetric  $\text{Cl}^-$  ions are introduced to compete with the acetate, indeed the nanofibers disassemble to become globular aggregates.

**Multivalent host–guest complexes** By systematically studying guest concentration-dependent multivalent binding, we found a clear multivalency effect at low guest concentrations: more headgroups do enhance binding. The increase is definitely not due to a physical difference in headgroup binding, it is identical for all guests. The headgroups connected by a flexible spacer bind more often, as when the first is bound, the others are near a binding site as well. However, with increasing guest concentrations, the adjacency advantage over free headgroups fades. The simulations of semibound guests show that these multivalent guests' linkers are long enough to reach essentially all tertiary amines, yet linked headgroups tend to bind in close proximity. This, in combination with the observation that the effective concentration ( $C_{\text{eff,max}}$ ) is highest for small tethered headgroup–headgroup distance, would suggest small spacers are preferred. On the contrary, elongation of the chain was found to enhance binding, not because of better a fit or increased access to binding sites, but rather through increased binding incidence and longer lingering of dissociated headgroups which facilitates rebinding. At high guest concentrations the dendrimer becomes saturated with bound headgroups regardless of guest valency, thus the multivalent effect vanishes. Yet, when the monovalent and tetravalent guests are put in direct competition for binding sites, the multivalent guests continue to displace the monovalent guests from the dendrimer at all concentrations, thus reaffirming the increased binding power provided by multivalency.

## 7.2 Discussion

**Developments in membrane simulations** Apart from the developments related to our phospholipid vesicle fusion simulations, a few general developments merit to be highlighted. To enable lengthy simulations of transmembrane proteins in lipid bilayer systems, instead of coarse-graining, another interesting approach is utilizing hybrid simulations,<sup>[69,70]</sup> i.e., simulating an all-atom protein in a coarse-grained bilayer/water environment. Examples of successful application of this method include gramicidin A,<sup>[71]</sup> WALP,<sup>[72]</sup> and large-conductance mechanosensitive channel (MscL)<sup>[72]</sup> simulations. Another development that enables larger simulations is the utilization of graphics processing units (GPUs) for molecular dynamics. With the high degree of parallelism and floating point arithmetic capabilities of GPUs, speed-ups of about 10–20 times compared to calculations on conventional CPU cores are attainable.<sup>[73,74]</sup> The increased performance is applied in all-atom simulations of biomolecular systems,<sup>[75]</sup> for instance in a 928 ns simulation of the transmembrane protein octopamine receptor in a fully solvated membrane.<sup>[76]</sup> The increased performance provided by GPUs can also be exploited to accelerate coarse-grained simulations<sup>[77]</sup> to realize even greater simulation time and length scales.

In the contributions section it has already been shown that massive improvements have been made in coarse-grained protein models compared to the simple protein models of *Chapter 3*. Currently, typically every amino acid is mapped to a general backbone particle and one or more particles for the distinctive side-chain.<sup>[78–84]</sup> For the coarse-grained simulation of comprehensive biomembranes, in particular the Martini model<sup>[80,82,85–87]</sup> has become ubiquitous.<sup>[88]</sup> It provides parameters to capture a host of different lipids,<sup>[86]</sup> and it includes polarizable protein particles<sup>[82]</sup> in conjunction with polarizable water particles<sup>[89]</sup> for when explicit screening of polar and charged residues is deemed important to produce realistic results; for instance when establishing the free-energy landscape of the binding of peripheral membrane proteins to complex biomembranes.<sup>[90]</sup> With the improved protein models, the secondary structure of peptides and their chemical specificity can be represented well. Compare for instance the coarse-grained SNARE protein complex mediated fusion represented with simple cylinders<sup>[91]</sup> versus the same with coarse-grained  $\alpha$ -helical peptides.<sup>[92]</sup> The increased fidelity of the latter model provides much greater insight into the various steps of SNARE-mediated fusion. With these coarse-grained models accurate protein interactions with ligands can be simulated over a quite long time scale. For example, an important step in photosynthesis has been followed in a series of simulations reaching 475  $\mu$ s, namely how a plastoquinone ligand enters the reaction cavity of a photosystem II protein, gets protonated, and exits via a newly discovered channel.<sup>[93]</sup> With this increased specificity, the more complex lipid–protein interactions, compared to the general hydrophobic matching already seen, can be investigated in detail. In the cell, the lipid composition of each or-

ganelle's membrane is different and asymmetric between monolayers, with >1000 lipid species identified.<sup>[94]</sup> A series of coarse-grained simulations of ten different membrane-bound proteins in realistic lipid compositions showed how each protein uniquely modulates its local lipid environment through enrichment or depletion of specific lipids, resulting in thickness and curvature gradients. Each protein thus features its own characteristic lipid arrangement like a fingerprint.<sup>[34]</sup> Thus big steps have been taken toward the ultimate goal of modeling a complete cell.<sup>[95]</sup>

**Complexity** The philosophy behind the design of our coarse-grained lipid model is to minimize complexity while retaining the phase behavior properties of lipids and consequently other amphiphiles. With only two types of particles, hydrophilic and hydrophobic, and a single harmonic bond potential, the model successfully displays the requisite self-assembly of micelles, bilayers, and vesicles,<sup>[96]</sup> and also the fusion of vesicles as demonstrated in this thesis. Especially compared to other more elaborate coarse-grained lipid models,<sup>[85,97–100]</sup> it proves that complex behavior can emerge from a minimal set of simple interactions. Even the model transmembrane proteins, although not life-like in their appearance, performed their water channel and lipid scrambling functions while built from the same simple ingredients. A good example of how the simple general lipid design enables us to gain insight into what affects lipid behavior are our simulations on vesicle deformation<sup>[101]</sup> and fission.<sup>[102]</sup> Broadly, vesicle fission is the reverse of vesicle fusion.<sup>[103,104]</sup> The end state of the large fused vesicles of *Chapter 2* have been used as starting point in these vesicle fission simulations. Spontaneous fission could be induced by introducing small differences between lipids of the inner and outer monolayers. Only small changes, equivalent of an altered pH or ion concentration, to the headgroup–headgroup or headgroup–water interactions of one of the monolayers suffice to split an initially stable vesicle into two smaller stable vesicles that both have the same lipid composition as the original vesicle.<sup>[102]</sup> Likewise, the lipid model was used in simulations of vesicle draining congruent with experiments. Simple drainage of a spontaneously formed spherical vesicle results in oblate ellipsoid and discous vesicles. However, when a negative spontaneous curvature is introduced by small parameter changes that decrease the hydration of the lipids in the outer membrane leaflet, cup-shaped vesicles are formed. Conversely, drainage in combination with positive spontaneous curvature leads to prolate ellipsoid, pear-shaped, budded, and even split vesicles.<sup>[101]</sup> That complex lipid behavior emerges from such simple interactions is a fascinating phenomenon.

The dendrimer–guest model was also envisioned as a simplification of a fairly complex system, yet, as they are designed to represent specific molecules rather than a generic class of lipids, required retaining more chemical fidelity. This was realized by Boltzmann inversion from bond and angle distributions of atomistic simulations, while still reducing the tabulated potentials into harmonic potentials. The poly(propylene imine) and urea–adamantyl-functionalized dendrimer models are separately indeed fairly simple with four types of particles including water,



but the ureido acetic acid guest required five more. This greatly increased the number of spring constants (11 bonds, 17 angles) and non-bonded pair potentials (45) involved. While it is good to aspire to build the most accurate dendrimer-guest model, it is debatable whether the added complexity of a faithful ureido acetic acid guest in particular is noticeable in the in essence qualitative results. Calibrating the interaction between acetic acid headgroup and tertiary amines on the one hand, and the interaction between ethylene oxide tails and water on the other is definitely required, but the benefit of meticulously reproducing the part connecting the headgroup/spacer to the tails or specific bonds and angles thereof is less certain, especially in light of the success of the lipid model. An alternative multivalent guest model, one wherein the intermediate parts are represented by a single particle type, is also conceivable.

**Simulations aid the design of biological and chemical systems** Throughout this thesis, there have been many instances where computer simulations have challenged prior assumptions by testing them with a comprehensive model and providing alternative views. Often this is simply because, contrary to more abstract models, molecular dynamics simulations allow the disorderly nature of the molecules to come through. In the vesicle fusion simulations, for instance, stalk formation was shown to be initiated by a few lipids that protrude their tails into the interface between bilayers. The elastic continuum models which conceptualize the bilayers as continuous leaflets could not foresee this mechanism. Analogously, the anisotropic stalk-pore evolution was first observed in Brownian dynamics simulations of vesicles of small coarse-grained fatty acids.<sup>[17]</sup> Computer simulations thus augment the vesicle fusion views of experimentalists by providing a molecular picture. With respect to the dendrimer structure, the concept of a dense shell around a vacant core region<sup>[105]</sup> is a logical consequence of the way dendrimers are synthesized, with a doubling of the number of branches per generation, and how this is pictured with skeletal models (e.g., Figure 1.3). Only with early computer simulations of dendrimer growth in which a self-avoiding walk algorithm allowed the flexible branches to become back-folded,<sup>[63]</sup> did the dense core view become established. In the interpretation of SANS measurements of concentrated colloidal solutions, typically methods are employed that are based on certain approximations and assumptions on perfect lattices. Comparing these techniques with direct calculations from our simulations enabled us to determine the ramifications of these techniques for the structure factor and nearest neighbor results. In our dendrimer-guest system, the binding of the guest to the dendrimer was originally envisioned to occur with the pincer construct, but atomistic simulations found the headgroup too large to fit the pincer and the proposed interactions to be more scattered.<sup>[106]</sup> This dendrimer-guest system also presented a nice example where simulations can benefit the direct interpretation of experiments, i.e., by combining MD simulations with the dynamic light scattering and cryo-TEM analyses, we found the supramolecular assembly consisting of three dendrimers in the trapped core to be the most abundant.<sup>[107]</sup> Moreover, it illustrated the potential of simula-

tions to tune individual parameters, which we used to get an idea of the maximum number of headgroups that can be bound by dramatically increasing the headgroup-dendrimer interaction strength. Finally, the coarse-grained simulations allowed us to systematically investigate the concept of multivalency and demonstrate the enhancing effect of multivalency on guest binding over a full concentration range.

Altogether, with our vesicle and dendrimer simulations we have shown that molecular simulations, by providing unique insights, greatly benefit the study of such dynamic nanoparticle systems.

## Bibliography

- [1] M.A. Tahir, R.C. Van Lehn, S.H. Choi, and A. Alexander-Katz, Solvent-exposed lipid tail protrusions depend on lipid membrane composition and curvature. *Biochim. Biophys. Acta Biomembr.* 2016, *1858*, 1207–1215.
- [2] S.J. Marrink and A.E. Mark, The mechanism of vesicle fusion as revealed by molecular dynamics simulations. *J. Am. Chem. Soc.* 2003, *125*, 11144–11145.
- [3] M.J. Stevens, J.H. Hoh, and T.B. Woolf, Insights into the molecular mechanism of membrane fusion from simulation: Evidence for the association of splayed tails. *Phys. Rev. Lett.* 2003, *91*, 188102.
- [4] D. Mirjanian, A.N. Dickey, J.H. Hoh, T.B. Woolf, and M.J. Stevens, Splaying of aliphatic tails plays a central role in barrier crossing during liposome fusion. *J. Phys. Chem. B* 2010, *114*, 11061–11068.
- [5] V. Knecht and S.J. Marrink, Molecular dynamics simulations of lipid vesicle fusion in atomic detail. *Biophys. J.* 2007, *92*, 4254–4261.
- [6] P.M. Kasson, E. Lindahl, and V.S. Pande, Atomic-resolution simulations predict a transition state for vesicle fusion defined by contact of a few lipid tails. *PLoS Comput. Biol.* 2010, *6*, 1–8.
- [7] Y.G. Smirnova, S.J. Marrink, R. Lipowsky, and V. Knecht, Solvent-exposed tails as prestalk transition states for membrane fusion at low hydration. *J. Am. Chem. Soc.* 2010, *132*, 6710–6718.
- [8] S. Kawamoto and W. Shinoda, Free energy analysis along the stalk mechanism of membrane fusion. *Soft Matter* 2014, *10*, 3048–3054.
- [9] S. Boonstra, J.S. Blijleven, W.H. Roos, P.R. Onck, E. van der Giessen, and A.M. van Oijen, Hemagglutinin-mediated membrane fusion: A biophysical perspective. *Annu. Rev. Biophys.* 2018, *47*, 153–173.
- [10] B. Weinhausen, S. Aeffner, T. Reusch, and T. Salditt, Acyl-chain correlation in membrane fusion intermediates: X-ray diffraction from the rhombohedral lipid phase. *Biophys. J.* 2012, *102*, 2121–2129.
- [11] V.S. Markin and J.P. Albanesi, Membrane fusion: Stalk model revisited. *Biophys. J.* 2002, *82*, 693–712.
- [12] Y. Kozlovsky and M.M. Kozlov, Stalk model of membrane fusion: Solution of energy crisis. *Biophys. J.* 2002, *82*, 882–895.
- [13] L.V. Chernomordik and M.M. Kozlov, Mechanics of membrane fusion. *Nat. Struct. Mol. Biol.* 2008, *15*, 675–683.
- [14] J. Yoo, M.B. Jackson, and Q. Cui, A comparison of coarse-grained and continuum models for membrane bending in lipid bilayer fusion pores. *Biophys. J.* 2013, *104*, 841–852.
- [15] M.M. Kozlov and L.V. Chernomordik, Membrane tension and membrane fusion. *Curr. Opin. Struct. Biol.* 2015, *33*, 61–67.
- [16] Y. Kozlovsky, L.V. Chernomordik, and M.M. Kozlov, Lipid intermediates in membrane

- fusion: Formation, structure, and decay of hemifusion diaphragm. *Biophys. J.* 2002, *83*, 2634–2651.
- [17] H. Noguchi and M. Takasu, Fusion pathways of vesicles: A Brownian dynamics simulation. *J. Chem. Phys.* 2001, *115*, 9547–9551.
- [18] M. Müller, K. Katsov, and M. Schick, New mechanism of membrane fusion. *J. Chem. Phys.* 2002, *116*, 2342–2345.
- [19] H.J. Risselada, G. Bubnis, and H. Grubmüller, Expansion of the fusion stalk and its implication for biological membrane fusion. *Proc. Natl. Acad. Sci.* 2014, *111*, 11043–11048.
- [20] H.H.G. Tsai, C.M. Chang, and J.B. Lee, Multi-step formation of a hemifusion diaphragm for vesicle fusion revealed by all-atom molecular dynamics simulations. *Biochim. Biophys. Acta Biomembr.* 2014, *1838*, 1529–1535.
- [21] S. Esteban-Martín and J. Salgado, Self-assembling of peptide/membrane complexes by atomistic molecular dynamics simulations. *Biophys. J.* 2007, *92*, 903–912.
- [22] C.F. Lopez, S.O. Nielsen, B. Ensing, P.B. Moore, and M.L. Klein, Structure and dynamics of model pore insertion into a membrane. *Biophys. J.* 2005, *88*, 3083–3094.
- [23] G. Illya and M. Deserno, Coarse-grained simulation studies of peptide-induced pore formation. *Biophys. J.* 2008, *95*, 4163–4173.
- [24] P. Gkeka and L. Sarkisov, Spontaneous formation of a barrel-stave pore in a coarse-grained model of the synthetic LS3 peptide and a DPPC lipid bilayer. *J. Phys. Chem. B* 2009, *113*, 6–8.
- [25] L. Thøgersen, B. Schiøtt, T. Vosegaard, N.C. Nielsen, and E. Tajkhorshid, Peptide aggregation and pore formation in a lipid bilayer: A combined coarse-grained and all atom molecular dynamics study. *Biophys. J.* 2008, *95*, 4337–4347.
- [26] J.A. Killian, Hydrophobic mismatch between proteins and lipids in membranes. *Biochim. Biophys. Acta Rev. Biomembr.* 1998, *1376*, 401–416.
- [27] A. Holt and J.A. Killian, Orientation and dynamics of transmembrane peptides: The power of simple models. *Eur. Biophys. J.* 2010, *39*, 609–621.
- [28] O. Soubias, W.E. Teague Jr, K.G. Hines, and K. Gawrisch, Rhodopsin/lipid hydrophobic matching—rhodopsin oligomerization and function. *Biophys. J.* 2015, *108*, 1125–1132.
- [29] M. Venturoli, B. Smit, and M.M. Sperotto, Simulation studies of protein-induced bilayer deformations, and lipid-induced protein tilting, on a mesoscopic model for lipid bilayers with embedded proteins. *Biophys. J.* 2005, *88*, 1778–1798.
- [30] F.J.M. de Meyer, M. Venturoli, and B. Smit, Molecular simulations of lipid-mediated protein–protein interactions. *Biophys. J.* 2008, *95*, 1851–1865.
- [31] S.O. Nielsen, B. Ensing, V. Ortiz, P.B. Moore, and M.L. Klein, Lipid bilayer perturbations around a transmembrane nanotube: A coarse grain molecular dynamics study. *Biophys. J.* 2005, *88*, 3822–3828.
- [32] T. Kim and W. Im, Revisiting hydrophobic mismatch with free energy simulation studies of transmembrane helix tilt and rotation. *Biophys. J.* 2010, *99*, 175–183.
- [33] J.W. Klingelhoefer, T. Carpenter, and M.S.P. Sansom, Peptide nanopores and lipid bilayers: Interactions by coarse-grained molecular-dynamics simulations. *Biophys. J.* 2009, *96*, 3519–3528.
- [34] V. Corradi, E. Mendez-Villuendas, H.I. Ingólfsson, R.X. Gu, I. Siuda, M.N. Melo, A. Mousatova, L.J. DeGagné, B.I. Sejdiu, G. Singh, T.A. Wassenaar, K. Delgado Magnero, S.J. Marrink, and D.P. Tieleman, Lipid–protein interactions are unique fingerprints for membrane proteins. *ACS Cent. Sci.* 2018, *4*, 709–717.
- [35] F. Yin and J.T. Kindt, Atomistic simulation of hydrophobic matching effects on lipid composition near a helical peptide embedded in mixed-lipid bilayers. *J. Phys. Chem. B* 2010, *114*, 8076–8080.
- [36] T. Kim, K.I. Lee, P. Morris, R.W. Pastor, O.S. Andersen, and W. Im, Influence of hydrophobic mismatch on structures and dynamics of Gramicidin A and lipid bilayers. *Biophys. J.* 2012, *102*, 1551–1560.
- [37] I. Basu, A. Chattopadhyay, and C. Mukhopadhyay, Ion channel stability of Gramicidin A in lipid bilayers: Effect of hydrophobic mismatch. *Biochim. Biophys. Acta Biomembr.* 2014, *1838*, 328–338.

- [38] C. Muhle-Goll, S. Hoffmann, S. Afonin, S.L. Grage, A.A. Polyansky, D. Windisch, M. Zeitler, J. Bürck, and A.S. Ulrich, Hydrophobic matching controls the tilt and stability of the dimeric platelet-derived growth factor receptor (PDGFR)  $\beta$  transmembrane segment. *J. Biol. Chem.* 2012, *287*, 26178–26186.
- [39] F. Yin and J.T. Kindt, Hydrophobic mismatch and lipid sorting near OmpA in mixed bilayers: Atomistic and coarse-grained simulations. *Biophys. J.* 2012, *102*, 2279–2287.
- [40] L. Johannes, W. Pezeshkian, J.H. Ipsen, and J.C. Shillcock, Clustering on membranes: Fluctuations and more. *Trends Cell Biol.* 2018, *28*, 405–415.
- [41] M. Baaden and S.J. Marrink, Coarse-grain modelling of protein–protein interactions. *Curr. Opin. Struct. Biol.* 2013, *23*, 878–886.
- [42] D.L. Parton, J.W. Klingelhoefer, and M.S.P. Sansom, Aggregation of model membrane proteins, modulated by hydrophobic mismatch, membrane curvature, and protein class. *Biophys. J.* 2011, *101*, 691–699.
- [43] N. Flinner and E. Schleiff, Dynamics of the glycophorin A dimer in membranes of native-like composition uncovered by coarse-grained molecular dynamics simulations. *PLoS One* 2015, *10*, 1–16.
- [44] T.H.T. Nguyen, N.Z. Rao, W.M. Schroeder, and P.B. Moore, Coarse-grained molecular dynamics of tetrameric transmembrane peptide bundles within a lipid bilayer. *Chem. Phys. Lipids* 2010, *163*, 530–537.
- [45] M. Chavent, A.L. Duncan, P. Rassam, O. Birkholz, J. Hélie, T. Reddy, D. Beliaev, B. Hambly, J. Piehler, C. Kleanthous, and M.S.P. Sansom, How nanoscale protein interactions determine the mesoscale dynamic organisation of bacterial outer membrane proteins. *Nat. Comm.* 2018, *9*, 1–12.
- [46] B. van Hoof, A.J. Markvoort, R.A. van Santen, and P.A.J. Hilbers, On protein crowding and bilayer bulging in spontaneous vesicle formation. *J. Phys. Chem. B* 2012, *116*, 12677–12683.
- [47] B. van Hoof, A.J. Markvoort, R.A. van Santen, and P.A.J. Hilbers, Molecular simulation of protein encapsulation in vesicle formation. *J. Phys. Chem. B* 2014, *118*, 3346–3354.
- [48] H. Sui, B.G. Han, J.K. Lee, W. Peter, and B.K. Jap, Structural basis of water-specific transport through the AQP1 water channel. *Nature* 2001, *414*, 872–878.
- [49] Y. Fujiyoshi, K. Mitsuoka, B.L. de Groot, A. Philippsen, H. Grubmüller, P. Agre, and A. Engel, Structure and function of water channels. *Curr. Opin. Struct. Biol.* 2002, *12*, 509–515.
- [50] D. Alberga, O. Nicolotti, G. Lattanzi, G.P. Nicchia, A. Frigeri, F. Pisani, V. Benfenati, and G.F. Mangiatordi, A new gating site in human aquaporin-4: Insights from molecular dynamics simulations. *Biochim. Biophys. Acta* 2014, *1838*, 3052–3060.
- [51] J. Liu, J. Fan, M. Tang, M. Cen, J. Yan, Z. Liu, and W. Zhou, Water diffusion behaviors and transportation properties in transmembrane cyclic hexa-, octa- and decapeptide nanotubes. *J. Phys. Chem. B* 2010, *114*, 12183–12192.
- [52] M.A. Kol, A.I.P.M. de Kroon, D.T.S. Rijkers, J.A. Killian, and B. de Kruijff, Membrane-spanning peptides induce phospholipid flop: A model for phospholipid translocation across the inner membrane of *E. coli*. *Biochemistry* 2001, *40*, 10500–10506.
- [53] M. Langer, R. Sah, A. Vesper, M. Gütlich, and D. Langosch, Structural properties of model phosphatidylcholine flippases. *Chem. Biol.* 2013, *20*, 63–72.
- [54] K. Matsuzaki, O. Murase, N. Fujii, and K. Miyajima, An antimicrobial peptide, magainin 2, induced rapid flip-flop of phospholipids coupled with pore formation and peptide translocation. *Biochemistry* 1996, *35*, 11361–11368.
- [55] R. Jahn and H. Grubmüller, Membrane fusion. *Curr. Opin. Cell Biol.* 2002, *14*, 488–495.
- [56] H. Leontiadou, A.E. Mark, and S.J. Marrink, Antimicrobial peptides in action. *J. Am. Chem. Soc.* 2006, *128*, 12156–12161.
- [57] G. Moiset, A.D. Cirac, M.C.A. Stuart, S.J. Marrink, D. Sengupta, and B. Poolman, Dual action of BPC194: A membrane active peptide killing bacterial cells. *PLoS One* 2013, *8*, 1–10.
- [58] P. Larsson and P.M. Kasson, Lipid tail protrusion in simulations predicts fusogenic activity of influenza fusion peptide mutants and conformational models. *PLoS Comput. Biol.* 2013,

- 9, 1–9.
- [59] T.G. Pomorski and A.K. Menon, Lipid somersaults: Uncovering the mechanisms of protein-mediated lipid flipping. *Prog. Lipid Res.* 2016, *64*, 69–84.
- [60] S. Baoukina, L. Monticelli, H.J. Risselada, S.J. Marrink, and D.P. Tieleman, The molecular mechanism of lipid monolayer collapse. *Proc. Natl. Acad. Sci.* 2008, *105*, 10803–10808.
- [61] X.L. Sun, S. Pei, J.F. Wang, P. Wang, Z.B. Liu, and J. Zhang, Coarse-grained molecular dynamics simulation study on spherical and tube-like vesicles formed by amphiphilic copolymers. *J. Polym. Sci., Part B: Polym. Phys.* 2017, *55*, 1220–1226.
- [62] R. Scherrenberg, B. Coussens, P. van Vliet, G. Edouard, J. Brackman, E. de Brabander, and K. Mortensen, The molecular characteristics of poly(propyleneimine) dendrimers as studied with small-angle neutron scattering, viscosimetry, and molecular dynamics. *Macromolecules* 1998, *31*, 456–461.
- [63] R.L. Lescanec and M. Muthukumar, Configurational characteristics and scaling behavior of starburst molecules: A computational study. *Macromolecules* 1990, *23*, 2280–2288.
- [64] A. Ramzi, R. Scherrenberg, J. Brackman, J. Jacques, and K. Mortensen, Intermolecular interactions between dendrimer molecules in solution studied by small-angle neutron scattering. *Macromolecules* 1998, *31*, 1621–1626.
- [65] A. Topp, B.J. Bauer, T.J. Prosa, R. Scherrenberg, and E.J. Amis, Size change of dendrimers in concentrated solution. *Macromolecules* 1999, *32*, 8923–8931.
- [66] N. Zacharopoulos and I.G. Economou, Morphology and organization of poly(propyleneimine) dendrimers in the melt from molecular dynamics simulation. *Macromolecules* 2002, *35*, 1814–1821.
- [67] T.M. Hermans, M.A.C. Broeren, N. Gomopoulos, P. van der Schoot, M.H.P. van Genderen, N.A.J.M. Sommerdijk, G. Fytas, and E.W. Meijer, Self-assembly of soft nanoparticles with tunable patchiness. *Nat. Nanotechnol.* 2009, *4*, 721–726.
- [68] M. Garzoni, N. Cheval, A. Fahmi, A. Danani, and G.M. Pavan, Ion-selective controlled assembly of dendrimer-based functional nanofibers and their ionic-competitive disassembly. *J. Am. Chem. Soc.* 2012, *134*, 3349–3357.
- [69] A.J. Rzepiela, M. Louhivuori, C. Peter, and S.J. Marrink, Hybrid simulations: Combining atomistic and coarse-grained force fields using virtual sites. *Phys. Chem. Chem. Phys.* 2011, *13*, 10437–10448.
- [70] R. Potestio, C. Peter, and K. Kremer, Computer simulations of soft matter: Linking the scales. *Entropy* 2014, *16*, 4199–4245.
- [71] Q. Shi, S. Izvekov, and G.A. Voth, Mixed atomistic and coarse-grained molecular dynamics: Simulation of a membrane-bound ion channel. *J. Phys. Chem. B* 2006, *110*, 15045–15048.
- [72] T.A. Wassenaar, H.I. Ingólfsson, M. Prieß, S.J. Marrink, and L.V. Schäfer, Mixing MARTINI: Electrostatic coupling in hybrid atomistic–coarse-grained biomolecular simulations. *J. Phys. Chem. B* 2013, *117*, 3516–3530.
- [73] J.E. Stone, D.J. Hardy, I.S. Ufimtsev, and K. Schulten, GPU-accelerated molecular modeling coming of age. *J. Mol. Graphics Modell.* 2010, *29*, 116–125.
- [74] J. Glaser, T.D. Nguyen, J.A. Anderson, P. Lui, F. Spiga, J.A. Millan, D.C. Morse, and S.C. Glotzer, Strong scaling of general-purpose molecular dynamics simulations on GPUs. *Comput. Phys. Commun.* 2015, *192*, 97–107.
- [75] C. Kutzner, S. Páll, M. Fechner, A. Esztermann, B.L. de Groot, and H. Grubmüller, Best bang for your buck: GPU nodes for GROMACS biomolecular simulations. *J. Comput. Chem.* 2015, *36*, 1990–2008.
- [76] K.W. Kastner and J.A. Izaguirre, Accelerated molecular dynamics simulations of the octopamine receptor using GPUs: Discovery of an alternate agonist-binding position. *Proteins* 2016, *84*, 1480–1489.
- [77] D.H. de Jong, S. Baoukina, H.I. Ingólfsson, and S.J. Marrink, Martini straight: Boosting performance using a shorter cutoff and GPUs. *Comput. Phys. Commun.* 2016, *199*, 1–7.
- [78] A.Y. Shih, A. Arkhipov, P.L. Freddolino, and K. Schulten, Coarse grained protein–lipid model with application to lipoprotein particles. *J. Phys. Chem. B* 2006, *110*, 3674–3684.
- [79] J. Zhou, I.F. Thorpe, S. Izvekov, and G.A. Voth, Coarse-grained peptide modeling using a systematic multiscale approach. *Biophys. J.* 2007, *92*, 4289–4303.

- [80] L. Monticelli, S.K. Kandasamy, X. Periole, R.G. Larson, D.P. Tieleman, and S.J. Marrink, The MARTINI coarse-grained force field: Extension to proteins. *J. Chem. Theory Comput.* 2008, *4*, 819–834.
- [81] P. Spijker, B. van Hoof, M. Debertrand, A.J. Markvoort, N. Vaidehi, and P.A.J. Hilbers, Coarse grained molecular dynamics simulations of transmembrane protein-lipid systems. *Int. J. Mol. Sci.* 2010, *11*, 2393–2420.
- [82] D.H. de Jong, G. Singh, W.F.D. Bennett, C. Arnarez, T.A. Wassenaar, L.V. Schäfer, X. Periole, D.P. Tieleman, and S.J. Marrink, Improved parameters for the Martini coarse-grained protein force field. *J. Chem. Theory Comput.* 2013, *9*, 687–697.
- [83] T. Bereau and K. Kremer, Protein-backbone thermodynamics across the membrane interface. *J. Phys. Chem. B* 2016, *120*, 6391–6400.
- [84] S. Kmiecik, D. Gront, M. Kolinski, L. Wieteska, A.E. Dawid, and A. Kolinski, Coarse-grained protein models and their applications. *Chem. Rev.* 2016, *116*, 7898–7936.
- [85] S.J. Marrink, A.H. de Vries, and A.E. Mark, Coarse grained model for semiquantitative lipid simulations. *J. Phys. Chem. B* 2004, *108*, 750–760.
- [86] S.J. Marrink, H.J. Risselada, S. Yefimov, D.P. Tieleman, and A.H. de Vries, The MARTINI force field: Coarse grained model for biomolecular simulations. *J. Phys. Chem. B* 2007, *111*, 7812–7824.
- [87] S.J. Marrink and D.P. Tieleman, Perspective on the Martini model. *Chem. Soc. Rev.* 2013, *42*, 6801–6822.
- [88] K. Pluhackova and R.A. Böckmann, Biomembranes in atomistic and coarse-grained simulations. *J. Phys.: Condens. Matter* 2015, *27*, 323103.
- [89] S.O. Yesylevskyy, L.V. Schäfer, D. Sengupta, and S.J. Marrink, Polarizable water model for the coarse-grained MARTINI force field. *PLoS Comput. Biol.* 2010, *6*, 1–17.
- [90] F.B. Naughton, A.C. Kalli, and M.S.P. Sansom, Association of peripheral membrane proteins with membranes: Free energy of binding of GRP1 PH domain with phosphatidylinositol phosphate-containing model bilayers. *J. Phys. Chem. Lett.* 2016, *7*, 1219–1224.
- [91] S. Wu and H. Guo, Simulation study of protein-mediated vesicle fusion. *J. Phys. Chem. B* 2009, *113*, 589–591.
- [92] H.J. Risselada and H. Grubmüller, How SNARE molecules mediate membrane fusion: Recent insights from molecular simulations. *Curr. Opin. Struct. Biol.* 2012, *22*, 187–196.
- [93] F.J. van Eerden, M.N. Melo, P.W.J.M. Frederix, X. Periole, and S.J. Marrink, Exchange pathways of plastoquinone and plastoquinol in the photosystem II complex. *Nat. Comm.* 2017, *8*, 15214.
- [94] G. van Meer, D.R. Voelker, and G.W. Feigenson, Membrane lipids: Where they are and how they behave. *Nat. Rev. Mol. Cell Biol.* 2008, *9*, 112–124.
- [95] S.J. Marrink, V. Corradi, P.C.T. Souza, H.I. Ingólfsson, D.P. Tieleman, and M.S.P. Sansom, Computational modeling of realistic cell membranes. *Chem. Rev.* 2019, *119*, 6184–6226.
- [96] A.J. Markvoort, K. Pieterse, M.N. Steijaert, P. Spijker, and P.A.J. Hilbers, The bilayer-vesicle transition is entropy driven. *J. Phys. Chem. B* 2005, *109*, 22649–22654.
- [97] J.C. Shelley, M.Y. Shelley, R.C. Reeder, S. Bandyopadhyay, and M.L. Klein, A coarse grain model for phospholipid simulations. *J. Phys. Chem. B* 2001, *105*, 4464–4470.
- [98] T. Murtola, M. Karttunen, and I. Vattulainen, Systematic coarse graining from structure using internal states: Application to phospholipid/cholesterol bilayer. *J. Chem. Phys.* 2009, *131*, 055101.
- [99] W. Shinoda, R. DeVane, and M.L. Klein, Zwitterionic lipid assemblies: Molecular dynamics studies of monolayers, bilayers, and vesicles using a new coarse grain force field. *J. Phys. Chem. B* 2010, *114*, 6836–6849.
- [100] T.C. Moore, C.R. Iacovella, A.C. Leonhard, A.L. Bunge, and C. McCabe, Molecular dynamics simulations of stratum corneum lipid mixtures: A multiscale perspective. *Biochem. Biophys. Res. Commun.* 2018, *498*, 313–318.
- [101] A.J. Markvoort, P. Spijker, A.F. Smeijers, K. Pieterse, R.A. van Santen, and P.A.J. Hilbers, Vesicle deformation by draining: Geometrical and topological shape changes. *J. Phys. Chem. B* 2009, *113*, 8731–8737.
- [102] A.J. Markvoort, A.F. Smeijers, K. Pieterse, R.A. van Santen, and P.A.J. Hilbers, Lipid-

- based mechanisms for vesicle fission. *J. Phys. Chem. B* 2007, *111*, 5719–5725.
- [103] A.J. Markvoort and S.J. Marrink, Lipid acrobatics in the membrane fusion arena. In *Membrane fusion*, eds. L.V. Chernomordik and M.M. Kozlov, vol. 68 of *Current Topics in Membranes*, chap. 11, 259–294, Academic Press, Waltham, 2011.
- [104] K. Yang and Y.q. Ma, Computer simulations of fusion, fission and shape deformation in lipid membranes. *Soft Matter* 2012, *8*, 606–618.
- [105] P.G. de Gennes and H. Hervet, Statistics of “starburst” polymers. *J. Physique Lett.* 1983, *44*, 351–360.
- [106] T. Chang, K. Pieterse, M.A.C. Broeren, H. Kooijman, A.L. Spek, P.A.J. Hilbers, and E.W. Meijer, Structural elucidation of dendritic host–guest complexes by X-ray crystallography and molecular dynamics simulations. *Chem.–Eur. J.* 2007, *13*, 7883–7889.
- [107] T.M. Hermans, M.A.C. Broeren, N. Gomopoulos, A.F. Smeijers, B. Mezari, E.N.M. van Leeuwen, M.R.J. Vos, P.C.M.M. Magusin, P.A.J. Hilbers, M.H.P. van Genderen, N.A.J.M. Sommerdijk, G. Fytas, and E.W. Meijer, Stepwise noncovalent synthesis leading to dendrimer-based assemblies in water. *J. Am. Chem. Soc.* 2007, *129*, 15631–15638.

# Summary

## Molecular simulations of vesicles and dendrimers

Regulated transport of molecules is critical in drug delivery systems as well as in living cells. At the molecular level, targeted transport is handled by nanoparticles. In the cell these carriers are vesicles, i.e., spherical lipid bilayers enclosing a liquid, that can fuse with other membranes to deliver their contents. For drug delivery, where drug efficacy can be increased by releasing the drug at the afflicted location, apart from vesicles also polymeric nanoparticles are used. Among these, dendrimers are unique for their well-controlled branched architecture and, with ends functionalized to form binding sites, they are ideal for host-guest chemistry.

As the transitions during vesicle fusion and the interactions of the dendrimer host with individual guest molecules occur on small temporal and spatial scales, they are experimentally infeasible to observe directly; we therefore study both systems with molecular dynamics simulations. Because the required time and length scales are too large for conventional all-atom simulations, we use a coarse-graining approach wherein roughly four heavy atoms form a single particle. This greatly reduces the number of particles and interactions while smoother potentials furthermore enable larger time steps.

To resolve various hypotheses on the molecular mechanisms of vesicle fusion, we investigate fusion with an elementary model with one particle type for the solvent and two more to build the lipid's hydrophilic head and two hydrophobic tails. We demonstrate that small vesicles fuse when they spontaneously come into contact. In fact, contact is initiated by individual lipids that freely extend their tails into the interstice between membranes. The contact is subsequently stabilized by additional lipids, completing the stalk structure. Addressing an issue raised by conflicting predictions from elastic continuum models, the stalk is revealed to be composed of only the contacting monolayers, yet hydrophobic voids are prevented by lipids that freely tilt and splay. From there, anisotropic and radial expansion of the stalk are both valid pathways to the hemifusion diaphragm intermediate. When the diaphragm finally degrades, the vesicle is fully fused. The vesicle does not become spherical in the remainder of the simulation, however, because the lipid and water distribution is inappropriate and spontaneous reformation is slow. By introducing several model transmembrane proteins that facilitate water transport and lipid flip-flop, we show that equilibration of both is essential for spherical vesicles. In planar bilayers these transmembrane proteins aggregate; the intensity of aggregation not only depends on the hydrophobic mismatch with the bilayer,



but also on how well they fit together.

To increase our understanding of the poly(propylene imine) (PPI) dendrimer and its host-guest system analogue of urea-adamantyl-functionalized PPI (PPIUA) dendrimer and ureido acetic acid guests, we develop a comprehensive coarse-grained model. For this model, harmonic bond and angle potentials are derived from atomistic simulations with an iterative Boltzmann inversion scheme and the force field is based on thermodynamic data. Using this model, first dendrimers up to generation 7 are studied separately, effectively in a dilute solution. The dendrimers' size, shape, and branch distributions are in good agreement with atomistic simulations and SANS experiments. We find that the structural characteristics of these dendrimers stem from flexible chains constrained by configurational and spatial requirements; small dendrimers are alternatively rod-like and globular, large ones are more rigid and spherical. Concentrated solutions of dendrimers are difficult to assess at the molecular level experimentally. We study PPI dendrimers in dilute to melt conditions in large scale simulations. We find that with increasing concentration the dendrimer volume diminishes by expulsion of internal water, ultimately resulting in solvent filled cavities between stacked dendrimers. Challenging prior findings, a better calculation reveals that dendrimer interpenetration increases only slightly with concentration; even at high concentrations each dendrimer remains a distinct entity. Using the simulation data, we also demonstrate that structure factors computed analogously to experimental calculations already start to diverge at low concentrations from directly derived structure factors. PPIUA dendrimers combined with ureido acetic acid guests form dynamic patchy nanoparticles. Our simulations show that the architecture of the self-assembled macromolecular nanostructures is indeed dictated by the guest concentration. As multivalency is an effective approach to establish strong collective interactions, we systematically study guest concentration-dependent multivalent binding using mono-, bi-, and tetravalent guests. At low guest concentrations, multivalency clearly increases binding as tethered headgroups bind more often than free guests' headgroups. We find that despite an abundance of binding sites and regardless the spacer length, most of the tethered headgroups bind in close proximity. At high guest concentrations, the dendrimer becomes saturated with bound headgroups, independent of guest valency. However, in direct competition the tetravalent guests prevail over the monovalent ones. These findings demonstrate the advantage of multivalency at high as well as low concentrations.

Overall, this dissertation illustrates that molecular simulations, by providing a clear molecular picture acknowledging the disorderly nature of molecules, greatly benefit the study of nanoparticle systems at the nanoscale.

# Publications

A.F. Smeijers, A.J. Markvoort, K. Pieterse, and P.A.J. Hilbers, A detailed look at vesicle fusion. *Journal of Physical Chemistry B* 2006, *110*, 13 212–13 219.

A.F. Smeijers, K. Pieterse, A.J. Markvoort, and P.A.J. Hilbers, Coarse-grained transmembrane proteins: Hydrophobic matching, aggregation, and their effect on fusion. *Journal of Physical Chemistry B* 2006, *110*, 13 614–13 623.

A.J. Markvoort, A.F. Smeijers, K. Pieterse, R.A. van Santen, and P.A.J. Hilbers, Lipid-based mechanisms for vesicle fission. *Journal of Physical Chemistry B* 2007, *111*, 5719–5725.

Thomas M. Hermans, Maarten A.C. Broeren, Nikos Gomopoulos, A.F. Smeijers, Brahim Mezari, Ellen N.M. van Leeuwen, Matthijn R.J. Vos, Pieter C.M.M. Magusin, Peter A.J. Hilbers, Marcel H.P. van Genderen, Nico A.J.M. Sommerdijk, George Fytas, and E.W. Meijer, Stepwise noncovalent synthesis leading to dendrimer-based assemblies in water. *Journal of the American Chemical Society* 2007, *129*, 15 631–15 638.

A.J. Markvoort, P. Spijker, A.F. Smeijers, K. Pieterse, R.A. van Santen, and P.A.J. Hilbers, Vesicle deformation by draining: Geometrical and topological shape changes. *Journal of Physical Chemistry B* 2009, *113*, 8731–8737.

A.F. Smeijers, A.J. Markvoort, K. Pieterse, and P.A.J. Hilbers, Coarse-grained modelling of urea–adamantyl functionalised poly(propylene imine) dendrimers. *Molecular Simulation* 2016, *42*, 882–895.

A.F. Smeijers, A.J. Markvoort, K. Pieterse, and P.A.J. Hilbers, Coarse-grained simulations of poly(propylene imine) dendrimers in solution. *Journal of Chemical Physics* 2016, *144*, 074 903.

A.F. Smeijers, Koen Pieterse, Peter A.J. Hilbers, and Albert J. Markvoort, Multi-valency in a dendritic host–guest system. *Macromolecules* 2019, *52*, 2778–2788.



# Acknowledgments

Although the cover of this thesis only features my name, the scientific work contained within required a collaborative effort, as the credits at the start of each chapter attest. It is therefore with pleasure that I hereby express my appreciation for the people that helped me in completing this study.

My thanks go out to my promotor Peter Hilbers who introduced me to the field of computer simulations in the first place. Your fascination for emergent behavior in coarse-grained molecular dynamics simulations proved infectious. Our talks were consistently reinvigorating and insightful. When prompted, you seem always able to effortlessly suggest a fresh research approach to attempt. The ground work my copromotor Bart Markvoort together with Koen Pieterse laid with the coarse-grained lipid model established a great foundation for the vesicle fusion part of my research. I also made extensive use of the PumMa platform for parallel MD simulations; the atomistic extension for PumMa provided crucial input for the Boltzmann inversion process. Bart, over time you became my primary guide and sounding board. You were always available for sound advice, like how to best present the results or respond to peer review. You helped maintain a strategic overview which enhanced my research efforts. Every part of this thesis was scrutinized by you and with your keen sense of mathematics I am 120% certain that each equation in the dissertation is accurate. I value your stimulating guidance and commitment immensely. Koen Pieterse helpfully provided the original atomistic model of the ‘click dendrimer’. I furthermore thank you for your welcome insights into various chemical aspects. Your most striking contribution is undoubtedly the renderer you designed that is used for all the molecular images throughout this thesis. Its distinct style even landed Chapter 2’s vesicle fusion paper on the cover of *J. Phys. Chem. B*. I also appreciate you letting me occupy a corner in your old office and also computer storage room, and every lighthearted remark whenever you popped in. I further thank Bert Meijer and Thomas Hermans for offering the multivalent guest and dendritic host topic, and the people at the Institute for Complex Molecular Systems (ICMS) discussion meetings for helping maintain a broad perspective. I cordially thank the other members of the doctorate committee members, i.e., prof.dr.ir. Jan van Hest, prof.dr. Siewert-Jan Marrink, prof.dr. Giovanni Pavan, and chair prof.dr. Maarten Merks for reading and commenting on this dissertation and for their participation in my public defense of thesis proceedings.

In my time at the Computational Biology (CBio), formerly BioModeling and bioInformatics (BMI), research group, I have met many fine people that undoubtedly influenced this work in subtle ways through all kinds of meetings. I have to mention the academic staff: Peter, Huub, Dragan, Nico, Bart, Koen, Natal, Tom, Federica;

the support staff: Margret, Rina, Sylvia; and my fellow PhD students: Ronald, Anthony, Peter, Marvin, Luc, René, Willem, Bram, Willemijn, Christian, Joep, another Joep, Ceylan, Huili, Rik, Fianne, Yvonne, Zandra, Daniela, Job, Boris, Andrea, Gizem, Oscar, and Jonna. I was even assigned two students to coach: Diana and Haili. Apart from the meetings, I fondly remember joint activities such as PhD dinners, barbecues, canoe trips, weddings, Swedish wood chucking games, minigolf, after-hours Far Cry, movie nights, bouncy castle-style obstacle course, bowling, racing frogs, competing for the top spots in the Uisge Beatha knowledge quiz, escape room, and even getting chained to an escape table. Yet perhaps the most telling example of the old group spirit is the illustrious lunch logbook. A simple notebook turned the regular lunch hour discussions into a competition to interject the conversation with the funniest, most outrageous remark to score an entry in the logbook. Needless to say, it is best if its content remains forever lost. Of this group I must give a special shout-out to René, Willem, Luc, and Diana because with you guys the fun was rarely limited to a lunch hour and it extended well beyond the laboratory.

Then there are my extended group of college friends: Mark, Suzanne, René, Marijn & Sandro, Rikkert, and Virjanand. I know most of you since our start at university. Our recent get-together at René and Hong's place for a housewarming and Chinese New Year celebration was great fun. It reinforced the idea that we don't have to see each other often to have an good time like in the old days when we do meet. Rikkert and René, I am very glad the duties of this paranymp triad pact of ours are now fulfilled at last.

And last but not least a big thank you to my family, especially my parents Ad & Nellie for starting me on this path. I am truly grateful for your enduring support along the way.

# Curriculum vitae



Adrianus Franciscus (Sander) Smeijers was born on November 7, 1979 in Tilburg. After finishing VWO in 1998 at the Mill Hill College in Goirle, he studied Biomedical Engineering at the Eindhoven University of Technology. His external internship was done at the pharmaceutical company Organon in Oss. In August 2005 he graduated cum laude within the BioModeling and bioInformatics group of prof.dr. P.A.J. Hilbers on a coarse-grained molecular dynamics study of vesicle fusion and membrane-affecting proteins. In 2006 he started a PhD project at the Eindhoven University of Technology with prof. Hilbers' group, later renamed the Computational Biology group. In recent years he also did a couple of stints with consulting company Open Analytics for Janssen Pharmaceutica in Beerse, Belgium. The results of the PhD project are presented in this dissertation.







